Measurement and Application of Unusual NMR Parameters for the Structural Characterization of Organic Molecules

Zur Erlangung des akademischen Grades einer
DOKTORIN DER NATURWISSENSCHAFTEN
(Dr. rer. nat.)

von der KIT-Fakultät für Chemie und Biowissenschaften des
Karlsruher Instituts für Technologie (KIT)
genehmigte

DISSERTATION

von

Dipl.-Chem. Malin Christina Reller

KIT-Dekan: Prof. Dr. Reinhard Fischer
Referent: Prof. Dr. Burkhard Luy
Korreferent: Prof. Dr. Peter Roesky
Tag der mündlichen Prüfung: 19.07.2018

Ich versichere wahrheitsgemäß, die Arbeit selbstständig angefertigt, alle benutzten Hilfsmittel vollständig und genau angegeben und alles kenntlich gemacht zu haben, was aus Arbeiten anderer unverändert oder mit Änderungen entnommen wurde. Weiterhin versichere ich, dass der Inhalt dieser Arbeit bis auf die unten angegebenen Teilpublikationen noch nicht veröffentlicht wurde und dass ich eine solche Veröffentlichung nicht vor Abschluss des Promotionsverfahrens vornehmen werde.

Karlsruhe, 06.06.2018

. . . .

(Dipl.-Chem. Malin Christina Reller)

Publikationsliste

M. Reller, S. Wesp, M. R. M. Koos, M. Reggelin, B. Luy, “Biphasic Liquid Crystal and the Simultaneous Measurement of Isotropic and Anisotropic Parameters by Spatially Resolved NMR Spectroscopy”, *Eur. Chem. J.* **2017**, *23*, 13351–13359.

Abstract

Nuclear Magnetic Resonance (NMR) spectroscopy is an essential analytical tool for the structure determination of molecules, complementary to other analytical methods such as X-Ray spectroscopy and mass spectrometry. NMR spectroscopy has an outstanding role since it allows the analysis of molecules in solution. This is crucial for structural assignment, conformational study and dynamical studies of molecules for pharmaceutical research as well as in chemistry, biochemistry and other related fields.

With NMR spectroscopy several properties of the substances under investigation are accessible to determine and assign structures. The chemical shift for a particular nucleus leads to first indications of the surrounding chemical structure. The J coupling constant can lead to information about the neighboured nuclei and their network. Moreover, the nuclei act as small magnets which influence each other through space. This property can refine the information about the three-dimensional structure of molecules and is known as Nuclear Overhauser Enhancement (NOE). Beside these usual NMR parameters, other parameters such as Residual Dipolar Couplings (RDCs), Residual Quadrupolar Couplings (RQCs), Residual Chemical Shift Anisotropys (RCSAs), Pseudo Contact Shifts (PCSs) increase the obtainable structural information. The first three parameters (RDC, RQC and RCSA) depend on the orientation of the molecule in the static magnetic field. In liquid state NMR spectroscopy, they are averaged out to zero. To measure these parameters, it is crucial to partially align the analytes. Therefore, a molecular grid, e. g., a strained polymer gel or a liquid crystalline phase, is added to the samples to restrain free molecular tumbling. Under such circumstances, RDC, RQC and RCSA can be measured and used as orientational and structural constraints for the structural assignment of the analyte. This method enables obtaining structures, in cases where isotropic NMR parameters are not sufficient for a clear determination of the analyte's structure. A PCS is induced by the interaction of unpaired electrons and a magnetic moment of a nucleus. The interaction perturbs the chemical shift and the resulting spectra lead to structural information about the molecule under investigation.

The further development of existing methods to measure the aforementioned parameters, which increase potentially the spread and refine the outcome of NMR data, is an important task to further improve the NMR-based refinement of molecular structures. The scope of this work is to develop and improve various aspects of isotropic and anisotropic data acquisition for structure refinement.

To show how RDCs contribute to the structural assignment of small molecules, they are measured and applied to refine the structure of 8-5(c)-DFA.

Since quaternary carbons have no directly bound protons, ${}^{2}J_{\mathrm{CH}}$ and corresponding ${}^{2}D_{\mathrm{CH}}$ couplings are among the scarce NMR parameters providing valuable structural information. Especially the sign is very important for the determination of ${}^{2}D_{\mathrm{CH}}$ couplings, as ${}^{2}J_{\mathrm{CH}}$ coupling can have both negative and positive sign and the sign of the ${}^{2}D_{\mathrm{CH}}$ coupling yields

structural information and cannot be neglected. Existing experiments do not allow the determination of the sign of these couplings for every chemical moiety. The experiments presented herein, the ω_1-coupled ADEQUATE and the ω_1-coupled BIRD^r ADEQUATE, measure the sign of the coupling relative to a neighboring $^1J_{\mathrm{CH}}$ coupling and are therefore applicable to a broader range of molecules. Both experiments are evaluated with several molecules and the values verified with literature values and other experimental values.

In medicine, Magnetic Resonance Imaging (MRI) is an important technique to elucidate the tissue distribution in humans. The imaging technique can be transferred to the small molecule approach. Thereby, an additional spatially resolved dimension is introduced in the spectra, which can reveal the sample constitution over the sample height. The resulting spectra provide information about Larmor frequency shifts due to field homogeneity and sample constitution over the sample. With the presented experiments, isotropic and anisotropic data are accessible in one sample. The experiments are applied to a biphasic liquid crystalline sample, showing both an isotropic and an anisotropic phase. The resulting data is applied to IPC for structure refinement, assignment of the diastereotopic methylene groups and for enantiodiscrimination of (−)-IPC from (+)-IPC.

Europium complexes have proven to have potential for the differentiation of enantiomers in NMR. Here, Eu(BINOL)$_3$Li$_3$ and Eu(pnb)$_3$ are studied as chiral lanthanide complexes and compared with the commercially available Eu(hfc)$_3$. Especially, Eu(BINOL)$_3$Li$_3$ shows a good separation of enantiomers. Additionally, Eu(BINOL)$_3$Li$_3$ is analyzed as enantiodiscriminating complex at low magnetic fields, which can potentially increase the use of tabletop spectrometers for the enantiodifferentiation.

Zusammenfassung

Die hochauflösende Kernmagnetresonanzspektroskopie (engl. *Nuclear Magnetic Resonance (NMR)*) ist aufgrund ihrer Vielseitigkeit eine der wichtigsten Analysetechniken unserer Zeit. Gegenüber anderen Analysemethoden, wie der Röngtenbeugung und Massenspektrometrie, lassen sich mit der NMR durch Untersuchung von Molekülen in Lösung wertvolle zusätzliche Informationen erhalten. Vor allem in der Chemie, Biochemie und der pharmazeutischen Forschung ergeben sich dadurch ergänzende Möglichkeiten zur Struktur - und Dynamikbestimmung von Molekülen.

Für Moleküle in Lösung ermöglichen die aus den NMR Spektren abgeleiteten Parameter in vielen Fällen eine vollständige Strukturaufklärung. Besondere Bedeutung besitzen in diesem Kontext die chemischen Verschiebung, verschiedene Kopplungskonstanten und der abstandsabhängige Nuclear Overhauser Enhancement (NOE). Die chemische Verschiebung wird aufgrund der Abschirmung durch die induzierten magnetischen Momente der umgebenden Bindungselektronen erhalten und ist dadurch für jeden Kern abhängig von der ihn umgebenden chemischen Struktur. Kopplungen werden durch Wechselwirkung der Atomkerne untereinander verursacht. Skalare Kopplungen werden dabei durch die Bindungselektronen vermittelt. Sie geben Aufschluss über die Bindungssituation. Der NOE gibt die Wechselwirkung der Kerne durch den Raum wieder, wodurch die dreidimensionale Struktur von Moleküle aufgeklärt werden kann. In einigen Fällen reicht es jedoch nicht aus, lediglich die erwähnten Parameter zu ermitteln, um eine Molekülstruktur vollständig aufzuklären. Die Grenze wird beispielsweise bei der Zuordnung diastereotoper Methylengruppen und bei der relativen Konfigurations- und Konformationsbestimmung kleiner Moleküle erreicht. Viel wertvoller sind dann anisotrope NMR Parameter, die bei der Stukturaufklärung helfen können und normalerweise in der Festkörper NMR gemessen werden. Aufgrund der starken Orientierung in Festkörpern dominieren diese anisotropen Parameter die Gestalt der Spektren. Dipolare Kopplungen beeinflussen die Spektren so stark, dass chemische Verschiebung und skalare Kopplungen nicht mehr messbar sind. Die dipolare Kopplung kann jedoch mit Orientierungsmedien skaliert werden und somit die Messung von dipolaren Restkopplungen unter Erhalt der chemischen Verschiebung ermöglichen. Bekannte Orientierungsmedien sind Flüssigkristalle, gestreckte Polymergele und paramagnetische Ionen.

In dieser Arbeit wurden verschiedene Ansätze verfolgt, um die Bestimmung anisotroper Parameter zu verbessern. Zum einen wurden neue Experimente entwickelt, oder bestehende Experimente optimiert, die die Eignung der NMR auf diesem Gebiet verbessern. Weitere Ergebnisse der Forschungsarbeit beziehen sich auf Anwendungen und Probenpräparation. Zunächst wird die Bedeutung der anisotropen NMR Parameter anhand der relativen Konfigurationsbestimmung eines kleinen Moleküls, der 8-5(c)-DFA, verdeutlicht. Für die Messung an zweiphasigen Proben werden verschiedene NMR Experimente weiterentwickelt, wie das räumlich selektiv anregende 1D-^{13}C Spektrum und das ent-

sprechend CLIP-HSQC Spektrum und das 1D-^{13}C und CLIP-HSQC mit einer zusätzlich eingeführten z-aufgelösten Dimension. Des weiteren werden zwei Experimente zur vorzeichenempfindlichen Messung von $^{2}J_{\mathrm{CH}}$-Kopplungskonstanten entwickelt, das ω_1-coupled ADEQUATE und das ω_1-coupled BIRD^{r} ADEQUATE. Zusätzlich werden Lanthanoidkomplexe auf ihre Verwendungsmöglichkeit als Lanthanoidverschiebungsreagenzien getestet, um beispielsweise die Enantiomerenreinheit per NMR bestimmen zu können.

Mit den räumlich selektiv gemessenen Experimenten werden neue Experimente vorgestellt, die es durch die Verwendung einer zweiphasigen Probe erlaubt gleichzeitig anisotrope und isotrope NMR Parameter zu bestimmen. Der außerordentliche Nutzen der Methode wird anhand der Bestimmung der Stereochemie und der Zuordnung diastereotoper Methylengruppen eines Testmoleküls ((−)-IPC) demonstriert.

Neben anisotropen Parametern besitzen auch $^{2}J_{\mathrm{CH}}$-Kopplungen große Bedeutung in der Strukturaufklärung von Molekülen. Die vorzeichenempfindliche Bestimmung dieser Kopplung ist besonders hilfreich, wenn das zu untersuchende Molekül quarternäre Kohlenstoffatome enthält, diese wichtige Information ist jedoch mit herkömmlichen Experimenten selten zugänglich. Mit dem ω_1-coupled ADEQUATE und das ω_1-coupled-BIRD^{r} ADEQUATE werden zwei Experimente vorgestellt, die die Vorzeichenbestimmung der $^{2}J_{\mathrm{CH}}$-Kopplung nicht relativ zu anderen bekannten Kopplungskonstanten bestimmt. Dadurch ist es vielseitiger einsetzbar als bisher bekannte Experimente. Die Methode wird anhand mehrerer Moleküle überprüft und durch Vergleich mit Literaturwerten und anderen experimentellen Daten verifiziert.

Für die Induktion von unterschiedlichen chemischen Verschiebungen für Enantiomere sind chirale Europium- und Yttriumkomplexe bereits bekannt, angesichts neuer Entwicklungen im Bereich kleiner NMR Spektrometer sind jedoch weitere chiral separierende Additive höchst wünschenswert. In dieser Arbeit werden Eu(BINOL)$_3$Li$_3$ und Eu(pnb)$_3$ als Lanthanoidshiftreagenzien verwendet und mit dem kommerziell erhältlichen Eu(hfc)$_3$ verglichen. Dabei zeigt sich für Eu(BINOL)$_3$Li$_3$ mit den getesteten Molekülen eine gute Trennung der Signale der Enantiomere sowohl bei niedrigen Magnetfeldern als auch bei hohen Magnetfeldern.

Contents

1. Introduction

Nuclear Magnetic Resonance (NMR) spectroscopy is a very versatile analytical method, which is used in many different fields of research, such as chemistry, biochemistry and pharmaceutics.[1] NMR enables structure elucidation,[2] food control[3] and monitoring chemical reactions,[4] as well as observation of ligand interactions of proteins.[5] In contrast to other analytical methods, like X-Ray diffraction and mass spectrometry, NMR permits measuring molecules in solution. Therefore, besides structural information also dynamical insights can be obtained.[6]

Structure determination is achieved by revealing the electron density distributions by measuring the chemical shift, which is influenced by the first and second sphere of the surrounding atoms.[7, 8] Bond situation and orientation as well as evidence for inter- and intramolecular interactions are obtained with scalar and dipolar couplings. For instance, scalar couplings can be used to determine the dihedral angle between two protons with the Karplus curve.[9] With dipolar couplings-based Nuclear Overhauser Enhancement (NOE) measurements, assignment of three dimensional structures can be achieved up to distances of 5 Å.[10]

All these properties (chemical shift, scalar coupling and NOE) are short ranged. Consequently, the configuration of stereogenic centers or diastereotopic methylene groups cannot be assigned in all cases. To overcome this restriction, dipolar couplings can be reintroduced by strained polymer gels or liquid crystalline phases which restrict the free tumbling of the molecules and Residual Dipolar Couplings (RDCs) are measurable.[11] The RDCs contain information about the orientation of the vector between two nuclei and the outer static magnetic field. The RDC can be used for prochiral assignment e. g., diastereotopic methylene groups,[12] for conformational studies of pharmacological compounds,[13] for the determination of relative configuration of stereocenters,[14–16] for enantiomeric discrimination of small molecules [17, 18] and for the analysis of proteins, e. g., for the determination of the exact angle between two non-parallel α-helices,[19] or the differentiation between straight or bent helical structures [20] and the relative orientation of protein domains.[21] The most commonly measured RDCs are the ones for nuclei separated by one bond that are in most cases proton-carbon pairs or proton-nitrogen pairs. RDCs have different sign depending on the orientation of the molecule relative to the static magnetic field. Therefore, the sign of the ${}^{1}D_{\mathrm{CH}}$ coupling contributes to the structural information. However, ${}^{1}J_{\mathrm{CH}}$ couplings for proton-carbon pairs are always positive and the sign of ${}^{1}D_{\mathrm{CH}}$ can be derived easily. This is different for ${}^{2}J_{\mathrm{CH}}$ couplings, as they can have both positive and negative sign. However, in molecules with low amount of protons ${}^{2}D_{\mathrm{CH}}$ couplings to quaternary carbons can add valuable structural information about the molecule. Therefore, experiments for the determination of the sign and magnitude for ${}^{2}J_{\mathrm{CH}}$ and ${}^{2}D_{\mathrm{CH}}$ are of special interest. Especially for quaternary carbons, there does not exist reliable and feasible experiments for the measurement of both sign and magnitude of ${}^{2}J_{\mathrm{CH}}$

couplings for every existing spin system. Hence, a new method to measure ${}^2J_{\mathrm{CH}}$ couplings for quaternary carbons is investigated and pushed to the boarders of its applicability.

Enantiodifferentiation by NMR is achieved by introducing a chiral medium into the sample. This medium can either be a chiral alignment medium to induce different alignment of the enantiomers,[22] a chiral Lanthanoide Shift Reagent (LSR) or Chiral Solvating Agent (CSA), which both form diastereotopic complexes with the analytes under investigation and lead to different chemical shifts for enantiomers.[23] The differentiation of racemic mixtures from their *meso*-compound is especially challenging since their physical properties are very similar. Since, they share the same molecular formula but differ in their stereoisomerism. $\mathrm{Eu(BINOL)_3Li_3}$ and $\mathrm{Eu(pnb)_3}$ are introduced as new LSR to induce Pseudo Contact Shifts (PCSs) for the differentiation of racemic mixtures from their *meso*-compound. Hence, the PCSs induced by the two complexes are first investigated and then NMR experiments to differentiate the racemic mixture from the *meso*-compound are applied. Additionally, the complexes are used at low magnetic field to differentiate enantiomers. This could potentially improve the utility of these spectrometers.

Magnetic Resonance Imaging (MRI) is a well known imaging method for human bodies. The physical principle can be transferred to the small molecule measurement. This is achieved by introducing an additional spatially resolved dimension, which is along the direction of the static magnetic field. The spatially resolved dimension leads to important information on spatially varying samples. Either the sample homogeneity, the Larmor frequency distribution or the sample composition is revealed.[24] Therefore, this can be a powerful method to measure biphasic samples. In this thesis, novel spatially resolved experiments are introduced and five biphasic samples characterized. Without the presented experiments, the spectra of both phases would overlap and no meaningful information about the samples would be obtained.

This thesis is structured as follows. First, there is a theoretical introduction into the main principles of NMR, how RDCs are induced, measured and used for structure elucidation and an explanation of the main pulse programs used in the thesis are given (Chapter 2). Second, a structure determination and relative stereogenic center determination by NOE and RDCs of an diferulic acid derivative is presented (Chapter 3). Third, the differentiation of enantiomers by NMR with LSR is evaluated (Chapter 4). Fourth, pulse sequences for the measurement of biphasic samples are presented and applied to them (Chapter 5). Fifth, sign sensitive measurements of ${}^2J_{\mathrm{CH}}$ couplings are evaluated and a new method to measure them especially for quaternary carbons is presented (Chapter 6). Finally, a summary and conclusion for the presented experiments and results is given (Chapter 7).

2. NMR Parameters

Isotropic NMR parameters are measured in isotropic liquids, whereas anisotropic NMR parameters dominate solid state spectra. Both kind of methods have their strengths in application and structure determination of molecule. To enhance the information content isotropic and anisotropic parameter can be measured simultaneously in weakly oriented samples. For these samples isotropic NMR parameters are retained and anisotropic NMR parameters are scaled down. In the following chapter isotropic and anisotropic NMR parameters will be explained along with the preparation of partially aligned samples, their properties, and how to measure, extract and evaluate structural information.

2.1. Nuclear Spin and the Quantum Mechanical Description

The simplest model to describe processes in NMR, is the classical vector model. The vector model describes the macroscopic effect of a magnetic field on nuclei which has a nuclear spin $I \neq 0$. This property of a nuclear spin ($I \neq 0$) in a magnetic field B_0 is an intrinsic source of angular momentum which is called "nuclear spin angular momentum". The nuclear spin angular momentum can have integer (1, 2, 3...) or half-integer ($\frac{1}{2}$, $\frac{3}{2}$,...). The simplest case and most of the nuclei measured in NMR are nuclei with $I = \frac{1}{2}$, as for example ^{1}H and ^{13}C nuclei. They have two possible orientations parallel and anti-parallel to the magnetic field. The resulting macroscopic magnetization in the magnetic field B_0 is described by the Bloch equations.[25] The vector model describes the chemical shift but not spin-spin couplings. Full description of the vector model is outside the scope of this thesis, but for further the reader is referred to literature [25] or conventional NMR books. The most important information from the vector model is the ability of nuclei with spin $I \neq 0$ to induce a free induction decay in a coil by precession in the x, y-plane.

The quantum mechanical description is more essential as it helps to understand how most pulse sequences work. The quantum mechanical approach does not deal directly with the observables. It deals with the spin state of the spin system and the time evolution of the spin states. The state of a system is described by the wave function $\Phi(t)$. The Hamiltonian operator for a single nuclear spin in a magnetic field is:

$$\hat{H}_{\text{single spin}} = -\gamma_i \mathrm{B}_0 \hat{I}_{iz} \tag{2.1}$$

γ_i is the gyromagnetic ratio and a fundamental property of a nucleus i. For protons (^{1}H) the gyromagnetic ratio is 42.576 $\mathrm{MHz\,T^{-1}}$. Additionally, the natural abundance is high with 99.9 %. Therefore, protons are the most commonly measured nuclei in NMR. $\hat{I}_{iz}$ is the operator for the z-component of the nuclear spin angular momentum and represents the component which interacts with the static magnetic field B_0. B_0 per definition is oriented along z.

For nuclei with $I = \frac{1}{2}$, $\hat{I}_{iz}$ has two eigenfunctions, which are characterized by the quantum number m. m is either $m = +\frac{1}{2}$ or $m = -\frac{1}{2}$ for nuclei with $I = \frac{1}{2}$.[26] The corresponding eigenfunctions are $\psi_{+\frac{1}{2}}$ and $\psi_{-\frac{1}{2}}$ with the eigenvalue:

$$\begin{aligned} \hat{I}_{iz}\psi_{+\frac{1}{2}} &= +\frac{1}{2}\hbar\psi_{+\frac{1}{2}} \\ \hat{I}_{iz}\psi_{-\frac{1}{2}} &= -\frac{1}{2}\hbar\psi_{+\frac{1}{2}} \end{aligned} \tag{2.2}$$

More generally written:

$$\hat{I}_{iz}\psi_m = m\hbar\psi_m \tag{2.3}$$

Each value of the quantum number m represents an eigenvalue as $m\hbar$.

The functions $\psi_{+\frac{1}{2}}$ and $\psi_{-\frac{1}{2}}$ are eigenfunctions of the Hamiltonian $\hat{H}_{\text{single spin}}$ shown in Equation 2.1.

$$\begin{aligned} \hat{H}_{\text{single spin}}\psi_m &= -\gamma_i \mathrm{B}_0 \hat{I}_{iz}\psi_m \\ &= -m\gamma_i \mathrm{B}_0 \psi_m \end{aligned} \tag{2.4}$$

For a nucleus with $I = \frac{1}{2}$ in a static magnetic field, two eigenvalues with two corresponding energy levels result:

$$E_m = -m\hbar\gamma_i \mathrm{B}_0 \tag{2.5}$$

The energy difference between these two levels is measured in NMR spectroscopy. Usually, they are referred to as α (lower energy level for nuclei with positive gyromagnetic ratio) and β (higher energy level for nuclei with positive gyromagnetic ratio) state.

$$\begin{aligned} \Delta E_{\alpha\rightarrow\beta} &= E_\beta - E_\alpha \\ &= \frac{1}{2}\hbar\gamma_i \mathrm{B}_0 - \frac{1}{2}\hbar\gamma_i \mathrm{B}_0 \\ &= \gamma_i\hbar \mathrm{B}_0 \end{aligned} \tag{2.6}$$

As a photon with a certain frequency ν has an energy of $h\nu$, the frequency of the energy gap $\Delta E_{\alpha\rightarrow\beta}$ is found dividing by h. It follows:

$$\begin{aligned} \nu_{\alpha\rightarrow\beta} &= \Delta E_{\alpha\rightarrow\beta}/h \\ &= \gamma_i \mathrm{B}_0/2\pi \end{aligned} \tag{2.7}$$

According to Equation 2.7, the frequency transition for a single spin is measured at $\gamma_i \mathrm{B}_0/2\pi$ Hz. This frequency transition is specific for a single spin and called the Larmor frequency, which is defined as:

$$\begin{aligned} \nu_{\alpha\rightarrow\beta} &= -\nu_0 \\ \nu_0 &= -\gamma_i \mathrm{B}_0/2\pi \end{aligned} \tag{2.8}$$

or as:

$$\omega_0 = 2\pi\nu_0 = -\gamma_i \mathrm{B}_0 \tag{2.9}$$

The Larmor frequency is dependent on the magnetic field strength and different for nuclear spins according to their gyromagnetic ratio. Moreover, the Larmor frequency depends on the chemical environment of a nucleus. This phenomenon is called chemical shift and explained in more detail in the next section.[26]

For the detailed quantum mechanical approach, I refer to books of theoretical physics, e. g. [27].

2.2. Isotropic NMR Parameters

The most important NMR parameters are the chemical shift, J couplings and NOE.

2.2.1. Chemical Shift

The chemical shift is a measure for the deshielding of the nuclear spin by the electrons of the surrounding bonds. First, an electronic current in the bonds is generated by the external magnetic field B_0. Then, the circulating electrons induce a magnetic field (B_i) which shields or deshields (adds or subtracts) to B_0 of the nuclear spins. Therefore, the electrons vary the Larmor frequency ω_0. The local field B_{loc} of the nuclear spin is defined as:

$$B_{\text{loc}} = B_0 + B_i. \tag{2.10}$$

B_i is the induced field. The strength of the induced field is linear dependent to B_0 and dependent on the chemical shielding tensor σ_i. Therefore, B_i can be rewritten as:

$$B_i = \sigma_i \cdot B_0. \tag{2.11}$$

σ_i is a $3x3$ matrix, since the chemical shielding depends on the orientation of the molecule in the magnetic field. The chemical shift is measured relative to an arbitrarily set reference value δ_0. Therefore, B_{loc} changes to:

$$B_{\text{loc}} = \delta_0 + \delta_{\text{iso}} + \Delta\delta. \tag{2.12}$$

δ_{iso} is the isotropic chemical shift and $\Delta\delta$ is the chemical shift anisotropy. Since B_0 is along z, the Hamiltonian for the chemical shielding reduces to:

$$\hat{H}_i^{\text{CS}} = \hbar\omega_0(1 - \sigma_i)\hat{I}_z. \tag{2.13}$$

In the secular approximation, only the zz-term of Equation 2.13 contributes to the chemical shift. Therefore, the Hamiltonian for the chemical shift reduces to:

$$\hat{H}_i^{\text{CS}} = \hbar\omega_0(1 - \sigma_{i,zz})\hat{I}_z. \tag{2.14}$$

Following the definition before $(1 - \sigma_{zz})$ is equal to $(\delta_0 + \delta_{\text{iso}} + \Delta\delta_{zz})$. Additionally, $\Delta\delta_{zz}$ is equal to zero in isotropic liquids:

$$\begin{aligned} \hat{H}_i^{\text{CS}} &= \omega_0(\delta_0 + \delta_{\text{iso}} + \Delta\delta_{zz})\hat{I}_z \\ \hat{H}_i^{\text{CS}} &= \omega_i\hat{I}_{i,z} \\ \hat{H}_i^{\text{CS}} &= 2\pi\nu_i\hat{I}_{i,z}. \end{aligned} \tag{2.15}$$

ω_i is the Larmor frequency of the nucleus i which contains the frequency of the applied magnetic field and the chemical shift.

The chemical shifts of the nuclei are determined relatively to the receiver frequency of the NMR instrument, which can be set at any point of the spectrum. Therefore, the frequency of a peak is shown at the frequency relative to the receiver frequency ω_{rx} which is called offset frequency ω_{offset} and defined as follows:

$$\omega_{\text{offset}} = \omega_i - \omega_{\text{ref}} \tag{2.16}$$

ω_i is the frequency of the nuclear spin. The chemical shift depends on the strength of the applied static magnetic field. To remove this dependency, the ppm scale is introduced:

$$\delta[\text{ppm}] = 10^6 \frac{\omega_i - \omega_{\text{ref}}}{\omega_{\text{rx}}} \tag{2.17}$$

If the receiver frequency is somewhere in the spectrum the difference between ω_{rx} and ω_{ref} is negligible.[28, 29]

2.2.2. Scalar Coupling

The scalar coupling (or *J* coupling) is mediated by chemical bonds and can show which nuclei are close to one another via the bonding network. Physically, it is the influence of the bonding electrons on the magnetic fields between the nuclear spins and mediated by the Fermi contact interaction as the main interaction. Beside the chemical shift, the scalar coupling provides a direct manifestation of the chemical bond. Therefore, a *J* coupling present between two coupled nuclei, splits the signal in the NMR spectrum. The *J* coupling is only measurable intramolecular and up to five chemical bonds for protons. The coupling constant, which is measured in the spectra, is field independent and can be associated to spin states and the number of coupled spins.

The *J* coupling Hamiltonian is given as:

$$\hat{H}_{\text{ij}}^{\text{iso}} = 2\pi J_{\text{ij}}(\hat{I}_{\text{ix}}\hat{I}_{\text{jx}} + \hat{I}_{\text{iy}}\hat{I}_{\text{jy}} + \hat{I}_{\text{iz}}\hat{I}_{\text{jz}}) \tag{2.18}$$

In the weak coupling case, the *J* coupling constant is at least five times smaller than the chemical shift difference between the coupling nuclei ($J_{ij} > 5\Delta\delta\omega_i j$). Therefore, the terms $\hat{I}_{\text{ix}}\hat{I}_{\text{jx}}$ and $\hat{I}_{\text{iy}}\hat{I}_{\text{jy}}$ are small and the Hamiltonian for the *J* coupling reduces to:

$$\hat{H}_{\text{ij}}^{\text{iso, weak}} = 2\pi J_{\text{ij}}\hat{I}_{\text{iz}}\hat{I}_{\text{jz}} \tag{2.19}$$

In the strong coupling limit, the frequency separation of the two coupled spin is in the range of the coupling constant. In this limit, the strong coupling Hamiltonian contributes to the coupling and leads to higher order spectra. The coupling constants cannot be extracted from the resulting multiplet as in the weak coupling case.

The *J* coupling has a sign. In most of the cases, it is positive for spins with the same sign of the gyromagnetic ratio and negative for spins with opposite signs in gyromagnetic ratio. The sign and size of long-range *J* coupling are variable and depend on, e. g., the molecular geometry.[29] They can be used for information about the conformation of the measured molecule. The most famous relationship between the ${}^3J_{\text{HH}}$ coupling and the dihedral angle between two protons is described by the empirically determined Karplus curve.[9] Depending on the nuclei and the number of bonds involved in the scalar couplings, they cover a range up to 250 Hz for proton-carbon pairs.

For further details on *J* coupling constants, the reader is encouraged to read these references [30, 31].

2.2.3. Dipolar coupling

To understand the concept of Dipolar Couplings (DCs), it is convenient to look at spins in the classical picture. Classically, spins are small magnets with an inherent rotation at their Larmor frequency. The spins are not directly aligned along the static magnetic field B_0, but integration over the fast rotating magnets leads to a secular magnetic moment, which is parallel or anti-parallel to B_0 (see Figure 2.1). For two spins I and S, the magnetic moment of spin I is dependent on r^{-3} of the magnetic field with respect to the internuclear distance to the magnet moment of spin S. Additionally, the dipolar couplings depend on θ relative to the axis of the magnetic field, which is the angle between the internuclear vector and the outer static magnetic field. θ and Θ are identical because both spins I and S are oriented along B_0. The magnetic field of spin I influences the static magnetic field experienced by spin S. This influence is the Dipolar Coupling and can be written as:

$$D_{IS} = -\frac{h\gamma_I\gamma_S\mu_0}{16\pi^2}\langle\frac{1}{r_{IS}^3}(3cos^2\Theta - 1)\rangle \tag{2.20}$$

γ_I and γ_S are the gyromagnetic ratios of the nuclei I and S. Θ is the angle between the internuclear vector and B_0. r_{IS} is the distance between spin I and spin S. The couplings are averaged over time for the distance and the angle as indicated by the brackets.

In liquid state NMR, dipolar couplings are averaged to zero out due to isotropic tumbling. They are not directly measurable but contribute to the Nuclear Overhauser Enhancement (NOE).[32]

The NOE is a cross relaxation effect, which describes the magnetization transfer between spins by dipolar coupling. For two isolated protons, the NOE is defined as follows:

$$\sigma^{\text{noe}} = \frac{\hbar\mu_0^2\gamma_H^4}{40\pi^2}\frac{\tau_C}{r^6}\left[\frac{6}{1\omega_0^2\tau_C^2}\right] \tag{2.21}$$

It is dependent on the gyromagnetic ratio of the involved spins (γ_H), the permeability of the vacuum (μ_0), the distance between the two nuclei (r), the Larmor frequency of the protons (ω_0) and the characteristic correlation time of the tumbling of the molecule (τ_C). With the NOE internuclear relaxation rates can be determined, which are proportional to the spin-spin distance according to the r^{-6} dependency shown in Equation 2.21. The cross relaxation can be measured by the intensities of NOE cross signals and used to determine absolute distances in molecules if at least one distance in the molecule is known for reference.[1]

2.2.4. Limitation of Isotropic NMR Parameters

The isotropic NMR parameters are mostly used by chemists for structure elucidation and they might be sufficient for most molecules. However, these interactions are short ranged and some structural problems cannot be solved without further parameters. For instance, stereogenic centers cannot always be determined (not even relatively) and the assignment of diastereotopic methylene groups might be impeded. Additionally, the structure elucidation of molecules with small amount of NMR-active nuclei can be

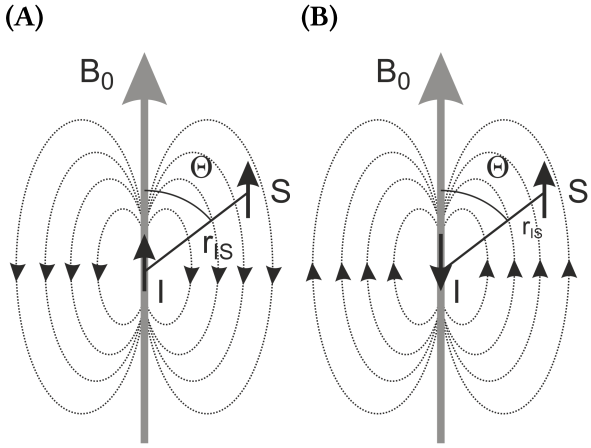

Figure 2.1.: Schematic representation of dipolar couplings in the magnetic field B_0. The magnetic moment of spin I adds up to B_0 and influences spin S. Spin I and S are equally populated, therefore the signal is split by $2D_{\mathrm{IS}}$. The scheme is adapted from [32].

challenging. To overcome this restriction, dipolar couplings can be used. They are usually measured in solid state NMR but dominate the spectra and other properties are not measurable as e. g. the *J* coupling. In isotropic samples, the dipolar couplings are averaged out. Therefore, the aim is to weakly orient a sample by preserving most of the isotropic parameters, like *J* couplings and the chemical shift resolution (δ). This is achieved by a partial orientation induced by an appropriate alignment medium, which restricts the movement of the analyte molecule. Hence, the anisotropic NMR parameters are scaled to be measurable as residual anisotropic parameters by preserving the chemical shift resolution.

2.3. Anisotropic NMR Parameters

2.3.1. Residual Dipolar Couplings (RDCs)

The Dipolar Coupling (DC) are in the range of several thousand Hertz. For a proton-carbon pair, in which the carbon is sp^3 hybridized, the internuclear distance is 109 pm and parallel to B_0, the DC is 23 kHz. One can recall the equation from before. The only difference is that the distance between the nuclei is assumed as constant. Therefore, the averaging of the coupling is resulting from the angle Θ between the internuclear vector to the static magnetic field.

$$D_{IS} = -\frac{h\gamma_I\gamma_S\mu_0}{16\pi^2}\left(\frac{1}{r_{IS}^3}(3\langle\cos^2\Theta\rangle - 1)\right) \tag{2.22}$$

In an intermediate state between total alignment (solid state) and isotropic averaging (solution), it is possible to measure RDCs. In this state, it is possible to retain the chemical shift information of the nuclei and measure an RDC, which contains the former explained information about the orientation of the internuclear vector of two nuclear spins and the outer magnetic field. The intermediate state is obtained if the isotropic tumbling is constrained such that some orientation is preserved. The DCs are scaled down and so called Residual Dipolar Coupling (RDC) are preserved. As the tumbling is time averaged during the measurement and the molecules are oriented for short time periods compared to the measurement time, the DCs are scaled down e. g., to 11.5 Hz dipolar coupling or 23 Hz splitting. By measuring RDCs, the correlation of distant parts of the molecule is possible. The central applications include the determination of relative configuration of chiral and prochiral centers, as well as conformational studies of biologically active molecules. In contrast to NOE, DCs have a distance dependence of $\frac{1}{r^3}$ and are measurable over a distance up to 7.5 Å.[33]

The most common RDCs are measured between proton carbon pairs. They are accessible if the solute molecule is measured isotropically for the extraction of ${}^1J_{\mathrm{CH}}$ coupling and aligned (anisotropically) for the ${}^1T_{\mathrm{CH}}$ couplings. The ${}^1D_{\mathrm{CH}}$ coupling is available by the relationship:

$$T = J + 2D \tag{2.23}$$

Usually, 2^1D_{CH} couplings is extracted and referred to as ${}^1D_{\mathrm{CH}}$ splitting.

2.3.2. Residual Chemical Shift Anisotropy (RCSA)

The chemical shift has anisotropic contributions which are averaged out in liquids. In solid state NMR and under weakly aligned conditions, the chemical shift anisotropy is measurable. It results from the anisotropic electronic distribution of a chemical moiety. Differences to the isotropic chemical shifts can be significant for nuclei in chemical groups with particularly large CSA, e. g., the ^{13}C chemical shift in a carbonyl group.

The RCSA displays a similar angular dependence as RDCs and can also be used as a molecular constraint in structure refinement. The chemical shift $\delta = \delta_{\mathrm{ref}} + \delta_{\mathrm{iso}} + \Delta\delta$ has an isotropic and an anisotropic part. It is defined as follows:

$$\delta^{\mathrm{RCSA}} = \sum_{\alpha,\beta=x,y,z} \delta_{\alpha\beta}\sigma_{\alpha\beta}\mathrm{A}_{\alpha\beta} \tag{2.24}$$

σ^{iso} is the isotropic chemical shift, $\sigma_{\alpha\beta}^{\mathrm{aniso}}$ is the anisotropic chemical shift, $\mathrm{A}_{\alpha\beta}$ is the Alignment tensor for the molecule. $\cos(\theta_{ik}), \cos(\theta_{jk})$ are the angles between the principal axes of the chemical shift tensor and an arbitrary frame. $\theta_{i,j}$ are the elements of the order tensor in the molecular frame.[22]

Depending on the chemical group, the RCSA are small in comparison to other anisotropic NMR parameter. Therefore, high resolution and precise chemical shift referencing is needed. Especially, the chemical shift referencing is challenging, as the isotropic reference spectrum and the anisotropic spectra must be preferably measured under the same conditions and avoid other chemical shift perturbations (as, for example, the alignment medium). The best method to measure under isotropic and anisotropic conditions is the stretching apparatus published by Kuchel et al.[34] Other methods include the variable angle spinning NMR for Liquid Crystal (LC) and variable angle NMR for strained gels. At the magic angle of 54.7°, isotropic chemical shifts are measured and the difference in chemical shifts to measurements at other angles is the RCSA.[1]

2.3.3. Residual Quadrupolar Couplings (RQCs)

Residual Quadrupolar Couplings (RQCs) are relevant for nuclei with spin $I = 1$ or higher, but are mostly relevant for deuterium ($I = 1$). The distribution of charges in these nuclei is non-spherical and leads to nuclear quadrupole moments Q. The nuclei do not only interact with the external and local magnetic fields but with the Electric Field Gradient (EFG) at these nuclei.

For deuterium, the quadrupolar coupling $\Delta\nu_Q$ reduces to:

$$\Delta\nu_Q = \frac{3}{4}\left(\frac{e^2qQ}{h}\langle 3\cos^2\theta - 1\rangle\right) \tag{2.25}$$

e is the charge of the deuterium, Q is the electric quadrupolar moment and q is the zz-contribution of the field gradient tensor. In Equation 2.25, it can be seen that RQCs have the same angular dependence as RDC. The electric field gradient is aligned within 1° with the directly attached heteronucleus. Therefore, RQCs contain the same information as one-bond RDCs.[35, 36] Therefore, RQCs can be used to determine the alignment strength of an alignment medium. However, this is only possible as reliable measure for different alignment media for solvents with a cylindrical symmetry, such as chloroform or methanol. As these molecules are highly symmetric, one RQC is enough to obtain the alignment tensor for the molecule. Consequently, $\Delta\nu_\text{Q}$ of these molecules can be used to compare alignment strengths of different alignment media. For other solvents, the comparison of RQC is not meaningful and gives no information about the alignment strength.

Next to measuring alignment strength $\Delta\nu_\text{Q}$ is also used to judge sample homogeneity, e. g the alignment and the homogeneity of the magnetic field by its distribution over the sample.[24]

2.4. Measurement of Anisotropic NMR Parameters

Anisotropic NMR parameters can either be measured in solid state NMR or in partially oriented samples. In partially oriented samples the orientation of a solute is neither static like in solid states, nor completely averaged out as in solution. This is achieved by introducing an alignment medium, which is an oriented molecular grid restraining the molecular tumbling. In principal, there exist three methods to weakly align a molecule, LC media, polymer gels and paramagnetic tags. Paramagnetic tags will not be explained here, for further details on this method see [37].

The requirements for an alignment medium are analyte and solvent compatibility, low residual NMR signals, weak alignment so that J couplings are one order of magnitude bigger than D couplings, low cost, simple sample preparation and homogeneity. In addition, chiral media can be used for enantiodifferentiation.

2.4.1. Liquid Crystals (LC)

The first RDCs were measured in a Liquid Crystal (LC) medium from Saupe and Englert in 1963.[38] They measured benzene in a p-azoxyanisole derivate. LC media are typically lyotropic mesophases, which are formed at a compound specific concentration of the LC. The alignment in a static magnetic field results from a spontaneous orientation of the LC. Due to the spontaneous orientation, an anisotropic grid arises in which the solute aligns.[39] LC media are limited to a certain concentration and temperature range. Due to the concentration limit, a minimum alignment strength is not arbitrarily adjustable. The minimum alignment strength in apolar media is relatively high compared to water, since, for example, Pf1 phage induce an alignment at very low concentration.[40].

LC media that are available for water are Pf1 phage[40, 41], bicelles[42–45], cellulose crystallites[46] to just mention a few. *n*-Alkylpentaethylene glycol can be used with water and DiMethyl SulfOxide (DMSO) in a range of 3 % to 13 %.[47]

The most widely used Lyotropic Liquid Crystalline (LLC) medium is Poly-γ-Benzyl-L-Glutamate (PBLG), which can be used with $CDCl_3$, CD_2Cl_2, benzene, dioxane, TetraHydroFurane (THF) and DiMethylFormamide-d_7 (DMF-d_7).[48–55] Poly-γ-Benzyl-D-Glutamate (PBDG) is the enantiomer to PBLG.[56] Other liquid crystalline phases based on polyamino acids are Poly-γ-Ethyl-L-Glutamate (PELG) and the enantiomer Poly-γ-Ethyl-D-Glutamate (PEDG) and Poly-ϵ-CarboBenzyloxy-L-Lysine (PCBLL) and Poly-ϵ-CarboBenzyloxy-D-Lysine (PCBDL).[52, 57] The main advantage of all these alignment media, is their commercial availability and the chemical inertness.[55]

Other LLC media are polyguanidines,[58] polyisocyanides,[59] and polyacetylenes[60, 61].

2.4.2. Polymer Gels

Strain-induced alignment in a polymer gel (SAG) was first presented by Deloche and Samulski 1981.[11] Polymers used to strain are cross-linked polymers which swell in the compatible solvents. The polymer network forms a molecular grid and if this network is stretched or compressed it leads to an anisotropic matrix. The solutes partially align by the interaction with the polymer gel. Deloche and Samulski introduced an alignment on a polymer by swelling it in a NMR tube. By reaching the walls of the tube, it self-aligns by the restrictions of the wall of the tube. Other methods to align a polymer gel is the stretching apparatus introduced from Kuchel *et al.*[34] and the compressing apparatus introduced from Gayathri *et al.*[62]

Numerous different polymer gels exist, since the polymers do swell in specific solvents and are therefore not compatible with every solvent. Here, a short overview over the most important polymer gels are given.

Poly(AcrylAmide) (PAA) is cheap and compatible with water. It is widely used to align enzymes and proteins.[63–65] Co-polymeric cross-linked PAA is also compatible with DMSO.[66] Gelatine is a triple helical, chiral alignment medium, which can be used as well as PAA with water and in mixtures of water and DMSO. Because of its chirality, it can be used to discriminate enantiomers.[18] If gelatine is irradiated by accelerated electrons, it is cross-linked and compatible with pure DMSO.[67] Other biopolymers as alignment media used with water are collagen [68] and gellan gum.[69]

Poly(VinylACetate) (PVAC) can be used with DMF-d_7, methanol, DMSO, acetone and acetonitrile.[70] Poly(AcryloNitrile) (PAN) can be used with DMSO and DMF-d_7.[71] Moreover, PAN can be used also perdeuterated to eliminate residual NMR signals.[72]

PolyStyrene (PS) is an alignment medium which can be used with $CDCl_3$, CD_2Cl_2, benzene, dioxane and THF. It is easy to synthesize, robust and if it is deuterated, it is interesting for low concentrated samples.[73–75] Another very versatile alignment medium is Poly(DiMethylSiloxane) (PDMS). PDMS can tolerate very apolar solvents, like hexane and is widely used as an apolar gel. The biggest advantage is that it has only one residual NMR signal at 0.1 ppm.[76, 77] A further alignment medium is Poly(MethylMethAcrylate) (PMMA) which has similar properties to PS. In contrast to PS, it has no aromatic signals. Consequently, PMMA can be used if signals of PS impede the signal analysis because of signal overlap.[78].

Further versatile alignment media are PolyUrethane (PU) and PEO-DA. PU is compatible with $CDCl_3$, CD_2Cl_2, DMF-d_7, THF, TriFluoroEthanol (TFE), acetone and hexane.[79] PEO-DA is compatible with a lot of different solvents: water, DMF-d_7, DMSO, $CDCl_3$, CD_2Cl_2, methanol, acetonitrile, TFE, toluene and acetone.[80]

One additional alignment medium is a cross-linked PBLG gel, which can be used with chloroform and for enantiodifferentiation.[81]

2.4.3. The Alignment Tensor

Assuming a rigid molecule in solution, the time averaged dipolar couplings are measured in partially aligned samples. With θ being the internuclear vector relative to the static magnetic field and the static magnetic field B_0, the effective dipolar couplings can be written as before in Equation 2.22. In isotropic solution $\langle\cos^2\Theta\rangle = \frac{1}{3}$ and all anisotropic interaction is averaged to zero. In partially aligned samples, the anisotropic interaction is not completely averaged. The description of the orientational averaging of the whole molecule is achieved by an arbitrary frame of reference x, y, z which is fixed in the rigid molecule itself. Consequently, the molecule is fixed and the magnetic field vector is changing. The distribution of the magnetic field can then be described by the probability tensor $\mathbf{P}$, which is a 3×3 matrix and describes the probability of finding the magnetic field along all axes. $\mathbf{P}_{\alpha\beta}$ are the probabilities to find the magnetic field along the three axes.

$$\mathbf{P}_{\alpha\beta} = \langle\cos\theta_\alpha, \cos\theta_\beta\rangle \; \alpha, \beta = (x, y, z) \tag{2.26}$$

Thus, $\cos^2\Theta$ can be represented by this probability distribution:

$$D_{IS} = -\frac{\hbar\gamma_I\gamma_S\mu_0}{16\pi^2}\left(\frac{1}{r_{IS}^3}(3\overrightarrow{r_{IS}}^T\mathbf{P}\overrightarrow{r_{IS}} - 1)\right) \tag{2.27}$$

$\mathbf{P}$ is symmetric along the diagonal and the values along the diagonal have to add up to 1 ($P_{xx}, P_{yy}, P_{zz} \overset{!}{=} 1$). Therefore, $\mathbf{P}$ is completely described by 5 independent parameters. The alignment tensor $\mathbf{A}$ is more common than the probability tensor $\mathbf{P}$ for the description of anisotropic parameters. They are related as follows:

$$\mathbf{A} = \mathbf{P} - \frac{1}{3}\mathbf{1} \tag{2.28}$$

where $\mathbf{1}$ is the unity matrix. $\mathbf{A}$ is a traceless, symmetric tensor and needs five parameters for full description. With the alignment tensor, the dipolar couplings can be calculated for a rigid molecule as shown in Equation 2.29.

$$D_{IS} = -\frac{\hbar\gamma_I\gamma_S\mu_0}{16\pi^2}\left(\frac{1}{r_{IS}^3}(3\overrightarrow{r_{IS}}^T\mathbf{A}\overrightarrow{r_{IS}})\right) \tag{2.29}$$

2.4.3.1. SVD-fit

If at least five RDCs from non-parallel vectors can be measured, the alignment tensor can be calculated. The alignment tensor is obtained by minimization of the difference between observed and computed RDCs.

$$\mathbf{A} = \begin{pmatrix} A_{xx} & A_{xy} & A_{xz} \\ A_{yx} & A_{yy} & A_{yz} \\ A_{zx} & A_{zy} & A_{zz} \end{pmatrix} = \begin{pmatrix} A_{xx} & A_{xy} & A_{xz} \\ A_{xy} & A_{yy} & A_{yz} \\ A_{xz} & A_{yz} & -A_{xx} - A_{yy} \end{pmatrix} \tag{2.30}$$

The determination of the alignment tensor is achieved by a Singular Value Decomposition (SVD)-fit. The SVD fit obtains a solution for a system of linear equations. This transformation returns an alignment tensor with the least-squares deviation between calculated and experimental RDCs. When the alignment tensor is calculated, RDCs can be calculated for each configuration and conformation of a molecule. How well the structures fit to the experimental RDCs can be evaluated by the Cornilescu Q-factor.[82] The Cornilescu Q-factor is calculated as shown in Equation 2.31.

$$Q = \frac{\text{RMSD}}{\text{RMS}} = \sqrt{\frac{\sum(D_i^{\text{exp}} - D_j^{\text{calc}})^2}{\sum D_i^{\text{exp}}}} \tag{2.31}$$

The Q-factor is the Root Mean Square Deviation (RMSD) of the experimental and calculated RDCs divided by the Root Mean Square (RMS) of the measured values. Therefore, it is scaled to the average size of the measured RDCs. Q should be as small as possible to give a good quality of the fit. It is significantly smaller as 1 at best. Usually, a fit which gives a Cornilescu Q-factor of below 0.2 is considered a good fit.

Another way to evaluate RDCs is the Pearson-correlation coefficient R.

$$R = \frac{\frac{1}{n}\sum^n\left[(x_{\text{exp}} - \overline{x}_{\text{exp}})(x_{\text{calc}} - \overline{x}_{\text{calc}})\right]}{\sqrt{\frac{1}{n}\sum^n(x_{\text{exp}} - \overline{x}_{\text{exp}})^2}\sqrt{\frac{1}{n}\sum^n(x_{\text{calc}} - \overline{x}_{\text{calc}})^2}} \tag{2.32}$$

n is the number of measured RDCs. x_{exp} and x_{calc} are the experimental and calculated RDCs. $\overline{x}_{\text{exp}}$ and $\overline{x}_{\text{calc}}$ are the mean values, calculated by $\overline{x} = \frac{1}{n}\sum_{i=1}^n x_i$. If the values for the measured and calculated RDCs correlate positively, R has a value of 1. If they correlate negatively, the R $= -1$. For all other values, the values show no good linearity.

The program used in this thesis to perform a SVD-fit was MSpin-RDC.[83]

2.5. Product Operator Formalism

To describe the evolution and transfer of coherences and the evolution of couplings through a pulse sequence, the product operator formalism can be used. They can be applied with a series of rules.

The state of the spin system is expressed by the density operator $\hat{\rho}$. For a single spin system, the active part of this density operator is a linear combination of nuclear angular spin momentum operators $\hat{I}_x$, $\hat{I}_y$ and $\hat{I}_z$.

$$\hat{\rho}(t) = a_x(t)\hat{I}_x + a_y(t)\hat{I}_y + a_z(t)\hat{I}_z \tag{2.33}$$

$a_{x,y,z}(t)$ vary with time and are related to the macroscopic x-, y- and z-magnetization. By using this relation, the interpretation of spectra is really fast. $\hat{I}_{x,y,z}$ are operators for the x-, y- and z-components of the nuclear spin angular momentum. The density operator $\hat{\rho}$ varies with time. Therefore, the time evolution of $\hat{\rho}(t)$ is calculated by:

$$\hat{\rho}(t) = \exp(-i\hat{H}t)\hat{\rho}(0)\exp(i\hat{H}t) \tag{2.34}$$

$\hat{\rho}(0)$ is usually known and the Hamiltonian $\hat{H}$ varies during pulses and delays. With $i\hat{H}t = i\phi\hat{B}$, the equation from above can be rewritten as:

$$\hat{\rho}(t) = \begin{cases} \hat{\rho}(0), & for[\hat{B}, \hat{\rho}(0)] = 0 \\ \cos(\phi)\hat{\rho}(0) + \sin(i\phi)[\hat{B}, \hat{\rho}(0)], & for[\hat{B}, \hat{\rho}(0)] \neq 0 \end{cases} \tag{2.35}$$

Instead of writing the complete expression, generally these calculations can be rewritten as:

$$\hat{\rho}(0) \xrightarrow{i\phi\hat{B}} \hat{\rho}(t) \tag{2.36}$$

Depending on the Hamiltonian $\hat{H}$, different kinds of evolution of $\hat{\rho}(0)$ can be calculated. The Hamiltonian $\hat{H}$ during free precession is:

$$\hat{H}_{\text{free}} = \Omega_i\hat{I}_{iz} \tag{2.37}$$

Ω_i is the offset of the nuclei i. The following equation has to be solved for the time dependent density function for the evolution of chemical shift:

$$\hat{\rho}(t) = \exp(-i\hat{H}t)\hat{\rho}(0)\exp(i\hat{H}t)\hat{\rho}(t) = \exp(-i\Omega\hat{I}_zt)\hat{I}_x\exp(i\Omega\hat{I}_zt) \tag{2.38}$$

The result of this equation is:

$$\hat{\rho}(t) = \cos(\Omega t)\hat{I}_x + \sin(\Omega t)\hat{I}_y \tag{2.39}$$

It means that the magnetization starts along the x-axis and rotates towards the y-axis. Using the above mentioned notation (see Equation 2.36, the evolution of the state $\hat{I}_x$ can be expressed as:

$$\hat{I}_x \xrightarrow{\Omega\hat{I}_zt} \cos(\Omega t)\hat{I}_x + \sin(\Omega t)\hat{I}_y \tag{2.40}$$

The Hamiltonian $\hat{H}$ for a hard pulse is:

$$\hat{H}_{\text{x, hard pulse}} = \omega_1 \hat{I}_x \tag{2.41}$$

ω_1 is the radio frequency field strength of the pulse. The index x indicates that the pulse rotates the magnetization around the x-axis. In the arrow notation the initial state $\hat{I}_{iz}$ evolves as follows:

$$\hat{I}_{iz} \xrightarrow{\omega_1 \hat{I}_x t_p} \cos(\omega_1 t_p)\hat{I}_{iz} - \sin(\omega_1 t_p)\hat{I}_{iy} \tag{2.42}$$

t_p is the duration of the pulse. Since, $\omega_1 t_p$ results in an excitation angle α, the equation can be rewritten as:

$$\hat{I}_{iz} \xrightarrow{\alpha \hat{I}_x} \cos(\alpha)\hat{I}_{iz} - \sin(\alpha)\hat{I}_{iy} \tag{2.43}$$

For 180° pulses, $\cos(\alpha) = -1$ and $\sin(\alpha) = 0$. Therefore, the equation is:

$$\hat{I}_{iz} \xrightarrow{180^\circ \hat{I}_x} -\hat{I}_{iz} \tag{2.44}$$

The result is a change of sign for the initial magnetization. For 90° pulses, $\cos(\alpha) = 0$ and $\sin(\alpha) = 1$. Therefore, the equation is:

$$\hat{I}_{iz} \xrightarrow{90^\circ \hat{I}_x} -\hat{I}_{iy} \tag{2.45}$$

Beside the Hamiltonian for free precession and a hard pulse (see Equations 2.37 and 2.41), the Hamiltonian for scalar coupling (see Equation 2.46) is important for the understanding of pulse sequences, as the coupling transfers coherence from one spin to a second spin.

$$\hat{H} = \pi J_{ij} 2\hat{I}_{iz}\hat{I}_{jz} \tag{2.46}$$

How the second spin j is introduced can be seen in Equation 2.47.

$$\hat{I}_{ix} \xrightarrow{\pi J_{ij} 2\hat{I}_{iz}\hat{I}_{jz}} \cos(\pi J_{ij})\hat{I}_{ix} + \sin(\pi J_{ij}) 2\hat{I}_{ix}\hat{I}_{jy} \tag{2.47}$$

As the operators for chemical shift and scalar coupling are commuting, the order, in which they are considered, is not relevant. In Table 2.1, the most important product operator transformations for pulses, chemical shift and coupling evolution are summarized. In the product operator formalism, the relaxation time is always neglected and pulses are assumed as infinitesimally short. For further details, the interested reader might look into [84] or for a more pictorial description [85].

2.6. One-Dimensional Experiments

A one-dimensional experiment is the easiest NMR experiment. The magnetization of one nucleus is excited by a 90° pulse and directly detected. In terms of product operators, the following happens:

Table 2.1.: Summary of important product operator transformations for radio frequency pulses, chemical shift and coupling evolution. Table according to [85].

Pulses	90° Pulses
$\hat{I}_z \xrightarrow{\beta \hat{I}_{y,x}} \hat{I}_z \cos(\beta) \pm \hat{I}_{x,y} \sin(\beta)$	$\hat{I}_z \xrightarrow{90^\circ \hat{I}_{y,x}} \pm \hat{I}_{x,y}$
$\hat{I}_{x,y} \xrightarrow{\beta \hat{I}_{x,y}} \hat{I}_{x,y}$	$\hat{I}_{x,y} \xrightarrow{90^\circ \hat{I}_{y,x}} \mp \hat{I}_z$
$\hat{I}_{x,y} \xrightarrow{\beta \hat{I}_{y,x}} \hat{I}_{x,y} \cos(\beta) \pm \hat{I}_z \sin(\beta)$	
Scalar coupling	Chemical shift
$\hat{I}_{iz} \xrightarrow{2\pi J_{ij} t \hat{I}_{iz} \hat{I}_{jz}} \hat{I}_z$	$\hat{I}_z \xrightarrow{\Omega t \hat{I}_z} \hat{I}_z$
$\hat{I}_{ix} \hat{I}_{jy} \xrightarrow{2\pi J_{ij} t \hat{I}_{iz} \hat{I}_{jz}} \hat{I}_{ix} \hat{I}_{jy}$	$\hat{I}_{x,y} \xrightarrow{\Omega t \hat{I}_z} \hat{I}_{x,y} \cos(\Omega t) \pm \hat{I}_{y,x} \sin(\Omega t)$
$\hat{I}_{ix,iy} \xrightarrow{2\pi J_{ij} t \hat{I}_{iz} \hat{I}_{jz}} \hat{I}_{ix,iy} \cos(\pi J_{ij} t) \pm \hat{I}_{iy,ix} \hat{I}_{jz} \sin(\pi J_{ij} t)$	
$\hat{I}_{ix,iy} \hat{I}_{jz} \xrightarrow{2\pi J_{ij} t \hat{I}_{iz} \hat{I}_{jz}} \hat{I}_{ix,iy} \hat{I}_{jz} \cos(\pi J_{ij} t) \pm \hat{I}_{iy,ix} \sin(\pi J_{ij} t)$	

$$\begin{aligned}
&\hat{I}_{1z} \xrightarrow{\frac{\pi}{2} \hat{I}_x} -\hat{I}_{1y} \\
&-\hat{I}_{1y} \xrightarrow{\hat{I}_z \omega_1 t} -\hat{I}_{1y} \cos(\omega_0 t) + \hat{I}_{1x} \sin(\omega_0 t) \\
&\xrightarrow{2\hat{I}_{1z} \hat{I}_{2z} \pi J_{12} t} -\hat{I}_{1y} \cos(\omega_0 t) \cos(\pi J_{12} t) + \hat{I}_{1x} \hat{I}_{2z} \cos(\omega_0 t) \sin(\pi J_{12} t) \\
&+\hat{I}_{1x} \sin(\omega_0 t) \cos(\pi J_{12} t) + \hat{I}_{1y} \hat{I}_{2z} \sin(\omega_0 t) \sin(\pi J_{12} t)
\end{aligned} \tag{2.48}$$

Generally, during acquisition both chemical shift and homonuclear and heteronuclear couplings evolve. In proton spectra, the heteronuclear coupling is only visible in the ^{13}C satellites, which are only 1 % of the signal intensity due to the low natural abundance of ^{13}C. In 1D ^{13}C spectra, the heteronuclear coupling to protons is usually suppressed by decoupling and the homonuclear coupling again only present as satellites since the probability of two carbons in one molecule is 0.01 %.

2.7. Two-Dimensional Experiments

Two- or more-dimensional experiments are used in structure determination to increase the resolution and the information about the molecule, which might be hidden in crowded one-dimensional spectra. Generally, two or more dimensional experiments are built up of a preparation, evolution (t_1), a mixing and a detection (t_2) plus relaxation period. By changing the preparation, evolution or the mixing period, different experiments can be realized. Depending on the number of incremented time delays which are in the sequence, the number of dimensions is changed. To obtain a two-dimensional spectrum with a frequency in each dimension, a Fourier transform along t_1 and t_2 has to be performed.[85] Here, the two-dimensional pulse sequences to record CLIP-HSQC, HSQC-TOCSY and INADEQUATE spectra are described.

2.7.1. CLIP-HSQC

The Heteronuclear Single-Quantum Correlation (HSQC) sequence correlates the proton chemical shifts to the chemical shifts of their directly bound carbons. Therefore, in spectral assignment by NMR it is an important experiment. In the conventional HSQC experiment, first the proton polarization is transferred via an Insensitive Nuclei Enhanced by Polarization Transfer (INEPT) to carbon polarization. Then, the carbon chemical shift evolves during t_1 and is transferred back to proton magnetization. During t_2, carbons are decoupled. Otherwise, the signals are split in the direct dimension by the ${}^{1}J_{\mathrm{CH}}$ coupling constant.

The CLean In-Phase (CLIP)-HSQC sequence is used to determine ${}^{1}J_{\mathrm{CH}}$ couplings and ${}^{1}T_{\mathrm{CH}}$ couplings for the calculation of ${}^{1}D_{\mathrm{CH}}$ splittings. It was published by Enthart *et al.* and is shown in Figure 2.2. In contrast to the conventional HSQC, the sequence has an additional 90° pulse on carbon before the start of the acquisition and no carbon decoupling during t_2. The additional 90° pulse is called the CLIP pulse and transforms anti-phase magnetization that has developed during the sequence because of mismatch of the coupling constant during the back-transfer to a multi quantum state, which is not detectable.[86]

For better performance all 90° and 180° pulses on carbon and proton are replaced by shaped pulses referred to as Broadband Excitation By Optimized Pulses (BEBOP)[87–91], Broadband Inversion By Optimized Pulses (BIBOP)[89, 92] and Broadband Universal Rotation By Optimized Pulses (BURBOP)[74, 93, 94]. Concurrent 90° and 180° pulses on both channels were replaced by the corresponding Broadband Excitation and time-reversed Broadband Excitation (BEBE$^{\mathrm{tr}}$), time-reversed Broadband Excitation and Broadband Excitation (BE$^{\mathrm{tr}}$BE) and Broadband Universal Broadband Inversion (BUBI) pulse sandwiches.[95] To increase the tolerance of different ${}^{1}J_{\mathrm{CH}}$ and ${}^{1}T_{\mathrm{CH}}$ couplings, a compensated INEPT and back-transfer step can be used.[96, 97] There also exist fast experiments and proton decoupled versions of this experiment.[98, 99]

The extraction of ${}^{1}J_{\mathrm{CH}}$ coupling and the procedure to determine errors in the couplings is described in [14].

2.7.2. HSQC-TOCSY

The HSQC-TOtal Correlation SpectroscopY (TOCSY) sequence is used for n-bond correlation of ^{13}C and ^{1}H nuclei. Equal to the HSQC, the HSQC-TOCSY first excites protons and transfers coherence via INEPT to carbons. During t_1, ^{13}C chemical shift evolves. Afterwards a back-transfer to protons and last a TOCSY mixing scheme is applied.[100, 101] The experiment is sensitive as protons are excited and measured. The resolution in the indirect dimension is increased, since ^{13}C chemical shifts are well spread.

Additionally, the HSQC-TOCSY pulse sequence can be run as a spin state selective pulse sequence. By recording two spectra the In-Phase (IP) and Anti-Phase (AP) spectrum, ${}^{n}J_{\mathrm{CH}}$ couplings can be determined sign sensitive relative to ${}^{1}J_{\mathrm{CH}}$ coupling. The ${}^{1}J_{\mathrm{CH}}$ coupling

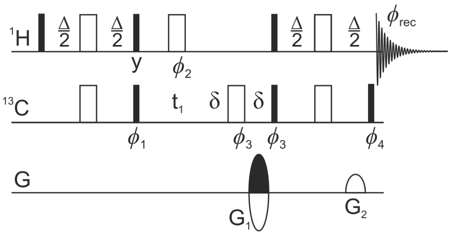

Figure 2.2.: CLIP-HSQC sequence. black filled narrow boxes represent 90° pulses, broad light boxes represent 180° pulses; Pulse phases are x unless indicated otherwise; Pulse phases are $\phi_1 = \text{x}, -\text{x}$, $\phi_2 = 4(\text{x}), 4(-\text{x})$, $\phi_3 = 2(\text{x}), 2(-\text{x})$, $\phi_4 = \text{x}, -\text{x}$, $\phi_{\text{rec}} = -\text{x}, \text{x}, \text{x}, -\text{x}$. Δ is matched to $\frac{1}{2\ ({}^1J_{\text{CH}})}$. Gradient strengths were $\text{G}_1 = 80\,\%$, $\text{G}_2 = 20.1\,\%$. Phase sensitive detection in the indirect dimension is achieved by Echo/AntiEcho on gradient G_1 and phase shifting of ϕ_3 and ϕ_{rec} by 180° for every second increment. For better performance all 90° and 180° pulses on carbon and proton were replaced by BEBOP[87–91], BIBOP[89, 92]- and BURBOP[74, 93, 94] pulses and the BEBE$^{\text{tr}}$, BE$^{\text{tr}}$BE and BUBI pulse sandwiches.[95] The pulse sequence was first presented from Enthart *et al.*[86].

is usually positive. This is important for the determination of long-range RDCs, as long-range RDCs as well as ${}^2J_{\text{CH}}$ couplings can have both positive and negative sign. With this sequence no coupling determination of ${}^nJ_{\text{CH}}$ to quaternary carbon is possible and not all protons might be reachable by the TOCSY mixing scheme.[102]

2.7.3. INADEQUATE

The Incredible Natural-Abundance DoublE-QUantum Transfer Experiment (INADEQUATE) experiment allows the identification of directly bound ^{13}C atoms. Consequently, carbon networks can be identified with it. The experiment excites and detects carbon magnetization and at first, a one-dimensional version was published by Bax *et al.*[104] Since the one-dimensional experiment can lead to overlap, a two-dimensional version was developed.[105] The sensitivity of the experiment is low, as ^{13}C nuclei have a natural abundance of 1 % and a low gyromagnetic ratio γ_C compared to ^{1}H nuclei. The probability of finding two carbon nuclei in one molecule is $0.01 \times 0.01 = 10^{-4}$. The probability for three carbon nuclei is too low, consequently this case can be excluded. Moreover, most ${}^1J_{\text{CC}}$ couplings are in the range of 30 Hz to 60 Hz, which is a completely different range then ${}^2J_{\text{CC}}$ or ${}^3J_{\text{CC}}$ coupling. Hence, only adjacent carbon nuclei evolve double quantum coherence.

The INADEQUATE spectrum shows two signals in the direct dimension at the same frequency for the indirect dimension. This means that the two carbons are adjacent.

In the next sections, the evolution of the double quantum coherence present during t_1 and the selection of the double quantum coherence is presented.

2.8. Introduction into Double Quantum Spectroscopy

As was explained in Section 2.5, product operators can be used to calculate the effect of pulses and evolution periods of spins during a pulse sequence. The result of the calculations

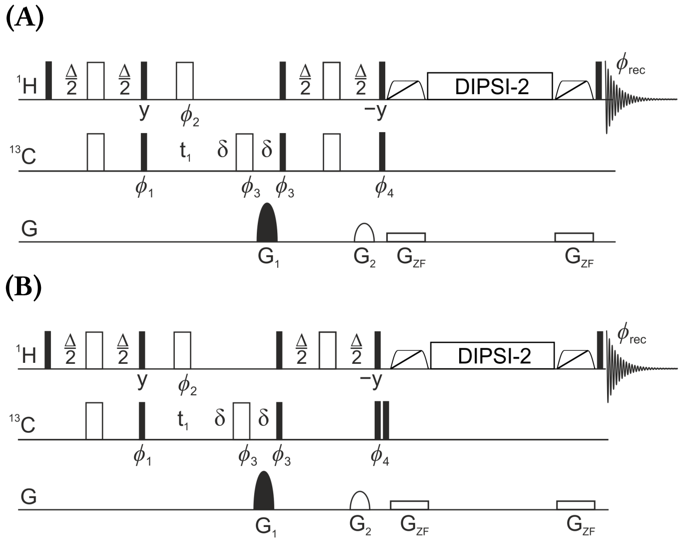

Figure 2.3.: IPAP-HSQC-TOCSY sequences. (A) IP HSQC-TOCSY. (B) AP HSQC-TOCSY.[102] black filled narrow boxes represent 90° pulses, broad light boxes represent 180° pulses; Pulse phases are $\phi_1 = x, -x$, $\phi_2 = x, x, -x, -x$, $\phi_3 = 4(x), 4(-x)$, $\phi_4 = x, x, -x, -x$, $\phi_{\text{rec}} = x, -x, x, -x, -x, x, -x, x$. Δ is matched to $\frac{1}{2\ (^1J_{\text{CH}})}$. Gradient strengths were $G_1 = 80\,\%$, $G_2 = 20.1\,\%$. ϕ_1 is incremented according to States-TPPI for phase sensitive detection. Trapezoid boxes rectangular represent smoothed Chirp pulses with 50 kHz sweep width and a duration of 30 ms and 50 ms. The gradient strength of G_{ZF}] of corresponding length was calibrated according to [103]. For better performance all 90° and 180° pulses on carbon were replaced by BEBOP[87–91], BIBOP[89, 92]- and BURBOP[74, 93, 94] pulses.

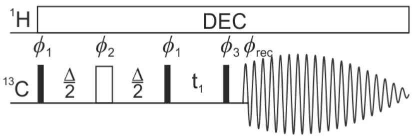

Figure 2.4.: Pulse sequence for the INADEQUATE. Δ is matched to $\frac{1}{2\ (^1J_{\text{CC}})}$ coupling ($^1J_{\text{CC}}$ = 40 Hz to 60 Hz). Phase cyclings are done according to [106]. Phase sensitive in the indirect dimension is achieved in States-TPPI fashion by incrementing ϕ_1 and ϕ_2 by 45° every increment.

shows how spectra could appear in theory. How different coherence orders are selected and what they are, was not considered until now. In two-dimensional NMR, coherence orders, their manipulations and their selection is the key to the different pulse sequences and the different kinds of information which are derived thereof.

The coherence order describes describes the angular behaviour of coherences, while a state of coherence order -1 rotates about an angle ϕ, whereas a state of coherence order 2 rotates about an angle -2ϕ.

$$\hat{\rho}^{(p)} \xrightarrow{\text{rotate by } \phi \text{ about z}} \hat{\rho}^{(p)} \times \exp(-ip\phi) \tag{2.49}$$

To calculate the coherence order of a spin state, the cartesian product operators $\hat{I}_x$, $\hat{I}_y$ have to be rewritten using the lowering and raising operators (see 2.50 and 2.51). $\hat{I}_z$ has the coherence order of 0, as the spins are along z and do not precess.

$$\hat{I}_i^+ \equiv \hat{I}_{ix} + i\hat{I}_{iy} \tag{2.50}$$

$$\hat{I}_i^- \equiv \hat{I}_{ix} - i\hat{I}_{iy} \tag{2.51}$$

By definition, $\hat{I}_+$ and $\hat{I}_-$ have a corresponding coherence order of $+1$ and -1. Following the definitions in Equation 2.50 and 2.51, one can rewrite $\hat{I}_x$ and $\hat{I}_y$ as follows:

$$\hat{I}_{ix} \equiv \frac{1}{2}(\hat{I}_i^+ + \hat{I}_i^-) \tag{2.52}$$

$$\hat{I}_{iy} \equiv \frac{1}{2i}(\hat{I}_i^+ - \hat{I}_i^-) \tag{2.53}$$

Conclusively, $\hat{I}_{ix}$ and $\hat{I}_{iy}$ are mixtures of $\hat{I}_{i+}$ and $\hat{I}_{i-}$ for the spin i. Important to notice is that by convention only magnetization of the coherence order -1 is observed. For product operators of more than one spin, the expressions for $\hat{I}_{ix}$ and $\hat{I}_{iy}$ can be multiplied, to derive the coherence order of multiple quantum states. This is done exemplary in Equation 2.54.

$$\begin{aligned} 2\hat{I}_{1x}\hat{I}_{2y} &\equiv 2 \cdot \frac{1}{2}(\hat{I}^{1+} + \hat{I}^{1-}) \cdot \frac{1}{2i}(\hat{I}^{2+} - \hat{I}^{2-}) \\ &\equiv \frac{1}{2i}(\hat{I}^{1+}\hat{I}^{2+} - \hat{I}^{1+}\hat{I}^{2-} + \hat{I}^{1-}\hat{I}^{2+} - \hat{I}^{1-}\hat{I}^{2-}) \end{aligned} \tag{2.54}$$

The coherence order of the terms in Equation 2.54 has to be calculated for each of the terms. *E.g.* for the term $\hat{I}^{1+}\hat{I}^{2+}$, $\hat{I}^{1+}$ and $\hat{I}^{2+}$ have each coherence order is $+1$ which add up to $+2$. So each term in Equation 2.54 either has coherence order ± 2 or 0. Therefore, the operator $2\hat{I}_{1x}\hat{I}_{1y}$ is a mixture of double- and zero-quantum coherence. The coherence order of a term can be changed by 90° pulses. By using 180° pulses the sign of the coherence order changes. So to create double quantum coherence during a pulse sequence, a 90°_y pulse has to be applied to an antiphase state, e. g., $2\hat{I}_{1y}\hat{I}_{2z}$

$$2\hat{I}_{1y}\hat{I}_{2z} \xrightarrow{\frac{\pi}{2}\hat{I}_{1y} + \frac{\pi}{2}\hat{I}_{2y}} -2\hat{I}_{1y}\hat{I}_{2x} \tag{2.55}$$

The anti-phase terms can only be created by coupling evolution. Therefore, for appearance of double quantum coherence a coupled spin system of at least 2 spins is needed. Anti-phase terms are crucial for coherence transfer and for the generation of multiple quantum coherence.[26]

2.8.1. Evolution of Multiple-Quantum Coherence

During a free evolution period, the free precession Hamiltonian is active for the multiple-quantum coherence, meaning the coupling operator and the chemical shift operators for both spins, see Equation 2.56. The coupling does not evolve between the spins that build up the multiple-quantum coherence, as all the components are transversal and cannot evolve under the coupling Hamiltonian. Whereas the chemical shift evolves for both spins. The chemical shift Hamiltonians for different spins commute, one chemical shift evolution can be taken into account after the other for all spins making up the multiple-quantum coherence.

For double quantum coherence the Hamiltonian for the chemical shift and the coupling evolution is given by the following:

$$\hat{H}_{\text{two spins}} = \Omega_1 t_1 \hat{I}_{1z} + \Omega_2 t_1 \hat{I}_{2z} + 2\pi J_{12} \hat{I}_{1z} \hat{I}_{2z} \tag{2.56}$$

If one starts looking at the operator $2\hat{I}_{1x}\hat{I}_{2y} + 2\hat{I}_{1y}\hat{I}_{2x}$, the chemical shift evolves as follows.

$$\begin{aligned} 2\hat{I}_{1x}\hat{I}_{2y} \xrightarrow{\Omega t_1 \hat{I}_{1z} + \Omega t_1 \hat{I}_{2z}} & 2\hat{I}_{1x}\hat{I}_{2y} \cos(\Omega_1 t_1)\cos(\Omega_2 t_1) - 2\hat{I}_{1x}\hat{I}_{2x} \cos(\Omega_1 t_1)\sin(\Omega_2 t_1) \\ & +2\hat{I}_{1y}\hat{I}_{2y} \sin(\Omega_1 t_1)\cos(\Omega_2 t_1) + 2\hat{I}_{1y}\hat{I}_{2x} \sin(\Omega_1 t_1)\sin(\Omega_2 t_1) \end{aligned} \tag{2.57}$$

$$\begin{aligned} 2\hat{I}_{1y}\hat{I}_{2x} \xrightarrow{\Omega t_1 \hat{I}_{1z} + \Omega t_1 \hat{I}_{2z}} & \hat{I}_{1y}\hat{I}_{2x} \cos(\Omega_1 t_1)\cos(\Omega_2 t_1) + \hat{I}_{1y}\hat{I}_{2y} \cos(\Omega_1 t_1)\sin(\Omega_2 t_1) \\ & -\hat{I}_{1x}\hat{I}_{2x} \sin(\Omega_1 t_1)\cos(\Omega_2 t_1) - \hat{I}_{1x}\hat{I}_{2y} \sin(\Omega_1 t_1)\sin(\Omega_2 t_1) \end{aligned} \tag{2.58}$$

If one looks at the terms $2\hat{I}_{1x}\hat{I}_{2y}$ and $2\hat{I}_{1y}\hat{I}_{2x}$ together, the sine and cosine terms can be simplified and give the following result:

$$\begin{aligned} (2\hat{I}_{1x}\hat{I}_{2y} + 2\hat{I}_{1y}\hat{I}_{2x}) \xrightarrow{\Omega t_1 \hat{I}_{1z} + \Omega t_1 \hat{I}_{2y}} \\ (2\hat{I}_{1x}\hat{I}_{2y} + 2\hat{I}_{1y}\hat{I}_{2x}) \cos((\Omega_1 + \Omega_2)t_1) - (2\hat{I}_{1x}\hat{I}_{2x} - 2\hat{I}_{1y}\hat{I}_{2y}) \sin((\Omega_1 + \Omega_2)t_1) \end{aligned} \tag{2.59}$$

In Equation 2.59, it becomes apparent that the chemical shifts of both spins evolve during t_1 and yield the sum of the frequencies. Hence, the signal of carbon double quantum coherence is at the sum of the two offsets of the chemical shifts of both nuclei. If one wants to calculate the position of the signals, the following formula can be used:

$$\Omega_{\text{DQ}} = \omega_{\text{offset,1}} + \omega_{\text{offset,2}} \tag{2.60}$$

$\omega_{\text{offset,1}}$ is the offset in Hz for spin 1. $\omega_{\text{offset,2}}$ is the offset in Hz for spin 2.

To select the desired coherence order during a pulse sequence, two methods can be used. First, coherence order selection can be achieved by phase cycling pulses. Second, coherence order selection is achieved by pulsed field gradients, which will be explained in the following subsections.[26]

2.8.2. Selection of Coherences

In the section before the concept of coherence order was explained. Now, the focus lies on how one can choose the desired coherence transfer pathway and how it leads to observable magnetization. As we have seen before, the coherence order is defined as follows:

$$\mathrm{p} : \hat{\rho}^{(p)} \xrightarrow{\text{rotate by } \phi \text{ about z}} \hat{\rho}^{(p)} \times \exp(-ip\phi) \tag{2.61}$$

$\hat{\rho}^{(p)}$ is an operator of coherence order p.

A coherence transfer pathway describes the coherence order present at any time during the sequence for every nucleus in the experiment. By considering a coherence transfer pathway, one can see which pulses have to be phase cycled or which Pulsed Field Gradient (PFG) has to be applied to select the wanted pathway and the related coherence order.

$$-\Delta\mathrm{p} \times \Delta\phi \tag{2.62}$$

Whereas $\Delta\phi$ is the phase of the pulse and $\Delta\mathrm{p}$ is defined as follows:

$$\Delta\mathrm{p} = \mathrm{p}_2 - \mathrm{p}_1 \tag{2.63}$$

p_1 is the coherence order before the pulse which might be phase cycled and p_2 is the coherence order after the pulse. Pathways with different $\Delta\mathrm{p}$ values acquire different phase shifts. This is how the differentiation between different pathways is accomplished. The experiment is repeated several times with different phases $\Delta\phi$ and combined afterwards. This leads to cancellation of unwanted signal and adds up the wanted pathways. The phase acquired during one pulse is maintained over the whole sequence, this is why the receiver phase has to be changed accordingly. The receiver phase therefore follows the phase shift. The calculation of one phase cycle for a coherence pathway where the coherence order goes from +2 to +1 yields:

$$\Delta\mathrm{p} = 2 - 1 = 1 \tag{2.64}$$

Coherence pathways can also be selected by field gradient pulses. Field gradient pulses are applied during the sequence and make the field inhomogeneous for a short period of time. This is achieved by adding an extra coil in the NMR probe which is designed in a way that if a current flows through the coil, the magnetic field varies linearly along the z-axis, meaning in the direction of the main field B_0. The spectrometer is able to control size and direction of the current flowing through the field gradient coil. The higher the current, the greater the field gradient. By changing the sign of the current, the field gradient changes sign. As B_0 is varied by the pulsed field gradient along z, the spins add different phases to them depending on their z-position.

Table 2.2.: Phase cycling for coherence pathway Δp = 1

$\Delta\phi_{\text{pulse}}$	$-\Delta\phi_{\text{calculated}}$	$\Delta\phi_{\text{adjusted}}$
0°	0°	0°
90°	−90°	270°
180°	−180°	180°
270°	−270°	90°

$$B_z = B_0 + Gzt \tag{2.65}$$

B_z is the field varied by the gradient, B_0 is the external magnetic field, G is the gradient strength in $\mathrm{T\,m^{-1}}$, z is the coordinate along B_0. The high resolution spectrometers, where the experiments are performed on, have a typical gradient strength of around $0.535\,\mathrm{T\,m^{-1}}$. By multiplying Equation 2.65 with the gyromagnetic ratio γ_i, the result is:

$$-B_z\gamma_i = -B_0\gamma_i - Gz\gamma_i \tag{2.66}$$

Forming into:

$$\omega(z) = \omega_0 - \gamma_i Gz \tag{2.67}$$

ω_0 is the Larmor frequency and not changed by the gradient. It is sufficient to consider only the space dependent part $\gamma_i Gz$.

$$\Omega(z) = -\gamma_i Gz \tag{2.68}$$

As the gradient adds up a frequency to the Larmor frequency, it can be pictured as an additional rotation around $\hat{I}_z$. Therefore, the effect of the gradient is also dependent on the coherence order of the state to which it is applied.

$$\hat{I}_+ \xrightarrow{\Omega(z)t\hat{I}_z} \exp(-i\Omega(z)t)\hat{I}_+ \tag{2.69}$$

The coherence $\hat{I}_+$ acquires a phase $\phi(z) = -\Omega(z)t$. Whereas, a double quantum state acquires a phase of $\phi(z) = -2\Omega(z)t$.

$$2\hat{I}_{1+}\hat{I}_{2+} \xrightarrow{\Omega(z)t(\hat{I}_{1z}+\hat{I}_{2z})} \exp(-2i\Omega(z)t)2\hat{I}_{1+}\hat{I}_{2+} \tag{2.70}$$

In a more generalized expression the spatial dependent phase acquired during a gradient is depending on the coherence order p, the gyromagnetic ration γ, the gradient strength G, the spatial position z and the time t during which the gradient is applied. This dephasing is shown schematically in Figure 2.5. As can be seen, the spatially dependent phase acquired by an applied pulsed field gradient is dependent on the coherence order of the present magnetization. Therefore, Equation 2.68 can be rewritten as follows:

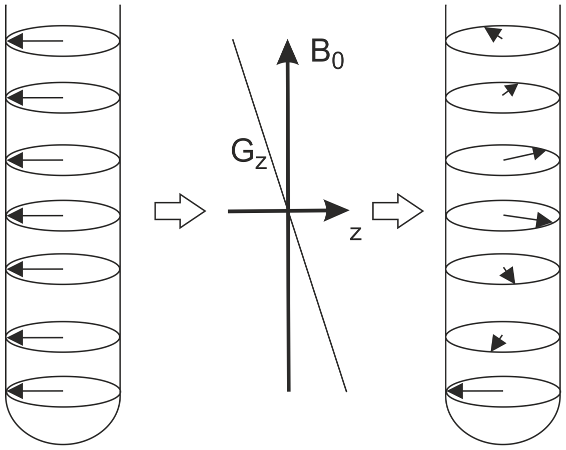

Figure 2.5.: Sketch of the effect of a gradient on the spins. As stated in Equation 2.71, the spins acquire a phase dependent on their z-position in the sample. This z-dependent phase can be refocused if the sign of the gradient is reversed for the same spin species (see Equation 2.72).

$$\phi(z) = -p \times \gamma_i G z t \tag{2.71}$$

By this dependency of the phase on the coherence order, it is possible to select coherence transfer pathways by gradients. By changing the sign of the gradient, it is possible to apply a phase in the opposite direction. Therefore, the spatial dephasing can refocus.

The refocusing condition is given by:

$$\phi_1(z) + \phi_2(z) = 0 - p_1 \times \gamma_1 G_1 z t_1 - p_2 \times \gamma_2 G_2 z t_2 = 0 \tag{2.72}$$

For the different spin species and the same gradient length t, this yields:

$$\frac{\gamma_1 G_1}{\gamma_2 G_2} = -\frac{p_2}{p_1} \tag{2.73}$$

With this condition, it is possible to select desired coherence order pathways by pulsed field gradients.[26]

2.9. Shaped pulses

The use of shaped pulses is relevant for high magnetic field strengths as the chemical shift ranges for nuclei such as ^{13}C, ^{19}F or ^{31}P are large. For instance 1 ppm corresponds to 150 Hz for ^{13}C nuclei at a field strength of 14.1 T. As the chemical shifts for carbon can range from 0 ppm to 250 ppm, the pulses on carbon have to cover a bandwidth of up to 37 500 Hz. This bandwidth cannot be covered by a hard pulse because there are limitations in the power level which can be used without harming the spectrometer hardware.[94] Besides the large bandwidths which might be problematic for ^{13}C, ^{19}F and ^{31}P, the optimization of ^{1}H pulses is also of interest. B_1 inhomogeneities and large variations of ^{1}H pulse lengths make it desirable to investigate robust pulses.[95] This is why methods to develop low-power pulses which can cover a large bandwidth are of interest.

Depending on the step in the pulse sequence different pulse classes have to be used. Two classes of pulses are of particular interest. One is the class of Point-to-Point (PP) pulses, the other the Universal Rotation (UR) pulses. A PP pulse transfers a single component of a magnetization into a specific target component. It controls only one axes. For a 180°_x PP pulse, the magnetization is transformed from an initial state $\hat{I}_z$ into $-\hat{I}_z$. Before the pulse, there might be magnetization along the y and x axis. What happens with this magnetization is not defined for the 180° PP pulses. Therefore, after the PP pulse this magnetization is distributed along the xy-plane (see Figure 2.6). This is different for a UR pulse. Here, all magnetization components are rotated around a well-defined rotation axis and angle. Meaning that the rotation of the magnetization about a specific axis is preserved for all components and the pulse controls every axis. For instance, if a UR 180°_x pulse is applied to the initial magnetization, which is distributed along the axis $\hat{I}_z$, $\hat{I}_x$ and $-\hat{I}_y$, $\hat{I}_z$ and $-\hat{I}_y$ are rotated by 180° to give $-\hat{I}_z$. $\hat{I}_y$ and $\hat{I}_x$ is preserved. Depending on the step where the shaped pulses are used in the pulse sequence, it is crucial to use a UR pulse. A PP pulse can be exchanged by a UR pulse, but not vice versa, as a PP pulse is more restricted compared to a UR pulse. The difference for the two pulses is shown schematically in Figure 2.6.[94]

2.10. Non Uniform Sampling (NUS)

In conventional NMR data every point in a grid for the indirect dimension is recorded. In some cases this can lead to extremely high measurement times, as for example for multidimensional NMR (3D, 4D, etc.). The digital resolution is defined by the acquisition time $\Delta\omega \sim \frac{1}{t_{\text{acqu}}}$. There is a sampling limit in a reasonable time span and a sensitivity limit (S/N), as the signal decays proportionally to $\Delta\omega \sim \frac{1}{T_2}$. This leads to a drop of the signal-to-noise ratio. By measuring a spectrum with Non Uniform Sampling (NUS), two things can be optimized for the recording. On one hand, the measurement time can be decreased by maintaining the same resolution. On the other hand for the same experimental time higher resolution can be achieved in the indirect dimension. This can be achieved by applying the NUS acquisition grid of the indirect dimension and by choosing different reconstruction algorithms for the spectra.

The NUS grid can be sampled in a radial way. Here, all cross-sections are sampled along lines that pass through the origin. This sampling scheme can only be applied to three or more dimensional spectra. The NUS sampling scheme can be weighted by matching it to the J coupling constant, to the T_2 relaxation time or to both.[107]

Furthermore, the algorithm to reconstruct the spectrum can be varied. Normally, the spectrum is a solution of a system of linear equations:

$$\begin{gathered} \text{FT-matrix} \cdot \text{spectrum} = \text{FID} \\ \text{spectrum} = \text{FT-matrix}^{-1} \cdot \text{FID} \end{gathered} \tag{2.74}$$

In the case of NUS, fewer points are recorded than would be needed for the conventional Fourier Transform. Therefore, the system of linear equations is under-determined and

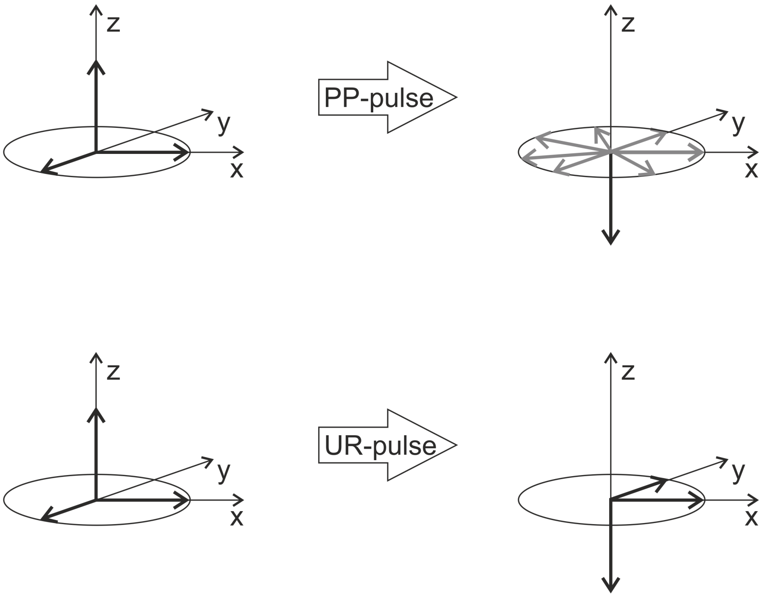

Figure 2.6.: Effect on spin states for PP pulses (inversion pulse) and UR pulses (refocusing pulse). In (A) a 180° PP pulse transfer is shown. The z-magnetization is transferred to $-z$. The rotation of the magnetization along x and y is not defined. Therefore, the magnetization along these axes results anywhere in the x,y plane. (B) The UR pulse transforms all magnetization components about a specific axis and angle. Here a 180° UR pulse along x is shown. In this case, all magnetization components are preserved and rotated by 180° except the magnetization which is along x which is unaffected by the pulse. Depending on the position in the pulse sequence, it might be crucial to use a UR pulse to conserve all magnetization components. The figure is adapted from [94].

the missing points of the measured NUS grid have to be reconstructed. To reconstruct the spectra, different initial conditions can be used for the reconstruction. There exist a variation of assumptions and NUS processing methods. These are: Maximum Entropy (ME), Compressed Sensing (CS), Low Rank (LR), Multidimensional Decomposition (MDD), Virtual Echo (VE) and Spectroscopy by Integration of Frequency and Time Domain (SIFT). Here, some details on the Compressed Sensing approach will be explained, as this algorithm was used to reconstruct spectra in this thesis. The CS approach assumes that the resulting spectrum is the sparsest.

$$||\text{FT-matrix} \times \text{spectrum} - \text{FID}||^2{}_{l_2} + \lambda||\text{spectrum}||^p{}_{l_p} \tag{2.75}$$

The sparsest solution can be found by the minimization of the penalty function $\lambda||\text{spectrum}||^p{}_{l_p}$. In principle, the sparsest solution would be found if $l_{p=0}$. This can never be achieved computationally, as it would pose an insolvable minimization problem. Yet, it was proven that using the $l_{p=1}$ norm allows to find the sparsest solution.[108] The norm $l_{p=1}$ is minimized for the Iterative Soft Thresholding (IST) algorithm. Whereas, $l_{p\to 0}$ is minimized for the Iterative Re-weighted Least Squares (IRLS) algorithm. If the IRLS algorithm is used with the norm $l_{p=1}$, the result is similar to the result for the IST algorithm but with longer computational times.[109, 110]

3. Determination of the Relative Configuration of Stereogenic Centers for 8-5(c)-DFA

8-5(c)-DehydrodiFerulate (8-5(c)-DFA) has two stereogenic centers with unknown relative configuration. Therefore, the spectra to assign the compound are recorded and the relative configuration attributed by the measurement of NOE and RDCs data. The relative configuration of 8-5(c)-DFA is determined as (*R*,*R*) or (*S*,*S*).

3.1. Introduction

This chapter is an example for the usefulness of NMR in structure analysis for 8-5(c)-DFA. With combination of *J* coupling, NOE data and RDC measurement, the relative configuration of the compound is assigned. The structure of 8-5(c)-DFA is shown in Figure 3.1. There are two stereogenic centers in the molecule at B-C7 and B-C8 and a E/Z-configuration along the double bond of A-C7 and A-C8. In total, four absolute configurations for the molecule are possible: (*R*,*R*)-, (*S*,*S*)-, (*S*,*R*)- or (*R*,*S*)-configuration. With NMR data from chemically unmodified 8-5(c)-DFA, the (*R*,*R*)- or (*S*,*S*)-configuration cannot be differentiated from each other as well as the (*S*,*R*)- or the (*R*,*S*)-configuration. Consequently, the (*S*,*R*)- and (*R*,*S*)-configuration are referred to as the cis configuration and the (*R*,*R*)- and (*S*,*S*)-configuration as trans. By the presented method, these two configurations are discriminated. In Figure 3.3B and Figure 3.3A, two of the four configurations are shown in 3D.

J coupling and NOE data are well-known and used for structural assignment. In some cases, they are not sufficient to assure the right assignment. In particular in five-membered rings with inherent flexibilities, the determination of configuration is not possible from NOE derived distances and $^3J_{\mathrm{HH}}$ couplings alone. Therefore, the structural refinement is done with RDC data. First, the spectra for normal assignment are recorded, such as 1D ^{1}H, 1D ^{13}C, CLIP-HSQC and Heteronuclear Multiple-Bond Correlation (HMBC) spectra. The *J* couplings are determined in the 1D ^{1}H spectrum. Additionally, NOE data is recorded to measure the distance between the protons at the stereogenic centers. Finally, the molecule is aligned in PBLG and PEO-DA for the extraction and evaluation of RDC data. The structure is optimized by Avogadro and the experimentally determined RDCs are used for a SVD-fit with MSpin.

In this chapter, first the assignment of 8-5(c)-DFA is shown. Then the E/Z-configuration along the double bond of A-C7 and A-C8 and the relative configuration of the stereogenic centers at B-C7 and B-C8 are determined and discussed.

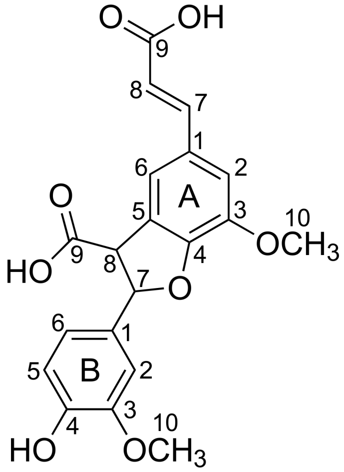

Figure 3.1.: Structure of 8-5(c)-DFA with numbered atoms. The letters A and B indicate the two ferulic acid units.

3.2. Assignment and Determination of the Relative Configuration of 8-5(c)-DFA

For the assignment of 8-5(c)-DFA, 1D ^{1}H, 1D ^{13}C, CLIP-HSQC and HMBC are recorded and are shown in Figure 3.2. The signals are numbered consecutively in the 1D ^{13}C spectra starting from the highest chemical shift. The assigned character has been transferred first to the CLIP-HSQC to connect the ^{13}C frequencies with the associated ^{1}H frequencies. To complete the assignment, the Heteronuclear Multiple Bond Correlation (HMBC) is used to determine the connectivities. The complete assignment is shown in Table 3.2. The numbered structure is shown in Figure 3.1.

The E/Z-configuration along the double bond of A-C7 and A-C8 is determined with the $^3J_{\mathrm{HH}}$ coupling. The $^3J_{\mathrm{HH}}$ coupling is 15.9 Hz. Consequently, the configuration of the double bond must be E. Together with the J coupling constant, a NOE distance measurement and the determination of RDCs, the relative configuration of the stereogenic centers at B-C7 and B-C8 is determined. The J coupling between the two protons of B-C7 and B-C8 is 7.9 Hz. For a clear assignment to either cis or trans configuration, this value is not sufficient, since common values for the $^3J_{\mathrm{HH}}$ coupling for protons with an angle of 180° are 10 Hz to 15 Hz and for protons with a dihedral angle of 60° are 4 Hz to 5 Hz according to the Karplus curve.[9] The value of 7.9 Hz indicates the trans configuration as in the (*R*,*R*)-configuration, the two C-H vectors have a dihedral angle of around 120° in the Newman projection. The NOE distance measurements lead to a distance of 3.0 Å between the two protons. Both structures for 8-5(c)-DFA are optimized with Avogadro and the MMFF94s force field.[111] The distance between the two protons in this structure is measured as 3.0 Å for the trans configuration. In the optimized cis configured structure, the distance is 2.2 Å. The NOE distance is measured relatively to the NOE signal of A-C7 and A-C8. Conclusively, the NOE measurement points to the trans configuration. However, the NOE distance measurement has to be carefully interpreted as the distances which are taken to compare the values, had no linear tendency in the NOE built up curve. Therefore, only the

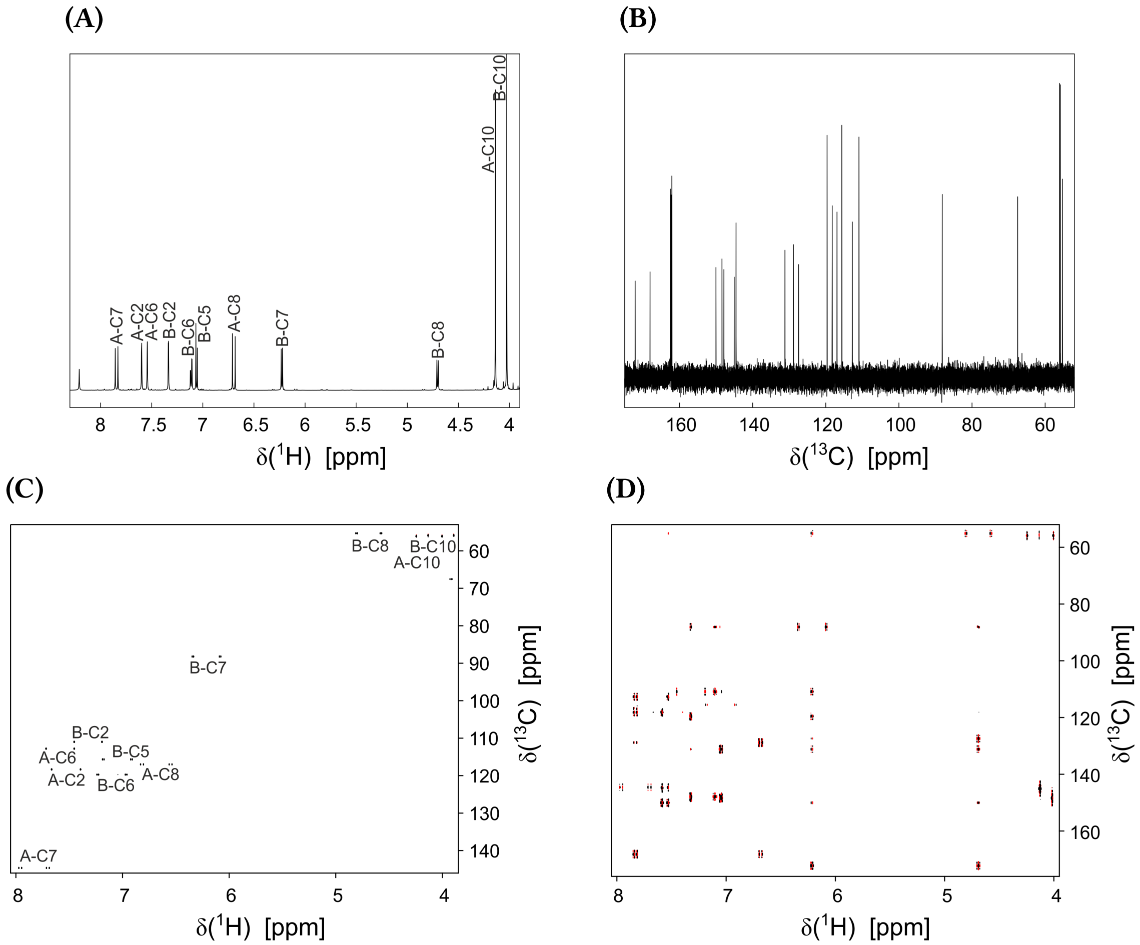

Figure 3.2.: Spectra of 8-5(c)-DFA. (A) 1D ^{1}H; (B) 1D ^{13}C spectrum; (C) CLIP-HSQC spectrum; (D) HMBC spectrum.

Table 3.1.: Assignment of 8-5(c)-DFA.

Signal	δ ^{13}C [ppm]	δ ^{1}H [ppm]	$^{3}J_{\mathrm{HH}}$ [Hz]	HMBC	Assignment
A	172.23			Q, T	B-C9
B	168.16			G, M	A-C9
C	150.14			L, Q, T	A-C4
D	148.49			N, S	B-C3
E	147.96			K, P	B-C4
F	145.14			R, T	A-C3
G	144.63	7.83	15.9	L, M	A-C7
H	131.26			N, Q, T, P	B-C1
I	128.94			G, M, S	A-C1
J	127.54			Q, T	A-C5
K	119.73	7.10	8.4,1.9	P, Q	B-C6
L	118.33	7.53	1.6	G, T	A-C6
M	117.02	6.69	15.9	G	A-C8
N	115.7	7.05	8.1	P	B-C5
O	112.83	7.59	1.1	G, L	A-C2
P	111.02	7.33	2	K, N, Q, S	B-C2
Q	88.23	6.21	7.9	P, K, T	B-C7
R	56.13	4.14			A-C10
S	55.92	4.02		N	B-C10
T	55.35	4.70	7.9	Q, O	B-C8

Table 3.2.: Experimental integrals determined in the Nuclear Overhauser Enhancement SpectroscopY (NOESY) spectrum of the reference signal between A-H7, A-H8 and the relevant signal B-H7, B-H8. Additionally, the reference distance, which is determined in the optimized structure for A-H7, A-H8 and the derived distance for B-H7, B-H8 is shown.

NOE-mixing time [s]	A-H7,A-H8	B-H7, B-H8
0.6	0.236 27	0.252 99
	[Å]	[Å]
Distance	2.1	3.0

value for the NOE spectrum with a mixing time of 0.6 s was used to calculate the value of 3.0 Å, which might lead to a large error on the value. Therefore, RDCs are recorded to support the evidence of the NOE data. Another indication for the cis configuration is the energy difference of the optimized structures. ΔE between the trans and cis structures is 12.3 kJ mol^{-1}. This indicates that the structure for the trans configuration is favored over the cis configuration.

To measure RDCs, 8-5(c)-DFA has been aligned in two different alignment media, PEO-DA and PBLG. In Table 3.3, the isotropic values for all $^1J_{\mathrm{CH}}$ couplings together with the anisotropically determined values in PEO-DA and PBLG are summarized for the compound. $\Delta\nu_{\mathrm{Q}}$ of the stretched PEO-DA gel is 9.9 Hz for the deuterium signal of DMF-d$_7$ at 7.98 ppm. RDCs in PBLG are determined with a deuterium quadrupolar splitting of $\Delta\nu_{\mathrm{Q}}$ = 24.6 Hz for the deuterium signal of DMF-d$_7$ at 7.98 ppm.

The RDCs for B-C7 and B-C8 are 25.8 Hz and 35.3 Hz in PEO-DA. In the case of RDCs for 8-5(c)-DFA in PBLG, the values the $^1D_{\mathrm{CH}}$ splittings are 1.9 Hz and 1.5 Hz for B-C7 and B-C8, respectively.

The determination of an alignment tensor for 8-5(c)-DFA is difficult, as the molecule is slightly flexible. The structure for the SVD-fit is optimized with Avogadro and the svd-fit is performed for the experimental RDCs in both alignment media with Mspin.[83] For the explanation of the SVD-fit calculation, see Section 2.4.3 and 2.4.3.1.The calculation of the alignment tensor and the back-calculation of the RDCs, leads to the assumption that the experimental RDCs determined in PBLG are not useful for the interpretation. As the back-calculated values and the experimental values do not coincide for any of the proposed structures. Therefore, the optimized structure is not sufficient to describe the real structure of the molecule, the experimentally determined RDCs are inaccurate or the SVD-fit for rigid molecules failed.

Table 3.3.: Values for the 8-5(c)-DFA in isotropic conditions and aligned in PBLG and PEO-DA. The errors indicate the ±3 standard deviation (±3σ) uncertainty.

Assignment	δ ^{13}C [ppm]	δ ^{1}H [ppm]	$^1J_{\mathrm{CH}}$ [Hz]	$^1D_{\mathrm{CH}}$ [Hz] PBLG	$^1D_{\mathrm{CH}}$ [Hz] PEO-DA
A-C7	144.63	7.83	155.2 ± 0.1	0.7 ± 2.0	−3 ± 1
B-C6	119.73	7.10	159.4 ± 0.2	−0.4 ± 1.7	−2.6 ± 0.7
A-C1	118.33	7.56	162.5 ± 0.2	1.1 ± 0.4	−0.7 ± 1.2
A-C8	117.02	6.69	160.6 ± 0.1	1.6 ± 1.9	−0.1 ± 0.7
B-C5	115.7	7.05	158.7 ± 0.2	−1.2 ± 1.4	−6.0 ± 0.6
A-C5	112.83	7.56	158.2 ± 0.1	−1.3 ± 0.8	−19.1 ± 1.0
B-C2	111.02	7.33	156.3 ± 0.1	−0.1 ± 0.5	−5.5 ± 0.6
B-C7	88.23	6.21	152.9 ± 0.3	1.5 ± 1.5	25.8 ± 1.5
A-C10	56.13	4.14	144.8 ± 0.1	10.8 ± 5.4[1]	3.8 ± 0.6
B-C10	55.92	4.02	144.2 ± 0.1	−18.3 ± 5.3[1]	0.8 ± 0.2
B-C8	55.35	4.70	137.0 ± 0.2	1.9 ± 2.2	35.3 ± 1.0

[1] Cross peaks to both C10 are very difficult to interpret in PBLG because of partial overlap and heavily distorted signal shape.

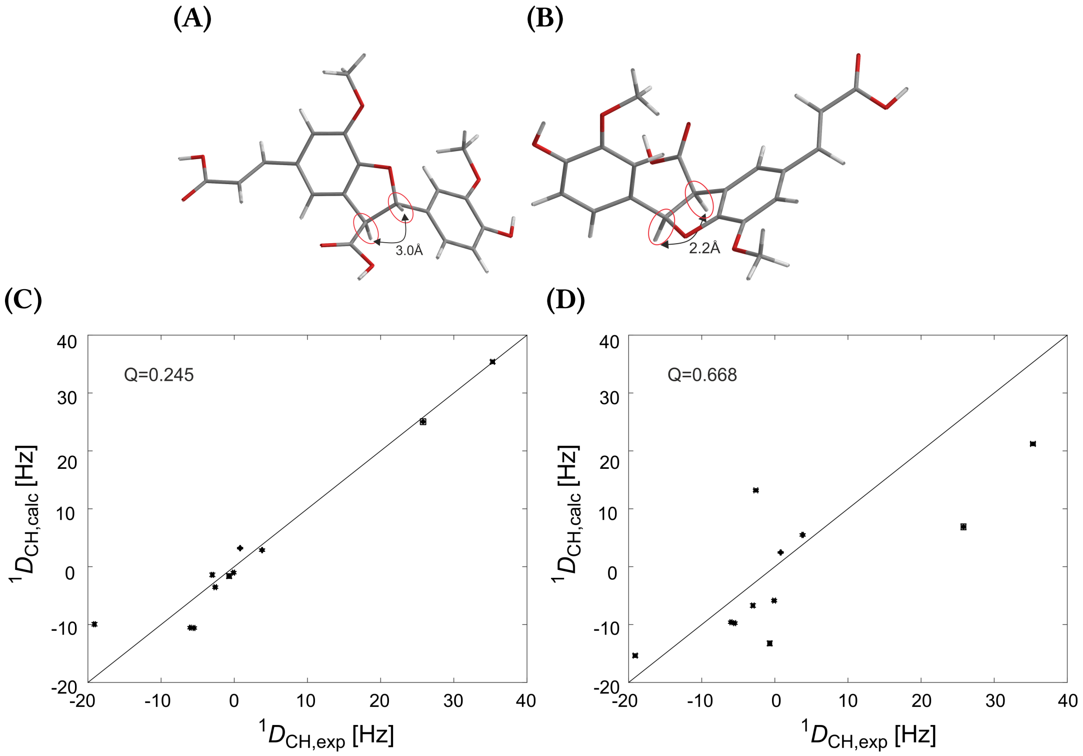

Figure 3.3.: Three-dimensional structure and RDC-fit for two relative configurations of 8-5(c)-DFA. (A) 3D structure of (*S*,*S*)-8-5(c)-DFA. (A) 3D structure of (*S,R)-8-5(c)-DFA*. (C) Experimental vs. calculated RDCs for (*S*,*S*)-8-5(c)-DFA. (B) Experimental vs. calculated RDCs for (*R*,*S*)-8-5(c)-DFA.

However, the experimental and calculated $^{1}D_{\mathrm{CH}}$ for 8-5(c)-DFA in PEO-DA show a good separation. For the trans configuration, the Corneliscu Q-factor is 0.245, whereas for the cis configuration the value is 0.668. In Figure 3.3C and 3.3D, the experimentally determined RDCs are plotted against the calculated RDCs. If the calculated RDCs correlate with the experimental RDCs, they are next to the black diagonal drawn in the Figure. Additionally, the comparison of measured RDCs and calculated RDCs for B-C7 and B-C8 are 25.8 Hz and 35.3 Hz and 26.66 Hz and 31.88 Hz for the trans configuration, respectively. Whereas, the calculated RDCs for the (*R*,*S*)-configuration for B-C7 and B-C8 are 5.14 Hz and 25.01 Hz, respectively. Consequently, the experimental RDCs at the stereogenic centers coincide with the calculated $^{1}D_{\mathrm{CH}}$ for the trans configuration and not for the values of the cis configuration.

As a result of the structure analysis, the relative configuration of the 8-5(c)-DFA is the trans configuration at the two stereogenic centers B-C7 and B-C8. The values determined in PBLG were not considered further as the experimental values seemed to be inaccurate.

3.3. Conclusion

The relative determination of the stereogenic centers of 8-5(c)-DFA was not straight forward with J coupling and NOE measurements. Therefore, RDCs were measured and evaluated as well. The data led to the conclusion that 8-5(c)-DFA is (R,R) or (S,S) configured at the two stereogenic centers B-C7 and B-C8, which corresponds to the trans configuration. To evaluate the RDCs more reliably, more elaborate approaches could be used for the fitting procedure, for example a population fitting through a single-tensor,[83] or with a model free approach.[112]

3.4. Experimental and Processing Parameter

The isotropic sample was prepared with 7.1 mg (18.4 µmol) 8-5(c)-DFA in 300 µl deuterated DMF-d_7, purchased from Eurisotop and used without further purification. The final concentration was 61.3 mmol l^{-1}. 150 µl of the solution was transferred into a 3 mm tube.

The spectra were recorded on a 600 MHz spectrometer from Bruker (Rheinstetten, Germany) equipped with a cryogenically cooled TXI-probehead. The ^{1}H-1D spectrum in Figure 3.2A was recorded with 65 536 time domain points and a sweep width of 20 ppm leading to an acquisition time of 2.73 s. The spectrum was processed to 131 072 points and apodized with an exponential function and a linebroadening of 0.3 Hz. The 1D ^{13}C spectrum in Figure 3.2B was recorded with 65 536 time domain points and a sweep width of 251.2 ppm leading to an acquisition time of 0.865 s. 64 scans were recorded with a relaxation delay of 1 s. The spectrum was processed to 262 144 points and apodized with an exponential function and a linebroadening of 1 Hz.

The spectra shown in Figure 3.2C were recorded with 16 384 time domain points in the direct dimension and 1024 time domain points in the indirect dimension. The corresponding sweep widths were 10 ppm and 140 ppm leading to an overall acquisition time of 1.365 s and 0.024 s. Before acquisition 16 dummy scans were applied for equilibration. The number of scans per increment was 2 with a recovery delay of 0.8 s. $^1J_{\mathrm{CH}}$ was set to 145 Hz and the corresponding delay Δ_1 was calculated accordingly. The total experimental time was 48 min 28 s. The spectra were zero filled to 32 768 points in the direct dimension and 2048 points in the indirect dimension. The Free Induction Decay (FID) was apodized with a squared cosine window function in both directions. The values for $^1J_{\mathrm{CH}}$ extracted from the CLIP-HSQC are shown in Table 3.3.

The spectra shown in Figure 3.2D were recorded with 16 384 in the direct dimension and 256 time domain points in the indirect dimension. The corresponding sweep width were 10 ppm and 160 ppm leading to an overall acquisition time of 1.365 s and 0.005 s. Before acquisition 32 dummy scans were applied for equilibration. The number of scans per increment were 8 with a recovery delay of 2 s. $^nJ_{\mathrm{CH}}$ was set to 8 Hz and the corresponding delay Δ_1 was calculated accordingly. The total experimental time was 1 h 38 s. The spectra were zero filled to 32 768 points in the direct dimension and 512 points in the indirect dimension. The FID was apodized with a squared cosine window function in the direct direction and a sine function in the indirect dimension.

The NOE spectrum was recorded with 16 384 time domain points in the direct dimension and 512 time domain points in the indirect dimension. The corresponding sweep widths were 16 ppm in both dimensions, leading to acquisition tmes of 0.855 s and 0.027 s. Before acquisition 16 dummy scans were applied for equilibration. The number of scans per increment was 8 with a recovery delay of 2 s. The NOE mixing time was 0.6 s. The total experimental time was 2 h 59 min. The spectra were zero-filled to 32 768 points in the direct dimension and 1024 points in the indirect dimension. The FID was apodized with a squared cosine window function in both directions.

The anisotropic sample of 8-5(c)-DFA in PBLG was prepared with 10 mg 25.9 µmol 8-5(c)-DFA in 350 mg deuterated DMF-d_7, purchased from Eurisotop and used without further purification. 58.9 mg PBLG (Sigma-Aldrich) was added to the sample. The molecular weight distribution of PBLG was 150 000 g mol^{-1} to 350 000 g mol^{-1}. The sample was prepared in a 5 mm tube with screw cap and centrifuged up and down until it was homogeneous. The deuterium quadrupolar splitting of the DMF-d_7 was $\Delta\nu_Q$ = 24.2 Hz at 8.1 ppm.

The CLIP-HSQC was recorded for the extraction of RDCs with 1024 in the direct dimension and 1024 time domain points in the indirect dimension. The corresponding sweep width were 10 ppm and 140 ppm leading to an overall acquisition time of 0.095 s and 0.024 s. Before acquisition 16 dummy scans were applied for equilibration. The number of scans per increment were 4 with a recovery delay of 0.85 s. $^1J_{CH}$ was set to 145 Hz and the corresponding delay Δ_1 was calculated accordingly. The total experimental time was 1 h 4 min. The spectra were zero filled to 2048 points in the direct dimension and 2048 points in the indirect dimension. The FID was apodized with a squared cosine window function in both directions. The $^1T_{CH}$ values extracted from the CLIP-HSQC are summarized in Table 3.3.

The anisotropic sample of 8-5(c)-DFA in PEO-DA was prepared with 19 mg (49.2 µmol) $^{13}C_2$-8-5(c)-DFA in 400 µl deuterated DMF-d_7, purchased from Eurisotop and used without further purification. The final concentration was 123 mmol l^{-1}. 400 µl of the solution were transferred dropwise onto a PEO-DA gel (20 %(w/w)) in a stretching apparatus. The gel was swollen over night at 30 °C. The isotropically swollen gel had a length of 1.3 cm and was stretched to 2.7 cm. The deuterium quadrupolar splitting of the DMF-d_7 was $\Delta\nu_Q$ = 9.2 Hz at 8.1 ppm.

The CLIP-HSQC was recorded for the extraction of RDCs with 16 384 in the direct dimension and 1024 time domain points in the indirect dimension. The corresponding sweep widths were 10 ppm and 140 ppm leading to an overall acquisition time of 1.365 s and 0.024 s. Before acquisition 16 dummy scans were applied for equilibration. The number of scans per increment was 2 with a recovery delay of 0.8 s. $^1J_{CH}$ was set to 145 Hz and the corresponding delay Δ_1 was calculated accordingly. The total experimental time was 48 min 28 s. The spectra were zero filled to 32 768 points in the direct dimension and 2048 points in the indirect dimension. The FID was apodized with a squared cosine window function in both directions. The values extracted from the CLIP-HSQC are summarized in Table 3.3. All spectra were phased and baseline corrected.

4. Differentiation of Racemic Mixtures from *meso* Compounds

In biological related sciences and pharmaceutical industry, chirality is an important property. Especially for pharmaceuticals, chirality is highly relevant as enantiomers can result in different reactions in the body. The well-known thalidomide (known in Germany as contergan© – see Figure 4.2 for the structures of the enantiomers) incident in the 1960s is a good example. The racemization in the body led to deformed children if mothers had taken the medicine during their pregnancy.[113]

As chirality results in different reactivity with, e. g., proteins, the differentiation and identification of enantiomers is crucial. However beside the reactivity and ability to polarize light differently, the chemical and physical properties of enantiomers are equivalent. Therefore, analytical methods to differentiate enantiomers, as chiral High Pressure Liquid Chromatography (HPLC), absorption of polarized light (Circular Dichroism (CD)) or NMR, are necessary.

Particularly, the differentiation of racemic mixtures from the corresponding *meso*-compound is challenging, especially when chemical synthesis is not specific enough to synthesize only one species. The challenge is to differentiate the racemic mixture, which are two chiral molecules, from the *meso*-compound, which is an achiral molecule. Both the racemic mixture and the *meso*-compound have similar chemical properties as they differ only in configuration. The differentiation of the compounds with HPLC can fail if the corresponding compounds are not purely available for comparison and do not separate during the analytic routine.[114] CD fails, because the racemic mixture and the *meso*-compound are both not optically active. Therefore, NMR is the method of choice as there are several options to achieve enantiodifferentiation without the need of a compound for comparison. Together with more advanced pulse sequences, the *meso*-compound as well as the racemic mixtures can be assigned unambiguously.

In this chapter, chirality in molecules is defined and cases in which racemic mixtures and *meso*-compound can occur are pointed out. Different methods exist to differentiate enantiomers by NMR, these will be explained in the next section. To differentiate the racemic mixture from the corresponding *meso*-compound, one exemplary test molecule, hydrobenzoin, is analyzed by NMR under various chiral conditions. Afterwards, two pulse sequences are applied to assign the stereoisomers. Last, measurements on a tabletop spectrometer are performed to evaluate the enantiodiscrimination of LSR at low magnetic fields.

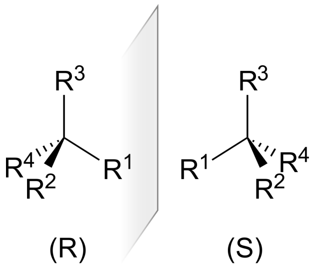

Figure 4.1.: Figure showing the chirality principle. R_1, R_2, R_3 and R_4 have to be different chemical groups.

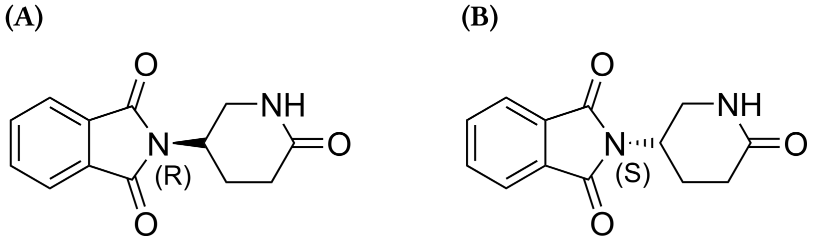

Figure 4.2.: Enantiomers of Thalidomide in (A) (*R*)- and in (B) (*S*)-configuration is shown.

4.1. Definition of Chirality

Chirality ($\chi\epsilon\iota\rho$ (kheir), greek: hand) is a property of asymmetry. The easiest and well-known example of a chiral object are our left and right hand which can only coincide by mirroring. In this case, the counterpart cannot be superimposed on the original by rotation. An organic molecules is chiral, if, for example, a carbon is differently substituted for all four bonds, see Figure 4.1. The two resulting molecules are called enantiomers. Only the symmetry operation of a mirror plane can transfer the enantiomers into each other. The carbons, which are asymmetrically substituted, are called stereogenic centers and can have either (*R*) or (*S*)-configuration. (*R*)- and (*S*)-configuration are defined by the Cahn-Ingold-Prelog priority rules. By application of the Cahn-Ingold-Prelog priority rules, the substitutes at the stereogenic centers have assigned priorities according to their atomic numbers. The higher the atomic number, the higher the priority. If there is a tie, the next bond must be taken into account for the prioritization.[115]

4.2. Racemic Mixtures vs. *meso* Compounds

In the special case of a molecule containing 2^n stereogenic centers and the possibility of having a mirror plane in the molecule, the differentiation of the two enantiomers from the *meso*-compound by NMR is challenging. In Figure 4.3, an example for a molecule which has three different diastereomers from which two are enantiomers and the third is the *meso*-compound, is shown.

In the simplest case, the molecule has two stereogenic centers which can have two different configurations. For all stereogenic center, there are two possible configurations, either they have (*R*)- or (*S*)-configuration. Therefore, a molecule with two stereogenic

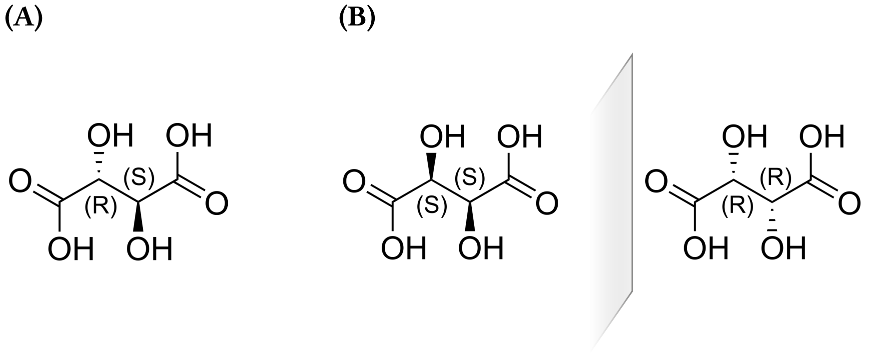

Figure 4.3.: Diastereoisomers of tartaric acid as an example for a molecule with the fulfilled properties for a racemic mixture and a *meso*-compound. (A) shows the *meso*-compound of tartaric acid. (B) shows the (*R,R*)- and (*S,S*)-enantiomer.

centers can have three different configurations. These are the (*R,R*)-, (*S,S*)-, (*R,S*)- and the (*S,R*)-configuration. The (*R,R*)- and the (*S,S*)-compound are enantiomers. Therefore, they are chiral and interact differently with polarized light (CD). Whereas, the (*R,S*) or (*S,R*)-configurations are equivalent and cannot be differentiated. The (*R,S*)-compound is an achiral diastereomer with respect to the other two configurations. If the (*R,R*)- and the (*S,S*)- compound are in a 1:1 solution of each enantiomer, the resulting mixture is called a racemic mixture and is not optically active. In this special case, the differentiation of the *meso*-compound from the racemic mixture via CD will fail as both solutions are not optically active. Additionally, the differentiation via HPLC might fail, as there is still uncertainty when only one peak is detected. From such an outcome, it is not possible to say if the method failed and the separation of (*R,R*) and (*S,S*) compound is not successful or if it is the *meso*-compound.

Under these circumstances, NMR may lead to the assignment of the *meso*-compound. For instance, if a molecule, like tartaric acid in Figure 4.3, has a proton attached at each of the chiral centers, the $^3J_{\mathrm{HH}}$ coupling between the protons indicates the *meso*-compound. If the mixture is racemic, there is no coupling visible between the protons at the chiral centers. However, if the *meso*-compound is not present for comparison, the racemic mixture cannot be clearly assigned to the analyzed solution. Since, the $^3J_{\mathrm{HH}}$ coupling can be too small or too strong to be measured. In both cases, the $^3J_{\mathrm{HH}}$ coupling is not visible in the proton spectra and cannot be used for differentiation. In other cases, there will be no protons at the stereogenic centers or the stereogenic centers are more than one bond distant from each other. Under such circumstances, the distinction between the racemic mixture and the *meso*-compound by NMR is not straightforward and a chiral environment has to be added to the analytes to achieve the differentiation.

4.2.1. Enantiodifferentiation by NMR

Enantiodifferentiation by NMR can be achieved by introducing a chiral environment. The analyzed molecules can interact differently with the chiral environment or diastereomeric complexes can be formed and differentiated by NMR because of different Residual Dipolar

Couplings (RDCs) or chemical shift differences for enantiomers. The chiral environment can be induced by chiral alignment media, by chiral Lanthanoide Shift Reagents (LSRs) or by Chiral Solvating Agents (CSAs). The chiral alignment medium interacts with the analyte and differently sized RDCs are measured for each diastereomer. The drawbacks of the method are the sample preparation, the line broadening due to the large number of proton-proton dipolar couplings and finding an appropriate alignment medium together with a suitable solvent for the molecule under investigation. Chiral LSRs interact with the analyte and form diastereomeric complexes. Enantiomers can be differentiated by different PCS for each of them. The sample preparation is fast, as the powder of the LSR has to be dissolved in the sample. One disadvantage is the line broadening due to Paramagnetic Relaxation Enhancements (PREs) which can impede the analysis at high fields. Moreover, the analyte needs a group which has properties of a hard Lewis acid for the interaction with the lanthanide ion. Consequently, LSRs are not compatible with every analyte. The last method are chiral solvents or chiral solvating agents. As well as LSR, they form diastereotopic complexes with the analytes and induce a chemical shift difference for the nuclei at the stereogenic centers. As for LSR, the sample preparation is easy and quick. However, to find an appropriate CSA is as well challenging and depending on solubility and functional groups of the analyte.

In the next sections, the different methods will be discussed in more detail.

4.2.2. Chiral Alignment Media

As mentioned before in Section 2.3.1, the size of the measured dipolar couplings are dependent on the angle of the vector of the bond and the outer magnetic field B_0. Here, it will be pointed out why chiral alignment media can be used to differentiate enantiomers and how the dipolar couplings are relevant for the differentiation. With the use of an alignment medium, chemical shift anisotropy, dipolar interactions and quadrupolar interactions are observable, which are averaged out in solution. By the interaction of a chiral analyte with a chiral alignment medium all these interactions are present as well but they are dependent on the stereochemistry of the molecule.

$$\nu^{R \text{ or } S} = \hbar \gamma B_0 \left[1 - \frac{1}{3}(\sigma_{xx} + \sigma_{yy} + \sigma_{zz}) - \frac{2}{3} \sum_{\alpha\beta = x,y,z} \sigma_{\alpha\beta} A_{\alpha\beta}^{R \text{ or } S} \right] \tag{4.1}$$

σ is the shielding tensor and $A^{R \text{ or } S}$ is the alignment tensor of either the (R)- or the (S)-enantiomer. The alignment tensor is different for each enantiomer, as they associate differently to the chiral alignment medium.

The dipolar coupling $D_{IS}^{R \text{ or } S}$ is also dependent on the alignment tensor, which is specific for each enantiomer, as follows in Equation 4.2.

$$D_{IS}^{R \text{ or } S} = \frac{-\mu_0 \hbar \gamma_I \gamma_S}{8\pi^2 r_{IS}^3} \sum_{\alpha,\beta = x,y,z} A_{\alpha,\beta}^{R \text{ or } S} r_\alpha r_\beta \tag{4.2}$$

γ is the gyromagnetic ratio of the nuclei I and S, r_{IS} is the distance between the two nuclei and $A_{IS}^{R \text{ or } S}$ is the alignment tensor for each enantiomer and the unity vector $r =$

(r_x, r_y, r_z). The equation shows that the dipolar interaction of the analyte is dependent on the alignment tensor, which is different for enantiomers in a chiral alignment medium.[17, 22]

The association of the solute is probably a function of the molecular shape and dependent on a specific binding to the polymer. However, in a homogeneously aligned sample, line widths are small. Additionally, in a $1:1$ mixture of PBLG and PBDG, it has been shown that the differential ordering for enantiomers vanishes [116]. Actually, these two properties lead to the assumption that the interaction of the analyte with the chiral alignment medium is a fast dynamic equilibrium on the NMR time scale.[17]

Chiral alignment media include PBLG [49], PBDG [116], PELG [52], PCBLL [52], polyisocyanides [59], polyguanidines [58], polyacetylenes [60, 61], cyclodextrines in LC, collagen [68], gellan gum [69], and gelatine [18, 67]. PBLG is widely used, as it is commercially available. PBLG is a chiral lyotropic liquid crystalline phase. The chirality is resulting from the α-helical conformation of the backbone. It has been extensively investigated and used to differentiate enantiomers.[17, 52, 117]

Racemic mixtures can be differentiated from *meso*-compound and unambiguously assigned by the two properties shown above in the Equations 4.1 and 4.2. First, the RCSA is different for the (R, R)-, the (S, S)- and the *meso*-compound. Therefore, the signals appear for each proton and carbon in a stereogenic center at different chemical shifts for each diastereomer. Equation 4.2 shows the dependency of the size for RDCs for both enantiomers. Consequently, RDCs must be different if the alignment tensor $A^{R \text{ or } S}$ is different for each molecule. Therefore, if the analyzed molecule has protons at the stereogenic centers, ${}^3T_{\mathrm{HH}}$ couplings are sufficient to differentiate the racemic mixture from the *meso*-compound. Since, the ${}^3T_{\mathrm{HH}}$ couplings for the racemic mixture have different size for each enantiomer if every enantiomer aligns differently. Conversely, the ${}^3T_{\mathrm{HH}}$ coupling for the *meso*-compound has the same magnitude for both stereogenic centers, as the alignment of the molecule in the chiral alignment medium determines the magnitude of the ${}^3T_{\mathrm{HH}}$ coupling. For molecules without protons at the stereogenic centers or if the stereogenic centers are not directly next to each other, ${}^3T_{\mathrm{HH}}$ couplings are not available consequently this method fails. Alternatively, the induced RCSA is too small to lead to resolved different chemical shifts for each stereogenic center in the *meso*-compound.[95]

Drawbacks of this method are the resolution due to numerous proton-proton dipolar couplings and the sample preparation, as the preparation of liquid crystalline phase samples can take up weeks. Additionally, LLCs have a critical concentration, a temperature range and a small range of available solvents. All these factors might complicate the analysis of enantiomers with RDCs.

4.2.3. Shift Reagents

LSRs are inducing a PCS because of paramagnetic ions present in the complex. (III) ions are paramagnetic (besides Lu^{+3}). The paramagnetism arises from unpaired electrons in the f-orbitals. The interaction of the unpaired electrons with other nearby located nuclei changes the chemical shift of these nuclear spins (besides Gd+3), enhances the nuclear relaxation (PRE), aligns molecules in a magnetic field and leads to cross correlation effects.[37] For LSRs, the paramagnetic shifts and the enhanced nuclear relaxation are the

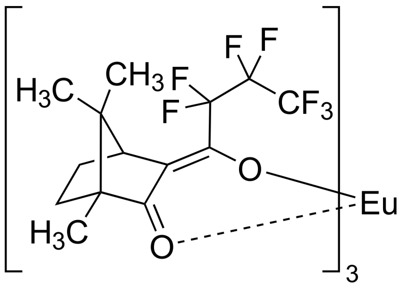

Figure 4.4.: Structure of Europium(III) tris[3-(heptafluoropropylhydroxymethylene)-d-camphorate] (Eu(hfc)$_3$).

essential characteristics, which have to be taken into account for the analysis. The induced paramagnetic shifts can arise either from contact interaction or from dipolar interaction. The contact interaction involves σ and π bonds. Whereas, the dipolar interaction leads to direct delocalization and/or spin polarization of the unpaired electron via the molecular orbitals of the substrate ligand.

The McConnell equation qualitatively defines the relationship between the induced shift $\Delta\delta$ and the distance of the lanthanide (r) and the number of degrees that the nucleus lies away from the axial axes of symmetry (θ):

$$\Delta\delta = k(1 - 3\cos^2\theta)r^{-3} \tag{4.3}$$

As mentioned before, the paramagnetism induces enhanced relaxation (called PRE). PRE leads to line broadening, which is proportional to the squared strength of the magnetic field (B_0^2). Therefore, the magnetic field strength used to measure the sample has to be chosen carefully.[23]

s are hard lewis acids. This is why, their affinity for donor sites of the ligands in the order of electronegativity and is going from $F^- > OH^- > H_2O > NO_3^- > Cl^-$. The coordination number of the lanthanide atom depends on the steric demand of the ligand. Other affinities of the lanthanide to a donor sites are in the order of: amine > hydroxyl > aldehyde > ether > ester > nitrile, which are all hard Lewis bases. In contrast to soft Lewis bases such as olefines, aromatics, halogenated compounds and phosphines that do not bind to or interact with the lanthanides.[118]

To induce a PCS, it is crucial that the test molecule is in fast exchange on the NMR time scale. Thereby, the solvent polarity and the analyte itself plays an important role. If the analyte is too strongly bound to the LSR, only the signals in the NMR spectra are broadened due to faster relaxation and no more information can be gathered.

If LSRs are chiral, they form diastereotopic complexes with the analytes under investigation. Consequently, the former enantiomers are bound in diastereotopic complexes which leads to different PCS for the nuclei of the enantiomers.[23]

Europium(III) tris[3-(heptafluoropropylhydroxymethylene)-d-camphorate] (Eu(hfc)$_3$) is the most widely used and commercially available complex used as a chiral LSR. Its structure is shown in Figure 4.4.

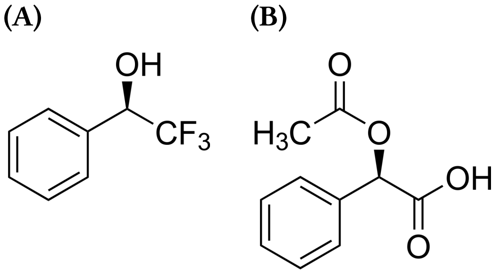

Figure 4.5.: Structure of (A) *R*-(−)-α-(TriFluoromethyl)Benzyl alcohol ((*R*)-TFB) and (B) O-acetylmandelic acid.

4.2.4. Chiral Solvating Agents

Like the LSR, CSA form diastereomeric complexes with the analyte. The analyte is in rapid equilibrium with the bulk solvent. There are two reasons for the resulting chemical shift anisochrony. First, the relative position of magnetically equivalent anisotropic groups (e. g., phenyl, carbonyl) with respect to other substituents in the diastereomeric complex. Second, the resonance signals from each enantiomer represents a population weighted average of chemical shifts, as the exchange between the chiral and achiral solvates is fast on the NMR time scale. Consequently, the observed resonance signals for each enantiomer δ_R(obs) and δ_S(obs) are averaged chemical shift for each enantiomer in the diastereomeric complex and solvated in the bulk solvent. In principle, lower temperatures favor the association. Therefore, reduced temperature can lead to increased chemical shift differences.

An advantage of the method is the sample preparation, which is quick and simple and racemization is not possible. On the other hand, the chemical shift difference ($\Delta\delta$) values are small and difficult to resolve. Under such circumstances, the measurement could be performed at higher magnetic field strengths, as $\Delta\delta$ is proportional to the field strength. Additionally, only a small range of solvents can be used (mostly $CDCl_3$, CCl_4 and C_6D_6). Polar solvents tend to solvate the solute and $\Delta\delta$ decreases to zero. As the chemical shift difference $\Delta\delta$ is dependent on the rate constant for the complex formation, the temperature may be decreased for higher $\Delta\delta$ values. The diastereomeric complexation is driven by hydrogen bond formation and π-stacking.[23]

The first CSA, (*R*)-α-phenylethylamine, is published in 1966 by Pirkle [119]. He used (*R*)-α-phenylethylamine to resolve the enantiomers of *R*-(−)-α-(TriFluoromethyl)Benzyl alcohol ((*R*)-TFB) (for structure, see Figure 4.5A) and (*S*)-TFB. The most common CSA are (*R*)-α-naphtylethylamine, 1,2-diphenyldiaminoethane, enantiopure carboxylic acids (e. g., O-acetylmandelic acid, for structure see Figure 4.5B), binaphthyl-2,2'-diyilphosphate and 1-(9-anthryl)-2,2,2-trifluoroethanol. [23]

Which CSA can be used to induce $\Delta\delta$ chemical shift difference for enantiomers is dependent on the solute and his functional groups.

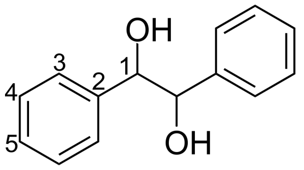

Figure 4.6.: Hydrobenzoine with numbered atoms.

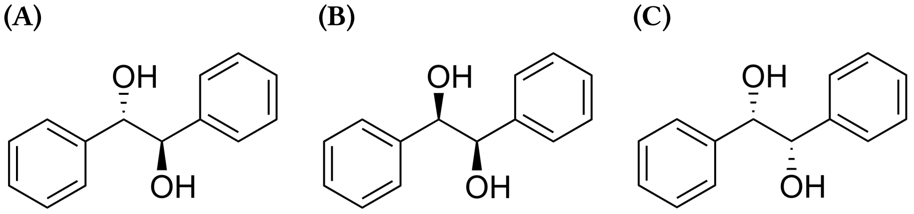

Figure 4.7.: Diastereoisomeres of hydrobenzoin. (A) *meso*-hydrobenzoin. (B) (*R,R*) hydrobenzoin, (C) (*S,S*) hydrobenzoin.

4.3. Shifting Agents with Hydrobenzoine

Here, the differentiation of *meso*-hydrobenzoin from the racemic mixture of hydrobenzoin is shown. See Figure 4.6 for the structure with numbered atoms and Figure 4.7 for the diastereomers of hydrobenzoin. Four methods to induce a chemical shift difference between the racemic mixture and the *meso*-compound are tested.

4.3.1. shift reagents

Hydrobenzoine (see Figure 4.6) is investigated with three LSRs and varying their concentration to induce PCS. The magnetic field strength and the temperature are, for all examples shown here, 400 MHz and 300 K. First, a commercially available lanthanide complex Eu(hfc)$_3$ is used to induce a PCS. Second, the ability to induce a PCS to differentiate racemic mixtures from the *meso*-compound of Tri lithium tris[(*R*)-1,1'-bi-2-naphtholate] europium(III) (Eu(BINOL)$_3$Li$_3$) and Europium(III) tris[(*R*)-1,1'-binaphthyl-2,2'-diyl phosphate] (Eu(pnb)$_3$) are analyzed.

In Figure 4.8, the 1D ^{1}H spectra of *meso*-hydrobenzoin with Eu(hfc)$_3$, Eu(BINOL)$_3$Li$_3$ and Eu(pnb)$_3$ are shown. In Figure 4.8A, the signals for the protons are shifted but do not have a different chemical shift for each stereogenic center. Whereas, Eu(BINOL)$_3$Li$_3$ induces chemical shift differences for the protons at C1 of *meso*-hydrobenzoin for each stereogenic center at higher concentrations of Eu(BINOL)$_3$Li$_3$, by retaining small linewidth. Therefore, the induced PRE of Eu(BINOL)$_3$Li$_3$ seems less as for Eu(hfc)$_3$, which is preferable for the analysis of the spectra.

In Figure 4.9, the 1D ^{13}C spectra for the *meso*-hydrobenzoin with Eu(hfc)$_3$, Eu(BINOL)$_3$Li$_3$ and Eu(pnb)$_3$ are shown. The numbers in Figure 4.9B indicate the assignment of the signals to the carbons of hydrobenzoin (see Figure 4.6). The C1 of *meso*-hydrobenzoin show different chemical shifts for the (*R*)- or (*S*)-configured carbon at a concentration of 10.2 mg of Eu(hfc)$_3$. However, the chemical shift difference between the two carbons is 2 Hz. At low concentrations of Eu(hfc)$_3$, the signal for the carbon C1 of *meso*-hydrobenzoin does

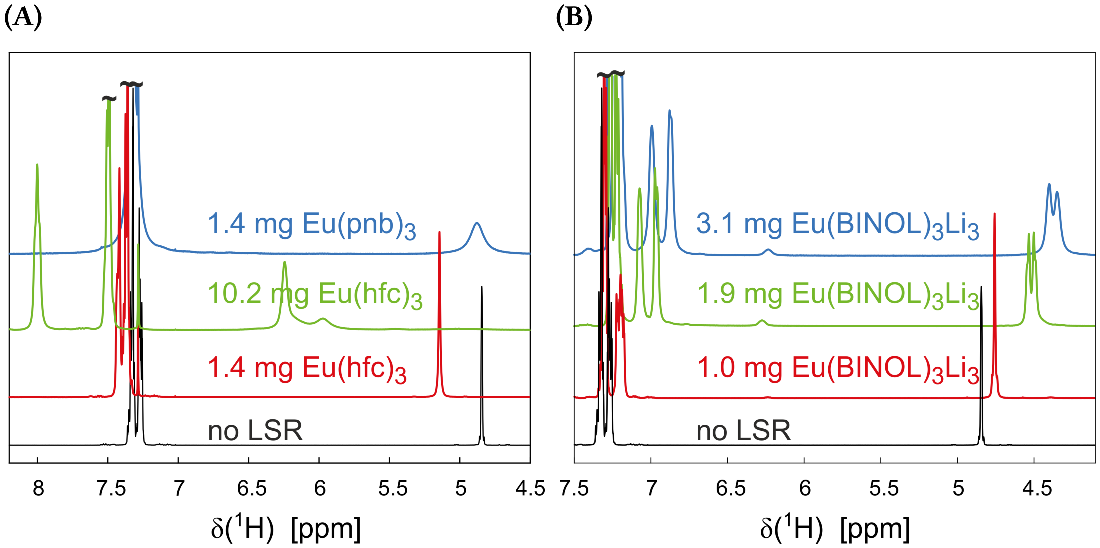

Figure 4.8.: 1D ^{1}H spectrum of *meso*-hydrobenzoin with (A) Eu(hfc)$_3$, Eu(pnb)$_3$ and (B) Eu(BINOL)$_3$Li$_3$.

not show different chemical shifts for each stereocenter (see the red spectrum in Figure 4.10B). For C2 of *meso*-hydrobenzoin, which is the quaternary carbon next to the stereogenic center (shown in Figure 4.10A), no chemical shift difference is resolved but the Full Width at Half Maximum (FWHM) is increased to 5 Hz. In Figure 4.9B, the 1D ^{13}C spectra for *meso*-hydrobenzoin with no, 0.7 mg, 1.5 mg and 2.9 mg Eu(BINOL)$_3$Li$_3$ are shown. In Figure 4.10C and 4.10D, the regions of C1 and C2 demonstrate the change of chemical shift and the line broadening due to the Eu(BINOL)$_3$Li$_3$. Here, it can be clearly seen that the chemical shift difference for each stereogenic center increases with higher amounts of Eu(BINOL)$_3$Li$_3$. Additionally, the effect of Eu(BINOL)$_3$Li$_3$ is not only leading to line broadening on the carbon next to the stereogenic center and the coordinating group of hydrobenzoin but the other carbons are affected as well and have different chemical shifts than in the solution without Eu(BINOL)$_3$Li$_3$. The chemical shift differs for each carbon nucleus and is the highest for C1 and C2 of *meso*-hydrobenzoin. *Meso*-hydrobenzoin is analyzed with another potential LSR, Eu(pnb)$_3$. The resulting 1D ^{13}C spectrum is shown in Figure 4.9C. The signals are severely line broadened. The FWHM is 31.7 Hz for the quaternary carbon C2 and 37.8 Hz for C1. No discrimination of two signals for each stereogenic center is possible.

In Figure 4.11A, the 1D ^{13}C spectrum for all three diastereoisomers of hydrobenzoin with Eu(hfc)$_3$ is shown. The structures for the three diastereoisomers of hydrobenzoin are shown in Figure 4.7. The signals resulting from C1 are in the region between 77 ppm and 87 ppm (see Figure 4.12B). The signal from the *meso*-compound is sharp but does not show different chemical shifts for the (*R*)- and the (*S*)-configured centers with Eu(hfc)$_3$. The signals for the (*R*,*R*)- or the (*S*,*S*) compound are line broadened and show different chemical shifts for the two concentrations of Eu(hfc)$_3$. The line width of the signals resulting from the quaternary carbon (C2, see Figure 4.12A) are broadened for all three species but no chemical shift difference for the racemic mixture is resolved. In Figure

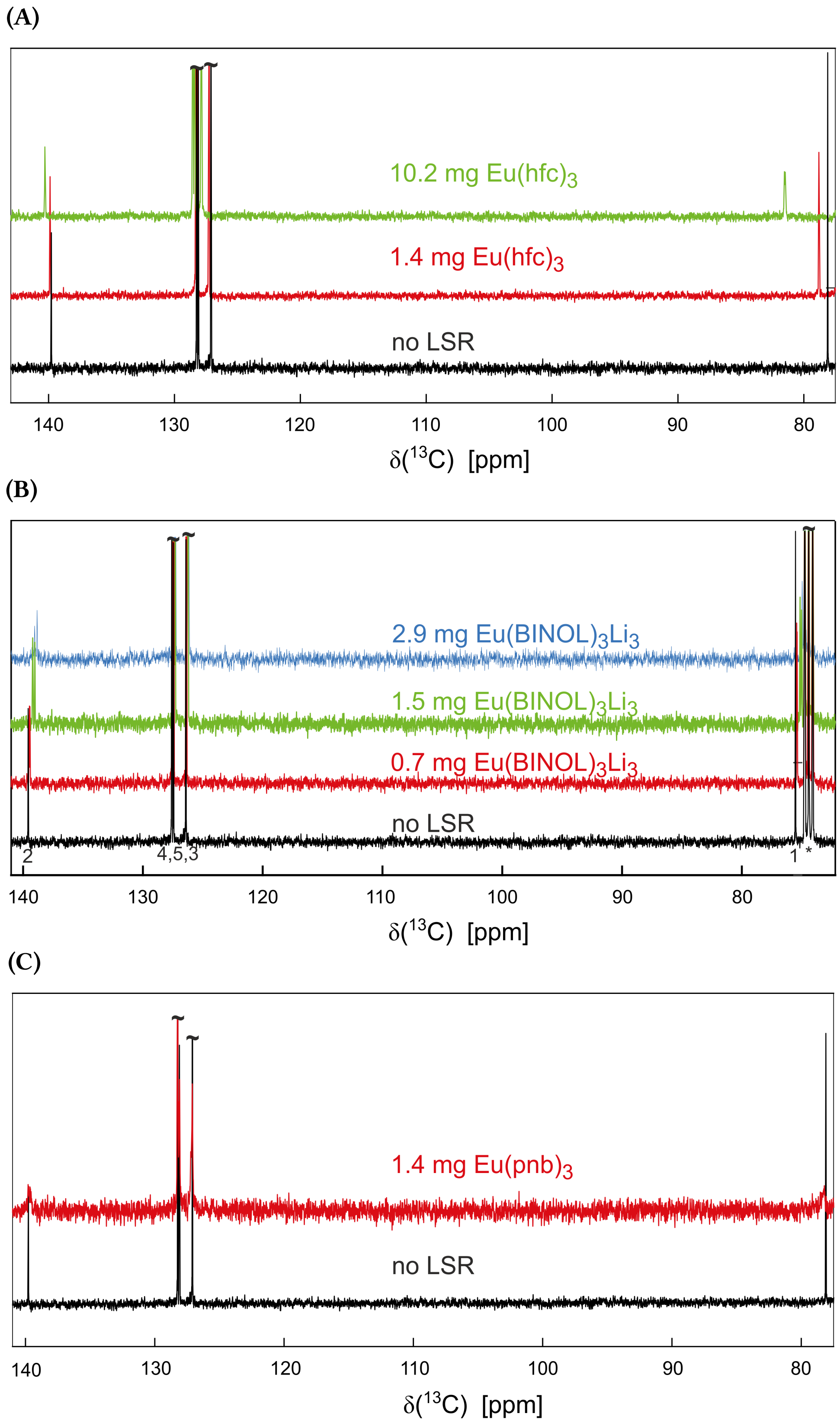

Figure 4.9.: 1D ^{13}C spectrum of *meso*-hydrobenzoin with (A) Eu(hfc)$_3$, (B) Eu(BINOL)$_3$Li$_3$ and (C) Eu(pnb)$_3$. The CDCl$_3$ signal is marked with an asterisk.

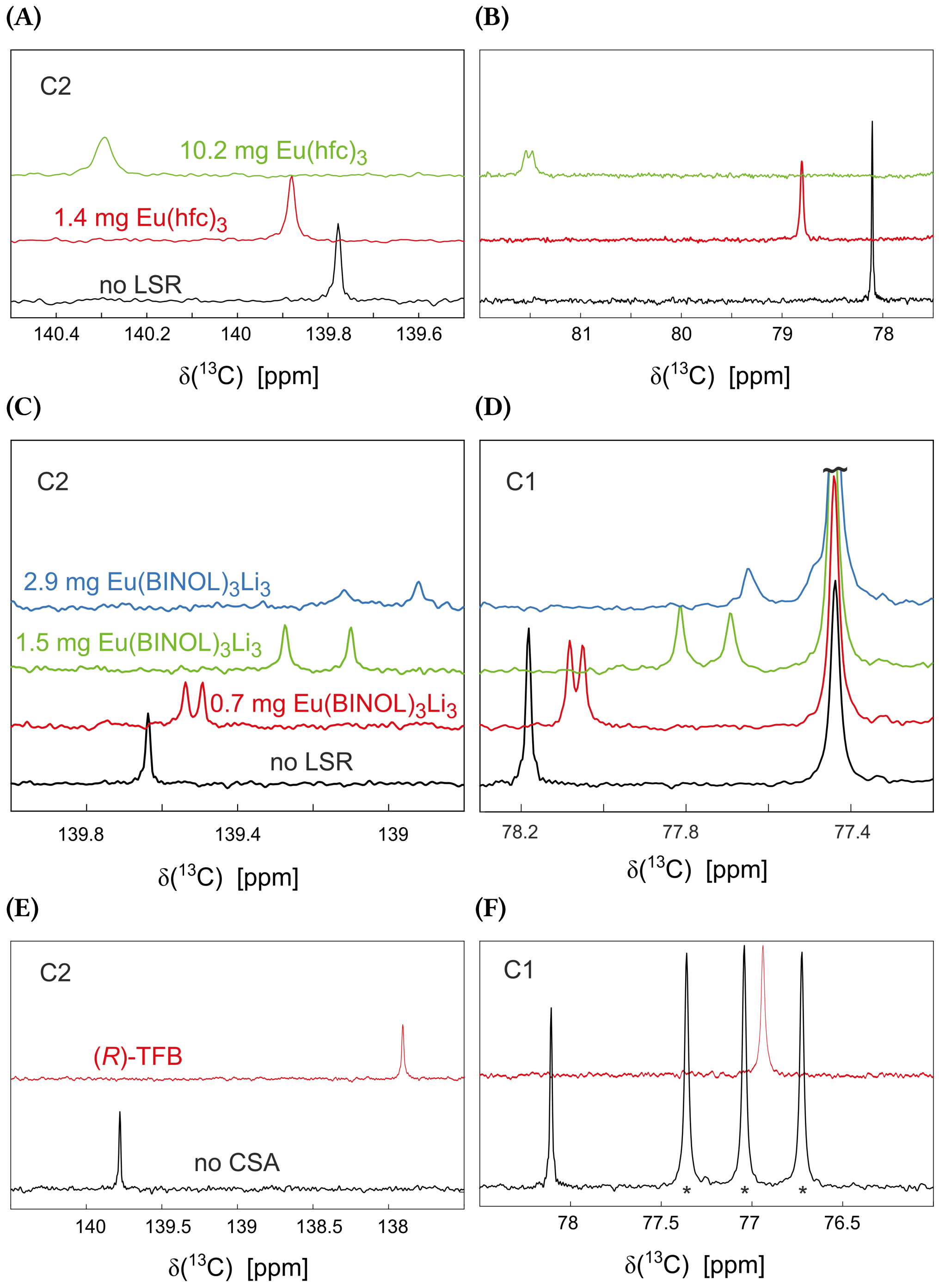

Figure 4.10.: 1D ^{13}C spectra ((A), (C) and (E)) of C2 and ((B) and (D) and (F)) of C1 of *meso*-hydrobenzoin with ((B) and (A)) Eu(hfc)$_3$, ((D) and (C)) Eu(BINOL)$_3$Li$_3$ and ((E) and (F)) dissolved in (*R*)-TFB.

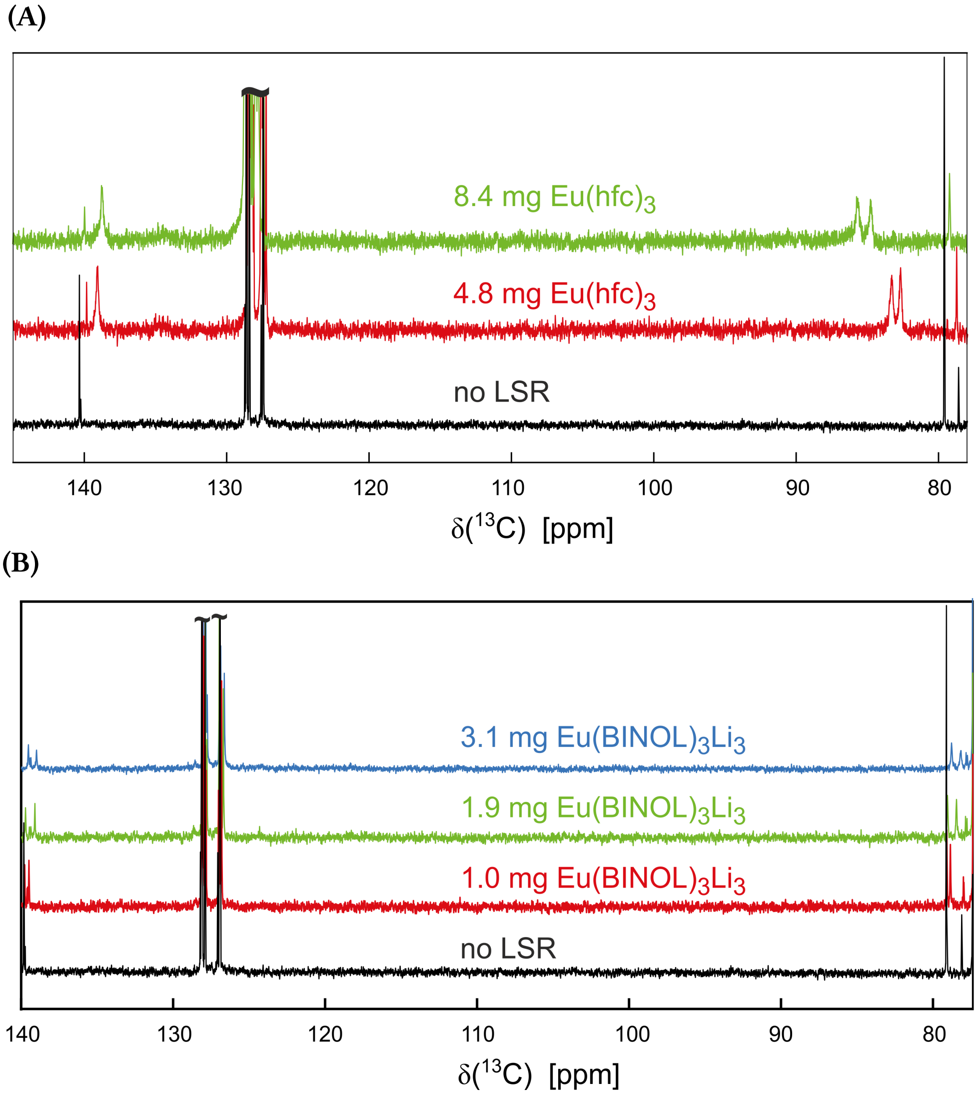

Figure 4.11.: 1D ^{13}C spectrum of the racemic mixture and *meso*-hydrobenzoin with (A) Eu(hfc)$_3$ and (B) Eu(BINOL)$_3$Li$_3$.

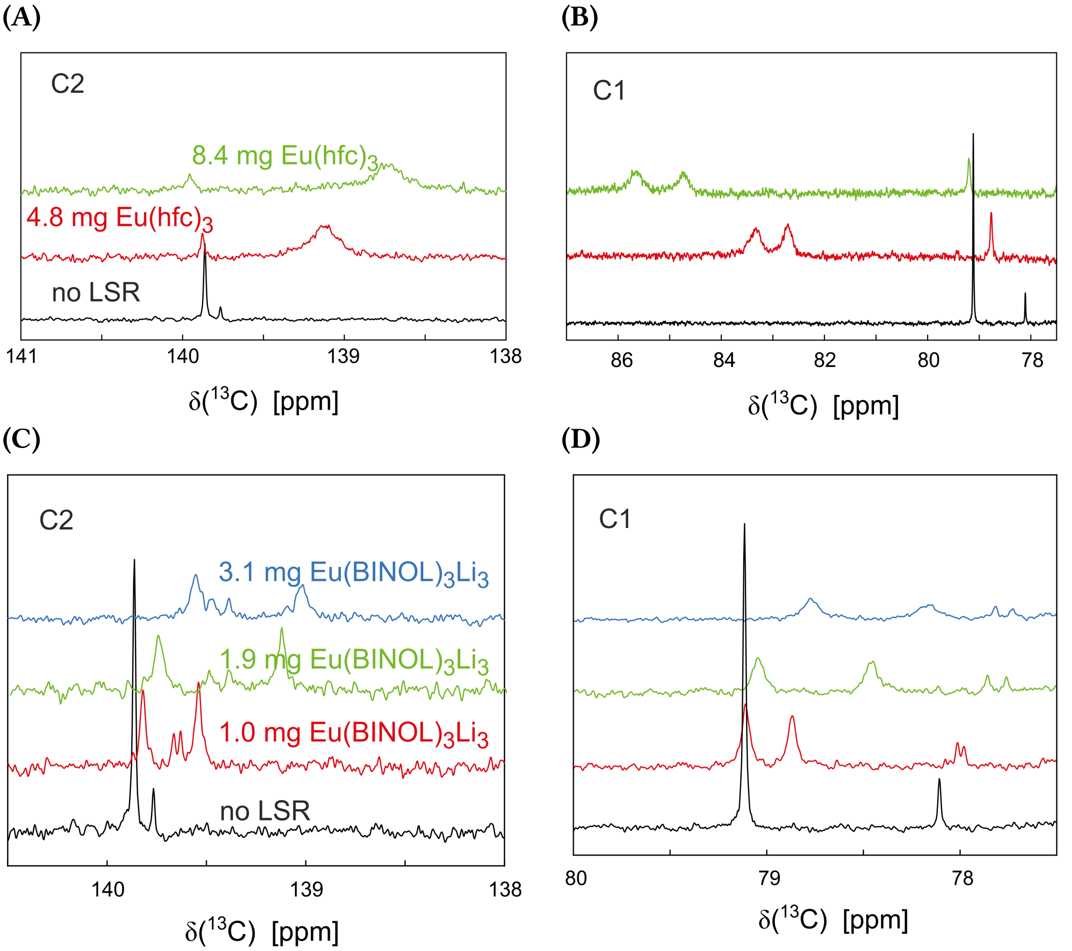

Figure 4.12.: 1D ^{13}C spectra of C1 and C2 of the racemic mixture and *meso*-hydrobenzoin with Eu(hfc)$_3$ and Eu(BINOL)$_3$Li$_3$.

4.11B, the 1D ^{13}C spectra for all three diastereomers with no, 0.9 mg, 1.9 mg and 3.1 mg Eu(BINOL)$_3$Li$_3$ are shown. All three diastereomers show different PCS for the increased amount of Eu(BINOL)$_3$Li$_3$. The higher the concentration of Eu(BINOL)$_3$Li$_3$, the broader the signals and the higher the PCS. This can be best seen in Figure 4.12C and 4.12D, where the regions of C1 and C2 are shown. The spectra show that 1 mg of Eu(BINOL)$_3$Li$_3$ is sufficient to lead to different PCS for all three diastereoisomers. For both carbons (C1 and C2), the signals for the racemic mixture are severely broadened.

In Table 4.1, the FWHM of the signals C1 and C2 for all diastereomers of hydrobenzoin are shown. The values for the line widths are determined in the 1D ^{13}C spectra for both the measurement of hydrobenzoin with Eu(hfc)$_3$ and Eu(BINOL)$_3$Li$_3$. The line broadening is for both (*R,R*)- and (*S,S*)-hydrobenzoin increased compared to *meso*-hydrobenzoin. Line broadening is higher for Eu(hfc)$_3$, but the used concentrations are also higher to achieve separate chemical shifts. In Figure 4.13, the pseudo contact shifts for carbon C1 and C2 are shown for hydrobenzoin measured relatively to hydrobenzoin dissolved in chloroform depending on the concentration of Eu(BINOL)$_3$Li$_3$. It can be seen that the PCS is increasing for an increased amount of Eu(BINOL)$_3$Li$_3$.

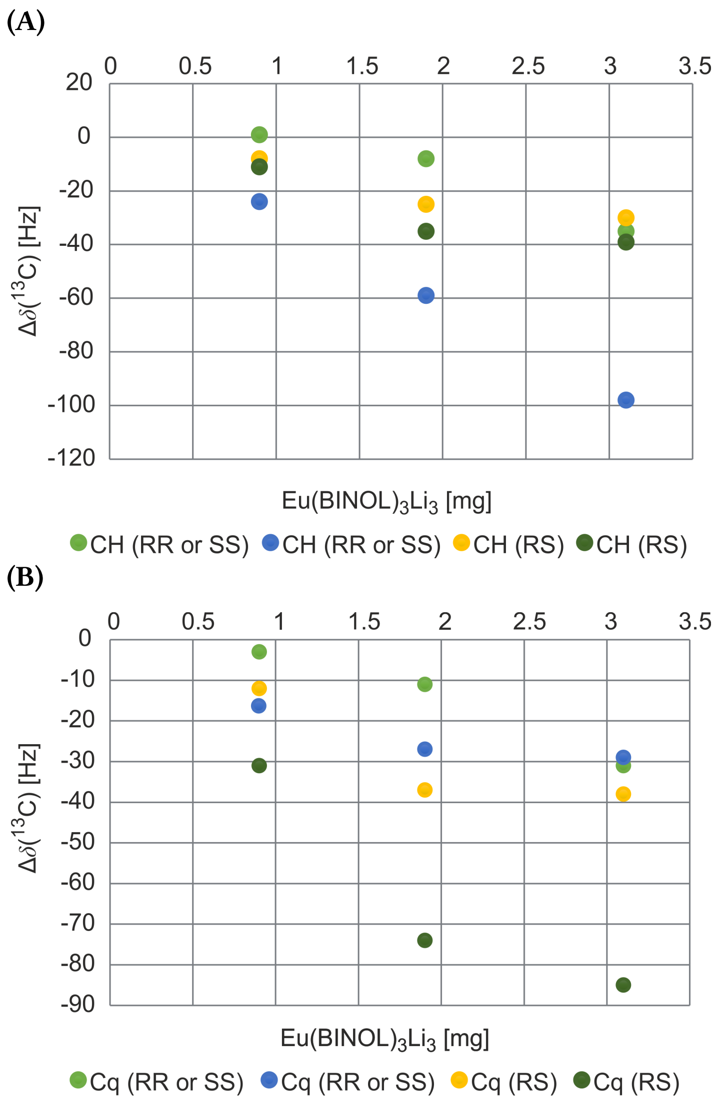

Figure 4.13.: $\Delta\delta^{13}$C chemical shift for hydrobenzoin. (A) is the chemical shift difference ($\Delta\delta$) for carbon C1 for hydrobenzoin for 0.9 mg, 1.9 mg and 3.1 mg Eu(BINOL)$_3$Li$_3$. (B) is the chemical shift difference ($\Delta\delta$) for carbon C2 for 0.9 mg, 1.9 mg and 3.1 mg Eu(BINOL)$_3$Li$_3$. (*R,R*) and (*S,S*) cannot be assigned by this method, but have different PCS. Therefore, the legend states (*R,R*) or (*S,S*).

Table 4.1.: FWHM for hydrobenzoin with Eu(hfc)$_3$ and Eu(BINOL)$_3$Li$_3$, measured for the 1D ^{13}C spectra shown in Figure 4.11.

	Eu(BINOL)$_3$Li$_3$ [mg]				Eu(hfc)$_3$ [mg]	
	0	0.9	1.9	3.1	4.8	8.4
rac hydrobenzoin C2 [Hz]	1.7	3.2	5.7	7	19.7	28.8
	1.7	3.2	4.6	5.9	19.7	28.8
meso-hydrobenzoin C2 [Hz]	1.5	2	5.7	4	3.6	5.6
	1.5	1.9	4.3	3.1	3.6	5.6
rac hydrobenzoin C1 [Hz]	1.7	2.9	7.7	10.4	30	28.8
		5	6.9	14.9	21	20.7
meso-hydrobenzoin C1 [Hz]	1.9	2.2	3.8	3.1	2.72	5.6
		2.3	3.2	3.3		

The interaction of the Eu(BINOL)$_3$Li$_3$ complex with *meso*-hydrobenzoin seems to be on a favorable time scale regime for the NMR measurements. Important is, that the exchange is fast compared to the NMR time scale. The OH-group of the *meso*-hydrobenzoin is interacting with the Europium ion. As the Europium ion is a hard lewis acid, this interaction is favorable. For *meso*-hydrobenzoin, the chemical shift of the (*R*) and (*S*) center are clearly distinguishable. This can be best seen in the Figures 4.10C and 4.10D. There, the region of C1 and C2 of *meso*-hydrobenzoin are shown and it is clearly visible that the induced PCS are increasing with higher concentration of Eu(BINOL)$_3$Li$_3$.

4.3.2. Chiral Solvating Agents

Chiral Solvating Agents (CSAs) induce a chemical shift difference for enantiomers by diastereomeric complex formation. *meso* Hydrobenzoine (for the structure see Figure 4.6) is dissolved in (*R*)-TFB, which is an commercially available CSA. In Figure 4.10E and 4.10F, two regions of the spectrum of *meso*-hydrobenzoin in (*R*)-TFB are shown. The Figure shows *meso*-hydrobenzoin dissolved in CDCl$_3$ for comparison (black). Whereas, the spectrum of *meso*-hydrobenzoin in (*R*)-TFB is shown in red. The signals of *meso*-hydrobenzoin are shifted for the spectrum in (*R*)-TFB with respect to the signals of *meso*-hydrobenzoin in Chloroform-D (CDCl$_3$) by 110 Hz. However, the chemical shift of each stereogenic center does not change for the two stereogenic centers ((*R*) and (*S*)). Therefore for *meso*-hydrobenzoin, (*R*)-TFB cannot be used to differentiate the racemic mixture from the *meso*-compound. The FWHM of the quaternary carbon C2 in chloroform is 1.5 Hz, in (*R*)-TFB, FWHM for the same carbon is 1.6 Hz. FWHM at half width for C1 in chloroform is 1.5 Hz, in (*R*)-TFB, FWHM for the same carbon is 3.9 Hz. In the proton spectra (not shown), no chemical shift difference for each proton is noticeable. The FWHM at half height for the proton at C1 is 4.5 Hz for *meso*-hydrobenzoin in chloroform and 4.6 Hz in (*R*)-TFB. With CSA, the line broadening are not as severe as with LSR because the substances are not paramagnetic. On the other hand, if the formation of the complexes does not take place, the scalability of the effect is reduced as the CSA is used as solvent. Therefore, the concentration cannot be increased further.

4.4. Discussion – Shift reagents with Hydrobenzoin

The induced Pseudo Contact Shift (PCS) for hydrobenzoin are measurable for $Eu(hfc)_3$ and $Eu(BINOL)_3Li_3$. No PCS is measurable with $Eu(pnb)_3$ due to severe line broadening and with (*R*)-TFB the signals are shifted but not different for (*R*)- and (*S*)-configured centers of *meso*-hydrobenzoin. The induced Pseudo Contact Shift (PCS) are the highest for $Eu(BINOL)_3Li_3$. To see a chemical shift difference for (*R*)- and (*S*)-configured centers of *meso*-hydrobenzoin with $Eu(hfc)_3$, 10.4 mg are added. However, the PCS differed only in 2 Hz for each center. Additionally, the line widths for (*R,R*)- and (*S,S*)-hydrobenzoin are broadened compared to line widths of *meso*-hydrobenzoin for $Eu(hfc)_3$ and $Eu(BINOL)_3Li_3$. This might be either due to less exchange with the LSR or due to less distance between the Europium and the carbon nuclei.

Comparing the spectra of *meso*-hydrobenzoin recorded with $Eu(BINOL)_3Li_3$ to the spectra with the third LSR ($Eu(pnb)_3$), it might be that the diastereotopic complex formation is on an unfavorable time scale with the latter. As the line widths are severely broadened and no PCS is measurable. The lower exchange rate might be due to more space at the Europium ion, as the ligand is more distant from the Europium ion in the $Eu(pnb)_3$ than in the case of $Eu(BINOL)_3Li_3$ (see Figures 4.20 and 4.21 for the structures of both complexes). Since, the $Eu(pnb)_3$ has the phosphate groups which separates the chiral part of the ligand from the europium. Additionally, the counter-ion (Li^+) in $Eu(BINOL)_3Li_3$ leads to weaker oxygen-europium bond which might increase the exchange rate with ligands and analytes and lead to more favorable exchange rate for the analytes for $Eu(BINOL)_3Li_3$ at a field strength of 400 MHz.

4.5. Identification of the *meso*-Compound and the Corresponding Racemic Mixture

By recording an 1D ^{13}C spectrum, an assignment of the *meso*-compound compared to the racemic mixture is achieved if one of the three isolated compounds is available for measurement. The assignment of the *meso*-compound or the racemic mixture can then be achieved by comparison of the spectra. As the isolated substances might not be available, this approach is not feasible for every case. If protons are at each stereogenic center and the two centers are neighbored, like in hydrobenzoin or tartaric acid, the $^3J_{HH}$ coupling from one stereogenic center to the other proves which diastereomer is present. The $^3J_{HH}$ coupling is only present for the *meso*-compound if both protons have different chemical shifts induced by the LSR or CSA. In this case, a *J*-resolved ^1H spectrum is sufficient. For the enantiomers, no coupling between the two stereogenic centers is visible, as the protons have the same chemical environment and have always the same chemical shift. However, the $^3J_{HH}$ coupling might be too small or too strong for the *meso*-compound. Another approach would be the CLIP-HSQC and HSQC-TOCSY.[86] For the two experiments, it is important that the carbons at the stereogenic centers of the *meso*-compound as well as the (*R,R*) and (*S,S*) compounds have different chemical shifts induced either by RCSA or PCS depending on the method of diastereotopic interaction. If this is not the case, the

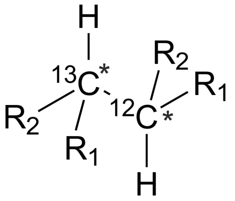

Figure 4.14.: Spin system for the differentiation of racemic mixtures from *meso*-compound. For racemic mixtures both stereogenic centers (marked with an asterisk) have either (*R,R*) or (*S,S*) configuration. For the *meso*-compound the stereogenic centers have different configuration (*R,S*).

measurement of two dimensional spectra with LSR does not help for the assignment of the diastereomers.

The differentiation of the three compounds is driven by the break of symmetry induced by ^{13}C chemical shift evolution. The responsible spin system is shown in Figure 4.14. However, if the ^{13}C chemical shift does not differ for each stereogenic center, the differentiation with CLIP-HSQC and HSQC-TOCSY is ambiguous.

If the carbon chemical shifts differ for both stereogenic centers of the *meso*-compound, the $^3J_{HH}$ coupling is active from one stereogenic center to the other. Therefore, the resulting signals appear at the proton frequency of the (*R*) or (*S*)-configured stereocenter and at the chemical shift of the opposite configured carbon. This is pointed out by the arrows in Figure 4.16 and 4.17. Since the signals arising from the carbon-proton pair are split by the $^1J_{CH}$ coupling, the signals due to the $^3J_{HH}$ coupling are tilted in the other way than the signals arising from the former coupling. In the case of the racemic mixture, the $^3J_{HH}$ coupling does not create a signal at the carbon frequency of the differently configured stereocenter. Hence, the racemic mixture is unambiguously assigned if two carbon chemical shifts arise and the long-range artifact due to the $^3J_{HH}$ coupling is in the middle of each of the signals.

In Figure 4.15, the CLIP-HSQC spectrum for *meso*-hydrobenzoin with 10.2 mg Eu(hfc)$_3$ is shown. The chemical shift difference of the carbons from each stereogenic center is 2 Hz. The $^3J_{HH}$ coupling is present and the spectrum shows a tilt. Nevertheless, the proton chemical shift difference for each proton of the stereogenic center is not resolved. Therefore, the unambiguous assignment of *meso*-hydrobenzoin for this concentration of Eu(hfc)$_3$ is not achieved.

In Figure 4.16, the CLIP-HSQC spectrum for *meso*-hydrobenzoin with 1.5 mg Eu(BINOL)$_3$Li$_3$ is shown. The carbon chemical shift difference is 13 Hz and the proton chemical shift difference is 17 Hz between the (*R*)- and (*S*)-stereogenic centers. The CLIP-HSQC spectrum shows the signals split by the $^1J_{CH}$ coupling and the long-range artifacts which result from the $^3J_{HH}$ coupling from one stereogenic center to the other. The signals resulting from the $^3J_{HH}$ coupling are tilted in the other way then the original signals. This indicates the transfer over the stereogenic center. Therefore, the *meso*-hydrobenzoin can be assigned unambigously. If the compounds are assigned with the CLIP-HSQC spectrum, it is important that the long-range artifacts are high enough in intensity and differentiable from the

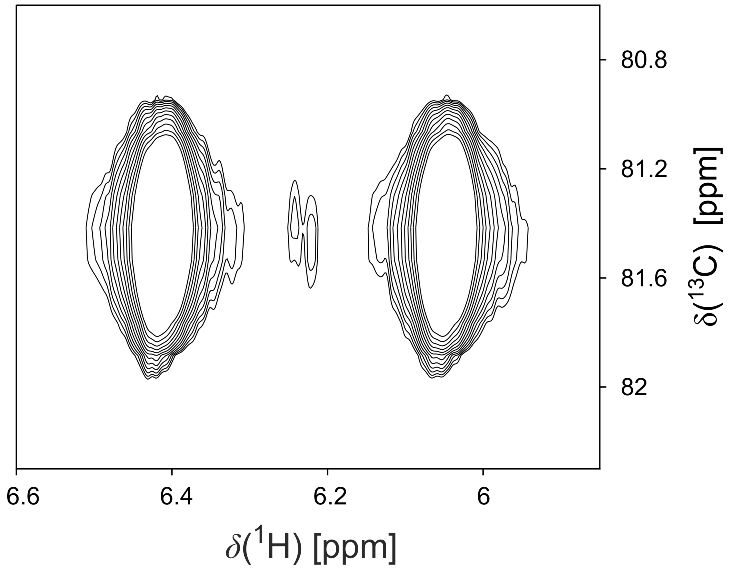

Figure 4.15.: CLIP-HSQC spectrum of *meso*-hydrobenzoin with 10.1 mg Eu(hfc)$_3$. The spectrum shows the two carbon-proton pairs of *meso*-hydrobenzoin with (*R*) or (*S*) configuration. The small signals in the middle are due to the long-range artifacts. Sample preparation and the experimental parameters are summarized in Section 4.8.4.

noise. This is the case for concentrations of LSR where the PRE effect is not dominant. In other words if the signals are not too broadened.

For cases where the long-range artifacts are not visible, the coupling transfer over the stereogenic center can be achieved more reliably by measuring a HSQC-TOCSY. This sequence is presented in Section 2.7.2. For the differentiation of the diastereomers, the HSQC sequence is important. As it leads to separation of the signals in the indirect dimension due to their different carbon chemical shifts of the stereogenic centers. Afterwards, the TOCSY transfer leads to the polarization transfer of one stereogenic center to the other. The result is the same as for the long-range artifacts, but the TOCSY transfer is more reliable. A CLIP-HSQC spectrum overlaid with a HSQC-TOCSY for *meso*-hydrobenzoin is shown in Figure 4.17. The CLIP-HSQC spectrum is shown in black and the HSQC-TOCSY spectrum is shown in blue. The spectra are recorded for *meso*-hydrobenzoin with 2.9 mg Eu(BINOL)$_3$Li$_3$. With increasing amount of Eu(BINOL)$_3$Li$_3$, the line width of the carbon signals are broadened, which reduces the signal-to-noise ratio.

The spectrum in Figure 4.18 shows a CLIP-HSQC spectrum overlayed with HSQC-TOCSY for three diastereomers of hydrobenzoin with 1.9 mg Eu(BINOL)$_3$Li$_3$. The signals for *meso*-hydrobenzoin show the former explained splitting. The signals arising from the (*R,R*)- or the (*S,S*) compound do not show this behavior. The signal due to the $^3J_{HH}$ coupling is in the middle of the signals split by the $^1J_{CH}$ coupling.

The differentiation of the racemic mixture from the *meso*-compound has been accomplished for Eu(BINOL)$_3$Li$_3$ with hydrobenzoin. Both sequences, the CLIP-HSQC and the HSQC-TOCSY, lead to the desired result because of different PCS for each stereogenic center in the *meso*-compound and the racemic mixture. Additionally, the transfer over the $^3J_{HH}$ is clearly visible for both kind of spectra. At lower concentration, the CLIP-HSQC

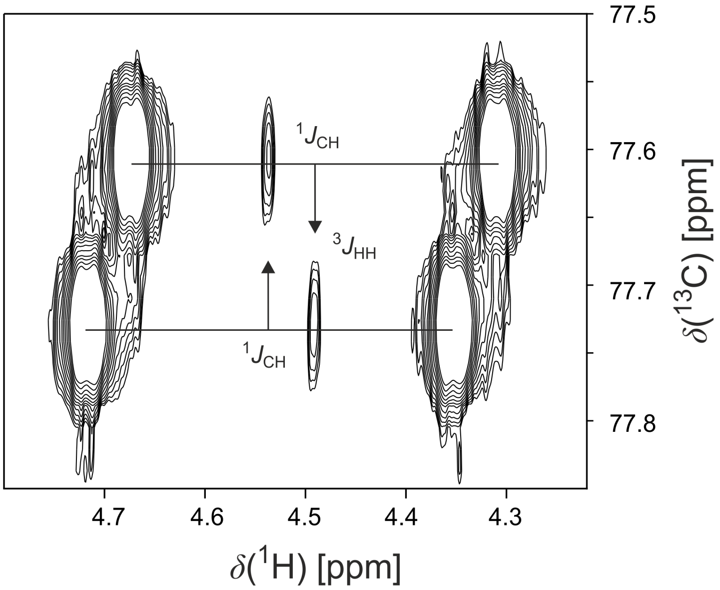

Figure 4.16.: CLIP-HSQC spectrum of *meso*-hydrobenzoin with 1.5 mg Eu(BINOL)$_3$Li$_3$. The spectra shows only the signal of C1 of *meso*-hydrobenzoin. These are the signals arising from the chiral centers of the (*R*) and the (*S*)-center. The spectrum shows the long-range artifact at low signal intensity between the signals split by the $^1J_{CH}$. The spectra are recorded and processed with the parameters summarized in Section 4.8.4.

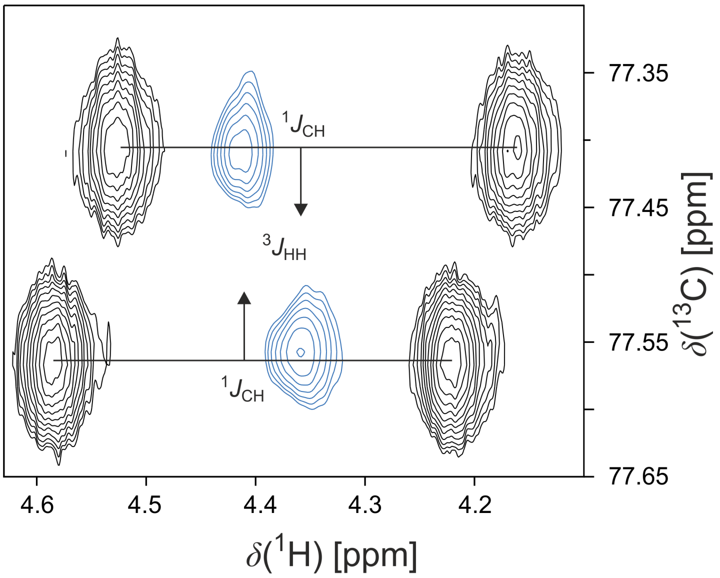

Figure 4.17.: CLIP-HSQC (black) and a HSQC-TOCSY (blue) spectrum of *meso*-hydrobenzoin with 2.9 mg of Eu(BINOL)$_3$Li$_3$. In the spectra only the signal of the C1-H of *meso*-hydrobenzoin is shown, which are the signals arising from the chiral centers of the (*R*) and the (*S*)-center. The spectra are recorded and processed with the parameters summarized in Section 4.8.4.

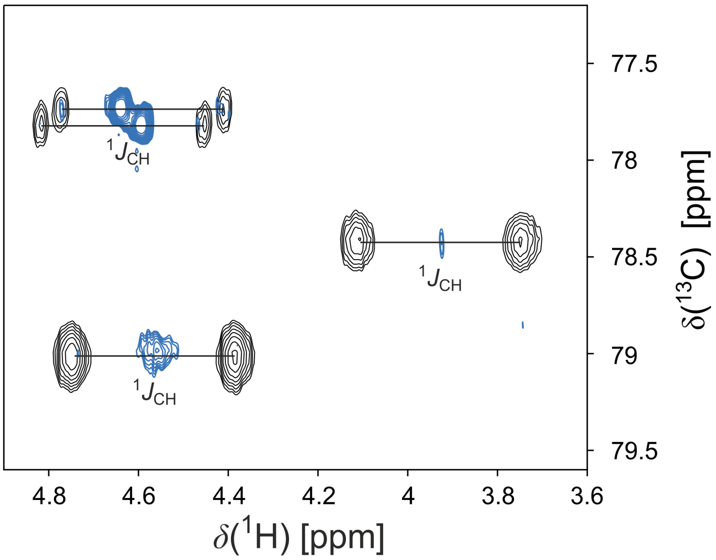

Figure 4.18.: CLIP-HSQC and HSQC-TOCSY spectrum of hydrobenzoin with 1.9 mg of Eu(BINOL)$_3$Li$_3$. In the spectra the signal of the C1-H of hydrobenzoin is shown. These are the signals arising from the chiral centers of the *meso* compound or the (*R*,*R*) or (*S*,*S*) compound. The spectra are recorded and processed with the parameters summarized in Section 4.8.4.

is sufficient to achieve a separation for compounds where protons are at the stereogenic centers and separated by one bond. If the two stereogenic centers are more than one bond apart from each other, the CLIP-HSQC is not enough to assign the three species. In this case, the HSQC-TOCSY is substantial as it allows the transfer over a whole spin system.

Neither the CLIP-HSQC nor the HSQC-TOCSY lead to the desired result if the two stereogenic centers are separated by quaternary carbons or other nuclei which impede the transfer over the $^3J_{\mathrm{HH}}$ coupling. Additionally, the protons in the stereocenters are crucial for the assignment with CLIP-HSQC or HSQC-TOCSY. For molecules, which have no protons at the stereogenic centers, other experiments have to be exploited, such as a INADEQUATE. An INADEQUATE spectrum correlates the chemical shift of two adjacent carbons with each other.

4.6. Chiral differentiation using Eu(BINOL)$_3$Li$_3$ at Low Magnetic Field

To evaluate the differentiation of *meso*-compound from racemic mixtures at low magnetic field, Eu(hfc)$_3$ and Eu(BINOL)$_3$Li$_3$ are measured with *meso*-hydrobenzoin at a spectrometer with a room temperature magnet and a resulting proton frequency of 62 MHz. The spectrometer is equipped with a proton coil only, therefore the unambiguous assignment through measurement of CLIP-HSQC or HSQC-TOCSY is not possible. In this case, the substances could be assigned if the diastereomers are available for comparison.

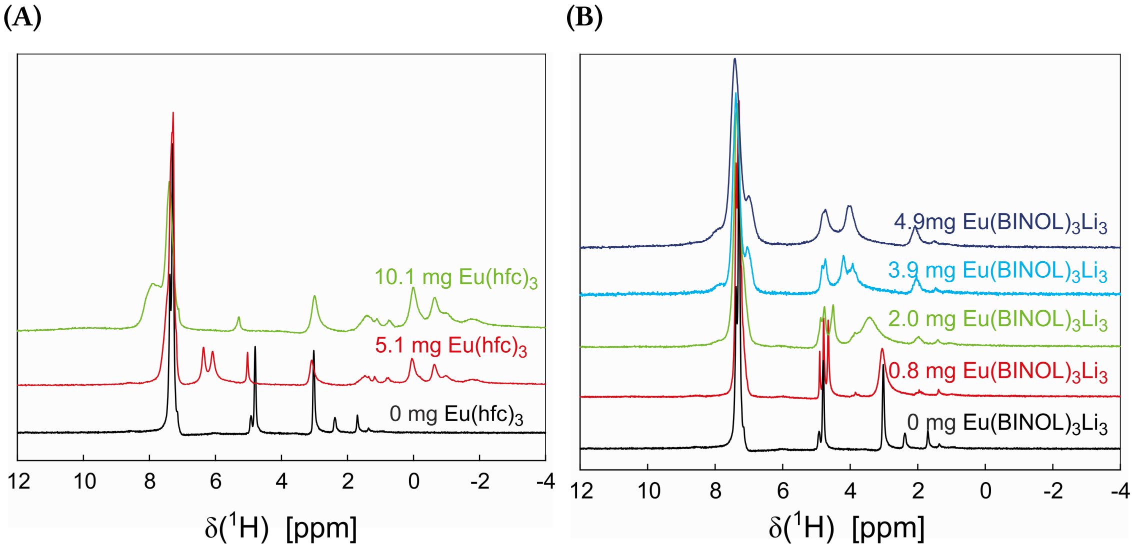

Figure 4.19.: 1D ^{1}H spectra of *meso*-hydrobenzoin with (A) Eu(hfc)$_3$ and (B) Eu(BINOL)$_3$Li$_3$ at 62 MHz proton frequency.

The 1D ^{1}H spectra for *meso*-hydrobenzoin are shown in Figure 4.19. For Eu(hfc)$_3$, the red spectrum with the concentration of 5.1 mg Eu(hfc)$_3$ shows two signals at 6 ppm, which correspond to each stereogenic centers of *meso*-hydrobenzoin. They are separated by 18 Hz. The FWHM for these signals is 6.2 Hz. At a concentration of 10.1 mg, the signals are not present anymore.

The spectra with *meso*-hydrobenzoin and Eu(BINOL)$_3$Li$_3$ show an increased broadening of the signals and a higher difference in chemical shift for the protons at the stereogenic centers, both increase with increasing amounts of Eu(BINOL)$_3$Li$_3$. The proton at the stereogenic centers have a chemical shift of 4.7 ppm. The chemical shift difference is 8.7 Hz at 0.8 mg Eu(BINOL)$_3$Li$_3$ and increases to 46.5 Hz at 4.9 mg Eu(BINOL)$_3$Li$_3$. The FWHM is 2.5 Hz at 0.8 mg Eu(BINOL)$_3$Li$_3$ and 17.4 Hz at 4.9 mg Eu(BINOL)$_3$Li$_3$.

Eu(hfc)$_3$ and Eu(BINOL)$_3$Li$_3$ are measured with *meso*-hydrobenzoin at a low magnetic field spectrometer. The differentiation of the two stereogenic centers is possible with both chiral LSR. The chemical shift differences are higher at lower concentration of Eu(BINOL)$_3$Li$_3$, but the line broadening is higher. Principally, Eu(BINOL)$_3$Li$_3$ can be a promising LSR for chiral differentiation also at low magnetic fields. Nevertheless, Eu(BINOL)$_3$Li$_3$ should be tested to differentiate enantiomers at low magnetic fields more extensively.

4.7. Conclusion

It had been shown that Eu(BINOL)$_3$Li$_3$ can be used as an LSR and to discriminate racemic mixtures from the *meso*-compound. It is also shown that Eu(BINOL)$_3$Li$_3$ leads to higher PCSs for carbon and proton than Eu(hfc)$_3$ for hydrobenzoin. Therefore, the discrimination of the racemic mixture from the *meso*-compound is easier for the sample containing the Eu(BINOL)$_3$Li$_3$. With Eu(hfc)$_3$, the PCS difference of 2 Hz is not sufficient to resolve the two signals of the two stereogenic centers for the *meso*-compound. Consequently, the differentiation with the CLIP-HSQC or HSQC-TOCSY fails. The differentiation between the *meso*-compound from the racemic mixture is shown for hydrobenzoin with the CLIP-HSQC and HSQC-TOCSY spectra.

To prove wider applicability, other substances fulfilling the rac/*meso* requirements should be investigated. It could be that Eu(BINOL)$_3$Li$_3$ is coordinating in a favorable way to hydrobenzoin but would fail in other cases. Furthermore, different compounds and concentrations should be examined with Eu(pnb)$_3$. It might be that for sterically hindered molecules, exchange rates with the complex are in a more favorable time scale and FWHMs are not severely broadened and lead to measurable PCSs.

Moreover molecules with no protons in the stereogenic centers could be challenging as they cannot be assigned by the CLIP-HSQC or HSQC-TOCSY experiments.

Additionally, the ability to induce PCS for *meso*-hydrobenzoin is measured with Eu(BINOL)$_3$Li$_3$ and compared to Eu(hfc)$_3$ at low magnetic field with a proton frequency of 62 MHz. It has been shown that Eu(BINOL)$_3$Li$_3$ induces a PCS at the stereogenic centers of *meso*-hydrobenzoin. However, since the spectrometer probehead is not equipped with a carbon coil, the measurements of CLIP-HSQC or HSQC-TOCSY spectra is not possible.

4.8. Material and Methods

Eu(BINOL)$_3$Li$_3$ and Eu(pnb)$_3$ are both synthesized by known routes.

4.8.1. Synthesis of Eu(BINOL)$_3$Li$_3$

The (*R*)-BINOL-complex is synthesized following the paper of Wooten et al.[120]. First the lithium salt of the BINOL is synthesized. (*R*)-BINOL is dissolved in 40 ml THF and 4 ml n-BuLi are added dropwise. This solution is added to Eu(Triflat)$_3$ dissolved in 10 ml THF and stirred at room temperature over night. The THF is removed in vacuo and the powder is again dissolved in THF and pentane is allowed to diffuse into the solution to crystallize Eu(BINOL)$_3$Li$_3$. The diffusion took several weeks at room temperature and led to brownish crystals.

4.8.2. Synthesis of Eu(pnb)$_3$

The synthesis is performed as described in [121]. 146 mg (3.65 mmol) sodium hydroxide (NaOH) is dissolved in 1 ml water and 1 g (2.87 mmol) of Binapthyl(2,2')-diylhydrogenphosphat (H-pbn) are added. Afterwards 334 mg (911 µmol) Europium(III)chloride(H$_2$O)$_6$ and 25 ml methanol are added and the solution stirred and refluxed over night. The precipitate is filtered and washed four times with methanol and dried over night in vacuo. The complex is used without further purification.

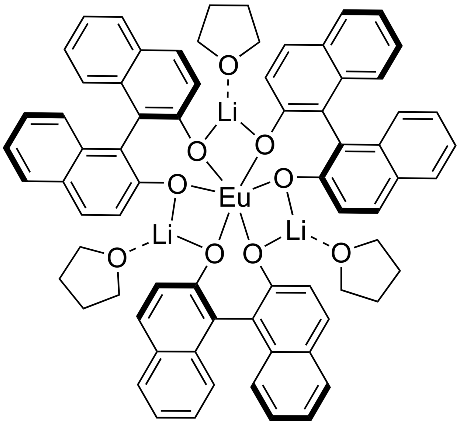

Figure 4.20.: Structure of Eu(BINOL)$_3$Li$_3$.

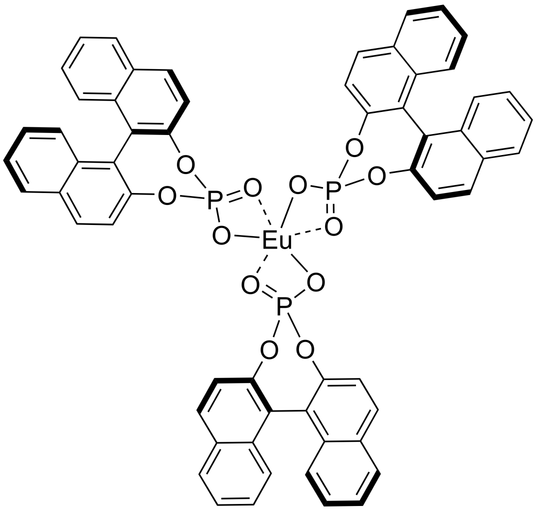

Figure 4.21.: Structure of Eu(pnb)$_3$.

4.8.3. Sample Preparation

4.8.3.1. *meso* Hydrobenzoine with Eu(hfc)$_3$

9.9 mg (46.2 µmol) *meso*-hydrobenzoin (Sigma-Aldrich) is dissolved in 500 µl $CDCl_3$ (Eurisotop). To this solution 1.4 mg of Eu(hfc)$_3$ is added and increased to 10.2 mg of the complex. The sample is prepared in a 5 mm tube with a screw cap.

4.8.3.2. *meso* Hydrobenzoine with Eu(BINOL)$_3$Li$_3$

13.5 mg (63 µmol) *meso*-hydrobenzoin (Sigma-Aldrich) is dissolved in 500 µl $CDCl_3$ (Eurisotop). Depending on the spectra measured it contained 0.7 mg, 1.5 mg, 2.9 mg of the Eu(BINOL)$_3$Li$_3$. The sample is prepared in a 5 mm tube with a screw cap.

4.8.3.3. *meso* Hydrobenzoine with Eu(pnb)$_3$

6 mg (28 µmol) *meso*-hydrobenzoin (Sigma-Aldrich) is dissolved in 500 µl $CDCl_3$ (Eurisotop). To this solution 1.4 mg Eu(pnb)$_3$ is added. The sample is prepared in a 5 mm tube with a screw cap.

4.8.3.4. Hydrobenzoine with Eu(BINOL)$_3$Li$_3$

9.9 mg (46.2 µmol) hydrobenzoin (Sigma-Aldrich) is dissolved in 500 µl $CDCl_3$ (Eurisotop). Depending on the spectra measured it contained 0.9 mg, 1.9 mg, 3.1 mg of Eu(BINOL)$_3$Li$_3$. The sample is prepared in a 5 mm tube with a screw cap.

4.8.3.5. Hydrobenzoine with Eu(hfc)$_3$

9.8 mg (45.7 µmol) hydrobenzoin (Sigma-Aldrich) is dissolved in 500 µl $CDCl_3$ (Eurisotop). Depending on the spectra, it contained 4.8 mg or 8.4 mg of Eu(hfc)$_3$. The sample is prepared in a 5 mm tube with a screw cap.

4.8.3.6. *meso* Hydrobenzoine in (*R*)-TFB

5.2 mg (24.2 µmol) *meso*-hydrobenzoin (Sigma-Aldrich) is dissolved in 220 µl (*R*)-TFB (Eurisotop). For the deuterium lock 5 µl benzene-d$_6$ are added. The sample is prepared in a 3 mm tube and sealed.

4.8.4. Experimental and Processing Parameter

The spectra are recorded on a 400 MHz spectrometer with an AVANCE III HD console from Bruker (Rheinstetten, Germany) equipped with a room temperature BBI probehead. The acquisition software used is Bruker TopSpin 3.6pl5.

The 1D ^{1}H spectra in Figure 4.8 are recorded with 32 768 time domain points and a sweep width of 10 ppm leading to an acquisition time of 2.72 s. 1 scan is recorded and the relaxation delay is 1 s. The spectra are processed to 65 536 points and apodized with an exponential function and a line broadening of 0.3 Hz.

The 1D ^{13}C spectra in Figure 4.9 and 4.11, are recorded with 32 768 time domain points and a sweep width of 251 ppm leading to an acquisition time of 0.649 s. 1024 or 256 scans are recorded with a relaxation delay of 2 s. The total experimental time is 35 min or 9 min, respectively. The spectra are processed to 262 144 points and apodized with an exponential function and a line broadening of 1 Hz.

The CLIP-HSQC spectrum shown in Figure 4.16 and Figure 4.17 are recorded with the same parameters. They are recorded with 8192 time domain points in the direct dimension and 1024 time domain points points in the indirect dimension. The corresponding sweep widths are 9.5 ppm and 65 ppm leading to acquisition times of 0.722 s and 0.078 s. Before acquisition 16 dummy scans are applied for equilibration. The number of scans per increment are 2 with a recovery delay of 0.8 s. $^1J_{CH}$ is set to 145 Hz and the corresponding delay Δ_1 is calculated accordingly. The total experimental time is 29 min. The spectra are zero-filled to 16 384 × 4096 matrix points. The FID is apodized with a squared cosine window function in both directions.

The HSQC-TOCSY spectrum shown in Figure 4.17 is recorded with 2048 time domain points in the direct dimension and 3072 time domain points in the indirect dimension. The corresponding sweep widths are 8 ppm and 120 ppm leading to acquisition times of 0.32 s and 0.127 s. Before acquisition 16 dummy scans are applied for equilibration. The number of scans per increment are 8 with a recovery delay of 1.2 s. $^1J_{CH}$ is set to 145 Hz and the corresponding delay Δ_1 is calculated accordingly. The TOCSY-mixing time is 80 ms. The total experimental time is 10 h. The spectra are zero-filled to 16 384 × 4096 matrix points. The FID is apodized with a squared cosine window function in both directions.

4.8.5. Sample Preparation and Experimental and Processing Parameter for the Measurements at Low Magnetic Field

Measurements are performed at a Magritek Spinsolve 60 spectrometer with a proton frequency of 62 MHz.

4.8.5.1. Sample Preparation

9.5 mg (44.3 µmol) *meso*-hydrobenzoin (Sigma-Aldrich) is dissolved in 500 µl $CDCl_3$ (Eurisotop). Depending on the spectra measured it contained no 0.8 mg, 2.0 mg, 3.9 mg or 5.0 mg of $Eu(BINOL)_3Li_3$. The sample is prepared in a 5 mm tube with a teflon cap.

10.2 mg (47.6 µmol) *meso*-hydrobenzoin (Sigma-Aldrich) is dissolved in 500 µl $CDCl_3$ (Eurisotop). Depending on the spectra, it contained 5.1 mg or 10.1 mg of $Eu(hfc)_3$. The sample is prepared in a 5 mm tube with a screw cap.

4.8.5.2. Experimental and Processing Parameter

The spectra shown in Figure 4.19 are recorded with 16 384 time domain points and a sweep width of 20 ppm leading to an acquisition time of 3.2 s. 1 or 4 scans are recorded and a repetition time of 4 s is used. The total experimental time is 1 min. The spectra are processed to 16 384 points and not apodized.

5. Pulse Sequence Development for the Measurement of Biphasic Samples

Parts of this chapter have been already published in [122].

5.1. Introduction

In this chapter, five different biphasic samples are analysed and characterized with slice selective measurement or by the introduction of an additional z-resolved dimension. Both spatially selective measurement techniques can generally be combined with almost any type of NMR pulse sequence. Here, they are used in combination with a 1D ^{13}C and a CLIP-HSQC pulse sequence.

First, the phase encoding principle will be described. Second, the slice selective excitation will be explained. Third, the resulting pulse sequences, which are developed, will be presented and applied to a biphasic water/chloroform sample as a test sample and four isotropic and anisotropic liquid crystalline biphasic samples.

5.2. Principles of Phase-Encoding

By phase-encoding is a well known method in MRI: PFGs are applied during a constant time period with the desired magnetization in the transverse plane. By increasing the gradient strength in consecutive NMR experiments, an spatially dependent phase adds up to the Larmor frequency of the nuclei. The resulting space-dependent frequency can be Fourier transformed and thereby lead to the z-resolved dimension.

This space-dependent frequency depends on the z-position along B_0 and on the gyromagnetic ratio of the spin under investigation (γ_n) in the following way:

$$\omega_{\text{eff}}(z) = \omega_0 + \gamma_n \cdot G \cdot z. \tag{5.1}$$

ω_{eff} is the effective frequency for the spins, ω_0 is the Larmor frequency of the nuclei, γ_n is the gyrogmagnetic ratio of the spins under investigation, G is the gradient strength and z the position of the spin along B_0. The principle for phase encoding is visualized in Figure 5.1 for different gradient strengths.

5.2.1. Pulse Sequence for Deuterium Phase-Encoded Spectra

In Figure 5.2A, the pulse sequence for phase-encoded deuterium spectra is shown. The PFG to achieve the phase-encoded dimension is highlighted by the grey box. The experi-

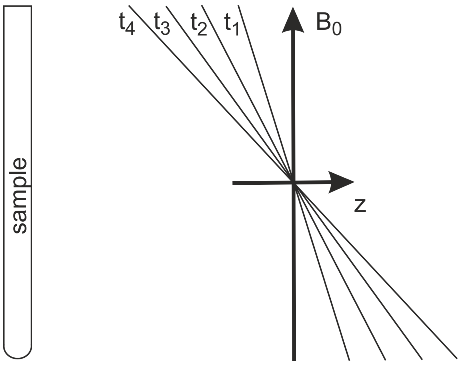

Figure 5.1.: Visualization of the principle for phase-encoded spectra. The narrow black lines indicate the gradient strength, which is increased from increment to increment (t_1 to t_4) for the phase-encoded dimension.

ment shows the deuterium chemical shift along the direct dimension and in the indirect dimension the z-dependent distribution thereof.

For a certain resolution, the duration of the gradient length has to be chosen correctly. The gradient length δ depends on the number of increments measured in the indirect dimension n_1, the gradient strength G, the gyromagnetic ratio of the nucleus under investigation (γ_n) and r_z, describes the field of view which corresponds to the z axes and is typically chosen as 3 cm.

$$\delta = \frac{n_1 \cdot \pi}{G \cdot \gamma_n \cdot r_z} \tag{5.2}$$

The resolution along z depends on the number of increments measured in this dimension. Usually, the gradient G is increased to the maximum gradient strength. In case of too short gradient length δ because of few increments in the indirect dimension, the maximum value for the gradient strength G can be decreased.

In aligned samples, the deuterium signal is split by the quadrupolar splitting $\Delta\nu_Q$. By showing the distribution of $\Delta\nu_Q$, the homogeneity and quality of an aligned sample can be determined, e. g., polymer gels which introduce an alignment can suffer from breaks which can be discovered in the phase-encoded spectra.[24] Additionally, if the sample is constituted of two different phases, the different deuterium chemical shifts or the distribution of the quadrupolar splitting $\Delta\nu_Q$ over the sample help to judge the sample constitution. In Figure 5.3, the one-dimensional and the phase-encoded deuterium spectra of the biphasic test sample of water and chloroform are shown. In the one-dimensional deuterium spectrum, two signals are present, one for each solvent. However, no conclusion for the z-distribution of the solvents can be drawn. In the z-resolved spectrum, it can be clearly seen that as expected the two solvents do form two phases. Furthermore, the shim can be evaluated by the experiment. As most of the aligned samples have to be shimmed manually, the phase-encoded deuterium spectrum helps to determine how the shim throughout a sample looks like. As well as before, this can be judged by the distribution of ω_0 of the solvents in the z-dimension of the sample. More details can be found in the corresponding publication.[24]

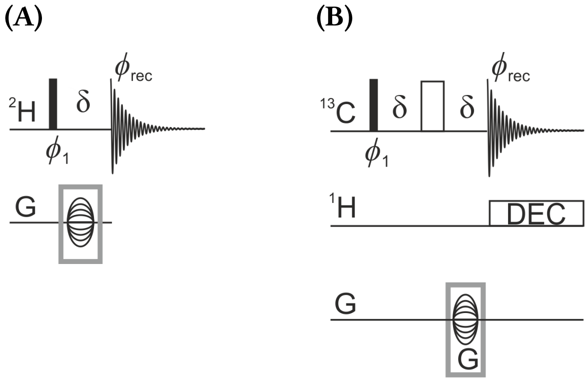

Figure 5.2.: (A) Pulse sequence for the phase-encoded deuterium spectrum.[24] (B) Pulse sequence for the phase-encoded carbon spectrum. The PFG which is performing the phase-encoding is highlighted with the grey box. The PFG delay is fixed and the gradient strength incremented in the sequence. The gradient length is calculated according to the equation shown in 5.2.The resulting spectra can be Fourier transformed in both dimensions. The indirect dimension resolves the z-distribution of the Larmor frequency of the spins. Black narrow bars correspond to 90° pulses, unfilled bars are 180° pulses. The phase of the pulse (ϕ_1) and the receiver phase (ϕ_{rec}) is shifted from x, −x, y, −y. The indirect dimension is recorded in the qf-mode. In the carbon phase-encoded spectrum, the protons are decoupled during t_{acq} proton.

The phase-encoded carbon experiment starts with a 90° pulse for excitation, the following delay is adjusted to the calculated gradient length of the phase encoding gradient. In between two delays a 180° pulse is applied to achieve refocusing of chemical shift evolution of the carbons and to refocus proton-carbon coupling which evolves during the delays. The resulting spectra show the carbon chemical shift in the direct dimension. The indirect dimension is the z-resolved dimension. In the case of a biphasic sample, the carbon spectrum should change from one phase to the other. The sequence is shown in Figure 5.2B.

To all spectra recorded with the phase-encoding principle, a first order phase correction of $n_1 \cdot 180^\circ$ has to be applied, since the recorded FID starts with the lowest intensity increases to the maximum intensity and decreases. This order has to be shifted to result in interpretable spectra.

5.3. Slice Selective Excitation

A second method to measure NMR spectra spatially selective is achieved by slice selective excitation. In this case, the spatial selection is achieved by a selective 90° or 180° pulse which is applied during a PFG. Together with the bandwidth of the shaped pulse and the gradient strength, the slice width can be changed, according to:

$$\Delta z = \frac{\Delta \nu}{G \cdot \gamma_n} \tag{5.3}$$

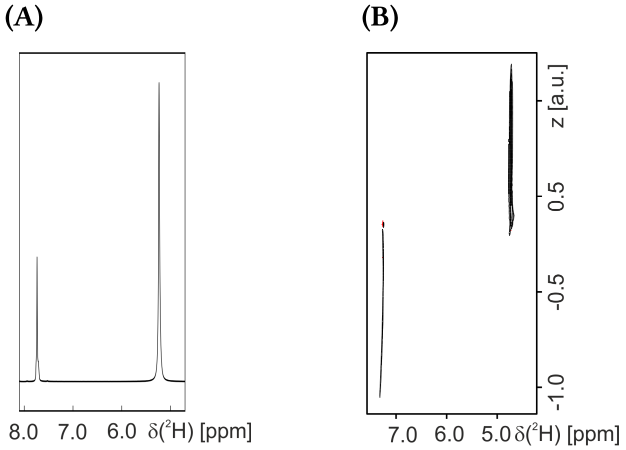

Figure 5.3.: Deuterium 1D spectrum (A) and phase-encoded deuterium spectrum of a biphasic sample (B). (B) is recorded with the sequence shown in 5.2A. The sample is made out of 100 mmol l^{-1} solution of sucrose in D_2O and 100 mmol l^{-1} in $CDCl_3$. One can see that the phases are well separated from each other. The signal at 4.76 ppm is resulting from D_2O and 7.26 ppm from $CDCl_3$.

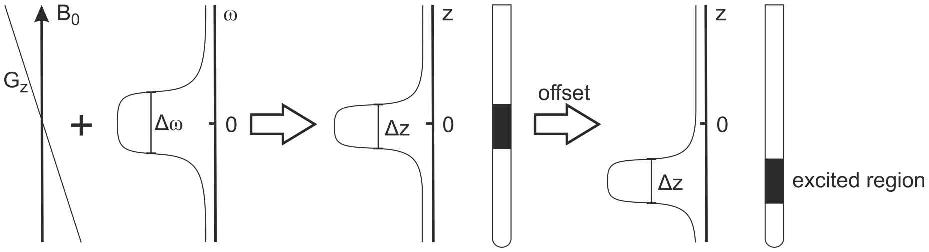

Figure 5.4.: Principle for slice selective excitation. At left the gradient which adds the z-dependent Larmor frequency on the nuclei is shown. Together with the shaped pulse, the thickness of the slice is determined. The offset of the pulse determines, which region of the sample is excited.

As the equation shows, the excited slice depends on the bandwidth of the shaped pulse $\Delta\nu$, on the gradient strength G and on the gyromagnetic ratio of the excited nucleus γ_n. The carrier frequency of the shaped pulse determines the z-position of the excited slice. By changing the carrier frequency of the shaped pulse, the excited slice is shifted. All this is shown schematically in Figure 5.4. The offset of the pulse determines the middle of the z-position as follows:

$$z = \frac{\nu_{\text{offset}}}{G \cdot \gamma_n}. \tag{5.4}$$

Here, ν_{offset} is the offset of the selective 180° pulse, G the gradient strength and γ_n the gyromagnetic ratio of the excited nucleus n.

Since the chemical shift of the excited nucleus and the coupling to coupled nuclei evolve during the pulse, the excitation sculpting sequence is favorable over a shaped 90° pulse during a gradient. Additionally, the excitation sculpting sequence can achieve a constant phase and constant amplitude excitation over an easily adjustable bandwidth. Additionally,

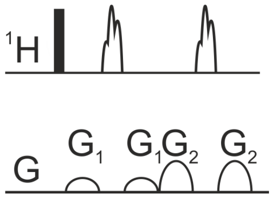

Figure 5.5.: Pulse sequence of the original excitation sculpting sequence.[123] It is used to selectively excited specific bandwidths of a spectrum, e. g, selective NOE spectra. Black narrow bar is a 90° pulses, unfilled irregularly shaped boxes are selective Gaussian Q3 180° pulses. Gradient strengths for G_1 and G_2 are 11 % and 31 %, respectively.

the method has no out-of-band side-lobes, it refocuses the evolution of the scalar coupling and is tolerant to radio-frequency (rf) field inhomogeneity of the generated pulse. The core of the method is a double pulsed field gradient spin echo (DFPGSE) (see Figure 5.5).[123–125]

The slice selective excitation is dependent on the equation shown in 5.3. Therefore, a general slice selective excitation scheme is a band-selective shaped pulse which is applied during a gradient. One can decide, if a selective 90° pulse during a gradient (see Figure 5.6A) or a selective 180° pulse during a gradient is used (see Figure 5.6B). The use of an unselective 90° pulse followed by the selective 180° can be favorable for chemical shift evolution and coupling evolution. Both are refocused in the excitation sculpting scheme. The slice selective excitation methods are shown in Figure 5.6B.

For the slice selective carbon spectra, a shaped 90° pulse is used during a gradient. The shaped pulse is a selective Gaussian cascade 90° pulse (Q5), see Figure 5.6C. By changing the bandwidth of the shaped pulse and the gradient strength, the selective slice can be changed. It results in a one-dimensional spectrum which results from this excited slice. During the acquisition time, proton decoupling has to be applied.

To be able to judge the slice which is excited by the excitation sculpting scheme, the two schemes for z-dependent measurement are merged. So in this case, first a slice selective excitation scheme via the excitation sculpting is applied. Second, a gradient to phase encode the spectrum is added (see Figure 5.7 for the sequence). This leads to a spectrum where the excited slice width and the position of the slice along the z dimension is shown. With this experiment, the optimal gradient strength and bandwidth of the shaped pulse can be determined and the determined parameters can be transferred to other slice selectively excited sequences. As this experiment is a deuterium spectrum, the gradient strength has to be adjusted depending on the nucleus used in the following experiments.

5.4. Spatially resolved CLIP-HSQC

5.4.1. Slice Selective Excited HSQC

The slice selectively excited CLIP-HSQC starts with an excitation sculpting sequence which is slice selective due to the gradient during the shaped 180° pulses. The excitation sculpting scheme is applied to achieve a constant phase and a constant amplitude excitation over

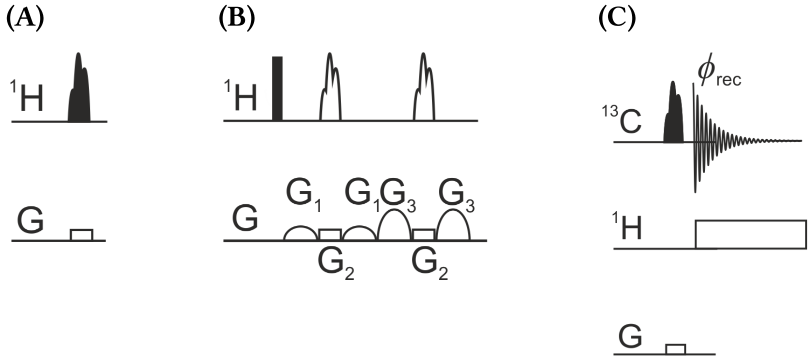

Figure 5.6.: Pulse sequences for slice selective excitation; (A) is the scheme for slice selective excitation by a 90° pulse during a gradient for protons. (B) is the slice selective excitation sculpting scheme for protons. (C) is the scheme for slice selective excitation by a 90° pulse during a gradient for carbons. Bandwidths of the shaped pulses and the applied gradient strength G_2 during the pulse define the excited z-range of the sample. The dependence is shown in Equation 5.3. The offset of the shaped pules determines the position of the excited slice. Filled symbols are 90° pulses, unfilled irregularly shaped boxes are 180° pulses. Gradient strengths in sequence (B) for G_1 and G_3 are 11 % : 31 % . G_2 is adjusted according to 5.3. (C) Slice selectively excited carbon 1D spectrum. The shaped pulse during the gradient is a selective Gaussian 90° pulse (Q5) or a selective Gaussian 180° pulse (Q3). $\phi_1 = \phi_{\text{rec}}$ = (x, −x, −x, x, y, −y, −y, y).

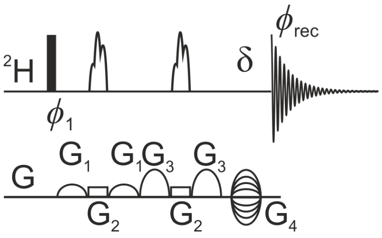

Figure 5.7.: Slice selectively excited phase-encoded deuterium spectrum. The black narrow bar stands for a 90° pulses, whereas unfilled irregularly shaped boxes represent 180° pulses. The gradient strengths for G_1 and G_3 are 11 % and 31 %, respectively. The gradient strength of gradient G_4 is increased from increment to increment. G_2 has to be adjusted according to the desired slice width. The selective 180° pulse is a Gaussian Q3 pulse. The phase of the 90° pulse and the receiver phase are changed by ϕ = x, −x, y, −y. The indirect dimension is recorded in the absolute value mode.

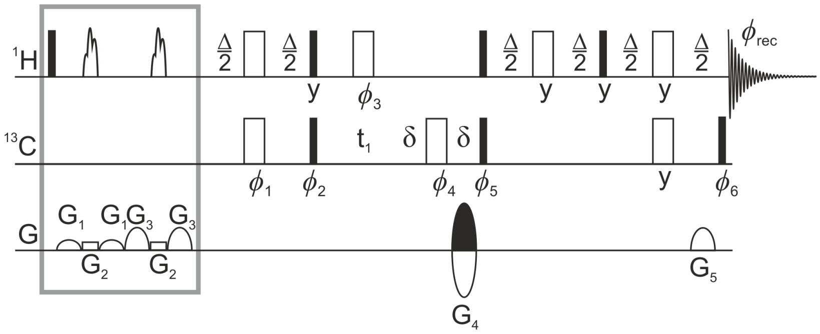

Figure 5.8.: Pulse sequence for the slice selective excited HSQC. The sequence starts with an excitation sculpting scheme which is modified to slice selectively excite a region of the sample (highlighted by the grey box). Then, the magnetization is transferred via an INEPT transfer step to carbon polarization. During t_1 carbon chemical shift evolves. For the backtransfer a perfect echo transfer step is used to achieve cleaner spectra. Δ is matched to $\frac{1}{2\,(^1J_{\mathrm{CH}})}$; black filled narrow boxes represent 90° pulses, broad unfilled boxes represent 180° pulses; Pulse phases are $\phi_1 = \mathrm{x}$, $\phi_2 = \phi_6 = \mathrm{x}, -\mathrm{x}$, $\phi_4 = \phi_5 = 4(\mathrm{x}), 4(-\mathrm{x})$, $\phi_{\mathrm{rec}} = \mathrm{x}, -\mathrm{x}, \mathrm{x}, -\mathrm{x}, -\mathrm{x}, \mathrm{x}, -\mathrm{x}, \mathrm{x}$. Gradient strengths are $\mathrm{G}_1 = 11\,\%$, $\mathrm{G}_2 = 11.36\,\%$, $\mathrm{G}_3 = 31\,\%$, $\mathrm{G}_4 = 80\,\%$, $\mathrm{G}_5 = 20.1\,\%$. Phase-sensitive acquisition in the indirect dimension is achieved using an echo-antiecho encoding on the gradient G_4. TPPI-progression is used on ϕ_1, ϕ_2 and ϕ_{rec} to shift artifacts from the center to the edges of the spectrum. To slice selective excite, a Gaussian cascade (Q3) 180° pulse is used during the excitation sculpting scheme. For better performance all 180° pulses on carbon are replaced by BIBOP- and BURBOP-pulses [94].

an easily adjustable bandwidth. The rest of the sequence is equal a normal CLIP-HSQC spectrum, beside the back transfer step. The back transfer is designed with a perfect echo back transfer which refocuses the evolution of homonuclear ^{1}H-^{1}H coupling which would lead to anti-phase contribution in the multiplet and impeding or leading to big errors for the extraction of the $^1J_{\mathrm{CH}}$ and $^1D_{\mathrm{CH}}$ coupling constants.[126, 127] After Fourier transform, a CLIP-HSQC spectrum is obtained which results from the region of the sample that is chosen by adjusting the gradient strength and the bandwidth of the selective 180° pulse. It is interpretable like an usual CLIP-HSQC spectrum. Since, the measurement does not take place over the whole sample volume, the signal-to-noise ratio is decreased according to the reduced, excited volume.

5.4.2. Phase-encoded CLIP-HSQC

The phase-encoded CLIP-HSQC spectrum is a CLIP-HSQC sequence which has a phase encoding gradient during the last delay of the backtransfer of the sequence. The sequence is shown in Figure 5.6C. The direct dimension is the proton dimension. The first indirect dimension is the carbon dimension. The second indirect dimension is the phase-encoded z-resolved dimension. To achieve this, a phase encoding gradient is added during the last delay of the backtransfer. This indirect dimension is recorded in absolute mode and achieved by increasing the gradient from increment to increment. The carbon dimension

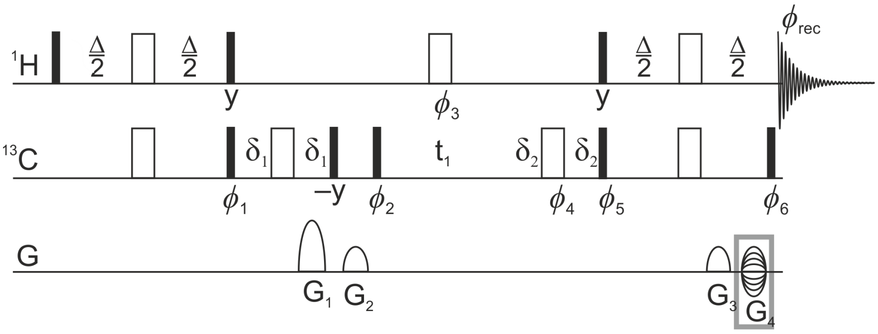

Figure 5.9.: Pulse sequence for a phase-encoded CLIP-HSQC. Δ is matched to $\frac{1}{2\,(^1J_{CH})}$; filled black boxes represent 90° pulses, light boxes represent 180° pulses; δ_1 and δ_2 are matched to the gradient length; phase cyclings are ϕ_1 = 4(y), 4(−y), ϕ_2 = x, ϕ_3 = 2(x), 2(−x), $\phi_4 = \phi_5 = \phi_6$ = x, −x, ϕ_{rec} = x, −x, x, −x, −x, x, −x, x. If 16 or more scans are recorded ϕ_4 may be cycled independently with ϕ_4 = 8(x), 8(−x). Gradient strengths are G$_1$ = 80 %, G$_2$ = 30 %, G$_3$ = 20.1 %. G$_4$ is incremented to achieve spatial encoding in the second indirect dimension. The duration of the gradient G$_4$ is calculated according to the equation shown in 5.2. Phase sensitive detection for the indirect carbon dimension is achieved by incrementing the phase of ϕ_1 by 90° in States-TPPI fashion. The phase-encoded dimension is recorded in QF-mode.

is recorded in States-TPPI fashion. To allow an interpretation similar to the one of the CLIP-HSQC spectrum, the planes of one phase have to be summed up.

5.5. Application of the Pulse Sequences to the Biphasic Samples

Four biphasic liquid crystalline samples are measured. Two of the samples are made out of mixed polymer phases. In each of the samples two polymers are dissolved in chloroform, in the first *poly*-**1** and *poly*-**2** and in the other *poly*-**1** and *poly*-**3**, respectively. The next two samples are biphasic liquid crystalline phase samples of *poly*-**4**. In addition, a test sample is made of two immiscible solvents, D_2O and $CDCl_3$.

5.5.1. Biphasic Liquid Crystalline Phase Sample of *poly*-1 and *poly*-2

Biphasic liquid crystalline phase sample is made out of *poly*-**1** and *poly*-**2** dissolved in $CDCl_3$. For the structure of the two polymers, see Figure 5.17A and 5.17B. The phase-encoded deuterium spectrum shows two clearly visible phases, see Figure 5.10A. In this spectrum two separate phases are clearly visible. The upper phase is isotropic and has no apparent deuterium splitting. The lower phase is anisotropic and has a $\Delta\nu_Q$ of (829.3 ± 1.1) Hz. As the constitution of the two phases is unclear, the slice selective carbon spectrum is recorded (see Figure 5.10B). The slice selective carbon spectrum shows that the two polymers *poly*-**1** and *poly*-**2** do not blend. One slice selective carbon spectrum differs from the other and corresponds to either *poly*-**1** or *poly*-**2**. This can be best seen for the signal

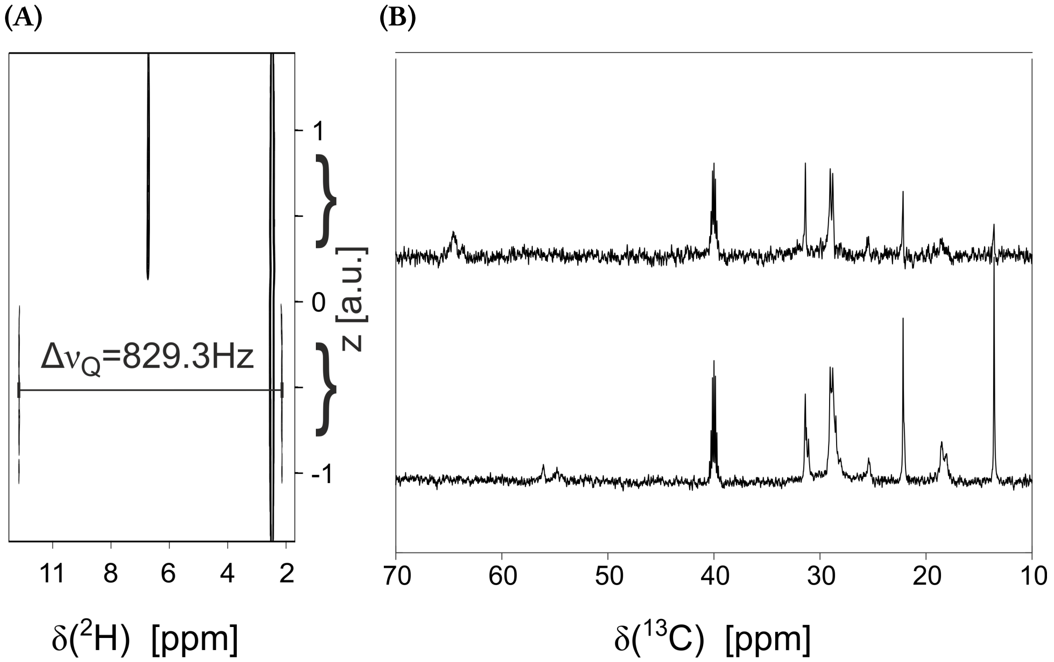

Figure 5.10.: Phase-encoded deuterium spectrum and slice selective carbon spectra for the *poly*-**1** - *poly*-**2** sample. (A) is the phase-encoded deuterium spectrum for the sample, it shows the two phases. The upper phase is nearly isotropic. It shows no visible deuterium splitting. The lower phase has a $\Delta\nu_Q$ of (829.3 ± 1.1) Hz. The spectrum is recorded with the sequence shown in 5.2A. The experimental parameter are described in 5.7.1.1. (B) is a slice selective carbon spectrum recorded for each slice. The carbon spectra show clearly the different carbon spectra for each polymer. The spectra are recorded with the sequence in Figure 5.6C with two different offsets for the shaped pulses, selecting for each spectrum one phase. The upper ^{13}C spectrum is resulting from the upper phases. Whereas, the lower spectrum shows the ^{13}C spectrum of the lower phase. The experimental parameters are shown in Subsection 5.7.1.1

at 65 ppm which appears in the upper phase and does not occur in the lower phase. The signal at 55 ppm in the lower phase does not appear in the upper phase. By comparison of the slice selectively recorded 1D ^{13}C spectra to the 1D ^{13}C spectra of the monomers, the upper phase is assigned to *poly*-**1** and the lower phase is assigned to *poly*-**2**. Therefore, the polymer *poly*-**2** dissolved in chloroform leads to the formation of a liquid crystalline phase which is completely separated from the phase of *poly*-**1** dissolved in chloroform. For the determination of the right gradient strength and the bandwidth of the pulse, the slice selectively excited and phase-encoded deuterium spectrum could be used. Subsequently, the determined parameters have to be transferred to the selective 1D ^{13}C spectrum and the gradient strength has to be adjusted for the gyromagnetic ratio of carbons. Thereby, the same slice is excited as in the slice selectively excited and phase-encoded deuterium spectrum.

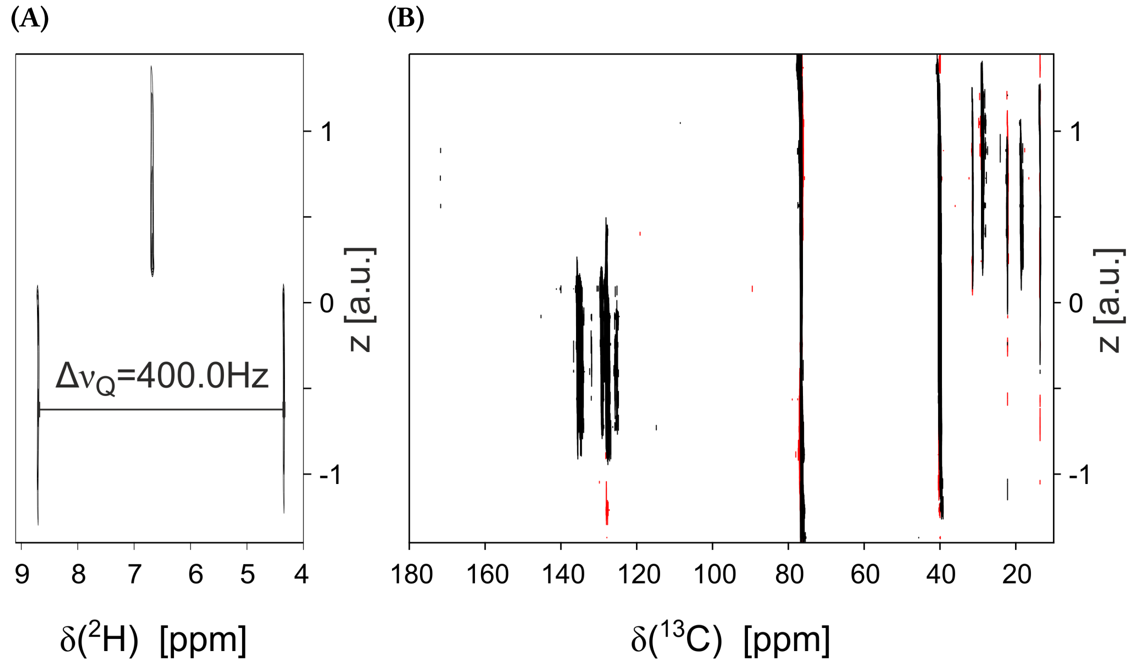

Figure 5.11.: Phase-encoded deuterium spectrum and phase-encoded carbon spectrum for a mixture of *poly*-**1**-*poly*-**3** in chloroform. In the phase-encoded deuterium spectrum (A), two phases are clearly separated from each other. The upper phase is nearly isotropic (this corresponds to $\Delta\nu_Q = 0$). The lower phase a $\Delta\nu_Q$ of (400.0 ± 1.0) Hz. (B) shows the phase-encoded carbon spectrum. It is clearly visible that the two polymers do not blend and each is responsible for one phase. *poly*-**1** is in the upper phase and *poly*-**3** is in the lower phase. The experimental parameters to both spectra are shown in Section 5.7.1.2

5.5.2. Biphasic Liquid Crystalline Phase Sample of *poly*-1 and *poly*-3

To evaluate the phase-encoded ^{13}C pulse sequence, a second sample of a mixed polymer sample is measured. It is prepared by dissolving *poly*-**1** and *poly*-**3** in chloroform. For the structure of the polymers, see Figure 5.17A and 5.17C. The phase-encoded deuterium spectrum shows two phases (see Figure 5.11A). The upper phase is nearly isotropic ($\Delta\nu_Q \approx 0$). The lower phase has a $\Delta\nu_Q$ of (400.0 ± 1.0) Hz. The constitution of each phase is unknown. Therefore, the phase-encoded ^{13}C spectrum is applied to the sample. It is shown in Figure 5.11B. The two phases are clearly distinguishable from each other. The aliphatic region in the upper part of the spectrum shows increased signal intensity. This points to *poly*-**1**. The lower phase shows increased signal intensity in the aromatic region of the spectrum referring to the spectrum of *poly*-**3**. Therefore, each polymer is responsible for one phase of the spectrum.

Since the polymers constitute one phase each and do not blend, the biphasic samples could be used for the determination of RDCs. The phase with no quadrupolar splitting could lead to the $^1J_{\mathrm{CH}}$ couplings for an added analyte. Whereas in the anisotropic phase, $^1T_{\mathrm{CH}}$ splittings could be determined for the molecule. Additionally, different alignment strengths could be measured by changing the concentrations of the polymers.

5.5.3. Biphasic Liquid Crystalline Phase Sample of *poly*-4

The polymer *poly*-**4** forms a LLC, the structure of *poly*-**4** is shown in Figure 5.18.[128] The LLC *poly*-**4** has a critical concentration of 13 %(w/w) at room temperature. In the phase-encoded deuterium spectrum, the biphasic liquid crystalline phase shows a high deuterium quadrupolar $\Delta\nu_{\mathrm{Q}}$ splitting in the upper phase of 345.5 Hz and for the lower phase of $\Delta_{\nu_Q} = 2.2$ Hz. As these properties show a strong alignment for the upper phase and the lower phase shows nearly no alignment, the sample is used for measurement of both isotropic and anisotropic data. The conventional CLIP-HSQC could not be used, as signals from both phases overlap and make the coupling extraction impossible.

As explained before (see Section 2.4), two samples have to be prepared for the determination of RDCs. The first sample is an isotropic sample with the analyte dissolved in a solvent. In the second sample, the analyte is oriented in an appropriate alignment medium. After preparation, both samples have to be measured and splittings for both samples have to be extracted. Since the phase-encoded deuterium spectrum showed the two differently aligned phases, the slice selective excited CLIP-HSQC is used to measure spectra of each phase. The isotropic spectrum results from the lower phase, whereas the anisotropic phase results from the upper phase. Afterwards, the isotropic and anisotropic data is used to determine RDCs for both IPC enantiomers. IPC is a rigid molecule, therefore a SVD-fit for the RDCs could be performed to assign the diastereotopic methylene groups and the configuration. Additionally, the ability for the discrimination of enantiomers is tested by comparing the experimental RDCs for both enantiomers of IPC, (−)-IsoPinoCampheol ((−)-IPC) and (+)-IsoPinoCampheol ((+)-IPC).

In Figure 5.12B, the phase-encoded deuterium spectrum is shown. The two different $\Delta\nu_{\mathrm{Q}}$ for both phases are clearly visible. To determine the slice width for the slice selective CLIP-HSQC, the slice selectively excited and phase-encoded deuterium spectrum is used. The resulting spectra are shown in Figure 5.12C. The dark blue and the light blue spectrum are two different spectra and are measured with different offsets for the shaped pulses. It is visible that either the oriented phase or the isotropic phase is excited. The thickness of the excited slice can be calculated by the formula shown in Equation 5.3 and is 0.2 cm for the slice selective excited and phase-encoded deuterium spectrum.

The slice selectively excited CLIP-HSQC spectra for (−)-IPC are shown in Figure 5.13. They are recorded with the sequence shown in Figure 5.8. As can be seen by the two signals which are zoomed in, the couplings differ largely for both spectra. The complete extracted couplings from both spectra are summarized in Table 5.1. ${}^{1}J_{\mathrm{CH}}$ couplings are extracted from the spectrum shown in Figure 5.13A, whereas the ${}^{1}T_{\mathrm{CH}}$ couplings are extracted from the spectrum shown in Figure 5.13B. The ${}^{1}D_{\mathrm{CH}}$ are obtained by Equation 5.5.

$${}^{1}D_{\mathrm{CH}} = {}^{1}T_{\mathrm{CH}} - {}^{1}J_{\mathrm{CH}} \tag{5.5}$$

The CLIP-HSQC spectra in a biphasic sample with *poly*-**4** are recorded as well for (+)-IPC, which are not shown. The experimental values are shown in Table 5.2.

5.5.3.1. Evaluation of the determined RDC of (−)-IPC and (+)-IPC

For the calculated ${}^{1}D_{\mathrm{CH}}$ an SVD-fit is performed. The experimental and calculated values for each proton-carbon-pair are in good agreement to each other, which can be seen in Figure 5.14A. The better the calculated ${}^{1}D_{\mathrm{CH}}$ fit to the experimental ${}^{1}D_{\mathrm{CH}}$, the closer they are to the grey line and therefore correlate. The Cornilescu quality factor for these values and the right structural assignment is $Q = 0.058$. How this quality factor is calculated is explained in Section 2.4.3.1. The assignment of the methylene protons for C4 is clearly possible. Due to a large error of 9 Hz for C7-Ha, the values for the ${}^{1}D_{\mathrm{CH}}$ for C7 do not allow the corresponding assignment. This can be seen in Figure 5.14B where the quality factors for the exchanged RDCs at the methylene groups as well as the different configurations of IPC are shown.

The ability to differentiate enantiomers of the liquid crystal *poly*-**4** is tested by preparing a biphasic liquid crystal for (+)-IPC. Here, both spectra for each phase is recorded and extracted. The extracted values are shown in Table 5.2. To evaluate the ability to enantiodiscriminate for *poly*-**4**, the experimental RDCs of (−)-IPC and (+)-IPC are plotted against each other for each corresponding carbon-proton-pair (see Figure 5.15). The enantiodiscrimination is better if the RDCs differ from each other for each pair. This can be evaluated by the Pearson correlation coefficient. It is a measure of the linear correlation between two variables. If the Pearson correlation coefficient is −1, the values do correlate antiproportional. If the Pearson correlation coefficient is 0, they do not correlate at all. If the Pearson correlation coefficient is 1, the correlate with linearly with each other. Here, the value is 0.6524, this means that the correlation is low between the experimental RDCs for the (−)-IPC compared to the experimental RDCs of (+)-IPC. Consequently, the correlation of the RDCs can be neglected and the enantiodiscrimination of (−)-IPC from (+)-IPC is possible with *poly*-**4**.

5.5.4. Biphasic Sample of two Immiscible Solvents

For the measurement of the phase-encoded CLIP-HSQC, a biphasic sample with two completely different phases is used. The resulting spectrum is easier to evaluate, if the sample is well known. Therefore, a sample with a concentration of 100 mmol l^{-1} sucrose in D_2O and a second phase made out of 100 mmol l^{-1} (−)-menthol in $CDCl_3$ is measured. The phase-encoded deuterium spectrum in Figure 5.3 shows the two well separated phases. The upper phase is the aqueous phase and the lower phase is the chloroform phase. This can be seen by the deuterium chemical shifts of each solvent. For D_2O this is 4.7 ppm and for $CDCl_3$ 7.26 ppm. The spectrum, (Figure 5.16A) recorded with the sequence shown in Figure 5.9, is a three-dimensional spectrum. One indirect dimension is the phase-encoded dimension, which shows the spatial distribution of the analytes over the sample. Here, the difference between the sucrose and (−)-menthol can clearly be seen by the chemical shifts of the signals, as the proton chemical shifts for sucrose are in the range of 3 ppm to 5 ppm and for (−)-menthol in the range of 0.5 ppm to 2.5 ppm. The second indirect dimension is the carbon dimension. To extract the couplings, the planes of the spectrum corresponding to one phase can be added up and interpreted. This is shown in Figure 5.16B.

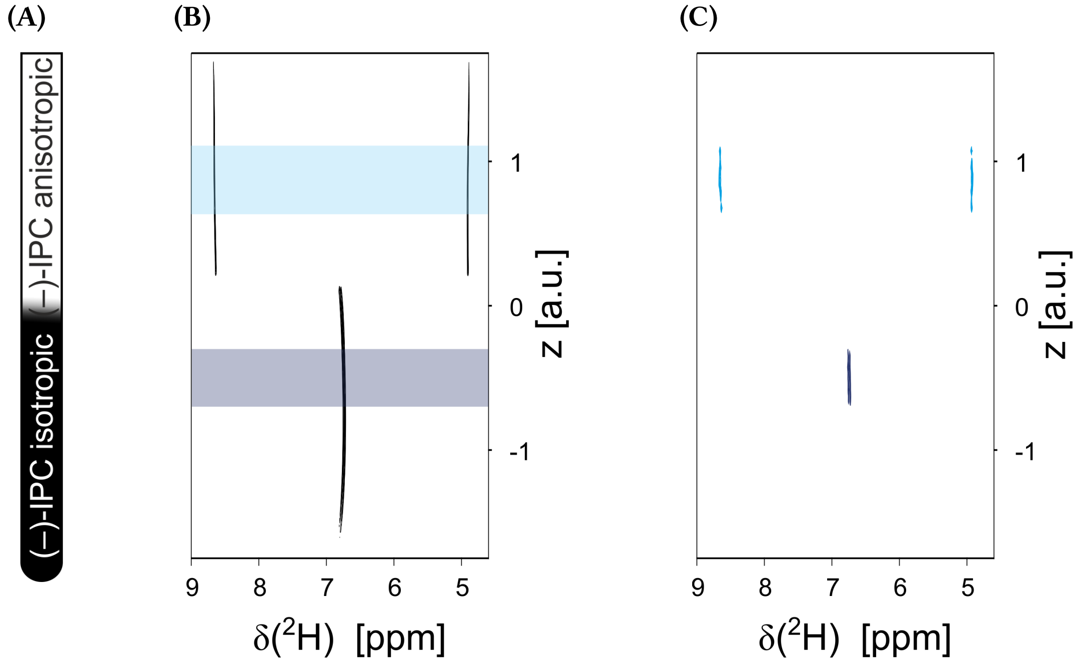

Figure 5.12.: (A) Scheme of the biphasic sample with the corresponding deuterium phase-encoded spectrum. (B) In this spectrum, the clear appearance of a deuterium quadrupolar splitting of Δ_{ν_Q} = 345.5 Hz is showing the alignment in the upper phase. The other phase is nearly isotropic with Δ_{ν_Q} = 2.2 Hz. (C) Slice selective and phase-encoded deuterium spectrum for the biphasic sample. Two spectra are shown in the same figure, which are recorded with different offsets of the shaped pulse. The upper spectrum is the light blue spectrum and resulting from the anisotropic phase. The lower spectrum is the dark blue spectrum and resulting from the isotropic phase. The spectra are recorded with the sequence shown in 5.7. The experimental and processing parameters for all shown spectra are summarized in Section 5.7.2.3.

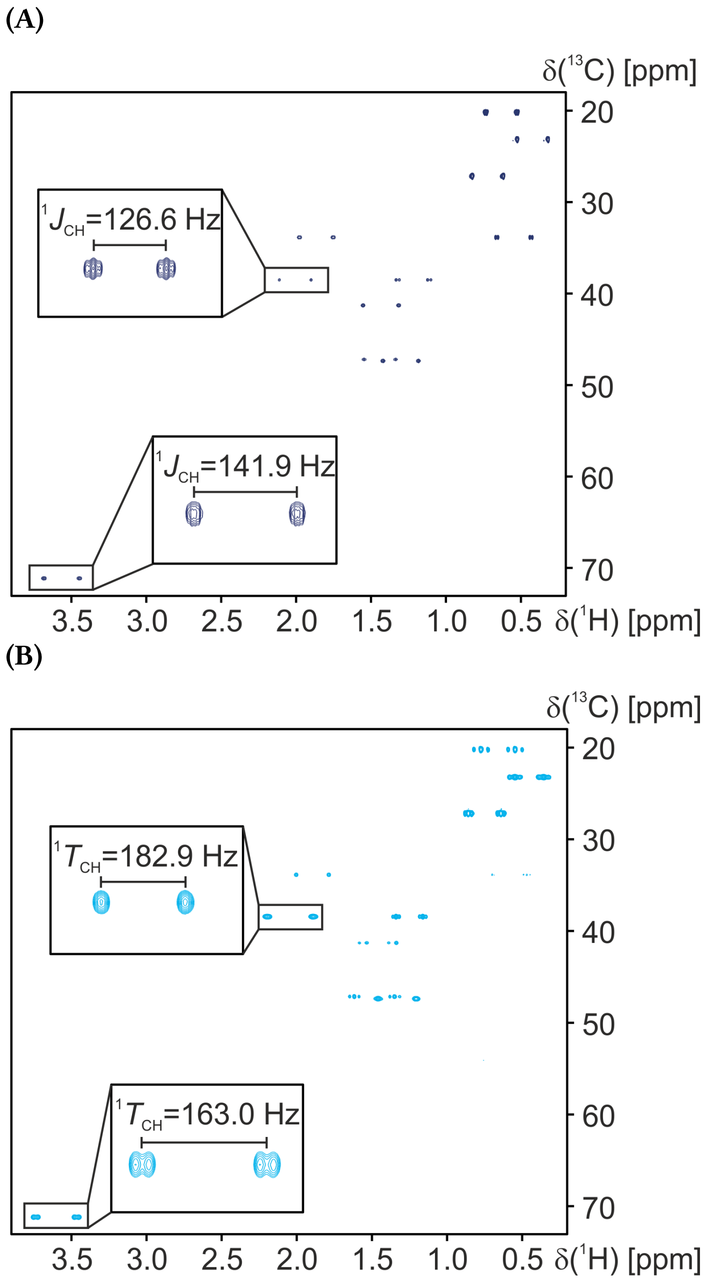

Figure 5.13.: Slice selectively excited CLIP-HSQC spectra of the isotropic and anistropic phase. (A) is the isotropic spectrum, which is recorded in the lower phase of the sample (dark blue). (B) is the anisotropic spectrum, which is recorded in the upper phase of the sample (light blue). Both spectra have a good signal-to-noise ratio, are clearly differentiable from each other . Thus, coupling extraction is straight forward. The spectra are recorded with the sequence shown in Figure 5.8 and measured and processed as explained in Section 5.7.2

Table 5.1.: Assignment and extracted values ($^1J_{\mathrm{CH}}$, $^1T_{\mathrm{CH}}$, $^1D_{\mathrm{CH,exp}}$ and $^1D_{\mathrm{CH,calc}}$ with corresponding errors) for (−)-IPC from the spectra shown in Figure 5.13. The errors indicate the ±3 standard deviation (±3σ) uncertainty.

Assignment	δ (^{13}C) [ppm]	δ (^{1}H) [ppm]	$^1J_{\mathrm{CH}}$ [Hz]	$^1T_{\mathrm{CH}}$ [Hz]	$^1D_{\mathrm{CH,exp}}$ [Hz]	$^1D_{\mathrm{CH,calc}}$ [Hz]
C3	71.18	3.61	141.7 ± 0.8	163.3 ± 0.5	21.6 ± 0.8	22.28 ± 0.76
C1	47.42	1.33	142.3 ± 1.6	152.1 ± 1.8	9.8 ± 1.8	10.52 ± 0.71
C2	47.08	1.49	126.4 ± 0.6	160.6 ± 2.2	34.2 ± 2.2	35.91 ± 0.84
C5	41.2	1.46	142.3 ± 0.7	117.1 ± 1.2	−25.2 ± 1.2	−25.91 ± 0.77
C4- H4s	38.41	2.04	126.7 ± 0.5	182.9 ± 1.2	56.2 ± 1.2	53.71 ± 0.51
C4-H4a		1.24	126.3 ± 0.6	106.6 ± 1.1	−19.7 ± 1.1	−20.85 ± 0.44
C6	38.16					
C7-H7s	33.85	1.89	135.0 ± 0.7	130.3 ± 1.4	−4.7 ± 1.4	−5.34 ± 0.38
C7-H7a		0.59	137.1 ± 0.4	136.6 ± 9.0	−0.5 ± 9.0	−1.22 ± 1.67
C8	27.24	0.74	124.4 ± 0.8	130.0 ± 1.1	5.6 ± 1.1	5.40 ± 0.37
C9	23.22	0.45	123.4 ± 0.5	114.7 ± 1.7	−8.7 ± 1.7	−8.23 ± 0.17
C10	20.18	0.65	124.7 ± 0.4	136.6 ± 0.8	11.9 ± 0.8	9.96 ± 0.36

Table 5.2.: Assignment and extracted values ($^1J_{\mathrm{CH}}$, $^1T_{\mathrm{CH}}$ and $^1D_{\mathrm{CH,exp}}$ with corresponding errors) for (+)-IPC. The errors indicate the ±3 standard deviation (±3σ) uncertainty.

Assignment	δ (^{13}C) [ppm]	δ(^{1}H) [ppm]	$^1J_{\mathrm{CH}}$ [Hz]	$^1T_{\mathrm{CH}}$ [Hz]	$^1D_{\mathrm{CH,exp}}$ [Hz]
C3	71.88	4.05	142.0 ± 0.9	181.2 ± 0.8	39.2 ± 0.9
C1	48.05	1.79	141.6 ± 1.2	133.3 ± 1.7	−8.3 ± 1.7
C2	47.91	1.92	126.4 ± 0.7	148.3 ± 4.7	21.9 ± 4.7
C5	41.98	1.91	142.0 ± 1.1	123.3 ± 0.9	−18.7 ± 1.1
C4-H4s	39.2	2.5	126.6 ± 1.0	150.8 ± 0.5	24.2 ± 1.0
C4-H4a		1.69	126.7 ± 0.5	141.2 ± 1.0	14.5 ± 1.0
C6	38.36				
C7-H7s	34.58	2.35	135.0 ± 0.8	123.7 ± 1.1	−11.3 ± 1.1
C7-H7a		1.02	137.0 ± 0.6	129.3 ± 1.1	−7.7 ± 1.1
C8	27.87	1.2	124.5 ± 0.7	134.6 ± 0.6	10.1 ± 0.7
C9	23.88	0.9	123.5 ± 0.5	110.4 ± 2.7	−13.1 ± 2.7
C10	20.93	1.11	124.6 ± 0.4	120 ± 1	−4.6 ± 1.0

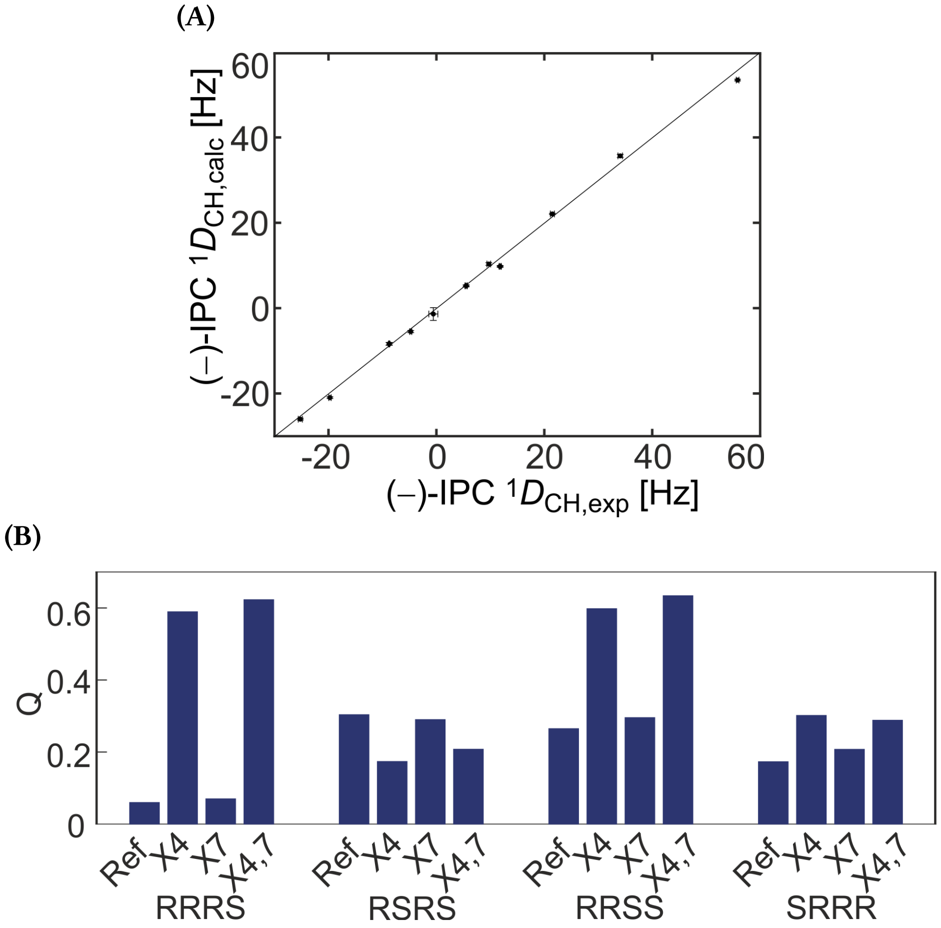

Figure 5.14.: Calculated vs. experimental RDCs for (−)-IPC and Q-factor for exchanged prochiral assignment. (A) Experimental RDCs plotted versus the calculated RDCs for (−)-IPC. Calculated values close to the diagonal line (calc = exp) are in good agreement. (B) The figure shows the different quality-factors for the four configurations of stereogenic centers, which can be assigned with RDCs. Additionally, the assignment of the prochiral protons at the methylene groups of (−)-IPC are exchanged. X4 means that the assignment of the protons at position C4 are exchanged. X7 means that the assignment of the protons at position C7 is exchanged. As a rule of thumb, the quality of a fit is considered good if the Q-factor is below 0.2.

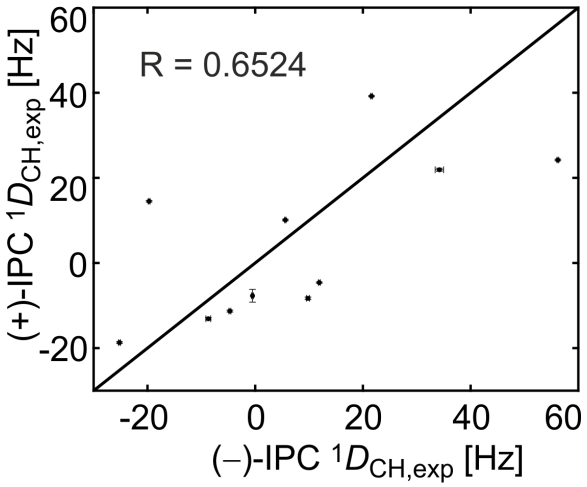

Figure 5.15.: Enantiodiscrimination of (−)-IPC from (+)-IPC by their experimentally determined RDCs measured in the liquid crystal *poly*-**4**. For enantiodiscrimination, the RDCs should be different for each C-H vector. The line indicates coinciding RDCs for the C-H vectors of each enantiomer. As RDCs are different for each C-H vector, the liquid crystal can be used for enantiodiscrimination.

Since the experiment is a three-dimensional spectrum, the measurement time is long compared to the slice selectively excited CLIP-HSQC. Additionally, the phasing and processing procedure can be difficult for the not experienced user. However, the whole sample volume is measured and the decision which planes of the spectrum are added, is done after the measurement. Therefore, the planes which differ because of, for example through decreased line-shape quality can be left out of the interpretation.

5.6. Conclusion

The pulse sequences presented can help to characterize biphasic samples of *poly*-**1** and *poly*-**2** and *poly*-**1** and *poly*-**3**. The slice selective carbon spectrum and the phase-encoded carbon spectrum helped to confirm the constitution of the biphasic samples. It is unknown which polymer is responsible for which phase or if they form two mixed phases. This has been shown with both kind of spectra. The phase-encoded spectrum is easier to interpret and the big advantage is that during the whole acquisition time, the complete sample volume is measured. Therefore, the signal-to-noise decreased due to narrowly excited slices. However, the measurement times for a two-dimensional phase-encoded carbon spectrum are higher than for a slice selectively excited carbon spectrum. After characterization, the samples could be used for the measurement of RDCs if an analyte is added during the preparation process.

The slice selectively excited CLIP-HSQC for the biphasic liquid crystalline sample *poly*-**4** lead to spectra where RDCs are extractable and used for interpretation. It is shown that prochiral assignment of (−)-IPC could be achieved, as well as the enantiodifferentiation of (−)-IPC from (+)-IPC with the values obtained by the biphasic liquid crystalline sample

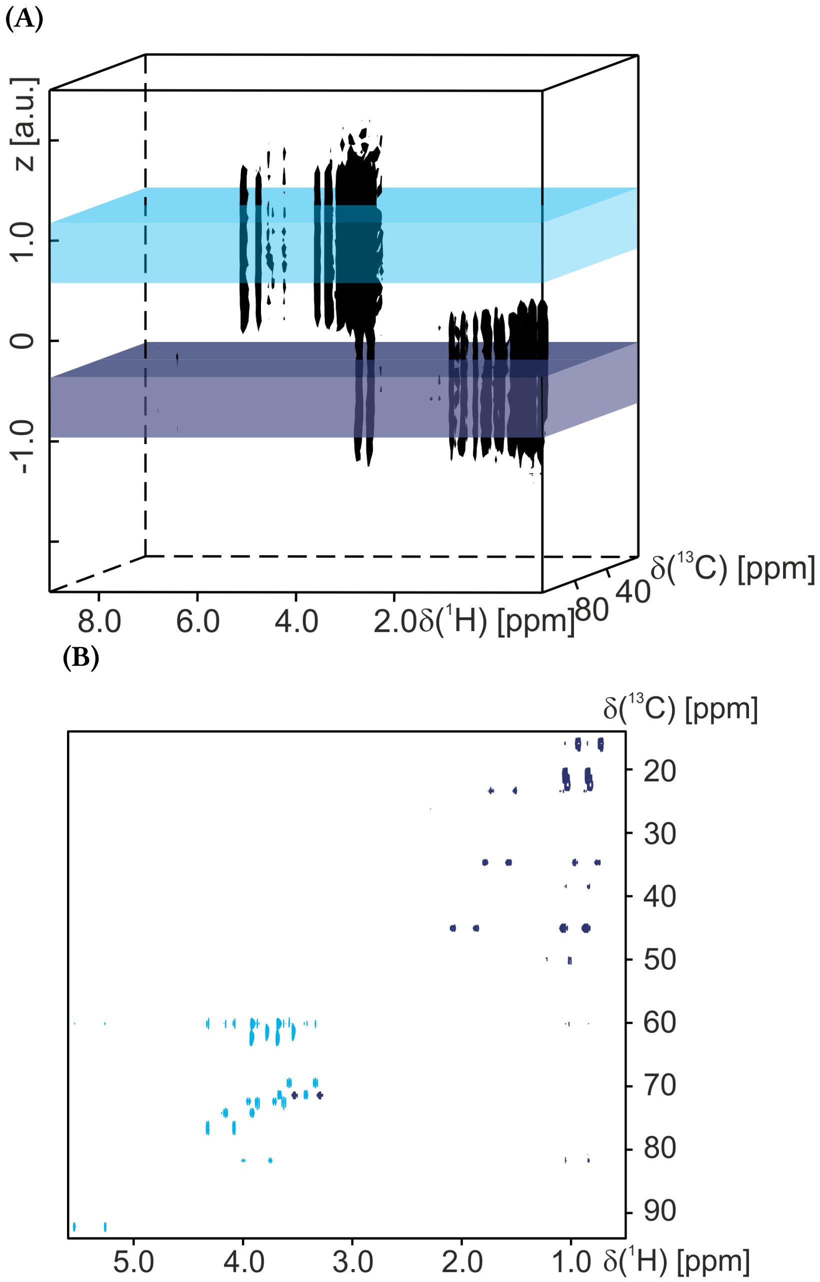

Figure 5.16.: (A) shows the three-dimensional phase-encoded CLIP-HSQC spectrum. The sequence used to record the spectrum is shown in Figure 5.9. (B) shows the calculated projections for each phase of the biphasic sample. The light blue spectrum shows the CLIP-HSQC spectrum of the upper phase which corresponds to the positive projection of the planes 34 to 51 which is a 100 mmol solution of sucrose in D_2O. The dark blue spectrum shows the positive projection of the planes 16 to 30 of the phase-encoded dimension. It shows the CLIP-HSQC spectrum from the lower phase which is 100 mmol solution of (−)-menthol in $CDCl_3$. The experimental parameters for the spectrum are summarized in Section 5.7.3.

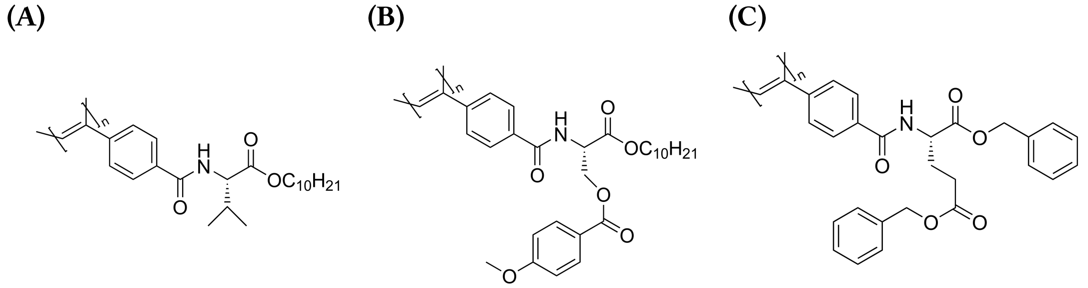

Figure 5.17.: Structures of the chiral polymers used for the mixed phase polymer samples. (A) *poly*-**1**.[61] (B) *poly*-**2**[129] and (C) *poly*-**3**.[130]

and with the sequences presented. Therefore, this sample preparation and the sequences can be used to record isotropic and anisotropic data in one sample.

Last, it is shown that the constitution of a biphasic sample created with two immiscible solvents can be measured by a phase-encoded CLIP-HSQC spectrum. In principle, this leads to the same information as the slice selectively excited CLIP-HSQC. Yet, there is the phase-encoded dimension which leads to more flexibility in terms of, for example, sample homogeneity and magnetic field stability. In the phase-encoded CLIP-HSQC spectrum, the regions of the sample which are homogeneous can be used for interpretation spectrum if the sample homogeneity changes over the sample height. Especially for polymer gels, which can break and can show different sample homogeneity over the sample height, the slice selectively excited as well as the phase-encoded CLIP-HSQC spectrum might be useful. The specific measurement of the samples is particular useful since the sample preparation for polymer gels as well as liquid crystalline phases can take up to months and they could be measured even though they are not homogeneous.

5.7. Material and Methods

Unless stated otherwise, all spectra are measured at a 600 MHz Avance III Bruker (Rheinstetten, Germany) spectrometer equipped with a cryogenically cooled TXI probehead. The maximum gradient strength of the z-gradient is $50.7\,\mathrm{G\,cm^{-1}}$. The acquisition software used is Bruker TopSpin 3.2.

5.7.1. Biphasic Liquid Crystalline Phase Sample of two Polymers

5.7.1.1. Biphasic Liquid Crystalline Phase Sample *poly*-1 and *poly*-2

The sample is prepared with 69.0 mg of *poly*-**1** and 46.5 mg *poly*-**2** and 606.5 mg (404 µL) $CDCl_3$. For better shim and lock performance, a DMSO-d_6 capillary is placed in the sample. The sample is prepared in a 5 mm tube.

The spectrum shown in Figure 5.10A is a deuterium phase-encoded spectrum recorded with 4096 time domain points in the direct dimension with spectral width of 20 ppm and a corresponding acquisition time of 0.556 s. 128 time domain points are recorded in the indirect dimension with the field of view set to 3 cm. The recovery delay is set to 1 s. The spectrum is measured with 4 dummy scans and 1 scan per increment leading to an overall experimental time of 4 min 18 s. The gradient length for the phase encoding is calculated to 759.9 µs and the maximal gradient strength is 95 %. The spectrum is processed to 16 384 points × 128 points. To the direct dimension an exponential apodization function is multiplied. No apodization is applied to the indirect dimension. The spectrum is processed in absolute value mode.

The spectra shown in Figure 5.10B are recorded with the sequence shown in Figure 5.6C. There are both recorded with 65 536 time domain points and a spectral width of 250.989 ppm. The resulting acquisition time is 0.865 s. The recovery delay is set to 5 s. The number of scans are 256. The total experimental time is 21 min 30 s. The 90° pulse for slice selective excitation is a Gaussian cascade pulse (Q5) and is applied with a length of 1200 µs and an rf-amplitude of 3978 Hz. The gradient strength applied during the selective pulse is 40 % of the maximal gradient strength. During acquisition proton decoupling is performed by the Waltz-16 sequence. The spectra are processed to 262 144 points and multiplied with an exponential apodization function. The difference in the aquisition parameters is the offset of the shaped carbon pulse. This is 10 000 Hz for the upper spectrum and −10 000 Hz for the lower phase.

5.7.1.2. Biphasic Liquid Crystalline Phase Sample *poly*-**1** and *poly*-**3**

The sample is prepared with 48.2 mg of *poly*-**1** and 60.0 mg *poly*-**3** and 568.6 mg (380 µL) $CDCl_3$. For better shim and lock performance, a DMSO capillary is placed in the sample. The sample is prepared in a 5 mm tube.

The spectrum shown in Figure 5.11A is recorded with 2048 time domain points in the direct dimension with spectral width of 20 ppm and a corresponding acquisition time of 0.556 s. The recovery delay is set to 1 s. 64 points are recorded in the indirect dimension with a field of view set to 3 cm, which corresponds to the sweep width in the indirect dimension. The spectrum is measured with 4 dummy scans and 1 scan per increment leading to an overall experimental time 2 min 18 s. The gradient length for the phase-encoding is calculated to 379.95 µs and the maximal gradient strength is 95 %. The spectrum is processed to 16 384 points × 64 points. To the FID an exponential apodization function is multiplied. No apodization is applied to the indirect dimension. The spectrum is processed in absolute value mode.

The spectrum shown in Figure 5.11B is recorded with 65 536 time domain points in the direct dimension with a spectral width for the direct dimension of 251.163 ppm and a corresponding acquisition time of 0.865 s. 32 points are recorded in the indirect dimension with a field of view (r_z) of 5 cm, which corresponds to the sweep width in the indirect dimension. The recovery delay is set to 5 s. The spectrum is measured with 0 dummy scans and 32 scans per increment leading to an overall experimental time 1 h 25 min. The gradient length for the phase-encoding is calculated to 69.6 µs and the maximal gradient strength is 95 %. The spectrum is processed with 262 144 points × 32 points in the direct and indirect dimension. The FID is multiplied with an exponential apodization function. No apodization is applied to the indirect dimension. The spectrum is phased with a high first order phase correction in the indirect dimension of $180° \cdot 32$.

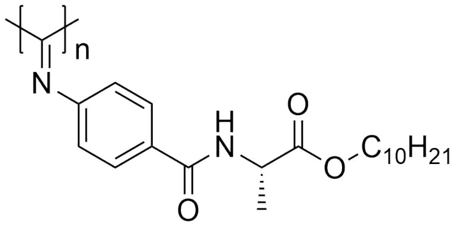

Figure 5.18.: Structure of the polymer forming the biphasic liquid crystalline phase *poly*-**4**.[128]

5.7.2. Biphasic Liquid Crystalline Phase Sample *poly*-4

The structure of the polymer making up the liquid crystalline phase, is shown in Figure 5.18.

5.7.2.1. Preparation of the Biphasic Liquid Crystalline *poly*-4 Sample with (−)-IPC

For the preparation of the biphasic sample, 88.9 mg polymer *poly*-**4**, 26.5 mg (172 µmol) (−)-IPC and 463 µL $CDCl_3$ are mixed. For better shim and lock performance, a DMSO-d_6 capillary is placed in the sample. The sample is prepared in a 5 mm tube.

5.7.2.2. Preparation of the Biphasic Liquid Crystalline *poly*-4 Sample with (+)-IPC

For the preparation of the biphasic sample, 78.7 mg polymer *poly*-**4**, 29.6 mg (191 µmol) (−)-IPC and 410 µL $CDCl_3$ are mixed. For better shim and lock performance, a DMSO-d_6 capillary is placed in the sample. The sample is prepared in a 5 mm tube.

5.7.2.3. Experimental and Processing Parameters for the Biphasic Liquid Crystalline Sample

The phase-encoded deuterium spectrum shown in Figure 5.12B is recorded with 2048 time domain points with a spectral width of 14.99 ppm in the direct dimension, leading to an acquisition time of 0.742 s. In the indirect dimension 256 points are recorded with a field of view set to 3 cm, which corresponds to the sweep width. The maximum gradient strength is 95 % and the corresponding pulse length is 759.91 µs. There is measured one scan per increment and a recovery delay of 1 s is used. The total experimental time is 4 min 33 s. The spectrum is processed with 2048 × 256 points. To the FID, an exponential apodization function is applied. The indirect dimension is not apodized. The spectrum is processed phase-sensitively.

The slice selectively excited and phase-encoded deuterium spectrum shown in Figure 5.12C are recorded with 2048 time domain points in the direct dimension. The spectral width in the direct dimension is 14.99 ppm, leading to an acquisition time of 0.742 ms. In the indirect dimension 128 points are recorded with a field of view set to 3 cm, which corresponds to the sweep width in phase-encoding. The maximum gradient strength is 95 % and the corresponding pulse length is 759.91 µs. The pulse length of the selective pulse (Q3) is 1580 µs with an rf-amplitude of 2123 Hz, the gradient strength during the pulse is 37.5 %. There is measured one scan per increment and a recovery delay of 1 s is used. The total experimental time is 4 min 20 s for each spectrum. The light blue spectrum is recorded with an frequency offset of 5000 Hz for the selective pulse, the dark blue with an offset of −5000 Hz. The spectrum is processed with 2048 × 128 points. To the FID is applied an exponential apodization function. The indirect dimension is not apodized. The spectra are processed phase-sensitively.

The slice selectively excited CLIP-HSQC spectra shown in Figure 5.13 are recorded with the sequence shown in Figure 5.8. The spectra are both recorded with 8192 time domain points in the direct and 512 time domain points in the indirect dimension with corresponding spectral widths of 6 ppm and 100 ppm. This lead to acquisition times of 1.139 s in the direct dimension and 0.017 s in the indirect dimension. The transfer Δ is matched to $J = 145$ Hz. The recovery delay is 0.8 s. Before acquisition 16 dummy scans are performed. Each increment is recorded with 4 scans. This led to an overall experimental time of 38 min 8 s. For the slice selective excitation, the selective 180° pulse is a Gaussian cascade pulse (Q3) with a length of 395 s and an rf-amplitude of 8528 Hz. The pulsed field gradient strength is 11.36 %. The light blue spectrum which results from the anisotropic phase, is recoded with a frequency offset for the shaped pulse of 10 000. The dark blue spectrum is recorded with an offset for the shaped pulse of −10 000. The spectra are processed with 16 384 points × 1024 points. Both dimensions are apodized with a cosine squared function.

5.7.3. Biphasic Sample of two Immiscible Solvents

The sample is prepared by dissolving 42.0 mg (122.7 µmol) sucrose purchased from Fluka in 1.2 ml D_2O purchased from Eurisotop. Both are used without further purification. The resulting concentration is 100 mmol l^{-1}. For the menthol (Sigma-Aldrich) solution, 9.3 mg (59.5 µmol) are dissolved in 0.6 ml $CDCl_3$ to give a 100 mmol l^{-1} solution. The chloroform is purchased from Eurisotop and used without further purification. From both solutions, 300 µl are overlaid on each other. As the chloroform has the higher density, the water phase is the upper phase. The sample is prepared in a 5 mm tube.

The spectra shown in Figure 5.3 and 5.16 are recorded on a Bruker 600 MHz Avance II+ spectrometer (Rheinstetten, Germany) equipped with a BBI-probehead. The program to run the experiments is Bruker TopSpin 3.2.

The spectrum shown in Figure 5.3 is recorded with the sequence in Figure 5.2A and with 2048 time domain points in the direct dimension. The spectral width of the direct dimension is 20.0 ppm and led to an aquisition time of 0.555 s. 256 points are recorded in the indirect dimension with a field of view in the phase-encoded dimension of 5 cm, which corresponds to the sweep width in this dimension The recovery delay is set to 0.001 s. No dummy scans are executed and one scan per increment is recorded. This led to an overall experimental time of 2 min 18 s. The maximal gradient strength for the phase encoding gradient is set to 95 %. The resulting gradient length is 911.89 µs. The acquisition mode in the indirect dimension is QF. The spectrum is phase-sensitively processed to 2048 points × 256 points. The FID is multiplied with an exponential apodization function, in the indirect dimension no apodization function is applied.

The spectrum shown in Figure 5.16 is recorded with the sequence shown in Figure 5.9. It is recorded with 8192 time domain points in the direct, 64 points in the phase-encoded and 128 time domain points in the carbon dimension. The corresponding spectral width with the acquisition time are 10.0 ppm, 0.682 s and 120 ppm, 0.004 s. The field of view in the phase-encoded dimension is set to the 3 cm, which corresponds to the sweep width in this dimension. The recovery delay is set to 1 s and $^1J_{\mathrm{CH}}$ is set to 145 Hz and Δ calculated accordingly. 16 dummy scans are executed before the start of the data acquisition which is recorded with 2 scans per increment. The maximal gradient strength for the phase encoding gradient is 47.5 %, the gradient pulse length is 106.23 µs. The overall acquisition time is 4 h 37 min. The acquisition mode in the indirect dimension is States-TPPI for the carbon dimension and QF for the phase-encoded dimension. The spectrum is processed phase-sensitively to 8192, 64 and 128 points. No apodization function is applied to the phase-encoded dimension, the other two dimensions are apodized with a cosine squared function.

6. Sign Sensitive Measurement of $^2J_{\mathrm{CH}}$ coupling constants to quaternary carbons

NMR spectroscopy is widely used for the structure determination of small molecules and biomolecules. Besides the chemical shift, coupling constants can improve the quality of structure determination. The most relevant couplings are the $^3J_{\mathrm{HH}}$ couplings, which are dependent on the dihedral torsion angle and are extracted for example from one-dimensional proton spectra.[9] If too many signals are crowded in one region of the spectrum, the signals may overlap and coupling extraction may be hindered. Therefore, the measurement of two-dimensional spectra can be beneficial. Other couplings used for structure refinement are $^1J_{\mathrm{CH}}$ couplings which are extracted out of CLIP-HSQC[86] or PIP-HSQC[131, 132] spectra. For these couplings proton-carbon-pairs are needed. Therefore, other couplings like $^2J_{\mathrm{CH}}$ couplings increase in importance for cases where $^3J_{\mathrm{HH}}$ and $^1J_{\mathrm{CH}}$ coupling constants are not sufficient, for example for quaternary carbons that have a stereogenic center. Obviously, also the $^2J_{\mathrm{CH}}$ can here contribute valuable information to the structure refinement. For protonated carbons $^2J_{\mathrm{CH}}$ coupling constant can be determined by the IPAP-HSQC-TOCSY-[102], the HECADE-experiments[133] or many others. For quaternary carbons the coupling determination can be achieved by the spin-tickling approach and Heteronuclear Single-Quantum Multiple-Bond Correlations (HSQMBCs) and derivatives thereof.[134–137] The HSQMBC-sequence is based on the HSQC, but the INEPT and the back transfer step are matched to $^nJ_{\mathrm{CH}}$. In this experiment, the challenges are homonuclear coupling evolution during t_2 and anti-phase signals. This leads to difficulties, e. g., for the extraction of small couplings. One major drawback of the HSQMBC is the long transfer period because the length of the period is inversely proportional to the coupling constants. During this time, proton-proton couplings are active, which leads to signal distortions. To overcome this problem, there have been several proposes, e. g. the selectively excited HSQMBC. However, these methods only offer the magnitude of the couplings and not their sign. Especially, for the use of Residual Dipolar Coupling the sign contains information about the orientation of the C-C-H group.

Therefore, two experiments to extract both magnitude and sign of the $^2J_{\mathrm{CH}}$ for quaternary carbons are developed. The experiments are based on the evolution of double quantum coherence and the simultaneous evolution of the sum of the couplings of $^1J_{\mathrm{CH}}$ and $^2J_{\mathrm{CH}}$ during t_1. In contrast to other already published experiments, the experiment uses a transfer function that does not depend on the $^2J_{\mathrm{CH}}$ or $^3J_{\mathrm{CH}}$ coupling constant, which can range from -10 Hz to 66 Hz or from 0 Hz to 15 Hz. This makes both the ω_1-coupled ADEQUATE and the ω_1-coupled-BIRD$^{\mathrm{r}}$ ADEQUATE experiment, a robust method to measure magnitude and sign of the couplings, since the transfer steps in the experiments are not based on these couplings.

6.1. State-of-the-Art methods to measure $^2J_{\mathrm{CH}}$ to quaternary carbons

Most of the methods that measure $^2J_{\mathrm{CH}}$ coupling constants do not allow the measurement if the carbon is quaternary, e. g., all sequences which are based first on an INEPT transfer step matched to the $^1J_{\mathrm{CH}}$ coupling constant, as for example IPAP HSQC-TOCSY[102], HECADE[133]. The focus is he comparison of pulse sequence where the size of the $^2J_{\mathrm{CH}}$ coupling constant to a quaternary carbon is accessible. In some sequences also the sign for these couplings is measurable.

One of the methods is based on the HSQMBC sequence.[138] The HSQMBC relies on the evolution of single quantum coherence over multiple bonds. This is achieved by matching the delay Δ during the INEPT and the back transfer to $^{\mathrm{n}}J_{\mathrm{CH}}$, which is usually the $^3J_{\mathrm{CH}}$ and in the range of 8 Hz to 15 Hz. Δ is defined as $\frac{1}{4(^nJ_{\mathrm{CH}})}$. Therefore, the delay Δ in this experiment is long compared to the delay Δ CLIP-HSQC spectra and in the range of proton-proton couplings. Both can cause problems. First, relaxation can take place during the long delay. Second, the proton-proton couplings can lead to distortions of the signals. The HSQMBC provides good sensitivity and easy implementation. In the typical HSQMBC methods, the proton-proton coupling evolution leads to distorted line shapes of the multiplet which is impeding the coupling extraction. Therefore, different approaches to suppress the proton-proton coupling have been implemented in the sequence. One variation suppresses the proton-proton coupling by using selective 180° pulses on protons. Hence, it is called *selective* HSQMBC.[139] Other methods use a perfect echo element or a Carr-Purcell-Meiboom-Gill (CPMG) pulse train.[134, 140, 141] All these variations are included in the long-range coupling-matched INEPT block and do not allow to determine the sign of the couplings. To measure sign of the coupling, two variations of the HSQMBC are published: the HSQMBC-COrrelation SpectroscopY (COSY) [136] and the HSQMBC-TOCSY (see Figure 6.2) [137]. In these pulse sequence, during the INEPT block, selective 180° proton pulses are used and afterwards a TOCSY transfer is added. During t_2 no carbon decoupling is applied. By recording an in-phase (IP) and anti-phase (AP) spectrum, the coupling and the sign determination is obtained by subtracting and adding the two spectra, the result gives spin state selective subspectra. Furthermore, also small couplings can be determined. The HSQMBC-TOCSY and HSQMBC-COSY spectra are of widespread application and provide a relatively good sensitivity compared to other approaches. Additionally, the implementation is easy. Problems remain in the proton-proton coupling which leads to signal distortion and the coupling extraction is related to a complicated fitting procedure. The biggest issue is the sign determination, as it relies on a second proton which is coupled to the same quaternary carbon (see Figure 6.1 for the needed spin system). As $^3J_{\mathrm{CH}}$ coupling constants are always positive, they can be used to determine the relative sign of the $^2J_{\mathrm{CH}}$ coupling. For spin systems where the second proton is missing, the sign determination fails.

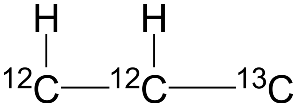

Figure 6.1.: Scheme of the spinsystem needed for the determination of the magnitude and sign of the $^2J_{\mathrm{CH}}$ coupling constants for the determination by the HSQMBC-COSY[136] or HSQMBC-TOCSY[137].

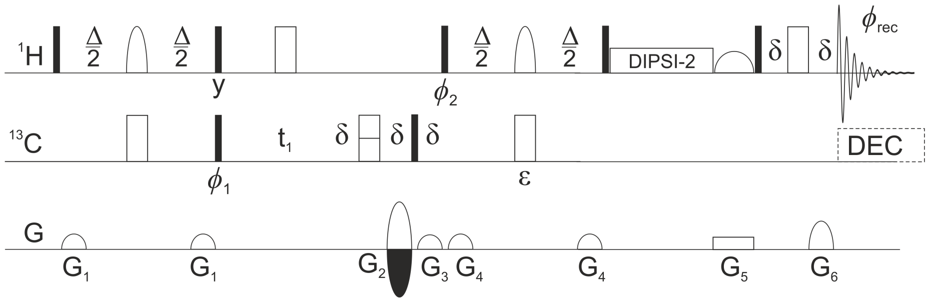

Figure 6.2.: Pulse sequence for the HSQMBC-TOCSY for the determination of the magnitude and sign of $^2J_{\mathrm{CH}}$ coupling constants. Δ is matched to $\frac{1}{2(^nJ_{\mathrm{CH}})}$. Selective 180° pulses on protons are used to suppress the proton-proton coupling. Two spectra for in-phase and anti-phase can be recorded. For in-phase phase $\phi_2 = y$ and ϵ is on. For anti-phase $\phi_2 = x$ and ϵ is off. Gradient strengths $G_1 : G_2 : G_3 : G_4 : G_5 : G_6$ are set to $33\,\% : 80\,\% : 50\,\% : 17\,\% : 3\,\% : 20.1\,\%$. Phase cycling where $\phi_1 = x, -x$ and $\phi_{\mathrm{rec}} = x, -x$ Phase sensitive detection in the indirect dimension is achieved by Echo/Antiecho. The sequence is published by Saurí et al.[137]

One other technique is the spin-tickling method. The spin-tickling approach has already been published in 1962.[142] With this method relative signs of J couplings can be determined. In this method a part of a selected multiplet is irradiated individually by selecting a single transition. Thereby, the population of states are inverted. The coupled multiplet changes accordingly. By deriving the specific coupling and energy scheme, the sign of the coupling constant can be determined relatively to a $^3J_{\mathrm{CH}}$ or $^3J_{\mathrm{HH}}$ coupling. As in the case above, a three spin system with three weakly coupled spins is needed. The sign is measured for each coupling independently, which is time consuming.[143]

For the determination of $^2J_{\mathrm{CH}}$ and other long-range carbon-proton couplings, a sequence of Bax and Freeman can be used.[105] The sequence starts with a 90° pulse on the proton, followed by an evolution time t_1. Then, a 45° pulse on proton and a simultaneous 90° pulse on carbon are applied before the acquisition. The sequence relies on three coupled spins which are nonequivalent (AMX spin system). The spin M is the passive spin. Two subspectra are created and each subspectrum corresponds to M in the α or β state. Therefore, the signals are split both in the indirect dimension and direct dimension first by the coupling of X to M (indirect) and second by the coupling of X to A. If the displacement in both dimensions is the same, the coupling constants have the same sign. As $^1J_{\mathrm{CH}}$ and $^3J_{\mathrm{CH}}$ couplings are always positive, they can be used for reference. Difficulties arise, if the resolution in the indirect dimension does not resolve the coupling constant. Moreover, carbon is detected which leads to sensitivity issues, as especially quaternary carbons have long relaxation times. The biggest drawback is the need of three coupled spins. Consequently, the sign can only be determined in the same cases as for the HSQMBC-TOCSY or the HSQMBC-COSY. Furthermore, the resolution and both coupling constants ($^2J_{\mathrm{CH}}$ and $^3J_{\mathrm{CH}}$) have to be large enough to be resolved and hence lead to the four multiplets which are needed for the determination of the relative sign.[105]

6.2. The ADEQUATE Pulse Sequence

The evolution of the Adequate sensitivity DoublE-QUAntum spEctroscopy (ADEQUATE) pulse sequence started because of the sensitivity issues of the INADEQUATE, explained in Section 2.7.3. The INADEQUATE is the first experiment to measure carbon-carbon-connectivities at natural abundance[104]. The pulse sequence is presented and shown in Section 2.7.3. The evolution of multiple quantum coherence of two adjacent ^{13}C nuclei is used to assign a carbon network. The suppression of the signal rising from a single ^{13}C nucleus in a molecule and to filter out the ^{13}C satellite signals is achieved in the INADEQUATE sequence by evolution of the homonuclear ^{13}C-^{13}C coupling and by appropriate phase cycling. The key-point is that molecules with a single ^{13}C nucleus cannot generate multiple-quantum coherence. Therefore, the signal arising from a single ^{13}C in a molecule can be suppressed by phase cycling as already explained in Section 2.8.2. Since in the INADEQUATE sequence neighbored ^{13}C-^{13}C nuclei at natural abundance are excited and detected, the sensitivity is low. Furthermore, the gyromagnetic ratio for ^{13}C nuclei is low.[104] This is why huge effort is set into the development of more sensitive experiments showing the ^{13}C-connectivities by using nuclei with higher gyromagnetic ratios. First publications involved the INEPT-INADEQUATE pulse sequence. Here, proton polarization is excited and transferred via an INEPT transfer step to carbon. However, carbon detection is still used.[144] In the next evolution step, carbon excitation and proton detection are used, the corresponding publication is from Keller etál.[145] The first one to publish and use proton excitation and detection are Weigelt and Otting. They published the proton detected INEPT-ADEQUATE in 1995.[146] Further changes are made by B. Reif et al. in 1996. They used a 60° pulse after the evolution of the double quantum coherence. This pulse transfers the maximum intensity from double quantum coherence to single quantum coherence.

The sequence starts with an INEPT transfer from protons to carbons. The second step in the pulse sequence is the creation of double quantum coherence on carbon. Therefore, the delay Δ_2 is matched to the ${}^{1}J_{\mathrm{CC}}$ which ranges from 35 Hz to 60 Hz. During t_1, double quantum coherence evolves. Afterwards, a 60° pulse returns the double quantum coherence into single quantum coherences along the x- and y-axis. The single quantum coherence on carbon is reconverted into single quantum coherence on protons via sensitivity enhancement. This sequence is published by Reif et al.[147] Double quantum coherence on carbon is created and partly refocused during the back transfer when carbon single quantum coherence is present. Therefore, the signals arise at the positions of carbon single quantum coherence in the indirect dimension. To overcome the wide spread of chemical shifts in the indirect dimension Köck et al. published in 2003 the ADEQUATE sequence with smoothed chirp pulses for the 180° pulses on carbon. The complete original sequence is shown in Figure 6.3.

The gradient has to select double quantum coherence on carbon during t_1 ($p = 2$), after the creation of single quantum coherence on carbon another gradient is applied ($p = 1$). Last, the second gradient which is the Echo/Antiecho gradient is applied when proton single coherence is present ($p = 1$). Therefore, the Equation 2.72 looks as follows for this experiment.

$$+ 2\gamma_C \times G_1 + \gamma_C \times G_2 - \gamma_H \times G_3 = 0 \tag{6.1}$$

As the duration of the gradient is always the same, it is omitted, as well as the z-coordinate. To achieve this refocusing condition G_1 and G_2 are set to arbitrary values and G_3 is calculated with the equation above. The resulting gradients are G_1: G_2: G_3 $-78.5\,\%$:$-77.6\,\%$:$-59\,\%$.

6.2.1. Product Operators present during the Evolution of the Indirect Dimension

In this section, the calculation with the product operator formalism due to the coupling evolution during t_1 is looked further into. At the starting point of t_1, the operator $4\hat{I}_z\hat{S}_{1x}\hat{S}_{2y}$ is present. During t_1, double quantum coherence of the two carbons and the coupling to the coupled protons evolve. Therefore, they coupling evolution with the sum of ${}^{1}J_{\mathrm{CH}}$ and ${}^{2}J_{\mathrm{CH}}$ couplings to the directly bound proton is observed. If other protons are coupled, the doublet is further split into a more complicated multiplet. For better comprehension, we start with a three spin system. At the beginning of t_1, the operator $2\hat{I}_{1z}(2\hat{S}_{2x}\hat{S}_{3y} + 2\hat{S}_{2y}\hat{S}_{3x})$

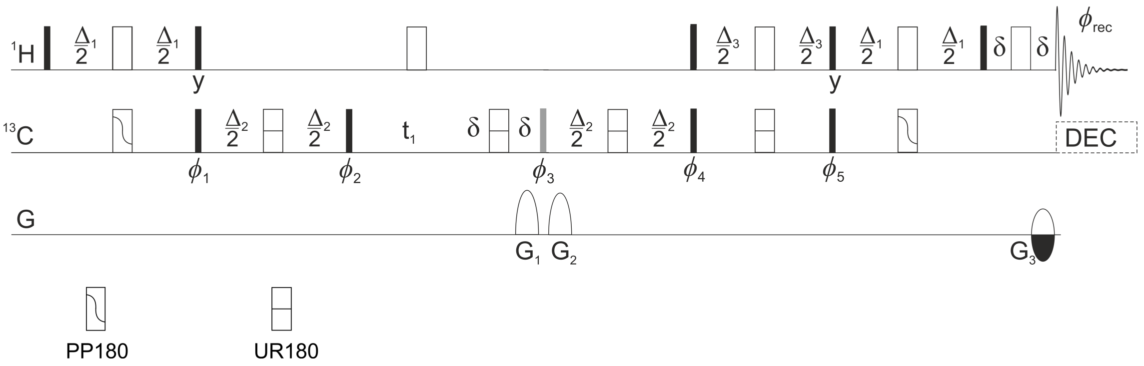

Figure 6.3.: Original pulse sequence published from M. Köck *et al.* with shaped Chirp-pulses for the 180° on carbon.[148]. Narrow black bars stand for 90° pulses, wide light bars stand for 180° pulses. The narrow gray bar stands for a 60° pulse. Regular smoothed chirp are used for the first and last 180° pulses on carbon. For the other four 180° pulses on carbon composite smoothed chirp pulses are used. The delay Δ_1 is matched to $\frac{1}{2(^1J_{CH})}$, Δ_2 is matched to $\frac{1}{2(^1J_{CC})}$ and Δ_3 is matched to $\frac{1}{3(^1J_{CH})}$ δ is a refocusing delay and matched to the gradient length. If not stated otherwise pulse phases are x. Phase cyclings are $\phi_1 = x, -x$, $\phi_2 = (x)_4, (-x)_4$, $\phi_3 = (x)_8, (-x)_8$, $\phi_4 = (x)_2, (-x)_2$, $\phi_5 = (y)_2, (-y)_2$, $\phi_{rec} = x, -x, -x, x, -x, x, x, -x, -x, x, x, -x\ x, -x, -x, x$. Gradient strengths are G_1: G_2: G_3 −78.5 %:−77.6 %:−59 %. Phase sensitive detection in the indirect dimension is achieved by Echo/AntiEcho type selection.

is present. Under coupling evolution to the proton $\hat{I}_1$, this term evolves to give:

$$\begin{aligned} &2\hat{I}_{1z}(2\hat{S}_{2x}\hat{S}_{3y} + 2\hat{S}_{2y}\hat{S}_{3x}) \xrightarrow{2\pi\ ^1J_{12}\hat{I}_{1z}\hat{S}_{2z}t_1} \xrightarrow{2\pi\ ^2J_{13}\hat{I}_{1z}\hat{S}_{3z}t_1} \\ &\quad 2\hat{I}_{1z}(2\hat{S}_{2x}\hat{S}_{3y} + 2\hat{S}_{2y}\hat{S}_{3x})\cos(\pi t_1(^1J_{12} +^2 J_{13})) \\ &\quad +(2\hat{S}_{2y}\hat{S}_{3y} - 2\hat{S}_{2x}\hat{S}_{3x})\sin(\pi t_1(^1J_{12} +^2 J_{13})). \end{aligned} \tag{6.2}$$

The first term is indicating that the splitting in the indirect dimension is the sum of the two couplings $^1J_{CH}$ and $^2J_{CH}$. The second term in Equation 6.2 does not contribute to observable magnetization and can be neglected. This means that the signal from a single proton bound to a carbon pair, is split into a doublet by the sum of the two couplings $^1J_{12}$ and $^2J_{13}$ (see Figure 6.5A).

In case of an additional spin, two more couplings have to be taken into account. Consequently, the terms in Equation 6.2 evolve under the couplings $^1J_{24}$ and $^2J_{34}$ to an additional spin $\hat{I}_4$. The result is shown in Equation 6.3.

$$\begin{gathered}
2\hat{I}_{1z}(2\hat{S}_{2x}\hat{S}_{3y} + 2\hat{S}_{2y}\hat{S}_{3x})\cos(\pi t_1(^1J_{12} +^2 J_{13})) \\
+(2\hat{S}_{2y}\hat{S}_{3y} - 2\hat{S}_{2x}\hat{S}_{3x})\sin(\pi t_1(^1J_{12} +^2 J_{13})) \\
\xrightarrow{2\pi t_1\ {}^1J_{24}\hat{I}_{2z}\hat{S}_{4z}}\xrightarrow{2\pi t_1\ {}^2J_{34}\hat{I}_{3z}\hat{S}_{4z}} \\
2\hat{I}_{1z}(2\hat{S}_{2x}\hat{S}_{3y} + 2\hat{S}_{2y}\hat{S}_{3x})\cos(\pi t_1(^1J_{12} +^2 J_{13}))\cos(\pi t_1(^1J_{24} +^2 J_{34})) \\
+4\hat{I}_{1z}\hat{I}_{4z}(2\hat{S}_{2x}\hat{S}_{3y} - 2\hat{S}_{2x}\hat{S}_{3x})\cos(\pi t_1(^1J_{12} +^2 J_{13}))\sin(\pi t_1(^1J_{24} +^2 J_{34})) \\
+(2\hat{S}_{2y}\hat{S}_{3y} - 2\hat{S}_{2x}\hat{S}_{3x})\sin(\pi t_1(^1J_{12} +^2 J_{13}))\cos(\pi t_1(^1J_{24} +^2 J_{34})) \\
-2\hat{I}_{4z}(2\hat{S}_{2x}\hat{S}_{3y} + 2\hat{S}_{2y}\hat{S}_{3x})\sin(\pi t_1(^1J_{12} +^2 J_{13}))\sin(\pi t_1(^1J_{24} +^2 J_{34}))
\end{gathered} \tag{6.3}$$

The terms $2\hat{I}_{1z}(2\hat{S}_{2x}\hat{S}_{3y} + 2\hat{S}_{2y}\hat{S}_{3x})$ and $2\hat{I}_{4z}(2\hat{S}_{2x}\hat{S}_{3y} + 2\hat{S}_{2y}\hat{S}_{3x})$ lead to observable magnetization. As it can be seen, one term is twice cosine modulated. Therefore the signal for this term is split first by the coupling of one sum and then split by the coupling of the second sum, leading to a doublet of doublet with the signal intensity $1 : 1 : 1 : 1$ for a methylene group with different coupling constants for each proton. The other term is a mixed term, which is first sine then cosine modulated. This terms leads to a doublet of doublet with signal intensities of $1 : -1 : -1 : 1$. As both terms add up in the spectra, the signal is split into $1 : 0 : 0 : 1$ intensity. As can be seen in Figure 6.5D. For a further proton the calculation is straightforward. The result is the following:

$$\begin{gathered}
2\hat{I}_{1z}(2\hat{S}_{2x}\hat{S}_{3y} + 2\hat{S}_{2y}\hat{S}_{3x})\cos(\pi t_1(^1J_{12} +^2 J_{13}))\cos(\pi t_1(^1J_{24} +^2 J_{34})) \\
+4\hat{I}_{1z}\hat{I}_{4z}(2\hat{S}_{2y}\hat{S}_{3y} - 2\hat{S}_{2x}\hat{S}_{3x})\cos(\pi t_1(^1J_{12} +^2 J_{13}))\sin(\pi t_1(^1J_{24} +^2 J_{34})) \\
+(2\hat{S}_{2y}\hat{S}_{3y} - 2\hat{S}_{2x}\hat{S}_{3x})\sin(\pi t_1(^1J_{12} +^2 J_{13}))\cos(\pi t_1(^1J_{24} +^2 J_{34})) \\
-2\hat{I}_{4z}(2\hat{S}_{2x}\hat{S}_{3y} + 2\hat{S}_{2y}\hat{S}_{3x})\sin(\pi t_1(^1J_{12} +^2 J_{13}))\sin(\pi t_1(^1J_{24} +^2 J_{34})) \\
\xrightarrow{2\pi t_1\ {}^1J_{25}\hat{I}_{2z}\hat{S}_{5z}}\xrightarrow{2\pi t_1\ {}^2J_{35}\hat{I}_{3z}\hat{S}_{5z}} \\
2\hat{I}_{1z}(2\hat{S}_{2x}\hat{S}_{3y} + 2\hat{S}_{2y}\hat{S}_{3x})\cos(\pi t_1(^1J_{12} +^2 J_{13}))\cos(\pi t_1(^1J_{24} +^2 J_{34}))\cos(\pi t_1(^1J_{25} +^2 J_{35}) \\
+4\hat{I}_{1z}\hat{I}_{5z}(2\hat{S}_{2y}\hat{S}_{3y} - 2\hat{S}_{2x}\hat{S}_{3x})\cos(\pi t_1(^1J_{12} +^2 J_{13})\cos(\pi t_1(^1J_{24} +^2 J_{34}))\sin(\pi t_1(^1J_{25} +^2 J_{35})) \\
+4\hat{I}_{1z}\hat{I}_{4z}(2\hat{S}_{2y}\hat{S}_{3y} - 2\hat{S}_{2x}\hat{S}_{3x})\cos(\pi t_1(^1J_{12} +^2 J_{13})\sin(\pi t_1(^1J_{24} +^2 J_{34}))\cos(\pi t_1(^1J_{25} +^2 J_{35})) \\
-8\hat{I}_{1z}\hat{I}_{4z}\hat{I}_{5z}(2\hat{S}_{2x}\hat{S}_{3y} + 2\hat{S}_{2y}\hat{S}_{3x})\cos(\pi t_1(^1J_{12} +^2 J_{13})\sin(\pi t_1(^1J_{24} +^2 J_{34}))\sin(\pi t_1(^1J_{25} +^2 J_{35})) \\
+(2\hat{S}_{2y}\hat{S}_{3y} - 2\hat{S}_{2x}\hat{S}_{3x})\sin(\pi t_1(^1J_{12} +^2 J_{13}))\cos(\pi t_1(^1J_{24} +^2 J_{34}))\cos(\pi t_1(^1J_{25} +^2 J_{35})) \\
-2\hat{I}_{5z}(2\hat{S}_{2x}\hat{S}_{3y} + 2\hat{S}_{2y}\hat{S}_{3x})\sin(\pi t_1(^1J_{12} +^2 J_{13}))\cos(\pi t_1(^1J_{24} +^2 J_{34}))\sin(\pi t_1(^1J_{25} +^2 J_{35})) \\
+2\hat{I}_{4z}(2\hat{S}_{2x}\hat{S}_{3y} + 2\hat{S}_{2y}\hat{S}_{3x})\sin(\pi t_1(^1J_{12} +^2 J_{13}))\sin(\pi t_1(^1J_{24} +^2 J_{34}))\cos(\pi t_1(^1J_{25} +^2 J_{35})) \\
-4\hat{I}_{4z}\hat{I}_{5z}(2\hat{S}_{2y}\hat{S}_{3y} - 2\hat{S}_{2x}\hat{S}_{3x})\sin(\pi t_1(^1J_{12} +^2 J_{13}))\sin(\pi t_1(^1J_{24} +^2 J_{34}))\sin(\pi t_1(^1J_{25} +^2 J_{35}))
\end{gathered} \tag{6.4}$$

Again only the three terms $((2\hat{I}_{1z} + 2\hat{I}_{4z} + 2\hat{I}_{5z})(2\hat{S}_{2x}\hat{S}_{3y} + 2\hat{S}_{2y}\hat{S}_{3x}))$ result in observable magnetization and add up to give a multiplet with the intensities of $3 : 1 : 1 : 3$ for a methylene group where all couplings are equal. As can be seen in Figure 6.5F.

The calculation for more complicated spin systems without a quaternary carbon involved are performed. The resulting multiplets are more complicated. The 1D-simulation shows the same multiplicities measured in the indirect dimension of the ADEQUATE sequence, see Figure 6.8 for the experimental result for the ω_1-coupled ADEQUATE and the simulations of ethanol. So it is in principle also possible to extract $^2J_{\mathrm{CH}}$ coupling constants from the spectra recorded with the ADEQUATE sequence for all other multiplicities. However, this is not preferable as there exist experiments which are easier to measure and easier to interpret, e. g., the experiment presented before in Section 2.7.2. As can be seen above, the double quantum coherence couples to every proton bond to the carbons by one or more bonds. Therefore, a BIRD$^{\mathrm{r}}$ filter is inserted in the middle of t_1 to decouple protons which are not directly bond to the carbons.

6.2.2. BIRD-Filter

The BIRD-filter stands for BIlinear π-Rotation Decoupling. Originally, it is used to homonuclear decouple proton spectra. It is a standard element in multi-pulse sequences, which can be used for different purposes. For example, it can be used in the center a free evolution period to selectively decouple or couple protons. By insertion of the BIlinear Rotation Decoupling (BIRD)-filter, the number of interactions is reduced and signal-to-noise ratios and resolution increase and spectra are simplified. The BIRD-filter relies on J-selective spin inversion and is especially useful for heteronuclear spin systems, as in heteronuclear spin systems the J couplings have different magnitude. For instance, a $^1J_{\mathrm{CH}}$ is in the range of 120 Hz to 250 Hz in contrast to all $^nJ_{\mathrm{CH}}$ and proton-proton coupling constants which are in the range of -10 Hz to 60 Hz. Moreover, this differentiation is based on the natural abundance of 1 % of ^{13}C nuclei. Based on this, the protons are divided into two groups. The directly to the ^{13}C nucleus attached protons are called the direct proton and all other protons are called remote protons. Depending on which spin species experience the 180° pulse, the BIRD-filter has different superscripts to classify and differentiate them. The pulse scheme is shown in Figure 6.4. In the middle of two 90° pulses on the proton channel is placed a 180° pulse on carbon and protons. The complete delay is matched to $\Delta = 1/(^1J_{CH})$. Depending on the phases ϕ_1, ϕ_2, ϕ_3 and ϕ_4, the BIRD-filter has different effects on the remote and direct protons and the X-nucleus. First the BIRD$^{\mathrm{d,X}}$ and BIRD$^{\mathrm{r,X}}$ are published. They invert both either direct protons and the X nucleus or the remote protons and the X nucleus, respectively.[149] For the BIRD$^{\mathrm{d}}$ and BIRD$^{\mathrm{r}}$, a second 180° pulse on carbons is added which is parallel to the second 90° pulse on protons. Hence, the BIRD$^{\mathrm{d}}$ and BIRD$^{\mathrm{r}}$ invert the direct protons or the remote protons but the inversion effect on the X-nucleus is removed.[150] As some of the protons will experience an effective 180° pulse, the BIRD-filter leads to a kind of editing. This depends on an even or odd number of protons which are attached to the X-nucleus. In Table 6.1, the effects of the different BIRD-filters on J coupling constants (J_{dr}, $J_{\mathrm{d,X}}$, $J_{\mathrm{r,X}}$, $J_{\mathrm{dd'}}$ and $J_{\mathrm{rr'}}$) and chemical shifts of the direct proton (ν_{d}), remote proton (ν_{r}) and the X-nucleus (ν_{X}) are summarized.

To calculate the effect of the BIRD$^{\mathrm{r}}$ filter during t_1 in the ω_1-coupled ADEQUATE sequence, chemical shift evolution is left out. Only the calculation for the term $4I^d_{1z}\hat{S}_{2x}\hat{S}_{3y}$ is looked at, as it is the term which leads to observable magnetization at the end of the pulse sequence. First, the evolution under J coupling to the remote proton is calculated

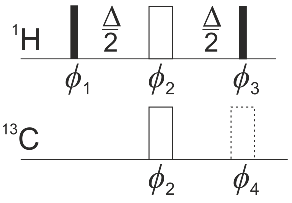

Figure 6.4.: Pulse scheme of the BIRD-filter. Black narrow boxes represent 90° and unfilled broad boxes 180° pulses. The transfer Δ is matched to $1/(^1J_{\mathrm{CH}})$. ϕ_1, ϕ_2 and ϕ_3 can be set to achieve different manipulations (BIRD$^{\mathrm{d,X}}$ or BIRD$^{\mathrm{r,X}}$). The second 180° pulse and the corresponding phase ϕ_4 can be set to achieve a BIRD$^{\mathrm{d}}$ or BIRD$^{\mathrm{r}}$ decoupling. For the phase cyclings of the different BIRD-filter, see [150]. For the BIRD$^{\mathrm{r}}$-filter used in the ω_1-coupled-BIRD$^{\mathrm{r}}$ ADEQUATE pulse sequence, the phases are set to $\phi_1 = x$, $\phi_2 = x$ $\phi_3 = -x$ and $\phi_4 = x$.

	no pulse	180° (^{1}H)	180° (X)	180° (^{1}H, X)	BIRD$^{\mathrm{d,X}}$	BIRD$^{\mathrm{r,X}}$	BIRD$^{\mathrm{d}}$	BIRD$^{\mathrm{r}}$
J_{dr}	✓	✓	✓	✓	×	×	×	×
$J_{\mathrm{d,X}}$	✓	×	×	✓	✓	×	×	✓
$J_{\mathrm{r,X}}$	✓	×	×	✓	×	✓	✓	×
ν_{d}	✓	×	✓	×	×	✓	×	✓
ν_{r}	✓	×	✓	×	✓	×	✓	×
ν_{X}	✓	✓	×	×	×	×	✓	✓
$J_{\mathrm{dd'}}$	✓	✓	✓	✓	✓	✓	✓	✓
$J_{\mathrm{rr'}}$	✓	✓	✓	✓	✓	✓	✓	✓

Table 6.1.: Comparison of effects on J_{dr} (coupling between the direct (d) and the remote proton (r)), $J_{\mathrm{d,X}}$ (coupling between the direct proton (d) and the X nucleus), $J_{\mathrm{r,X}}$ (coupling between the remote proton (r) and the X nucleus), ν_{d} (chemical shift of the direct proton (d)), ν_{r} (chemical shift of the remote proton (r)), ν_{X} (chemical shift of the X nucleus (X)), $J_{\mathrm{dd'}}$ (geminal coupling between direct protons (d and d')), $J_{\mathrm{rr'}}$ (coupling between remote protons (r and r') during a time where no pulse, a 180° on protons, a 180° on ^{13}C, a 180° on both protons and carbons and the four different BIRD-filter. ✓ means that the corresponding parameter evolves, whereas × means that the corresponding property does not evolve. Adapted from [150].

(see Equation 6.5).

$$4\hat{I}^d_{1z}\hat{S}_{2x}\hat{S}_{3y} \xrightarrow{\pi J_{CH^r}1\hat{I}_z\hat{S}_z} \hat{I}^d_{1z}\hat{S}_{2x}\hat{S}_{3y}\cos(\pi J_{CH^r}\frac{t_1}{2}) + 8\hat{I}^d_{1z}\hat{I}^r_{4z}\hat{S}_{2x}\hat{S}_{3y}\sin(\pi J_{CH^r}\frac{t_1}{2}) \tag{6.5}$$

The goal of the BIRD$^{\mathrm{r}}$ filter is to achieve a refocusing of the coupling evolution of the remote proton as shown in Equation 6.5. The calculation is first done for the first term and then for the second term of Equation 6.5.

$$\begin{aligned}
4\hat{I}^d_{1z}\hat{S}_{2x}\hat{S}_{3y}\cos(\pi J_{CH^r}\frac{t_1}{2}) &\xrightarrow{\frac{\pi}{2}\hat{I}_x(^1H)} -4\hat{I}^d_{1z}\hat{S}_{2x}\hat{S}_{3y}\cos(\pi J_{CH^r}\frac{t_1}{2})\\
&\xrightarrow[\pi\hat{S}_x]{\pi\hat{I}_x(^1H)} -4\hat{I}^d_{1z}\hat{S}_{2x}\hat{S}_{3y}\cos(\pi J_{CH^r}\frac{t_1}{2})\\
&\xrightarrow{-\frac{\pi}{2}\hat{I}_x(^1H)} 4\hat{I}^d_{1z}\hat{S}_{2x}\hat{S}_{3y}\cos(\pi J_{CH^r}\frac{t_1}{2})\\
&\xrightarrow{\pi\hat{S}_x} -4\hat{I}^d_{1z}\hat{S}_{2x}\hat{S}_{3y}\cos(\pi J_{CH^r}\frac{t_1}{2})
\end{aligned} \tag{6.6}$$

In Equation 6.6, the effect of the pulses of the BIRD-filter on the operator $4\hat{I}^d_{1z}\hat{S}_{2x}\hat{S}_{3y}$ is calculated. Finally a change of the sign of $4\hat{I}^d_{1z}\hat{S}_{2x}\hat{S}_{3y}$ is achieved. In the next Equation, the same is done for the term $8\hat{I}^d_{1z}\hat{I}^r_{4z}\hat{S}_{2x}\hat{S}_{3y}$.

$$\begin{aligned}
&8\hat{I}^d_{1z}\hat{I}^r_{4z}\hat{S}_{2x}\hat{S}_{3y}\sin(\pi J_{CH^r}\frac{t_1}{2})\\
&\xrightarrow{\frac{\pi}{2}\hat{I}_x(^1H)} 8\hat{I}^d_{1z}\hat{I}^r_{4z}\hat{S}_{2x}\hat{S}_{3y}\sin(\pi J_{CH^r}\frac{t_1}{2})\\
&\xrightarrow{\frac{\pi}{2}-\hat{I}_x(^1H)} 8\hat{I}^d_{1z}\hat{I}^r_{4z}\hat{S}_{2x}\hat{S}_{3y}\sin(\pi J_{CH^r}\frac{t_1}{2})\\
&\xrightarrow{\pi\hat{I}_x(^{13}C)} 8\hat{I}^d_{1z}\hat{I}^r_{4z}\hat{S}_{2x}\hat{S}_{3y}\sin(\pi J_{CH^r}\frac{t_1}{2})
\end{aligned} \tag{6.7}$$

As can be seen, the BIRD$^{\mathrm{r}}$ sequence does not change the outcome of the operator $8\hat{I}^d_{1z}\hat{I}^r_{4z}\hat{S}_{2x}\hat{S}_{3y}$. Last, the evolution of the carbon coupling to the remote proton is evolving.

$$\begin{gathered}
-4\hat{I}^d_{1z}\hat{S}_{2x}\hat{S}_{3y}\cos(\pi J_{CH^r}\frac{t_1}{2}) + 8\hat{I}^d_{1z}\hat{I}^r_{4z}\hat{S}_{2x}\hat{S}_{3y}\sin(\pi J_{CH^r}\frac{t_1}{2}) \xrightarrow{\pi J_{CH^r}\hat{I}_z\hat{S}_z}\\
-4\hat{I}^d_{1z}\hat{S}_{2x}\hat{S}_{3y}\cos(\pi J_{CH^r}\frac{t_1}{2})\cos(\pi J_{CH^r}\frac{t_1}{2}) - 8\hat{I}^d_{1z}\hat{I}^r_{4z}\hat{S}_{2x}\hat{S}_{3y}\cos(\pi J_{CH^r}\frac{t_1}{2})\sin(\pi J_{CH^r}\frac{t_1}{2})\\
+8\hat{I}^d_{1z}\hat{I}^r_{4z}\hat{S}_{2x}\hat{S}_{3y}\sin(\pi J_{CH^r}\frac{t_1}{2})\cos(\pi J_{CH^r}\frac{t_1}{2}) - 4\hat{I}^d_{1z}\hat{S}_{2x}\hat{S}_{3y}\sin(\pi J_{CH^r}\frac{t_1}{2})\sin(\pi J_{CH^r}\frac{t_1}{2})\\
= -4\hat{I}^d_{1z}\hat{S}_{2x}\hat{S}_{3y}
\end{gathered} \tag{6.8}$$

As can be seen, the terms coming from $8\hat{I}^d_{1z}\hat{I}^r_{4z}\hat{S}_{2x}\hat{S}_{3y}$ cancel out. Whereas, by using the trigonometric function $\cos^2(A) + \sin^2(A) = 1$, the therm $\hat{I}^d_{1z}\hat{S}_{2x}\hat{S}_{3y}$ is refocused. This means that the BIRD$^{\mathrm{r}}$ filter should be in principle working for the ω_1-coupled-BIRD$^{\mathrm{r}}$ ADEQUATE from the theoretical point of view.

Starting from the operators present at the start of t_1 for the ω_1-coupled ADEQUATE and the ω_1-coupled-BIRD$^{\mathrm{r}}$ ADEQUATE, 1D simulations are performed for different spin systems. The spin system which is simulated, is shown next to the simulation. The results can be seen in Figure 6.5. The results for the sum of the couplings for the first spin system (6.5 (A)) are not the same for the ω_1-coupled ADEQUATE and the ω_1-coupled-BIRD$^{\mathrm{r}}$ ADEQUATE. As the coupling of the remote proton adds up to the sum of the direct coupled protons. For the case of a methylene group, only the case for isochronous protons is simulated. The result is shown in Figure 6.5D. The doublet for the ω_1-coupled-BIRD$^{\mathrm{r}}$ ADEQUATE is split by two times the ${}^1J_{\mathrm{CH}}$ and the ${}^2J_{\mathrm{CH}}$ coupling. Whereas, the signal is further split by the sum of the ${}^2J_{\mathrm{CH}}$ and ${}^3J_{\mathrm{CH}}$ coupling in the simulated spectrum for ω_1-coupled ADEQUATE experiment.

6.3. Results

As explained above, the application of RDCs requires the determination of both sign and magnitude of the ${}^2J_{\mathrm{CH}}$ coupling constants to quaternary carbons. The biggest difference to already existing pulse sequences is that double-quantum coherence on carbon is present during t_1. Contrary to the original ADEQUATE pulse sequence, the 180° pulse on protons during t_1 is removed so that the coupling of the protons to the carbons evolve. As a consequence, the sum of the coupling constant which evolves during t_1 and leads to the extraction of the ${}^2J_{\mathrm{CH}}$ coupling constant after subtraction of the corresponding ${}^1J_{\mathrm{CH}}$ coupling. As one can see in the equations in Section 6.2.1, the double quantum coherence evolves under the sum to all direct and remote protons. Since the ${}^1J_{\mathrm{CH}}$ coupling adds up to the ${}^2J_{\mathrm{CH}}$ coupling, the splitting is clearly visible in t_1. Moreover, the ${}^1J_{\mathrm{CH}}$ coupling is accessible via a CLIP-HSQC (see Section 2.7.1) spectrum, therefore the ${}^2J_{\mathrm{CH}}$ coupling can be deduced straightforwardly. Additionally, 180° pulses on carbon and proton are replaced by offset-compensated shaped pulses. The BUBI pulse train is used in the INEPT, meaning that a UR pulse is used on protons and a PP inversion pulse is used on carbon.[95] Further pulses used comprise BIBOP[89, 92] on carbons and BURBOP[74, 93, 94] on proton and carbon. The back transfer from proton to carbon coherence is achieved by a sensitivity enhanced transfer. To achieve sensitivity enhancement, x and y coherence on carbons has to be transferred to x and y to proton coherence. Therefore, both magnetization components must be preserved in the first back transfer step. Consequently, a Broadband Universal Broadband Universal (BUBU) pulse train is used. In the second transfer step again a BUBI pulse sandwich is used.[95] The introduction of offset-compensated pulses was required, as the offset of double quantum coherence is higher than in usual two-dimensional spectra and the difference in signal intensity is clearly visible. Especially for signals, with too signal-to-noise ratio could not be observed in the ^{1}H hard-pulse version (e. g., C20-H22 of strychnine).

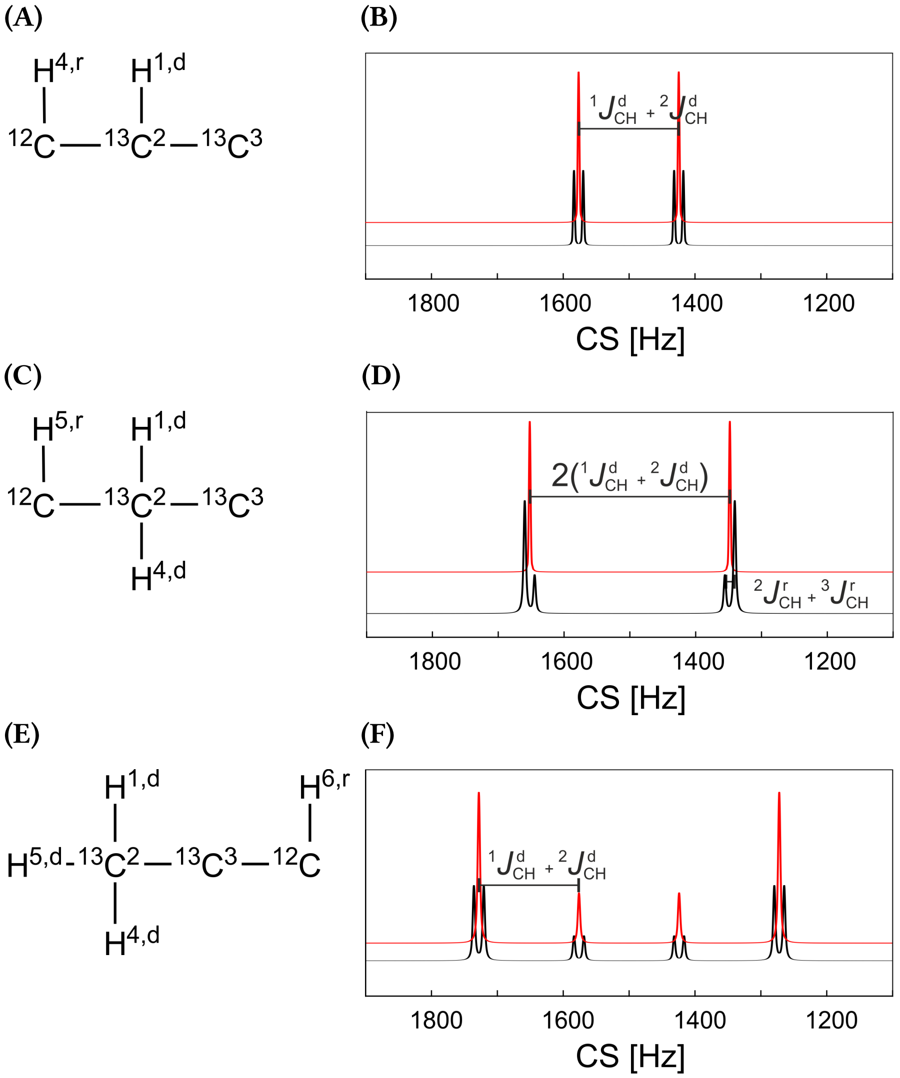

Figure 6.5.: Simulated multiplets for different spin systems, (A), (C) and (E). The simulated spectra in black show the multiplet for the corresponding spin system and for the couplings to direct and remote protons. The simulated spectra in red show the multiplicities for the corresponding spin systems if the remote proton is decoupled. The simulation show the predicted signal intensities from the calculations of the Equations 6.2, 6.3 and 6.4.

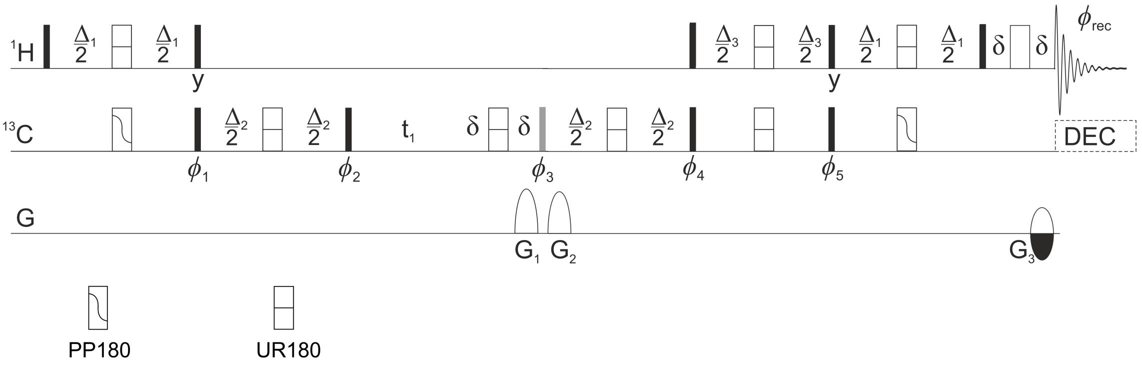

Figure 6.6.: ω_1-coupled ADEQUATE pulse sequence for the measurement of $^2J_{\mathrm{CH}}$ coupling constants. Narrow black bars stand for 90° pulses, wide bars stand for 180° pulses. The narrow gray bar stands for a 60° pulse. BIBOP and BURBOP pulses are used for proton and carbon 180° pulses as shown in the sequence. The delay Δ_1 is matched to $\frac{1}{2(^1J_{\mathrm{CH}})}$, Δ_2 is matched to $\frac{1}{2(^1J_{\mathrm{CC}})}$ and Δ_3 is matched to $\frac{1}{3(^1J_{\mathrm{CH}})}$. δ is a refocusing delay and matched to the gradient length. If not stated otherwise pulses are along x. Phase cyclings are $\phi_1 = x, -x$, $\phi_2 = (x)_4, (-x)_4$, $\phi_3 = (x)_8, (-x)_8$, $\phi_4 = (x)_2, (-x)_2$, $\phi_5 = (y)_2, (-y)_2$, $\phi_{rec} = x, -x, -x, x, -x, x, x, -x, -x, x, x, -x\ x, -x, -x, x$. Gradient strength are G_1: G_2: G_3 −78.5 %:−77.6 %:−59 %. Phase sensitive detection in the indirect dimension is achieved by Echo/antiEcho type selection.

6.3.1. ω_1-coupled ADEQUATE

The basic pulse sequence implemented for the measurement of both sign and magnitude of the $^2J_{\mathrm{CH}}$ coupling constant is shown in Figure 6.6. For validation of the right magnitude, molecules with an easily accessible $^2J_{\mathrm{CH}}$ constant are first measured. Fully ^{13}C-labeled acetate is used as a test sample. The resulting spectrum is shown in Figure 6.7A. The pulse sequence used to measure the spectrum is shown in Figure 6.6. During acquisition, no carbon decoupling is applied. Consequently, the signal is split in the direct dimension by the $^1J_{\mathrm{CH}}$ coupling. This does not affect the splitting in the indirect dimension.

To validate the extracted values from the ω_1-coupled ADEQUATE sequence, the magnitude of the $^1J_{\mathrm{CH}}$ coupling constant and the $^2J_{\mathrm{CH}}$ coupling constant for the acetate is determined by a fully coupled ^{13}C spectrum. In Figure 6.7 B, the signal for the quaternary carbon is shown, as it shows the splitting for the coupling constant to the protons of the methyl group. The $^1J_{\mathrm{CH}}$ coupling constant for acetate is 127.1 Hz and the $^2J_{\mathrm{CH}}$ coupling constant is 5.9 Hz.

The signal recorded with the ω_1-coupled ADEQUATE sequence for acetate shows a 3 : 1 : 1 : 3 signal intensity distribution. The multiplet structure is due to the methyl group and due to the anti-phase magnetization which is present at the beginning of t_1. In terms of product operators, this is $4\hat{I}_{1z}\hat{S}_{2x}\hat{S}_{3y}$. The complete calculation of the multiplet structure is shown in Section 6.2.1. It can be seen that the sum of the splitting is 121.2 Hz. The $^2J_{\mathrm{CH}}$ coupling is obtained by subtracting the always positive $^1J_{\mathrm{CH}}$ coupling from the sum of the splitting, as follows:

	ω_1-coupled ADEQUATE [Hz]	coupled 1D ^{13}C spectrum (no sign) [Hz]	Kalinowski (no sign)[143] [Hz]
$^2J_{\mathrm{CH}}$ ($\underline{\mathrm{C}}\mathrm{H_2C}\underline{\mathrm{H}}_3$)	-2.3 ± 0.6	2.4 ± 0.2	2.3
$^2J_{\mathrm{CH}}$ ($\mathrm{C}\underline{\mathrm{H}}_2\underline{\mathrm{C}}\mathrm{H_3}$)	-4.5 ± 0.7	4.7 ± 0.3	4.6

Table 6.2.: Extracted and literature values for the $^2J_{\mathrm{CH}}$ coupling constants for ethanol for different experiments. The first column are the values extracted from the ω_1-coupled ADEQUATE. The second column are the values extracted from a coupled 1D ^{13}C spectrum. In the third column, the literature values are summarized.[143] The magnitude of the couplings are for all three cases and for both $^2J_{\mathrm{CH}}$ couplings in the same range of magnitude, which shows that the coupling constants extracted from the ω_1-coupled ADEQUATE comply. The errors indicate the ±3 standard deviation ($\pm 3\sigma$) uncertainty.

$$\begin{gathered} {}^{1+2}J_{\mathrm{CH}} - {}^1J_{\mathrm{CH}} = {}^2J_{\mathrm{CH}} \\ 121.2\,\mathrm{Hz} - 127.1\,\mathrm{Hz} = -5.9\,\mathrm{Hz} \end{gathered} \tag{6.9}$$

For the methyl group of the acetate, the $^2J_{\mathrm{CH}}$ coupling constant determined with the ω_1-coupled ADEQUATE has a sign and magnitude of −5.9 Hz. As the acetate has only one proton species, this is an simple test example.

The same pulse sequence is applied to ethanol dissolved in D_2O. In this case, the resulting multiplets in the spectrum are more complicated and it is challenging to extract the $^2J_{\mathrm{CH}}$ coupling constants. The spectrum can be seen in Figure 6.8. The signal at 1.2 ppm is resulting from the methyl group, whereas the other signal is resulting from the methylene group of ethanol. For the extraction of the couplings, this would give:

$$\begin{gathered} {}^2J_{\mathrm{CH}}\ (\underline{\mathrm{C}}\mathrm{H_2C}\underline{\mathrm{H}}_3) = 136.8\,\mathrm{Hz} - 139.1\,\mathrm{Hz} = -2.3\,\mathrm{Hz} \\ {}^2J_{\mathrm{CH}}\ (\mathrm{C}\underline{\mathrm{H}}_2\underline{\mathrm{C}}\mathrm{H_3}) = 120.2\,\mathrm{Hz} - 124.7\,\mathrm{Hz} = -4.5\,\mathrm{Hz} \end{gathered} \tag{6.10}$$

As the signal at 1.2 ppm, which results from the methyl group, has a sum of the couplings of the methyl protons ($^1J_{\mathrm{CH}}$) and the methylene protons, the value for the $^2J_{\mathrm{CH}}$ coupling constant is the one for the methylene group. Therefore, the other sum results from the $^1J_{\mathrm{CH}}$ coupling constant from the methylene group and the $^2J_{\mathrm{CH}}$ coupling constant to the methyl group. The values calculated in Equation 6.10 are in good approximation of the values extracted from the fully coupled 1D ^{13}C spectrum and also with the values given in [143] as summarized in Table 6.2.

The interpretation of the ω_1-coupled ADEQUATE becomes difficult if more proton species are present in the molecule since the multiplicities of the signals are unusual and split by more than one coupling. This can be best seen in Figure 6.11A, where the signal of C6,C5-H5 of (+)-IPC is shown. The signal is split further and the signal looks tilted. Therefore, the sequence is improved further.

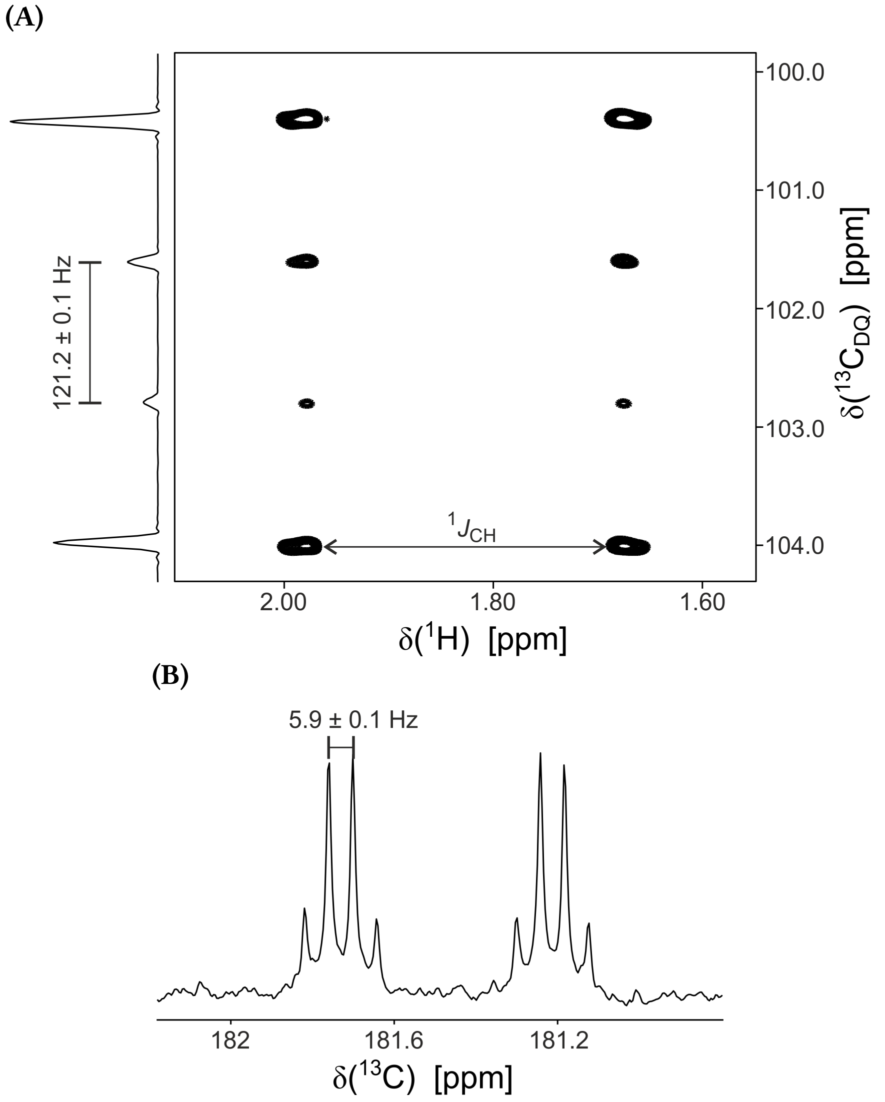

Figure 6.7.: (A) Spectrum of double labelled sodium acetate ($^{13}C_2$ NaOAc) recorded with the sequence shown in 6.6 without decoupling in the direct dimension. The spectrum shows the expected anti-phase quartet signal with the signal intensities of 3 : 1 : 1 : 3. (B) proton-coupled 1D ^{13}C spectrum of the quaternary carbon of sodium acetate. The splitting of the signal shows a coupling constant of 5.9 Hz for the $^2J_{CH}$ coupling constant from the methylgroup to the quaternary carbon. As is shown in (A), the splitting of the signal is 121.2 Hz together with the $^1J_{CH}$ coupling constant (127.1 Hz), the sign and the magnitude of the $^2J_{CH}$ coupling constant is available (−5.9 Hz).

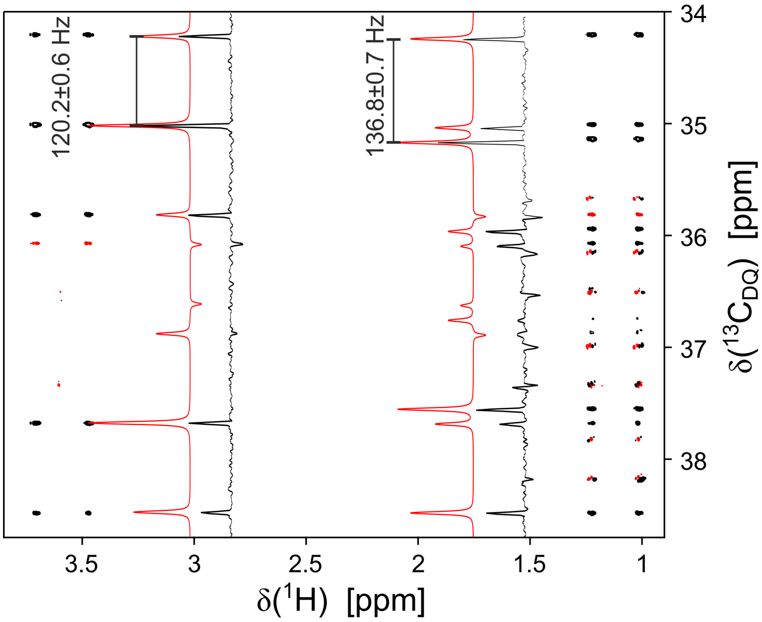

Figure 6.8.: Spectrum of single labeled ethanol (2-^{13}C EtOH) recorded with the sequence shown in 6.6 without decoupling during t_1 and t_2. The spectrum shows two complicated signals, one at 1.2 ppm for the methyl group and 3.59 ppm for the methylene group. In black an extracted row for each of the signals is shown, whereas the red line is the corresponding simulation. The sum of the $^{1}J_{\mathrm{CH}}$ and $^{2}J_{\mathrm{CH}}$ coupling is 136.8 Hz for the methyl group and 120.2 Hz for the methylene group.

6.3.2. ω_1-coupled BIRD^r ADEQUATE

As mentioned before, the right coupling determination might be challenging in the ω_1-coupled ADEQUATE. This is due to the coupling evolution of the remote protons to the carbons creating the double quantum coherence. Therefore, for real case scenarios, the sequence had to be changed further and the resulting pulse sequence is shown in Figure 6.9. By introducing a BIRD^r filter into the t_1 time, the remote protons experience a 180° pulse and the couplings to them are refocused. The theoretical part of the calculation is shown in Section 6.2.2.

The protons directly bound to the carbons, which create the double quantum frequency and the ^{13}C nuclei, feel both a 360° pulse. Accordingly, the coupling evolution and the double quantum chemical shift evolution is not affected by the BIRD-filter. As can be seen in the overview spectra for strychnine, (+)-IPC and (*S*)-ibuprofene (see Figures 6.12B, 6.13B and 6.14B), some of the signals experience a phase shift of 180°. This is due to the fact that the ^{13}C nuclei experience a 180° phase shift depending on how many protons are directly coupled to them and the BIRD^r filter acts as a multiplicity editing element. Therefore, an even number of protons coupled to the carbon does not change the phase of the carbon. Whereas, an uneven number of protons changes the phase of the carbon. In this case, the BIRD^r filter refocuses coupling evolution to double quantum coherence, consequently both carbons involved have to be considered for the outcome of the phase shift. For instance, a quaternary carbon has no protons meaning that it has an even number of protons. Next to it there is a carbon with one bound proton, which has an odd number of protons and it therefore experiences a phase shift of 180° pulse. All together both carbons involved in the double quantum coherence experience a phase shift around 180° and have therefore an opposite sign as the other signal resulting in a negative signal.

In Figure 6.11, all different kind of subspectra which can result from the different spin systems are shown. All signals are recorded using both the ω_1-coupled ADEQUATE and with the ω_1-coupled-BIRD^r ADEQUATE sequence. First, the signal of a methine group (C-H) next to a quaternary carbon are shown for C6,C5-H1 of (+)-IPC (6.11A and 6.11B). Second, a methylene (C-H_2) group next to a quaternary carbon where the protons are isochronous (see Figure 6.11C and 6.11D). The signal for the isochronous methylene group is the C7,C10-H10 of (*S*)-ibuprofene (for the structure, see Figure 6.10C). In Figure 6.11E and 6.11F, the multiplets for a methylene group where the protons are anisochronous are shown represented by the C11,C10-H10 cross peak of strychnine (see Figure 6.10A). Last, a methyl group next to quaternary carbon is shown in Figure 6.11G and 6.11H.This is the signal of the methyl group C6,C8-H8 of (+)-IPC. It can be seen that the signal for the methine proton next to a quaternary carbon is the simplest multiplet. It is split in a doublet in the indirect dimension. The extracted sum is (143.2 ± 3.5) Hz for the ω_1-coupled ADEQUATE and (138.8 ± 1.2) Hz for the ω_1-coupled-BIRD^r ADEQUATE. The signal shown for the ω_1-coupled ADEQUATE (Figure 6.11A) has lower signal-to-noise ratio than the signal for the ω_1-coupled-BIRD^r ADEQUATE (Figure 6.11B) and the signal seems to be split by further couplings. Therefore, the line width is reduced in the case of the ω_1-coupled-BIRD^r ADEQUATE. For the signals of the methylene group of (*S*)-ibuprofene (see Figure 6.11C and 6.11D), the multiplet has a signal intensity distribution of $1:0:1$. The signals have higher signal-to-noise ratios and reduced FWHM for the ω_1-coupled-

BIRD$^\mathrm{r}$ ADEQUATE than for the ω_1-coupled ADEQUATE. The signal in the middle is canceled, as both protons are isochronous and have the same coupling constants to the direct bound carbon and the quaternary carbon. The extracted sum is (241.3 ± 2.2) Hz for the ω_1-coupled ADEQUATE and (246.9 ± 1.0) Hz for the ω_1-coupled-BIRD$^\mathrm{r}$ ADEQUATE. The multiplet for the C11,C10-H10 cross peak of strychnine (shown in Figure 6.11E and 6.11F), is different from the multiplet in the case of the isochronous methylene group of (*S*)-ibuprofene, as the two protons are anisochronous and have different coupling sizes to the direct proton and the quaternary carbon. This is revealed by the small signals in the middle of the multiplet for the signal of the ω_1-coupled ADEQUATE. The extracted sum of this spectrum is (246.2 ± 0.5) Hz. If the signals in the middle do not cancel out, two different sums can be determined ((128.7 ± 1.3) Hz and (116.3 ± 1.6) Hz). The difficulty is here, to specifically assign the extracted sum to each proton. They are resulting from the incomplete cancellation of the signals in the middle of the anti-phase triplet. The sum of the couplings for the spectrum recorded with the ω_1-coupled-BIRD$^\mathrm{r}$ ADEQUATE sequence is (246.9 ± 1.0) Hz. The signal shows a signal intensity distribution of $1 : 0 : 1$ because the coupling to the remote protons is refocused. Therefore, the sum of the four coupling constants (two times $^1J_{\mathrm{CH}}$ and two times $^2J_{\mathrm{CH}}$) can be extracted. Consequently, from this spectrum only the sum of the $^2J_{\mathrm{CH}}$ coupling to both protons of the methylene group can be determined. The methyl group of (+)-IPC (C6,C8-H8) shows an anti-phase triplet with signal intensities of $3 : 1 : 1 : 3$. The signal recorded with the ω_1-coupled ADEQUATE, is further split into quartets which is the $^3J_{\mathrm{CH}}$ or the $^2J_{\mathrm{CH}}$ to the other methyl group (C9H$_3$). This coupling is refocused if the BIRD$^\mathrm{r}$ filter is applied. Therefore, the signal for the ω_1-coupled-BIRD$^\mathrm{r}$ ADEQUATE is sharper and higher in intensity. The extracted sum are (361.8 ± 1.1) Hz for the ω_1-coupled ADEQUATE and (361.6 ± 0.2) which have to be divided by three to give the single sum (120.6 ± 1.1) Hz and (120.5 ± 0.2) Hz.

All extracted values for the $^2J_{\mathrm{CH}}$ coupling constants to quaternary carbons are summarized for strychnine, (+)-IPC and (*S*)-ibuprofene in the Tables 6.3, 6.5 and 6.6. The corresponding spectra are shown in Figures 6.12, 6.13 and 6.14. Overall, the errors are smaller for the $^2J_{\mathrm{CH}}$ coupling constants extracted from the ω_1-coupled-BIRD$^\mathrm{r}$ ADEQUATE spectrum due to increased signal-to-noise ratio and simplified multiplet structures.

To evaluate, the experimental data for strychnine, literature values are compared to them. In Table 6.4, this is shown exemplary for one proton-carbon pair, namely C5-H4, and the corresponding $^2J_{\mathrm{CH}}$ coupling. For all experiments that show positive values for the $^2J_{\mathrm{CH}}$ coupling, no sign could be obtained by the method used. The values determined with the ω_1-coupled ADEQUATE and the ω_1-coupled-BIRD$^\mathrm{r}$ ADEQUATE are in the range of the coupling constants determined with the other methods. Clearly, the values of determined experimentally for the IPAP-selHSQMBC-COSY and IPAP-selHSQMBC-TOCSY vary severely for differently matched delays in the INEPT and back transfer step. Here, the ω_1-coupled ADEQUATE or ω_1-coupled-BIRD$^\mathrm{r}$ ADEQUATE determine the couplings more reliably.

For (+)-IPC, the ω_1-coupled-BIRD$^\mathrm{r}$ ADEQUATE spectra lead to $^2J_{\mathrm{CH}}$ coupling constants with smaller error. The values for the $^2J_{\mathrm{CH}}$ coupling constants of (+)-IPC to the quaternary carbons, are summarized in Table 6.5. The full spectra are shown in Figure 6.13. Additionally, (*S*)-ibuprofene is measured. The resulting spectra are shown in Figure 6.14A and 6.14B. The $^2J_{\mathrm{CH}}$ coupling constants for the quaternary carbon are summarized in Table

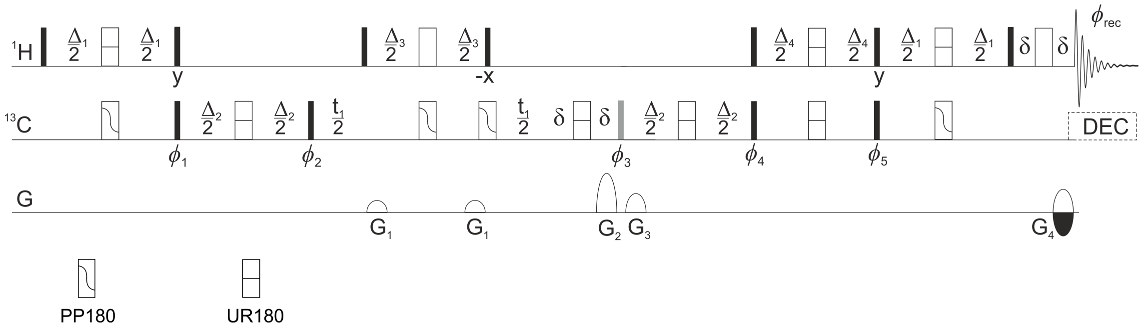

Figure 6.9.: ω_1-coupled-BIRD^r ADEQUATE pulse sequence for the measurement of $^2J_{CH}$ coupling constants. In contrast to the sequence shown in Figure 6.6, a BIRD^r filter is inserted in the middle of the t_1 time. Narrow black bars stand for 90° pulses, wide bars stand for 180° pulses. The narrow gray bar stands for a 60° pulse. BIBOP and BURBOP pulses are used for the 180° pulses on the proton and the carbon channel. The delay Δ_1 is matched to $\frac{1}{2(^1J_{CH})}$, Δ_2 is matched to $\frac{1}{2(^1J_{CC})}$ and Δ_3 is matched to $\frac{1}{1(^1J_{CH})}$ and Δ_4 is matched to $\frac{1}{3(^1J_{CH})}$. δ is a refocusing delay and matched to the gradient length. If not stated otherwise pulses are along x. Phase cyclings are $\phi_1 = x, -x$, $\phi_2 = (x)_4, (-x)_4$, $\phi_3 = (x)_8, (-x)_8$, $\phi_4 = (x)_2, (-x)_2$, $\phi_5 = (y)_2, (-y)_2$, $\phi_{rec} = x, -x, -x, x, -x, x, x, -x, -x, x, x, -x\, x, -x, -x, x$. Gradient strength are G_1: G_2: G_3: G_4 11 %:−78.5 %:−77.6 %:−59 %. Phase sensitive detection in the indirect dimension is achieved by Echo/antiEcho type selection.

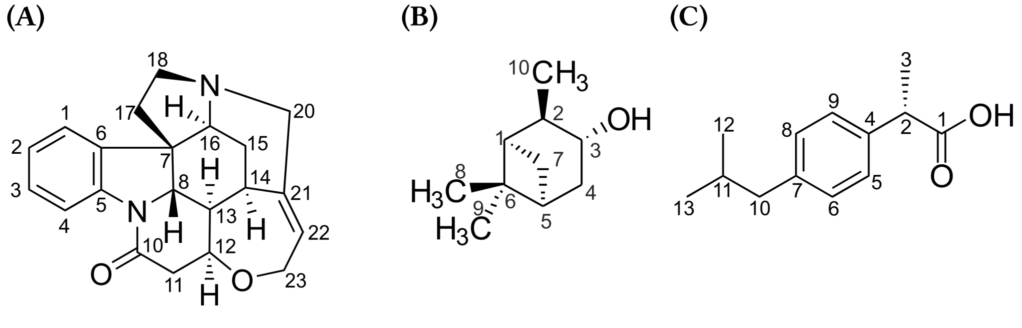

Figure 6.10.: (A) structure of strychnine with numbered atoms; (B) structure of (+)-IPC with numbered atoms; (C) structure of (*S*)-ibuprofene with numbered atoms.

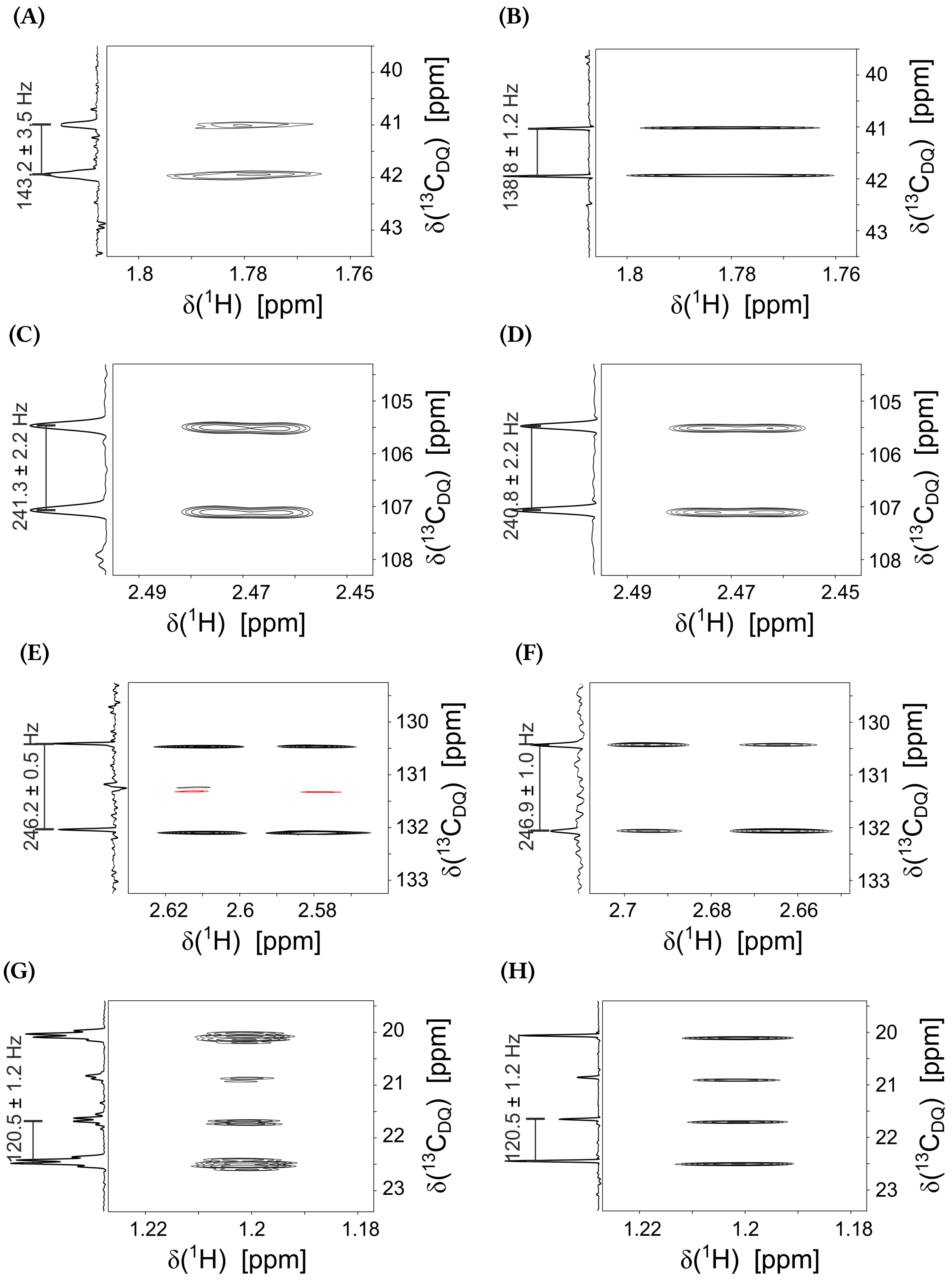

Figure 6.11.: Results for different spin systems with the ω_1-coupled ADEQUATE ((A), (C), (E) and (G)) shown in Figure 6.6 and ω_1-coupled-BIRD$^{\mathrm{r}}$ ADEQUATE ((B), (D), (D) and (H)) shown in Figure 6.9. (A) and (B) show the signal for C6,C5-H1 of (+)-IPC. (C) and (D) shows signal of C7,C10-H10 of (*S*)-ibuprofene. In Figure (E) and (F), the multiplets for C11,C10-H10 of strychnine are shown. (G) and (H) shows the signal for C6,C8-H8 of (+)-IPC. For the structures of the molecules with numbered atoms, see Figure 6.10.

Table 6.3.: $^{2}J_{\mathrm{CH}}$ coupling constants for the quaternary carbons of strychnine extracted from the two spectra shown in Figure 6.12. The errors indicate the ±3 standard deviation ($\pm 3\sigma$) uncertainty.

	ω_1-coupled ADEQUATE $^{2}J_{\mathrm{CH}}$ [Hz]	ω_1-coupled-BIRD$^{\mathrm{r}}$ ADEQUATE $^{2}J_{\mathrm{CH}}$ [Hz]
C5-H4	-3.1 ± 4.6	-2.2 ± 0.5
C6-H1	2.6 ± 4.0	1.5 ± 1.1
C21-H22	0 ± 3	-2.4 ± 0.3
C7-H16	1.3 ± 4.7	-1.3 ± 0.6
C7-H8	-1.4 ± 3.5	-2.4 ± 1.5
C21-H20	-7.2 ± 4.3	-6.5 ± 1.1
C21-H14	-5.1 ± 3.2	-5.8 ± 0.3
C10-H11	-14.3 ± 0.8	-14.4 ± 1.1
C21-H20	-5.4 ± 2.5	-7.1 ± 0.7
C10-H11	-14.6 ± 0.5	-14.1 ± 0.7
C7-H17	-7.0 ± 1.1	-5.8 ± 0.6

Table 6.4.: Comparison of experimental values and literature values for a single $^{2}J_{\mathrm{CH}}$ coupling of strychnine for carbon C5 to proton H4. For the atom numbers and structure of strychnine, see Figure 6.10A. For values where no citation is given, the values are determined experimentally. When no sign is shown for the $^{2}J_{\mathrm{CH}}$ coupling constant, the sign cannot be determined with this particular method. The errors indicate the ±3 standard deviation ($\pm 3\sigma$) uncertainty.

Experiment	$^{2}J_{\mathrm{CH}}$ [Hz]
ω_1-coupled ADEQUATE	-3.1 ± 4.8
ω_1-coupled-BIRD$^{\mathrm{r}}$ ADEQUATE	-2.2 ± 0.5
selHSQMBC ($^{n}J_{\mathrm{CH}}$ =8Hz)	4.0 ± 0.8
IPAP-selHSQMBC-COSY ($^{n}J_{\mathrm{CH}}$ =8Hz)	-5.5 ± 0.5
IPAP-selHSQMBC-TOCSY ($^{n}J_{\mathrm{CH}}$ =8Hz)	-4.7 ± 2.7
IPAP-selHSQMBC-TOCSY ($^{n}J_{\mathrm{CH}}$ =6Hz)	-3.1 ± 1.0
IPAP-selHSQMBC-TOCSY ($^{n}J_{\mathrm{CH}}$ =4Hz)	-2.7 ± 0.5
IPAP-selHSQMBC-TOCSY ($^{n}J_{\mathrm{CH}}$ =2Hz)	-1.8 ± 0.5
B3LYP/6-311+G(d,p)//B3LYP/6-31G(d)[151]	-2.04
HMBC [152]	0.9
Coupled 1D ^{13}C [153]	2.2 ± 1.1
IPAP-accordion-HSQMBC [153]	2.2
IPAP-HSQMBC-COSY ($^{n}J_{\mathrm{CH}}$ =6Hz) [153]	2.3
IPAP-HMBC ($^{n}J_{\mathrm{CH}}$ =6Hz) [153]	2.9
EXSIDE ($^{n}J_{\mathrm{CH}}$ =6Hz) [153]	2.2
J-HMBC ($^{n}J_{\mathrm{CH}}$ =1Hz) [153]	2
SelEXSIDE [154]	1.5

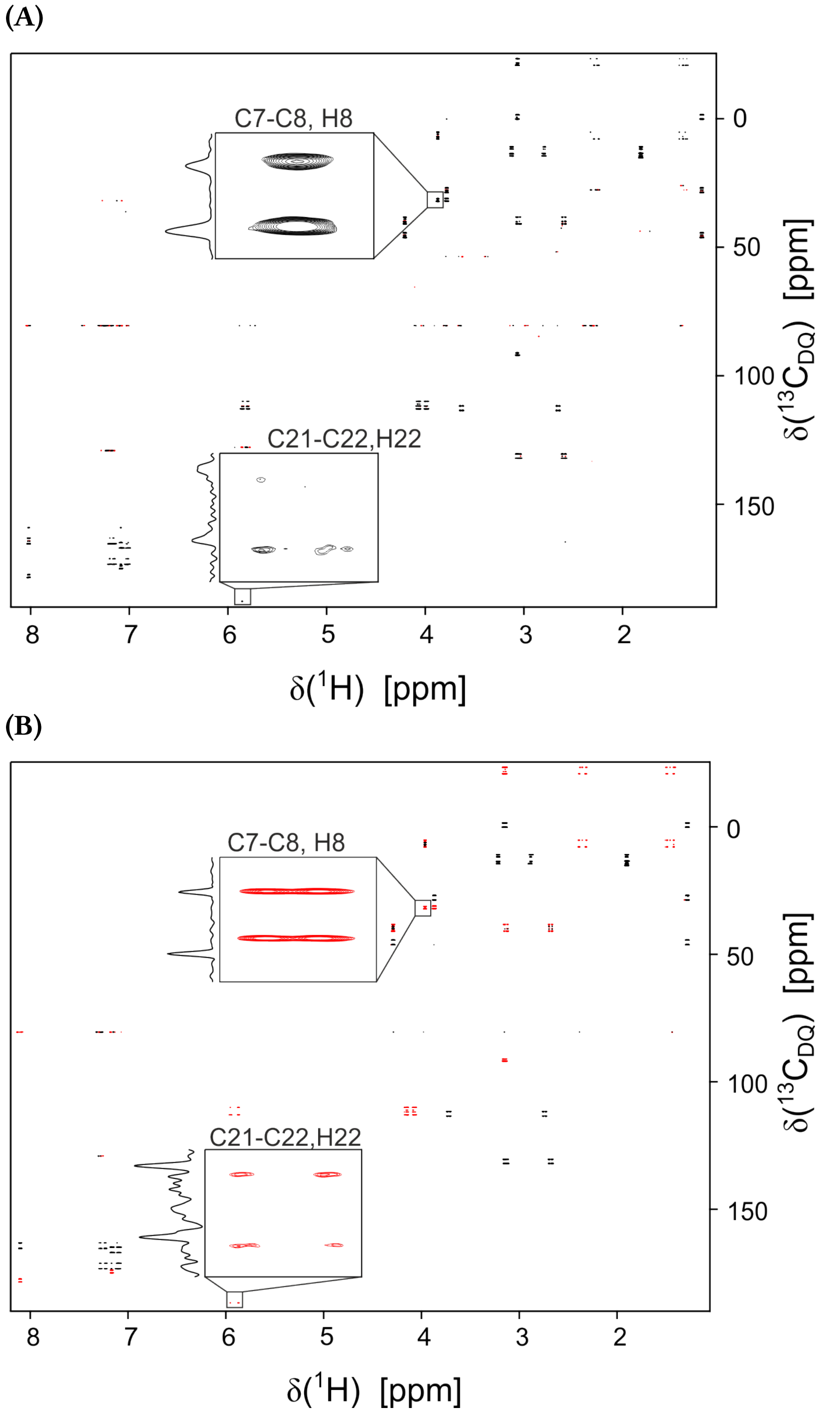

Figure 6.12.: Spectra of strychnine recorded (A) with the ω_1-coupled ADEQUATE sequence shown in Figure 6.3 and (B) recored with the ω_1-coupled-BIRD$^{\mathrm{r}}$ ADEQUATE sequence, shown in Figure 6.9. The sample preparation, the acquisition parameters and the processing parameters are summarized in 6.8.3.

6.6. The determined $^2J_{\mathrm{CH}}$ coupling for C4-H5,H9 differ largely for both experiments. This is due to difficulties in the signal-to-noise ratios and coupling evolution during in the ω_1-coupled ADEQUATE spectra. As in the other cases, the $^2J_{\mathrm{CH}}$ coupling extracted from the ω_1-coupled-BIRD$^{\mathrm{r}}$ ADEQUATE sequence is more reliably.

Table 6.5.: Extracted values for the $^2J_{\mathrm{CH}}$ coupling constants of (+)-IPC recorded with the ω_1-coupled ADEQUATE and the ω_1-coupled-BIRD$^{\mathrm{r}}$ ADEQUATE. The errors indicate the ±3 standard deviation (±3σ) uncertainty.

	ω_1-coupled ADEQUATE $^2J_{\mathrm{CH}}$ [Hz]	ω_1-coupled-BIRD$^{\mathrm{r}}$ ADEQUATE $^2J_{\mathrm{CH}}$ [Hz]
C6-H8	3.0 ± 3.1	−2.4 ± 0.6
C6-H9	−1.7 ± 1.3	−3.0 ± 0.4
C6-H1	−3.8 ± 1.1	−3.9 ± 0.2
C6-H5	−3.9 ± 0.6	−4.4 ± 0.3

Table 6.6.: Extracted values for the $^2J_{\mathrm{CH}}$ of (*S*)-ibuprofene recorded with the ω_1-coupled ADEQUATE and the ω_1-coupled-BIRD$^{\mathrm{r}}$ ADEQUATE. The errors indicate the ±3 standard deviation (±3σ) uncertainty.

	ω_1-coupled ADEQUATE $^2J_{\mathrm{CH}}$ [Hz]	ω_1-coupled-BIRD$^{\mathrm{r}}$ ADEQUATE $^2J_{\mathrm{CH}}$ [Hz]
C4-H9,H5	12.6 ± 1.3	1 ± 2
C7-H6,H8	8.7 ± 1.1	−0.8 ± 2.9
C11-H2	−7.9 ± 2.2	−9.5 ± 1.6
C4-H2	−4.2 ± 0.9	−7.5 ± 4.0
C7-H10	−4.2 ± 1.2	−5.3 ± 1.8

6.4. Measurement of 8-5(c)-DFA

To prove the applicability of the ω_1-coupled-BIRD$^{\mathrm{r}}$ ADEQUATE sequence to real-case scenario molecule, it is applied to 8-5(c)-DFA (see Figure 6.15 for the structure). The concentration of the sample is 61.3 $\mathrm{mmol\,l^{-1}}$ 8-5(c)-DFA in DMF-d_7 in a 3 mm NMR tube. The spectrum is acquired in 54 h 18 min on a 600 MHz spectrometer with a cryogenically cooled TXI probehead. The resulting spectrum is shown in Figure 6.16. All signals expected in the spectrum are present and the sum of the couplings is extractable for every sum. The calculated values for all possible $^2J_{\mathrm{CH}}$ couplings are summarized in Table 6.7, which also include $^2J_{\mathrm{CH}}$ couplings to non-quaternary carbons.

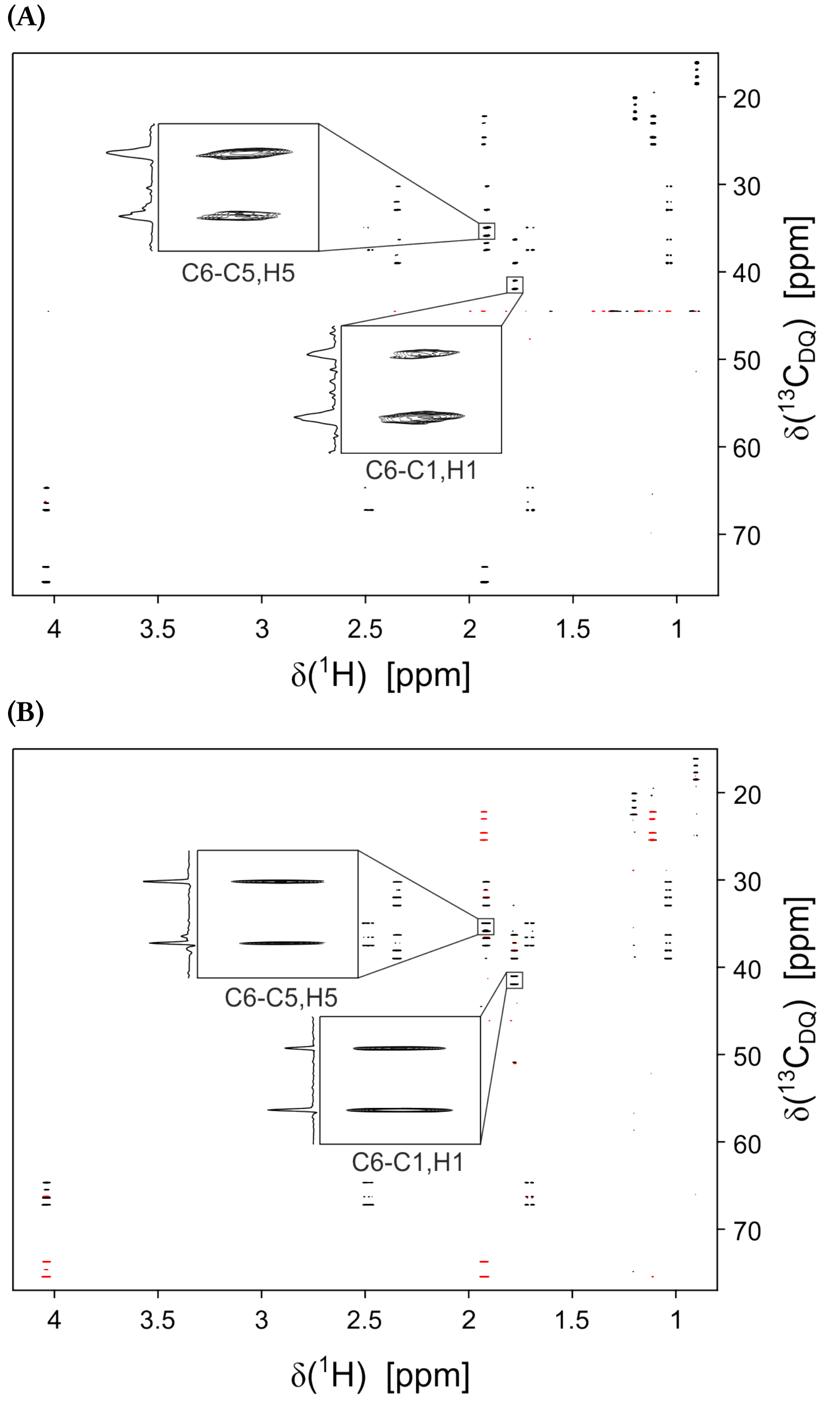

Figure 6.13.: Spectra of (+)-IPC recorded (A) recorded with the sequence ω_1-coupled ADEQUATE sequence shown in Figure 6.3 and (B) recorded with the ω_1-coupled-BIRD^r ADEQUATE sequence, shown in Figure 6.9. The experimental details for the sample, the acquisition of the data and the processing are summarized in Section 6.8.4.

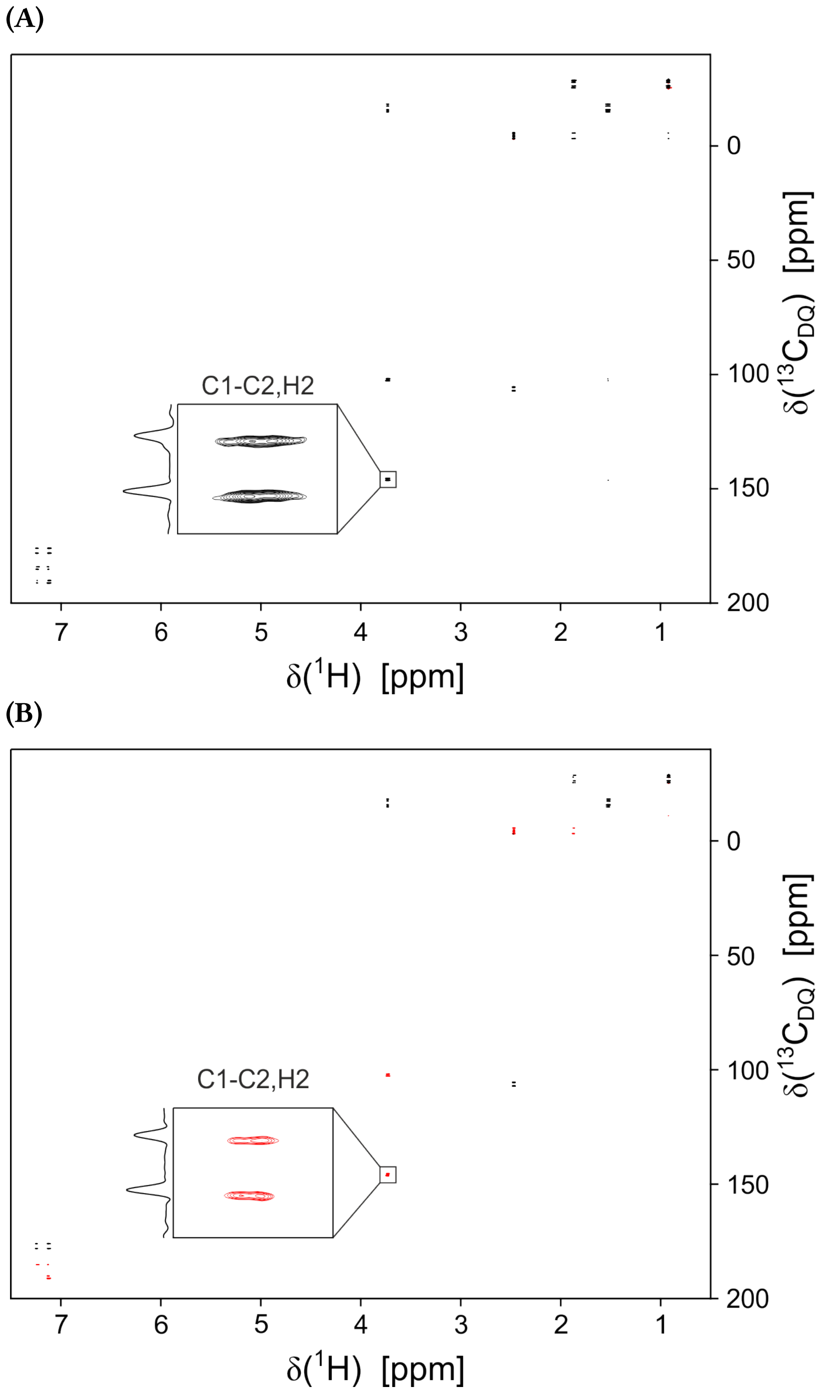

Figure 6.14.: Spectra of (*S*)-ibuprofene recorded (A) with the ω_1-coupled ADEQUATE sequence shown in Figure 6.3 and (B) recorded with ω_1-coupled-BIRD^r ADEQUATE sequence, shown in Figure 6.9. Sample preparation, acquisition and processing parameters are shown in 6.8.5.

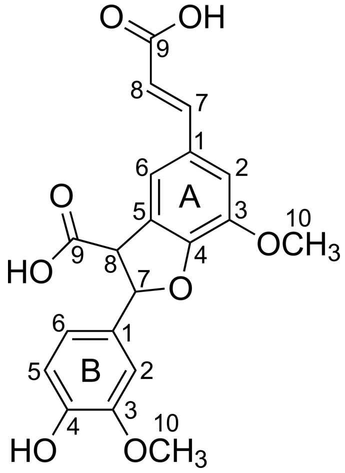

Figure 6.15.: Structure of 8-5(c)-DFA with numbered atoms.

Table 6.7.: The $^2J_{CH}$ coupling constants determined with the ω_1-coupled-BIRD^r ADEQUATE sequence for 8-5(c)-DFA. The errors indicate the ±3 standard deviation (±3σ) uncertainty.

Assignment	$^2J_{CH}$ [Hz]
A-H7,A-C1	3.3 ± 2.0
A-H7,A-C8	-4.0 ± 1.6
A-H2,A-C3	-3.6 ± 1.8
A-H2,A-C1	-0.6 ± 2.1
A-H6,A-C1	0.7 ± 2.4
A-H6,A-C5	-0.7 ± 0.6
B-H2,B-C3	-3.0 ± 1.3
B-H2,B-C1	-2.8 ± 1.2
B-H6,B-C1	-2.7 ± 2.6
B-H6,B-C5	0.2 ± 1.6
B-H5,B-C4	-4.1 ± 2.5
B-H5,B-C6	-0.7 ± 2.6
A-H8,A-C9	1.3 ± 2.3
A-H8,A-C7	-2.4 ± 1.7
B-H7,B-C1	-1.8 ± 1.8
B-H7,B-C8	-4.7 ± 1.4
B-H8,B-C9	-6 ± 2
B-H8,A-C5	-6.0 ± 1.7
B-H8,B-C7	-7.0 ± 2.7

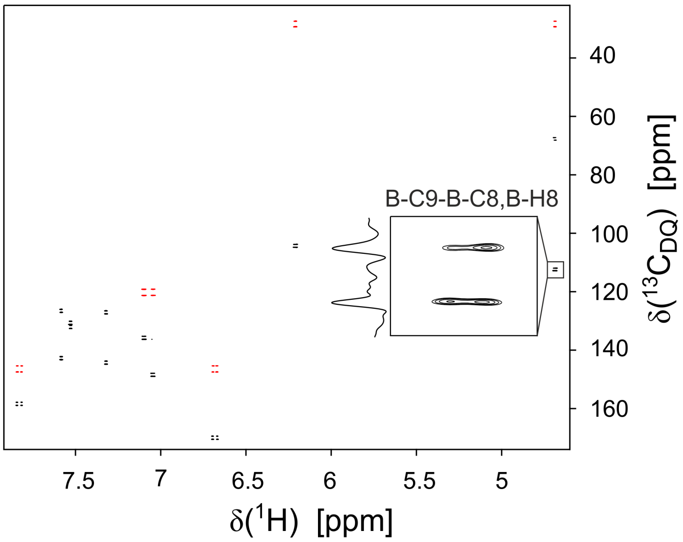

Figure 6.16.: ω_1-coupled-BIRD^r ADEQUATE of 8-5(c)-DFA.

6.5. Measurement of $^2T_{CH}$

The determination of sign and magnitude of two-bond coupling constants become crucial in case of partially ordered samples. The two sequences developed are both applied to (+)-IPC and (*S*)-ibuprofene oriented in a liquid crystalline phase composed of PBLG and $CDCl_3$ or CD_2Cl_2.

As the effect of the BIRD^r filter is under investigation in case of anisotropic samples, both the ω_1-coupled ADEQUATE and ω_1-coupled-BIRD^r ADEQUATE are recorded for the two samples and the corresponding T couplings are extracted. The $^1T_{CH}$ splittings are measured with the CLIP-HSQC spectra and the calculation of the $^2T_{CH}$ splittings is done as follows:

$$^2T_{CH} =^{1+2} T_{CH} -^1 T_{CH} \tag{6.11}$$

The calculation of the $^2D_{CH}$ splittings is then straight forward:

$$^2D_{CH} =^2 T_{CH} -^2 J_{CH} \tag{6.12}$$

The $^2J_{CH}$ coupling constants are taken from the isotropic ω_1-coupled-BIRD^r ADEQUATE spectra.

6.5.1. (+)-IPC

The spectra shown in Figure 6.17 show all expected signals. In contrast to the isotropic spectra, the coupling constants for the ω_1-coupled ADEQUATE and the ω_1-coupled-BIRD^r ADEQUATE do not differ. In Table 6.8, the values for the quaternary carbons for both sequences are summarized. As can be seen, the errors are in the range of the coupling sizes. This is due to broad lines in the aligned spectrum. Additionally, the signal intensity does not increase by using the ω_1-coupled-BIRD$^{\mathrm{r}}$ ADEQUATE. This might be due to the additional delays and faster relaxation in aligned samples.

As shown in Figure 6.18, the $^2D_{\mathrm{CH}}$ splittings decrease if the amount of PBLG is decreased. In this case, the coupling constants recorded with the ω_1-coupled ADEQUATE seems to be more accurate. For the $^2T_{\mathrm{CH}}$ of C6-H8, C6-H9 and the C6-H1, a linear trend can be seen. C6-H5 does not follow the trend. This might be due to the overlap of the signal with the signal C4-C5-H5 as it impedes the correct coupling extraction.

Table 6.8.: Comparison of the $^2T_{\mathrm{CH}}$ and $^2D_{\mathrm{CH}}$ couplings extracted from both ω_1-coupled ADEQUATE and ω_1-coupled-BIRD$^{\mathrm{r}}$ ADEQUATE for anisotropic (+)-IPC sample spectra. The sample contained 8.6 %(w/w) of PBLG in CD_2Cl_2 and a $\Delta\nu_Q$ of (107.6 ± 0.1) Hz. The errors indicate the ±3 standard deviation (±3σ) uncertainty.

	ω_1-coupled ADEQUATE		ω_1-coupled-BIRD$^{\mathrm{r}}$ ADEQUATE	
	$^2T_{\mathrm{CH}}$ [Hz]	$^2D_{\mathrm{CH}}$ [Hz]	$^2T_{\mathrm{CH}}$ [Hz]	$^2D_{\mathrm{CH}}$ [Hz]
C6-H8	−1.7 ± 3.5	2.9 ± 3.5	−1.6 ± 3.6	3.0 ± 3.6
C6-H9	−5.9 ± 0.3	−1.9 ± 2.6	−6.3 ± 1.2	−2.3 ± 2.6
C6-H1	1.4 ± 3.4	3.5 ± 3.6	0.6 ± 2.0	2.7 ± 3.6
C6-H5	1.6 ± 5.4	4.4 ± 5.4	−1.9 ± 6.2	0.9 ± 6.2

6.5.2. (*S*)-Ibuprofene

In Figure 6.19, both spectra for (*S*)-ibuprofene for the ω_1-coupled ADEQUATE- and the ω_1-coupled-BIRD$^{\mathrm{r}}$ ADEQUATE-sequence are shown. The $\Delta\nu_Q$ of the aligned sample is 220 Hz. The extracted values for the $^2T_{\mathrm{CH}}$ splittings for both spectra are summarized for the quaternary carbons and their coupled protons in Table 6.9. The splittings extracted from both ω_1-coupled ADEQUATE and ω_1-coupled-BIRD$^{\mathrm{r}}$ ADEQUATE are in the same range of magnitude. It is difficult to decide which pulse sequence leads to better results comparing both the results of the anisotropic values for (+)-IPC and (*S*)-ibuprofene. In Figure 6.20, the $^2T_{\mathrm{CH}}$ splittings for all quaternary carbons determined with the ω_1-coupled ADEQUATE, the ω_1-coupled-BIRD$^{\mathrm{r}}$ ADEQUATE and the selective IPAP-HSQMBC are plotted. For better comparison, the sign of the $^2T_{\mathrm{CH}}$ splittings are assumed for the selective IPAP-HSQMBC.

6.6. Discussion

The ω_1-coupled ADEQUATE sequence allows the extraction of sign and magnitude of $^2J_{\mathrm{CH}}$ coupling constants in the case of a very small molecule, as ethanol and acetate. The values are as reported by other experiments and by literature values. In the case of acetate, the determination of the $^2J_{\mathrm{CH}}$ coupling constant is straight forward. Since, there is no other proton species in the molecule which can impede the coupling extraction. The values for the $^2J_{\mathrm{CH}}$ coupling constant extracted from the 1D ^{13}C spectrum are in good agreement with the values extracted from the ω_1-coupled ADEQUATE spectrum.

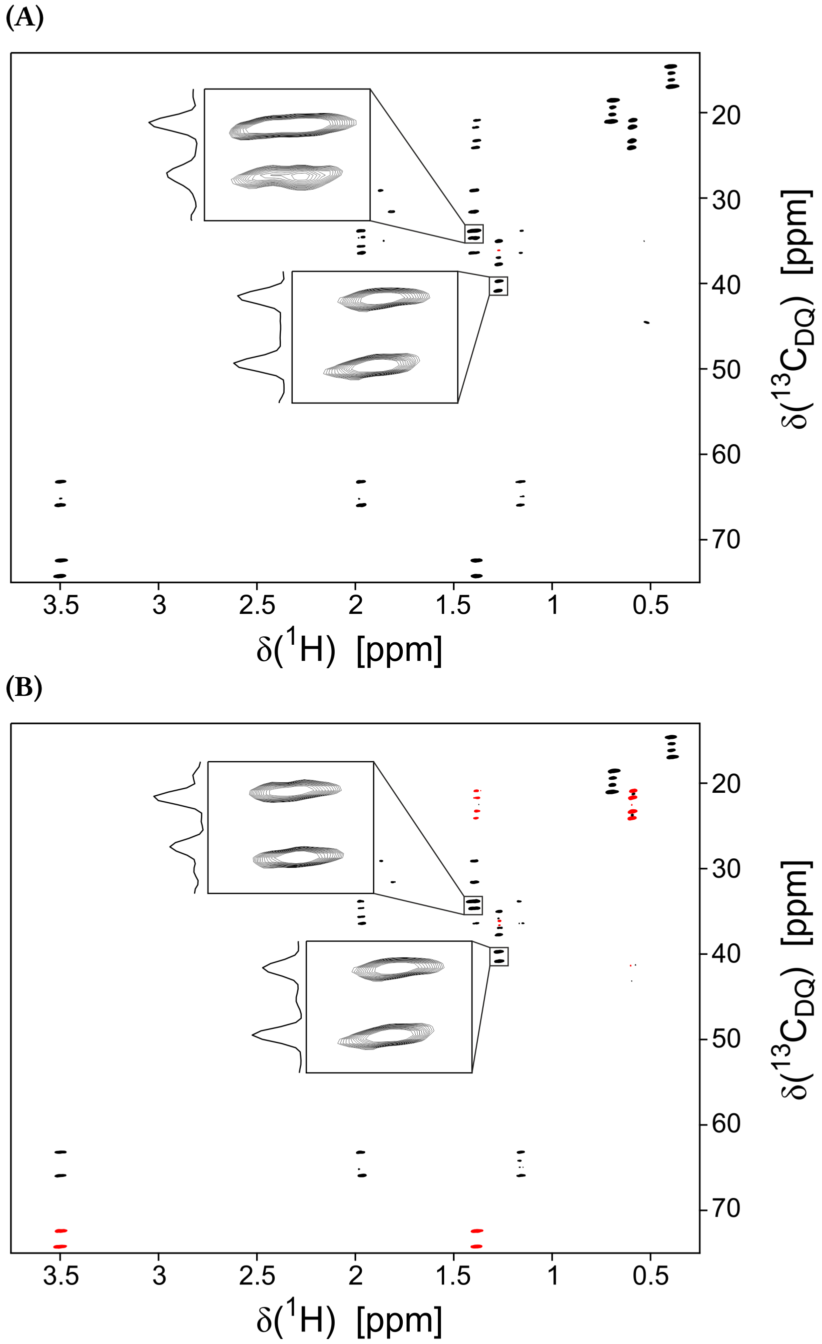

Figure 6.17.: Spectra of (+)-IPC recorded with the ω_1-coupled ADEQUATE and ω_1-coupled-BIRD^r ADEQUATE experiment measured in 8.6 %(w/w) PBLG and CD_2Cl_2. (A) is recorded with the sequence shown in Figure 6.3. (B) is recorded with the pulse sequence shown in Figure 6.9. $\Delta\nu_Q$ is (107.6 ± 0.1) Hz. The experimental and processing parameters are summarized in Section 6.8.4.

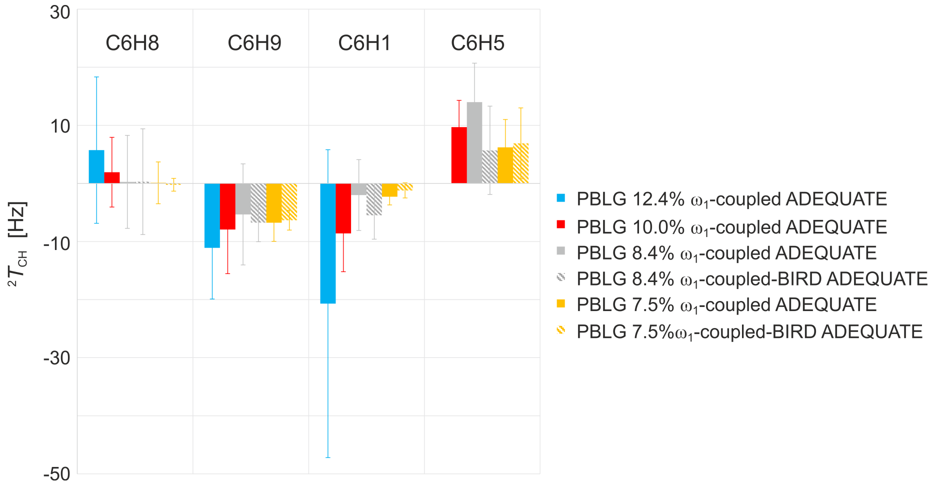

Figure 6.18.: The figure shows the $^2T_{CH}$ splittings for the quaternary carbons of (+)-IPC. The spectra are recorded for 12.4 %(w/w), 10.0 %(w/w), 8.4 %(w/w) and 7.5 %(w/w) of PBLG in $CDCl_3$. In the case of 12.4 %(w/w) and 10.0 %(w/w) PBLG, no ω_1-coupled-BIRD^r ADEQUATE is recorded. For the C6-H8, C6-H9 and the C6-H1, a linear trend for the $^2T_{CH}$ can be seen. C6,C5-H5 does not follow the trend. This might be due to the overlap of the signal with another signal as it impedes the correct coupling extraction.

Table 6.9.: Comparison of the $^2T_{CH}$ and $^2D_{CH}$ extracted from the ω_1-coupled ADEQUATE and from the ω_1-coupled-BIRD^r ADEQUATE for (*S*)-ibuprofene in 6.4 %(w/w) of PBLG in $CDCl_3$ and a $\Delta\nu_Q$ of 220 Hz. The errors indicate the ±3 standard deviation (±3σ) uncertainty.

	ω_1-coupled ADEQUATE		ω_1-coupled-BIRD^r ADEQUATE	
	$^2T_{CH}$ [Hz]	$^2D_{CH}$ [Hz]	$^2T_{CH}$ [Hz]	$^2D_{CH}$ [Hz]
C7-H10	-6.1 ± 1.1	-0.9 ± 1.1	-6.4 ± 3.9	-1.2 ± 3.9
C1-H2	-11.1 ± 3.3	-5.2 ± 3.3	-13.6 ± 2.4	-7.7 ± 2.4
C4-H2	-4.8 ± 4.1	0.0 ± 4.1	-6.9 ± 3.0	-2.1 ± 3.0
C7-H6,H8	-5.9 ± 2.7	-6.2 ± 2.7	-6.2 ± 3.0	-6.5 ± 3.0
C4-H5,H9	-5.8 ± 1.8	-6.7 ± 2.7	-5.7 ± 2.8	-6.6 ± 2.8

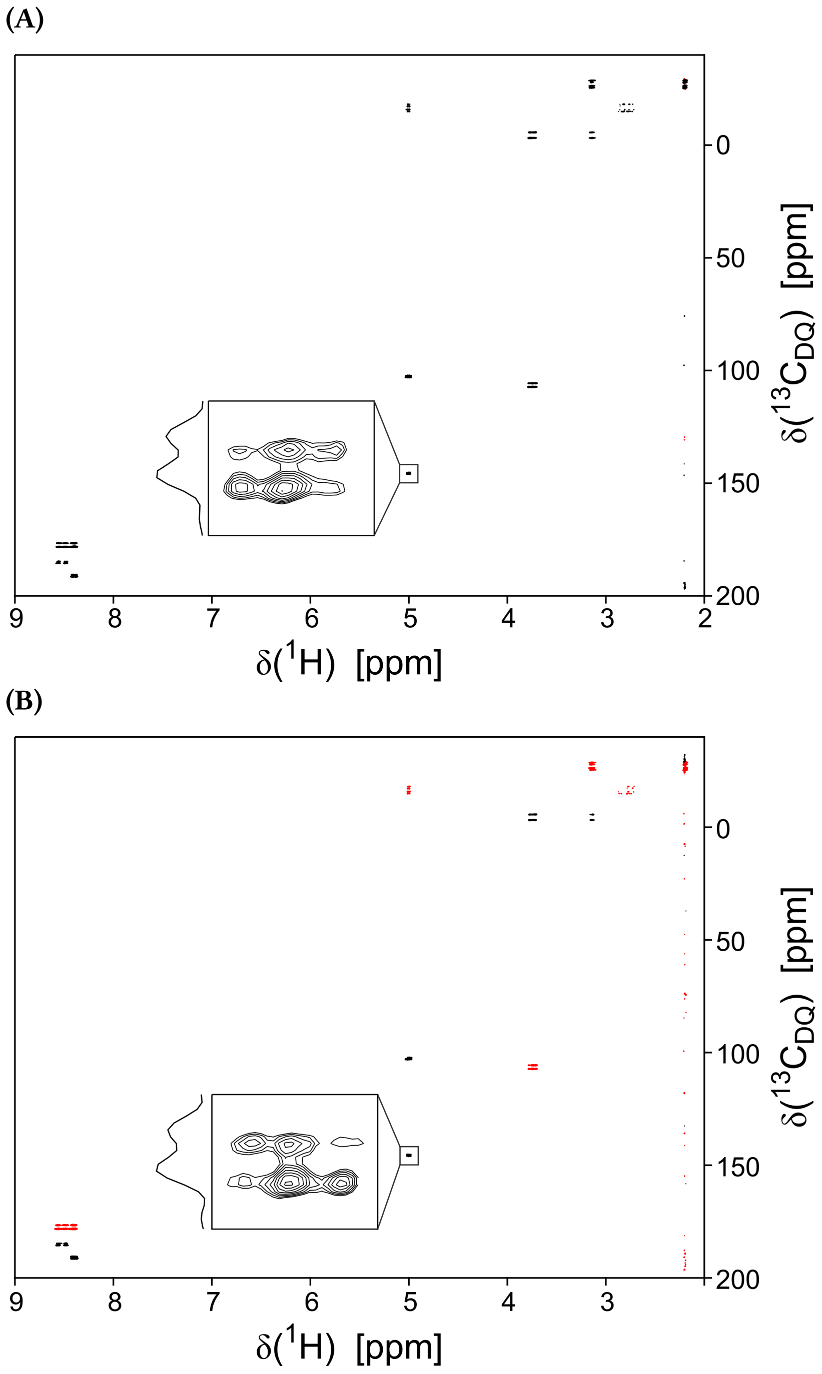

Figure 6.19.: The figure shows the ω_1-coupled ADEQUATE and ω_1-coupled-BIRD^r ADEQUATE spectra of (*S*)-ibuprofene in 6.4 %(w/w) of PBLG and a $\Delta\nu_Q$ of 220 Hz. (A) is recorded with the ω_1-coupled ADEQUATE sequence shown in Figure 6.3. (B) is recorded with the ω_1-coupled-BIRD^r ADEQUATE sequence shown in Figure 6.9. The experimental and processing parameters are summarized in Section 6.8.5.

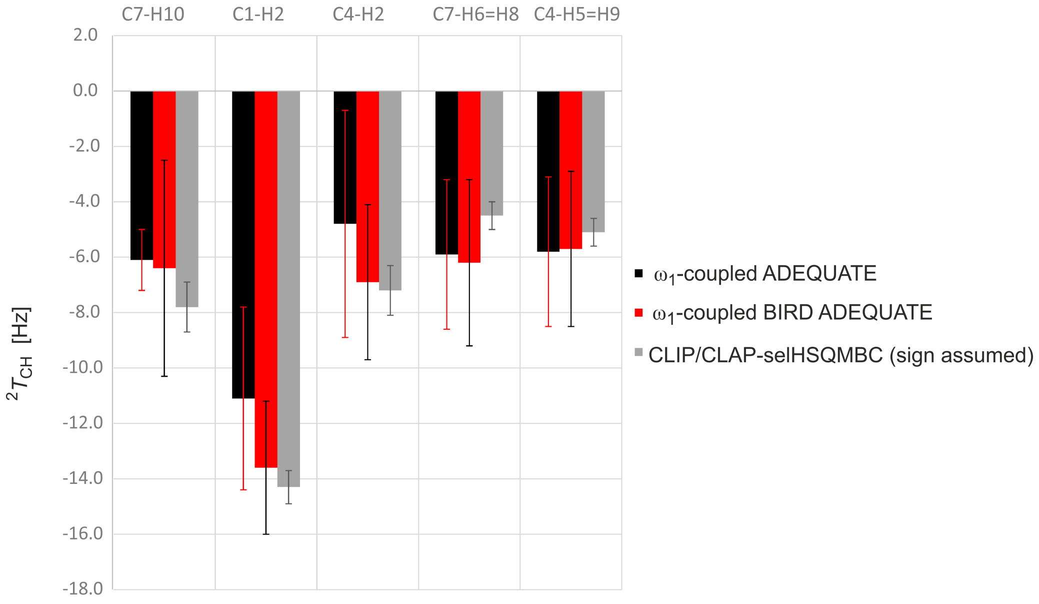

Figure 6.20.: Comparison of the $^2T_{CH}$ splittings measured with the ω_1-coupled ADEQUATE, ω_1-coupled-BIRD^r ADEQUATE and *selective* IPAP-HSQMBC for (*S*)-ibuprofene. The values of the splittings do not differ from experiment to experiment and lay in the same order of magnitude for all experiments.

For ethanol, the literature values for the $^2J_{CH}$ coupling constants had the same magnitude as the coupling constants determined in the coupled 1D ^{13}C spectrum and in the ω_1-coupled ADEQUATE spectrum. Although the multiplets are complicated in ethanol, the coupling constant could still be determined. The multiplets are simulated with Matlab and the extracted coupling constants. The simulations showed the same multiplet structure as the multiplet in the indirect dimension of the ω_1-coupled ADEQUATE. The multiplet structure is different for the methyl group and the methylene group as the starting magnetization at the beginning of t_1 is different for each proton species. Therefore, the multiplet evolves differently for the methyl group and the methylene group even though in both cases five protons are coupled to the carbons evolving the double quantum frequency.

For more complicated and bigger molecules where not only one or two proton species are present, the ω_1-coupled ADEQUATE spectrum shows a tilted pattern. This means that the signals are distorted along the t_1 dimension. These are resulting from the coupling evolution of the carbons to all other coupled protons in the spin system, due to homonuclear proton-proton coupling evolution and strong coupling artifacts, since no coupling evolution is refocused during t_1. Therefore, the extraction of the $^2J_{CH}$ couplings might be inaccurate. For these cases, the ADEQUATE with the BIRD^r filter during t_1 is important. It could be shown that the $^2J_{CH}$ coupling constant determination is more accurate for this sequence. For the isotropic case, it is clear that the spectra recorded with the ω_1-coupled-BIRD^r ADEQUATE is favorable over the ω_1-coupled ADEQUATE, as the values for the $^2J_{CH}$ couplings change significantly for the ω_1-coupled-BIRD^r ADEQUATE compared to the ones extracted from the ω_1-coupled ADEQUATE. This can be explained by the theoretical derivation. During the evolution time in the indirect dimension not only the coupling to the direct bound protons evolves but also to the remote bound protons, the resulting values are therefore affected by these further couplings. The $^2J_{\mathrm{CH}}$ coupling constants are determined for three molecules (strychnine, (+)-IPC and (*S*)-ibuprofene), which are all accessible in relatively high concentrations (120 mmol l^{-1}, 700 mmol l^{-1}, 121 mmol l^{-1}, respectively). A special case are the methylene groups. For an isochronous methylene group with isochronous protons, the sequence can be used to simply determine the sum of two times the $^1J_{\mathrm{CH}}$ and the $^2J_{\mathrm{CH}}$ coupling constants is determined. However, for methylene groups with anisochronous signals, the determination of indiviual coupling constant is difficult as the signals in the middle of the sequence cancel out for the ω_1-coupled-BIRD$^{\mathrm{r}}$ ADEQUATE spectrum. In the ω_1-coupled ADEQUATE, signals in the middle of the triplet might be there, but which sum of coupling constants belongs to which proton, is unclear. They could be included in simulations if one tries both assignments.

For a real case scenario, 8-5(c)-DFA is measured using the ω_1-coupled-BIRD$^{\mathrm{r}}$ ADEQUATE sequence and the coupling constants are extracted. All coupling constants could be obtained for every carbon-proton-pair.

In the case of anisotropic data, the difference between extracted couplings for the ω_1-coupled ADEQUATE and the ω_1-coupled-BIRD$^{\mathrm{r}}$ ADEQUATE is in the range of the determined error. Therefore, the determination of the $^2T_{\mathrm{CH}}$ splitting is in principle possible for both types of sequences. As the ω_1-coupled ADEQUATE sequence is shorter, it might be preferable over the ω_1-coupled-BIRD$^{\mathrm{r}}$ ADEQUATE for anisotropic samples due to faster relaxation times in anisotropic samples.

For the measurement of the spectra shown here, NUS is used. This can reduce the measurement time if signal-to-noise losses are tolerated. However, the reconstruction algorithms lead to artifacts which might decrease the accuracy of the coupling extraction.

Both presented sequences are difficult to apply to low concentrated samples, in which the concentration of the sample is low. Since the experiment uses double quantum coherence on carbon and the natural abundance of a single carbon is 1.1 %, measurement time are long. Therefore, the experiments will be only used in special cases, where the structure determination of the compound is not possible without knowing these coupling constants.

Bot introduced experiments might not suffice. However, as long as the underlying $^2J_{\mathrm{CH}}$ coupling constant can be determined with the experiment, more sensitive experiments like the *selective* IPAP-HSQMBC can be used together with different scalings of residual anisotropic parameters, e. g. by the stretching device or variable angle NMR to determine $^2D_{\mathrm{CH}}$ couplings.

6.7. Conclusion

For the sign determination of $^2J_{\mathrm{CH}}$ coupling constants, two new sequences are presented, the ω_1-coupled ADEQUATE and the ω_1-coupled-BIRD$^{\mathrm{r}}$ ADEQUATE experiments. For isotropic samples, the ω_1-coupled-BIRD$^{\mathrm{r}}$ ADEQUATE is preferable over the ω_1-coupled ADEQUATE sequence, as signal-to-noise ratios are increased and the coupling extraction is more reliable.

The theoretical derivation of the product operators for the ω_1-coupled ADEQUATE and the ω_1-coupled-BIRD$^{\mathrm{r}}$ ADEQUATE have been shown and how the multiplet structures look like. The theoretical calculations are simulated for the indirect dimension and the experimental results are reproduced.

The spectra of $^{13}C_2$ acetic acid and $^{13}C_1$ ethanol are used to validate the theoretical calculations. The $^2J_{\mathrm{CH}}$ coupling constants for acetate had the same magnitude for the 1D ^{13}C and the ω_1-coupled ADEQUATE. For ethanol, literature values are used to compare with the experimental results. The experimental values have the same magnitude and the same sign as the corresponding literature values.

Strychnine, (+)-IPC, (*S*)-ibuprofene and 8-5(c)-DFA are measured with both experiments ω_1-coupled ADEQUATE and ω_1-coupled-BIRD$^{\mathrm{r}}$ ADEQUATE. The comparison to literature values and experimental values determined with other experiments shows that the $^2J_{\mathrm{CH}}$ couplings determined with the presented experiments are reliable. The signal-to-noise is increased for the spectra recorded with the ω_1-coupled-BIRD$^{\mathrm{r}}$ ADEQUATE sequence compared to the ω_1-coupled ADEQUATE. Therefore, the couplings extracted from the BIRD$^{\mathrm{r}}$ decoupled version are preferable.

The sequences are performed on anisotropic samples of (*S*)-ibuprofene and (+)-IPC. Here, the difference in the results for the $^2J_{\mathrm{CH}}$ coupling constants for the two sequences are not significant which is probably related to fast relaxation time of the analytes in oriented media. Additionally, the values are compared with the values extracted from the *selective* IPAP-HSQMBC. The values for all three sequences are in the same range.

6.8. Material and Methods

If not stated otherwise, the spectra are recorded on a 600 MHz spectrometer equipped with a cryogenically cooled TXI probehead and an AVANCE III console of Bruker GmbH (Rheinstetten, Germany). The spectra are recorded with Topspin 3.2 or with Topspin 3.5pl6.

6.8.1. Experimental Parameters for Spectra of $^{13}C_2$ acetate

The sample of $^{13}C\ _2$ acetate from Sigma-Aldrich is prepared with 10.8 mg (128 µmol) of the substance. The compound is used without further purification. It is dissolved in 600 µL D_2O which is purchased from Euroisotop not further purified. The overall concentration of acetate is 214 mmol l^{-1}. The sample is prepared in a 5 mm NMR tube.

The spectra shown in Figure 6.7 are recorded at a Bruker 400 MHz spectrometer equipped with a Avance III HD console and a room temperature BBI probehead.

The 13C-1D shown in Figure 6.7 is recorded with the standard Bruker pulse sequence zgpg30. It is recorded with 65 536 points and a sweep width of 250 ppm, leading to an acquisition time of 1.298 s and a recycling delay of 2 s. One scan is recorded. No decoupling is applied during acquisition. The spectrum is processed to 65 536 points and an exponential apodization function is applied to the FID.

The ω_1-coupled ADEQUATE spectrum in Figure 6.7 is recorded with 512 points in the direct and 128 points in the indirect dimension with corresponding sweep widths of 2 ppm and 10.0 ppm. This led to acquisition times of 0.213 s and 0.064 s. Before acquisition 16 dummy scans are applied for equilibration. The spectrum is recorded with 4 scans per increment and a recycling delay of 1 s. $^1J_{CH}$ is set to 127 Hz and $^1J_{CC}$ is set to 52 Hz. During acquisition the decoupling is switched off. The overall experimental time is 9 min 20 s. The spectrum is processed to 2048 points and 1024 points. The FID is multiplied with a squared cosine apodization function in both dimensions.

6.8.2. Experimental Parameters for Spectra of 2-$^{13}C_1$-ethanol

The sample of2-^{13}C $_1$-ethanol is prepared with 3.5 µl (60 µmol) purchased from Sigma-Aldrich and used without further purification. It is dissolved in 596.5 µL D_2O which is purchased from Euroisotop not further purified. The overall concentration of acetate is 100 mmol l^{-1}. The sample is prepared in a 5 mm NMR tube.

The spectrum shown in Figure 6.8 is recorded with 2048 points and 1024 points in the direct and indirect dimension with corresponding sweep widths of 8.5 ppm and 10.0 ppm. This led to acquisition times of 0.2 s and 0.34 s. Before acquisition 16 dummy scans are applied for equilibration. The spectrum is recorded with 4 scans per increment and a recycling delay of 1 s. $^1J_{CH}$ is set to 127 Hz and $^1J_{CC}$ is set to 35 Hz. During acquisition the decoupling is switched off. The overall experimental time is 1 h 28 min. The spectrum is processed to 4096 points and 1024 points. The FID is multiplied with a squared cosine apodization function in both dimensions.

6.8.3. Experimental Parameters for Spectra of strychnine

The sample of strychnine is prepared with 21.2 mg (63.4 µmol) of strychnine purchased from Fluka. The compound is used without further purification. It is dissolved in 500 µL $CDCl_3$ which is purchased from Euroisotop and distilled before use. This led to an overall concentration of strychnine is 120 mmol l^{-1}. The sample is prepared in a 5 mm NMR tube and sealed.

The spectra of strychnine shown in Figure 6.12 are recorded with 2048 points in the direct and 7552 points in the indirect dimension. The corresponding sweep widths are 9.970 ppm and 240 ppm leading to acquisition times of 0.171 s and 0.104 s, respectively. The recovery delay is set to 1 s. The overall experimental time is 1 d 15 h. The spectra are processed to 4096 points and 16 384 points in the direct and indirect dimension. The FID is apodized along both dimension with a squared cosine function. The only difference between the two spectra, are the sequences used.

6.8.4. Experimental Parameters for Spectra of (+)-IPC

The sample of (+)-IPC (isopinocampheol) is prepared with 64.8 mg (420 µmol) of (+)-IPC of purchased Sigma-Aldrich and used without further purification. It is dissolved in 600 µL $CDCl_3$ which is purchased from Euroisotop, not further purified. The overall concentration is 700 mmol l^{-1}. The sample is prepared in a 5 mm NMR tube and sealed.

The spectra shown in Figure 6.13 are recorded with 2048 in the direct and 4096 in the indirect dimension with corresponding sweep widths of 8.997 ppm and 240 ppm resulting in acquisition times of 0.190 s in the direct and of 0.057 s in the indirect dimension. The spectra are recorded with 16 Dummy scans and 16 scans per increment. The overall experimental time is 5 h 12 min for the ω_1-coupled ADEQUATE and 5 h 14 min for the ω_1-coupled-BIRD$^{\mathrm{r}}$ ADEQUATE. The spectra are recorded with 25 % NUS leading to 512 complex points recorded in the indirect dimension. The spectra are reconstructed with the Topspin 3.5pl6 with the included Compressed Sensing (CS) mode and the IST algorithm to 4096 in the direct and 8192 in the indirect dimension. The FID is multiplied with a cosine squared apodization function in both dimensions. The difference between the two spectra are the sequences.

The sample for the spectrum shown in Figure 6.17 for (+)-IPC is prepared with 40 mg (259 µmol) (+)-IPC purchased from Sigma-Aldrich. It is used without further purification. It is dissolved in 812 mg deuterated dichloromethane and 81 mg PBLG are added. To give a resulting concentration of 8.6 %(w/w). The chloroform and the PBLG are purchased from Sigma-Aldrich. The molecular weight distribution of PBLG is 150 000 g mol^{-1} to 350 000 g mol^{-1}. The sample is prepared in a 5 mm NMR tube with screw cap and centrifuged up and down until it is homogeneous.

The spectra shown in Figure 6.17 are recorded with 2048 in the direct dimension and 640 points in the indirect dimension. The corresponding sweep widths are 10 ppm and 72 ppm leading to an overall acquisition time of 0.170 s and 0.03 s. Before acquisition 16 dummy scans are applied for equilibration. The number of scans per increment are 48 with a recovery delay of 1 s. $^1J_{\mathrm{CH}}$ is set to 145 Hz and $^1J_{\mathrm{CC}}$ is set to 40 Hz and the corresponding delays Δ_1 and Δ_2 are calculated accordingly. The total experimental time is 9 h 37 min. The spectra are recorded with 50 % NUS with a t_2 and J coupling value of 0.2 s and 140 Hz to increase the points measured on important parts of the FID. The spectra are reconstructed using the CS mode of Topspin 3.5pl6 with the IRLS algorithm. The spectra are reconstructed to 2048 in the direct dimension and 1024 in the indirect dimension. The FID is apodized with a squared cosine window function. Each spectrum is recorded with the corresponding ω_1-coupled ADEQUATE or ω_1-coupled-BIRD$^{\mathrm{r}}$ ADEQUATE sequence.

6.8.5. Experimental Parameters for Spectra of (*S*)-ibuprofene

The sample of (*S*)-ibuprofene is prepared with 12.5 mg (60.5 mmol) of (*S*)-ibuprofene purchased from Sigma-Aldrich and used without further purification. It is dissolved in 500 µL $CDCl_3$ (Euroisotop) to a concentration of (*S*)-ibuprofene of 121 mmol l^{-1}. The sample is prepared in a 5 mm NMR tube and sealed.

The spectra shown in Figure 6.14 are recorded with 2048 in the direct dimension and 4096 points in the indirect dimension. The corresponding sweep width are 8.997 ppm and 240 ppm leading to an overall acquisition time of 0.190 s and 0.057 s. The number of scans per increment are 16. The total experimental time is 5 h 12 min. The spectra are recorded with 25 % NUS with a t_2 and J coupling value of 0.2 s and 125 Hz to increase the points measured on important parts of the FID. The spectra are reconstructed using the CS mode of Topspin 3.5pl6 with the IST algorithm. The spectra are reconstructed to 4096 in the direct dimension and 16 384 in the indirect dimension. The FID is apodized in both dimensions with a squared cosine window function. Each spectrum is recorded with the corresponding ω_1-coupled ADEQUATE or ω_1-coupled-BIRD$^{\mathrm{r}}$ ADEQUATE sequence.

The sample for the spectrum shown in Figure 6.19 for (*S*)-ibuprofene is prepared with 22.2 mg (108 µmol) (*S*)-ibuprofene purchased from Sigma-Aldrich. It is used without further purification. It is dissolved in 1104 mg chloroform and 76.5 mg PBLG are added, to give a resulting concentration of 6.4 %(w/w). The chloroform and the PBLG are also purchased from Sigma-Aldrich. The molecular weight distribution of PBLG is 150 000 $\mathrm{g\,mol^{-1}}$ to 350 000 $\mathrm{g\,mol^{-1}}$. The sample is prepared in a 5 mm NMR tube with screw cap and centrifuged up and down until it is homogeneous.

The spectra shown in Figure 6.19 are recorded with 2048 in the direct dimension and 1024 points in the indirect dimension. The corresponding sweep widths are 9 ppm and 230 ppm leading to acquisition times of 0.190 s and 0.015 s. Before acquisition 16 dummy scans are applied for equilibration. 64 scans are recorded per increment with a recycling delay of 1 s. ${}^{1}J_{\mathrm{CH}}$ is set to 125 Hz and ${}^{1}J_{\mathrm{CC}}$ is set to 40 Hz and the corresponding delays Δ_1 and Δ_2 are calculated accordingly. The total experimental time is 10 h 13 min. The spectra are recorded with 50 % NUS with a t_2 and J coupling value of 0.2 s and 125 Hz to increase the points measured on important parts of the FID. The spectra are reconstructed using the CS mode of Topspin 3.5pl6 with the IST algorithm. The spectra are reconstructed to 2048 in the direct dimension and 4096 in the indirect dimension. The FID is apodized with a squared cosine window function. Each spectrum is recorded with the corresponding ω_1-coupled ADEQUATE or ω_1-coupled-BIRD$^{\mathrm{r}}$ ADEQUATE sequence.

7. Conclusion

Although state-of-the-art NMR methods enable insight into a vast range of structural problems, there is still room for improvement. Anisotropic NMR parameters are so far only known to a community of NMR experts. To spread the practical application, the relative configuration of a small molecule is assigned by using both isotropic and anisotropic NMR parameters. This is done exemplary for a ferulic acid derivative. The ferulic acid is the most abundant hydroxycinnamate in plant cell walls. The dehydrodiferulate derivatives stabilize plant cell walls by covalently cross-linking polysaccharides and lignin.[155] One specific dehydrodiferulate, 8-5(c)-DFA, has an unknown configuration of two neighbored stereogenic centers in the molecule. The determination of this configuration is of great interest, therefore 8-5(c)-DFA is assigned with 1D ^{1}H, 1D ^{13}C, CLIP-HSQC, NOESY and HMBC spectra. The NOE data is used to determine the distance between the protons, which indicates a trans configuration of the protons in the stereocenters. To confirm this indication, RDCs are determined for 8-5(c)-DFA in two alignment media, PEO-DA and PBLG. The analysis of the data shows that the trans configuration must be the right configuration. While the relative stereochemistry could be determined unambiguously, the fitting of 8-5(c)-DFA to a single rigid structure cannot describe its conformational space. This might be accessible with the measured data using more complex analysis, which are for example based on molecular dynamics with orientational constraints [112] or a population fitting of a single-tensorial fit.[83] To perform the assignment of the absolute configuration to 8-5(c)-DFA, additional analytical methods such as Vibrational Circular Dichroism (VCD) could be pursued.

The differentiation of enantiomers by NMR is an important analytical tool for small molecules. To achieve differentiation, a chiral environment has to be introduced that can be chiral alignment media, chiral solvents or CSA. In the literature, several CSA are described. Within these CSAs, the chiral LSR are particularly important as they induce higher chemical shift differences for enantiomers than other compounds. Therefore, the chemical shifts induced by several LSR agents and a CSA are compared for hydrobenzoine at low and high magnetic field strengths. The performance of Eu(hfc)$_3$, a commercially available LSR, is compared to Eu(BINOL)$_3$Li$_3$ and Eu(pnb)$_3$. Moreover, chemical shifts differences induced by (*R*)-TFB are considered. Eu(BINOL)$_3$Li$_3$ induces the highest pseudo contact shifts by retaining sharp line widths for hydrobenzoine. Hence, Eu(BINOL)$_3$Li$_3$ is used to differentiate the racemic mixtures of hydrobenzoine from its *meso*-compound in combination with CLIP-HSQC and HSQC-TOCSY spectra, as they reveal a $^3J_{\mathrm{HH}}$ coupling from one stereogenic center to the other. These experiments are feasible if protons are directly at the stereogenic centers and if $^3J_{\mathrm{HH}}$ couplings cross the symmetry plane of the structure. In particular Eu(BINOL)$_3$Li$_3$ shows very promising properties as a chiral LSR and both Eu(BINOL)$_3$Li$_3$ and Eu(pnb)$_3$ should be applied to a broader range of functional groups and molecules. Especially, tabletop spectrometers benefit from a strong effect of chiral LSR. Therefore, the ability to differentiate enantiomers at a proton frequency of 62 MHz has been studied. Again Eu(BINOL)$_3$Li$_3$ is particularly efficient. However, only a low number of solutes has been studied and a broader evaluation of Eu(BINOL)$_3$Li$_3$ should be attempted.

Many NMR samples suffer from inhomogeneity, for example samples with a concentration gradient, with precipitates at bottom or top of the sample or broken polymer gels or inhomogeneously prepared orienting media in partially aligned samples. If these samples are measured with conventional NMR experiments, the whole sample volume is excited, which leads to unsuitable spectra for evaluation. However, modern spectrometer probe heads are equipped with pulsed field gradients. These allow the spatial selective measurement, as applied on humans in MRI for medical studies. Consequently, this technique is combined with conventional NMR to procure spatially resolved spectra. In combination with 1D ^{13}C and CLIP-HSQC experiments, the resulting spectra can reveal the composition of biphasic samples or isotropic and anisotropic data can be recorded in one sample. Therefore, a slice selectively exciting and a z-resolved 1D ^{13}C pulse sequence are used to reveal the phase constitution of two polymer mixtures. Additionally, a slice selectively exciting and a z-resolved CLIP-HSQC are used for the RDCs determination in one sample. With this data, the configurational and prochiral assignment of (−)-IPC is shown as well as the enantiodiscrimination of (−)-IPC and (+)-IPC. The second experiment, the z-resolved CLIP-HSQC, is a three dimensional experiment. It is applied to a biphasic sample of two immiscible solvents, water and chloroform. Both phases could be well separated and used to assign structures. The spatially resolved experiments could be used for reaction monitoring, which has been shown for 1D ^{1}H experiments by John et al.[16] Future method development might comprise a combination with fast experiments like the ASAP-type sequences,[99, 156] which could speed up the acquisition considerably.

For molecules with few protons and for quaternary carbons with a stereogenic center, $^{2}J_{\mathrm{CH}}$ and $^{2}D_{\mathrm{CH}}$ couplings can contribute remarkably to the structure determination by NMR. Particularly for the determination of $^{2}D_{\mathrm{CH}}$ couplings, the sign of both $^{2}J_{\mathrm{CH}}$ and $^{2}D_{\mathrm{CH}}$ couplings add structural information about the molecule. Therefore, two experiments are presented to measure sign and magnitude of $^{2}J_{\mathrm{CH}}$ couplings to quaternary carbons. In contrast to already published experiments, the experiments presented in this thesis, i. e. the ω_1-coupled ADEQUATE and the ω_1-coupled-BIRD$^{\mathrm{r}}$ ADEQUATE, use double quantum coherence evolution on carbon. This leads to a signal which is split in the indirect dimension by the sum of the $^{1}J_{\mathrm{CH}}$ and the $^{2}J_{\mathrm{CH}}$ coupling. For a methine group, a doublet results, which is the simplest possible multiplet. In this thesis, the theoretical derivation of the present product operators reveals that the $^{1}J_{\mathrm{CH}}$ coupling constant and the $^{2}J_{\mathrm{CH}}$ coupling constant add up. Consequently, the $^{1}J_{\mathrm{CH}}$ coupling constant has to be determined beforehand. To evaluate the multiplet that occurs for each spin system, the one-dimensional simulations show that the sum of the couplings in the ω_1-coupled-BIRD$^{\mathrm{r}}$ ADEQUATE is not influenced by $^{3}J_{\mathrm{CH}}$ couplings. After the theoretical derivation and simulation, the sequences are applied to acetate, ethanol, strychnine, (+)-IPC and (S)-ibuprofene and the extracted values compared to literature values and to values determined with other experiments to evaluate the experimental outcome. Splendidly, the experimental and literature values exhibit the same magnitude and sign for the $^{2}J_{\mathrm{CH}}$ couplings. Additionally, 8-5(c)-DFA is measured with the ω_1-coupled-BIRD$^{\mathrm{r}}$ ADEQUATE sequence and the couplings extracted.

Last, the sequence is applied to two aligned samples and the ${}^{2}T_{\mathrm{CH}}$ couplings for the quaternary carbons in (+)-IPC and (*S*)-ibuprofene are compared for different alignment strengths. The extracted ${}^{2}T_{\mathrm{CH}}$ couplings display a linear relationship between the alignment strength and the coupling size. Certainly, the ω_1-coupled ADEQUATE and ω_1-coupled-BIRD$^{\mathrm{r}}$ ADEQUATE experiment could be used for the determination of ${}^{2}J_{\mathrm{CH}}$ couplings for quaternary carbons, which are not accessible by other methods.

Bibliography

[1] G. Cruciani, *Molecular interaction fields: Applications in drug discovery and ADME prediction*, Wiley-VCH, Weinheim, **2006**.

[2] G. A. Morris, "Modern NMR techniques for structure elucidation", *Magn. Reson. Chem.* **1986**, 371–403.

[3] U. K. Sundekilde, L. B. Larsen, H. C. Bertram, "NMR-Based Milk Metabolomics", **2013**, *3*, 204–222.

[4] M. Maiwald, H. H. Fischer, Y.-K. Kim, K. Albert, H. Hasse, "Quantitative high-resolution on-line NMR spectroscopy in reaction and process monitoring", **2004**, *166*, 135–146.

[5] B. Meyer, T. Peters, "NMR Spectroscopy Techniques for Screening and Identifying Ligand Binding to Protein Receptors", *Angew. Chem. Int. Ed.* **2003**, 864–890.

[6] F. Gasparrini, L. Lunazzi, D. Misiti, C. Villani, "Organic Stereochemistry and Conformational Analysis from Enantioselective Chromatography and Dynamic Nuclear Magnetic Resonance Measurements", *Acc. Chem. Res.* **1995**, *28*, 163–170.

[7] S. G. Levine, "A Short History of the Chemical Shift", *J. Chem. Educ.* **2001**, *78*, 133.

[8] L. H. Meyer, A. Saika, and H. S. Gutowsky, "Electron Distribution in Molecules. III. The Proton Magnetic Spectra of Simple Organic Groups", *J. Am. Chem. Soc.* **1953**, 4567–4573.

[9] M. Karplus, "Contact Electron-Spin Coupling of Nuclear Magnetic Moments", *J. Chem. Phys.* **1959**, *30*, 11–15.

[10] Jonathan Stonehouse, Pere Adell, James Keeler, and A. J. Shaka, "Ultrahigh-Quality NOE Spectra", *J. Am. Chem. Soc.* **1994**, 6037–6038.

[11] B. Deloche, E. T. Samulski, "Short-range nematic-like orientational order in strained elastomers: a deuterium magnetic resonance study", **1981**, *14*, 575–581.

[12] C. M. Thiele, S. Berger, "Probing the diastereotopicity of methylene protons in strychnine using residual dipolar couplings", *Org. Lett.* **2003**, *5*, 705–708.

[13] M. E. Di Pietro, G. Celebre, C. Aroulanda, D. Merlet, G. de Luca, "Assessing the stable conformations of ibuprofen in solution by means of Residual Dipolar Couplings", **2017**, *106*, 113–121.

[14] G. Kummerlöwe, S. Schmitt, B. Luy, "Cross-Fitting of Residual Dipolar Couplings", *Open Spectrosc. J.* **2010**, *4*, 16–27.

[15] P. Tzvetkova, B. Luy, S. Simova, "Configuration verification via RDCs on the example of a tetra-substituted pyrrolidine ring", *Magn. Reson. Chem.* **2012**, *50*, 92–101.

[16] T. Niklas, D. Stalke, M. John, "Single-shot titrations and reaction monitoring by slice-selective NMR spectroscopy", *Chem. Commun.* **2015**, *51*, 1275–1277.

[17] I. Canet, J. Courtieu, A. Loewenstein, A. Meddour, J. M. Pechine, "Enantiomeric analysis in a polypeptide lyotropic liquid crystal by deuterium NMR", *J. Am. Chem. Soc.* **1995**, *117*, 6520–6526.

[18] K. Kobzar, H. Kessler, B. Luy, "Stretched gelatin gels as chiral alignment media for the discrimination of enantiomers by NMR spectroscopy", *Angew. Chem. Int. Ed.* **2005**, *44*, 3145–3147.

[19] L. Trantírek, R. Štefl, J. Feigon, V. Sklenář, "A Method for Direct Determination of Helical Parameters in Nucleic Acids Using Residual Dipolar Couplings", *J. Am. Chem. Soc.* **2000**, *122*, 10454–10455.

[20] W. Andrałojć, E. Ravera, L. Salmon, G. Parigi, H. M. Al-Hashimi, C. Luchinat, "Inter-helical conformational preferences of HIV-1 TAR-RNA from maximum occurrence analysis of NMR data and molecular dynamics simulations", **2016**, *18*, 5743–5752.

[21] B. E. Ramirez, O. N. Voloshin, R. D. Camerini-Otero, A. Bax, "Solution structure of DinI provides insight into its mode of RecA inactivation", **2000**, *9*, 2161–2169.

[22] B. Luy, "Distinction of enantiomers by NMR spectroscopy using chiral orienting media", *J. Indian Inst. Sci.* **2010**, 119–132.

[23] D. Parker, "NMR determination of enantiomeric purity", *Chem. Rev.* **1991**, *91*, 1441–1457.

[24] P. Trigo-Mouriño, C. Merle, Koos, Martin R. M., B. Luy, R. R. Gil, "Probing Spatial Distribution of Alignment by Deuterium NMR Imaging", *Chem. Eur. J.* **2013**, *19*, 7013–7019.

[25] F. Bloch, "Nuclear Induction", *Phys. Rev.* **1946**, 460–474.

[26] J. Keeler, *Understanding NMR spectroscopy*, 2. ed., Wiley, Chichester, **2010**.

[27] J. J. Sakurai, *Modern quantum mechanics*, 24., Addison-Wesley, Reading Mass, **2008**.

[28] B. Luy, Lecture notes for the lecture "Mehrdimensionale NMR Spectroskopie" at the Karlsruhe Institute of Technologie SS14, **2014**.

[29] M. H. Levitt, *Spin dynamics: Basics of nuclear magnetic resonance*, 2. ed., Wiley, Chichester, **2008**.

[30] Matthias Eberstadt, Gerd Gemmecker, Dale F. Mierke, Horst Kessler, "Scalar Coupling Constants-Their Analysis and Their Application for the Elucidation of Structures", *Angew. Chem. Int. Ed.* **1995**, 1671–1695.

[31] R. Contreras, "Angular dependence of spin–spin coupling constants", *Prog. Nucl. Magn. Reson. Spectrosc.* **2000**, *37*, 321–425.

[32] G. Kummerlöwe, B. Luy, "Residual dipolar couplings as a tool in determining the structure of organic molecules", *Trends Anal. Chem.* **2009**, *28*, 483–493.

[33] M. R. Hansen, M. Rance, A. Pardi, "Observation of Long-Range H–H Distances in Solution by Dipolar Coupling Interactions", *J. Am. Chem. Soc.* **1998**, *120*, 11210–11211.

[34] P. W. Kuchel, B. E. Chapman, N. Müller, W. A. Bubb, D. J. Philp, A. M. Torres, "Apparatus for rapid adjustment of the degree of alignment of NMR samples in aqueous media: verification with residual quadrupolar splittings in (23)Na and (133)Cs spectra", *J. Magn. Reson.* **2006**, *180*, 256–265.

[35] H. Saitô, I. Ando, A. Naitō, *Solid State NMR Spectroscopy for Biopolymers*, Springer Netherlands, Dordrecht, **2006**.

[36] V. I. Bakhmutov, *Solid-State NMR in Materials Science: Principles and Applications*, Chapman and Hall/CRC, Baton Rouge, UNITED STATES, **2016**.

[37] G. Pintacuda, M. John, X.-C. Su, G. Otting, "NMR structure determination of protein-ligand complexes by lanthanide labeling", *Acc. Chem. Res.* **2007**, *40*, 206–212.

[38] A. Saupe, G. Englert, "High-Resolution Nuclear Magnetic Resonance Spectra of Orientated Molecules", *Phys. Rev. Lett.* **1963**, *11*, 462–464.

[39] G. Kummerlöwe, B. Luy, "Residual Dipolar Couplings for the Configurational and Conformational Analysis of Organic Molecules", *Annu. Rep. NMR Spectrosc.*, Annual Reports on NMR Spectroscopy **2009**, *68*, (Ed.: G. A. Webb), 193–230.

[40] M. R. Hansen, L. Mueller, A. Pardi, "Tunable alignment of macromolecules by filamentous phage yields dipolar coupling interactions", **1998**, *5*, 1065–1074.

[41] G. M. Clore, M. R. Starich, A. M. Gronenborn, "Measurement of Residual Dipolar Couplings of Macromolecules Aligned in the Nematic Phase of a Colloidal Suspension of Rod-Shaped Viruses", *J. Am. Chem. Soc.* **1998**, *120*, 10571–10572.

[42] N. Tjandra, "Direct Measurement of Distances and Angles in Biomolecules by NMR in a Dilute Liquid Crystalline Medium", *Science* **1997**, *278*, 1111–1114.

[43] M. Ottiger, A. Bax, "Characterization of magnetically oriented phospholipid micelles for measurement of dipolar couplings in macromolecules", *J. Biomol. NMR* **1998**, *12*, 361–372.

[44] J. A. Losonczi, J. H. Prestegard, "Improved dilute bicelle solutions for high-resolution NMR of biological macromolecules", **1998**, *12*, 447–451.

[45] J. Sass, F. Cordier, A. Hoffmann, M. Rogowski, A. Cousin, J. G. Omichinski, H. Löwen, S. Grzesiek, "Purple Membrane Induced Alignment of Biological Macromolecules in the Magnetic Field", *J. Am. Chem. Soc.* **1999**, *121*, 2047–2055.

[46] K. Fleming, D. Gray, S. Prasannan, S. Matthews, "Cellulose Crystallites: A New and Robust Liquid Crystalline Medium for the Measurement of Residual Dipolar Couplings", *J. Am. Chem. Soc.* **2000**, *122*, 5224–5225.

[47] V. V. Klochkov, A. V. Klochkov, C. M. Thiele, S. Berger, "A novel liquid crystalline system for partial alignment of polar organic molecules", *J. Magn. Reson.* **2006**, *179*, 58–63.

[48] K. Czarniecka, E. T. Samulski, "Polypeptide Liquid Crystals: A Deuterium NMR Study", *Mol. Cryst. Liq. Cryst.* **1981**, *63*, 205–214.

[49] M. D. Poliks, Y. W. Park, E. T. Samulski, “Poly-g-Benzyl-L-Glutamate: Order Parameter, Oriented Gel, and Novel Derivatives”, *Mol. Cryst. Liq. Cryst.* **1987**, *153*, 321–345.

[50] J.-P. Bayle, J. Courtieu, E. Gabetty, Loewenstein A., J. M. Pechine, “Enantiomeric analysis in a polypeptide lyotropic liquid crystal through proton decoupled deuterium NMR”, *New J. Chem.* **1992**, 837–838.

[51] P. Lesot, Y. Gounelle, D. Merlet, A. Loewenstein, J. Courtieu, “Measurement and Analysis of the Molecular Ordering Tensors of Two Enantiomers Oriented in a Polypeptide Liquid Crystalline System”, *J. Phys. Chem.* **1995**, *99*, 14871–14875.

[52] C. Aroulanda, M. Sarfati, J. Courtieu, P. Lesot, “Investigation of the Enantioselectivity of Three Polypeptide Liquid-Crystalline Solvents Using NMR Spectroscopy”, *Enantiomer* **2001**, 281–287.

[53] V. Madiot, D. Grée, R. Gree, P. Lesot, J. Courtieu, “Highly enantioselective propargylic monofluorination established by carbon-13 and fluorine-19 NMR in chiral liquid crystals”, *Chem. Commun.* **2000**, 169–170.

[54] A. Meddour, P. Berdague, A. Hedli, J. Courtieu, P. Lesot, “Proton-Decoupled Carbon-13 NMR Spectroscopy in a Lyotropic Chiral Nematic Solvent as an Analytical Tool for the Measurement of the Enantiomeric Excess”, *J. Am. Chem. Soc.* **1997**, *119*, 4502–4508.

[55] A. Marx, C. Thiele, “Orientational properties of poly-gamma-benzyl-L-glutamate: influence of molecular weight and solvent on order parameters of the solute”, *Chem. Eur. J.* **2009**, *15*, 254–260.

[56] C. Aroulanda, V. Boucard, F. Guibe, J. Courtieu, D. Merlet, “Weakly oriented liquid-crystal NMR solvents as a general tool to determine relative configurations”, *Chem. Eur. J.* **2003**, *9*, 4536–4539.

[57] C. M. Thiele, “Simultaneous assignment of all diastereotopic protons in strychnine using RDCs: PELG as alignment medium for organic molecules”, *J. Org. Chem.* **2004**, *69*, 7403–7413.

[58] L. Arnold, A. Marx, C. M. Thiele, M. Reggelin, “Polyguanidines as chiral orienting media for organic compounds”, *Chem. Eur. J.* **2010**, *16*, 10342–10346.

[59] M. Dama, S. Berger, “Polyisocyanides as a new alignment medium to measure residual dipolar couplings for small organic molecules”, *Org. Lett.* **2012**, *14*, 241–243.

[60] A. Krupp, M. Reggelin, “Phenylalanine-based polyarylacetylenes as enantiomer-differentiating alignment media”, *Magn. Reson. Chem.* **2012**, *50*, 45–52.

[61] N.-C. Meyer, A. Krupp, V. Schmidts, C. M. Thiele, M. Reggelin, “Polyacetylenes as Enantiodifferentiating Alignment Media”, *Angew. Chem.* **2012**, *124*, 8459–8463.

[62] C. Gayathri, N. V. Tsarevsky, R. R. Gil, “Residual dipolar couplings (RDCs) analysis of small molecules made easy: fast and tuneable alignment by reversible compression/relaxation of reusable PMMA Gels”, *Chem. Eur. J.* **2010**, *16*, 3622–3626.

[63] R. Tycko, F. J. Blanco, Y. Ishii, “Alignment of Biopolymers in Strained Gels: A New Way To Create Detectable Dipole–Dipole Couplings in High-Resolution Biomolecular NMR”, *J. Am. Chem. Soc.* **2000**, *122*, 9340–9341.

[64] H.-J. Sass, G. Musco, S. J. Stahl, P. T. Wingfield, S. Grzesiek, “Solution NMR of proteins within polyacrylamide gels: Diffusional properties and residual alignment by mechanical stress or embedding of oriented purple membranes”, *J. Biomol. NMR* **2000**, *18*, 303–309.

[65] T. Cierpicki, J. H. Bushweller, “Charged gels as orienting media for measurement of residual dipolar couplings in soluble and integral membrane proteins”, *J. Am. Chem. Soc.* **2004**, *126*, 16259–16266.

[66] P. Haberz, J. Farjon, C. Griesinger, “A DMSO-compatible orienting medium: towards the investigation of the stereochemistry of natural products”, *Angew. Chem. Int. Ed.* **2005**, *44*, 427–429.

[67] G. Kummerlöwe, M. U. Kiran, B. Luy, “Covalently cross-linked gelatin allows chiral distinction at elevated temperatures and in DMSO”, *Chem. Eur. J.* **2009**, *15*, 12192–12195.

[68] U. Eliav, G. Navon, “Collagen fibers as a chiral agent: A demonstration of stereochemistry effects”, *J. Am. Chem. Soc.* **2006**, *128*, 15956–15957.

[69] S. Büchler, G. Kummerlöwe, B. Luy, “Naturally occurring biodegradable polymers as the basis of chiral gels for the distinction of enantiomers by partially oriented NMR spectroscopy”, *Int. J. Artif. Organs* **2011**, 134–138.

[70] J. C. Freudenberger, S. Knor, K. Kobzar, D. Heckmann, T. Paululat, H. Kessler, B. Luy, “Stretched poly(vinyl acetate) gels as NMR alignment media for the measurement of residual dipolar couplings in polar organic solvents”, *Angew. Chem. Int. Ed.* **2005**, *44*, 423–426.

[71] G. Kummerlöwe, J. Auernheimer, A. Lendlein, B. Luy, “Stretched poly(acrylonitrile) as a scalable alignment medium for DMSO”, *J. Am. Chem. Soc.* **2007**, *129*, 6080–6081.

[72] G. Kummerlöwe, E. F. McCord, S. F. Cheatham, S. Niss, R. W. Schnell, B. Luy, “Tunable alignment for all polymer gel/solvent combinations for the measurement of anisotropic NMR parameters”, *Chem. Eur. J.* **2010**, *16*, 7087–7089.

[73] B. Luy, K. Kobzar, H. Kessler, “An easy and scalable method for the partial alignment of organic molecules for measuring residual dipolar couplings”, *Angew. Chem. Int. Ed.* **2004**, *43*, 1092–1094.

[74] B. Luy, K. Kobzar, T. E. Skinner, N. Khaneja, S. J. Glaser, “Construction of universal rotations from point-to-point transformations”, *J. Magn. Reson.* **2005**, *176*, 179–186.

[75] G. Kummerlöwe, S. Knor, A. O. Frank, T. Paululat, H. Kessler, B. Luy, “Deuterated polymer gels for measuring anisotropic NMR parameters with strongly reduced artefacts”, *Chem. Commun.* **2008**, 5722–5724.

[76] J. C. Freudenberger, P. Spiteller, R. Bauer, H. Kessler, B. Luy, “Stretched poly(dimethylsiloxane) gels as NMR alignment media for apolar and weakly polar organic solvents: an ideal tool for measuring RDCs at low molecular concentrations”, *J. Am. Chem. Soc.* **2004**, *126*, 14690–14691.

[77] Y. E. Moskalenko, V. Bagutski, C. M. Thiele, “Chemically synthesized and crosslinked PDMS as versatile alignment medium for organic compounds”, *Chem. Commun.* **2016**, *53*, 95–98.

[78] R. R. Gil, C. Gayathri, N. V. Tsarevsky, K. Matyjaszewski, “Stretched poly(methyl methacrylate) gel aligns small organic molecules in chloroform. stereochemical analysis and diastereotopic proton NMR assignment in ludartin using residual dipolar couplings and 3J coupling constant analysis”, *J. Org. Chem.* **2008**, *73*, 840–848.

[79] P. Kaden, J. C. Freudenberger, B. Luy, “Noncovalently and covalently cross-linked polyurethane gels as alignment media and the suppression of residual polymer signals using diffusion-filtered spectroscopy”, *Magn. Reson. Chem.* **2012**, *50*, 22–28.

[80] C. Merle, G. Kummerlöwe, J. C. Freudenberger, F. Halbach, W. Stöwer, C. L. v. Gostomski, J. Höpfner, T. Beskers, M. Wilhelm, B. Luy, “Crosslinked Poly(ethylene oxide) as a Versatile Alignment Medium for the Measurement of Residual Anisotropic NMR Parameters”, *Angew. Chem.* **2013**, *125*, 10499–10502.

[81] T. Montag, C. M. Thiele, “Cross-linked helically chiral poly-(gamma-benzyl-L-glutamate) as enantiodiscriminating alignment medium”, *Chem. Eur. J.* **2013**, *19*, 2271–2274.

[82] G. Cornilescu, J. L. Marquardt, M. Ottiger, A. Bax, “Validation of Protein Structure from Anisotropic Carbonyl Chemical Shifts in a Dilute Liquid Crystalline Phase”, *J. Am. Chem. Soc.* **1998**, *120*, 6836–6837.

[83] A. Navarro-Vazquez, “MSpin-RDC. A program for the use of residual dipolar couplings for structure elucidation of small molecules”, *Magn. Reson. Chem.* **2012**, *50*, 73–79.

[84] O. W. Sørensen, G. W. Eich, M. H. Levitt, G. Bodenhausen, R. R. Ernst, “Product operator formalism for the description of NMR pulse experiments”, *Prog. Nucl. Magn. Reson. Spectrosc.* **1984**, *16*, 163–192.

[85] H. Kessler, M. Gehrke, C. Griesinger, “Zweidimensionale NMR-Spektroskopie, Grundlagen und Übersicht über die Experimente”, *Angew. Chem.* **1988**, *100*, 507–554.

[86] A. Enthart, J. C. Freudenberger, J. Furrer, H. Kessler, B. Luy, “The CLIP/CLAP-HSQC: pure absorptive spectra for the measurement of one-bond couplings”, *J. Magn. Reson.* **2008**, *192*, 314–322.

[87] T. E. Skinner, T. O. Reiss, B. Luy, N. Khaneja, S. J. Glaser, “Application of optimal control theory to the design of broadband excitation pulses for high-resolution NMR”, *J. Magn. Reson.* **2003**, *163*, 8–15.

[88] T. E. Skinner, T. O. Reiss, B. Luy, N. Khaneja, S. J. Glaser, “Reducing the duration of broadband excitation pulses using optimal control with limited RF amplitude”, *J. Magn. Reson.* **2004**, *167*, 68–74.

[89] T. E. Skinner, T. O. Reiss, B. Luy, N. Khaneja, S. J. Glaser, “Tailoring the optimal control cost function to a desired output: application to minimizing phase errors in short broadband excitation pulses”, *J. Magn. Reson.* **2005**, *172*, 17–23.

[90] T. E. Skinner, K. Kobzar, B. Luy, M. R. Bendall, W. Bermel, N. Khaneja, S. J. Glaser, “Optimal control design of constant amplitude phase-modulated pulses: application to calibration-free broadband excitation”, *J. Magn. Reson.* **2006**, *179*, 241–249.

[91] N. I. Gershenzon, T. E. Skinner, B. Brutscher, N. Khaneja, M. Nimbalkar, B. Luy, S. J. Glaser, “Linear phase slope in pulse design: application to coherence transfer”, *J. Magn. Reson.* **2008**, *192*, 235–243.

[92] K. Kobzar, T. E. Skinner, N. Khaneja, S. J. Glaser, B. Luy, “Exploring the limits of broadband excitation and inversion: II. Rf-power optimized pulses”, *J. Magn. Reson.* **2008**, *194*, 58–66.

[93] T. E. Skinner, N. I. Gershenzon, M. Nimbalkar, W. Bermel, B. Luy, S. J. Glaser, “New strategies for designing robust universal rotation pulses: application to broadband refocusing at low power”, *J. Magn. Reson.* **2012**, *216*, 78–87.

[94] K. Kobzar, S. Ehni, T. E. Skinner, S. J. Glaser, B. Luy, “Exploring the limits of broadband 90° and 180° universal rotation pulses”, *J. Magn. Reson.* **2012**, 142–160.

[95] S. Ehni, B. Luy, “BEBE(tr) and BUBI: J-compensated concurrent shaped pulses for 1H-13C experiments”, *J. Magn. Reson.* **2013**, *232*, 7–17.

[96] S. Ehni, B. Luy, “A systematic approach for optimizing the robustness of pulse sequence elements with respect to couplings, offsets, and B1-field inhomogeneities (COB)”, *Magn. Reson. Chem.* **2012**, *50*, 63–72.

[97] S. Ehni, B. Luy, “Robust INEPT and refocused INEPT transfer with compensation of a wide range of couplings, offsets, and B1-field inhomogeneities (COB3)”, *J. Magn. Reson.* **2014**, *247*, 111–117.

[98] T. Reinsperger, B. Luy, “Homonuclear BIRD-decoupled spectra for measuring one-bond couplings with highest resolution: CLIP/CLAP-RESET and constant-time-CLIP/CLAP-RESET”, *J. Magn. Reson.* **2014**, 110–120.

[99] J. Becker, B. Luy, “CLIP-ASAP-HSQC for fast and accurate extraction of one-bond couplings from isotropic and partially aligned molecules”, *Magn. Reson. Chem.* **2015**, *53*, 878–885.

[100] W. Koźmiński, “Simplified multiplet pattern HSQC-TOCSY experiment for accurate determination of long-range heteronuclear coupling constants”, *J. Magn. Reson.* **1999**, *137*, 408–412.

[101] M. Kurz, P. Schmieder, H. Kessler, “HETLOC, an Efficient Method for Determining Heteronuclear Long-Range Couplings with Heteronuclei in Natural Abundance”, *Angew. Chem. Int. Ed.* **1991**, *30*, 1329–1331.

[102] K. Kobzar, B. Luy, “Analyses, extensions and comparison of three experimental schemes for measuring ((n)J(CH)+D(CH))-couplings at natural abundance”, *J. Magn. Reson.* **2007**, *186*, 131–141.

[103] M. J. Thrippleton, J. Keeler, “Elimination of zero-quantum interference in two-dimensional NMR spectra”, *Angew. Chem. Int. Ed.* **2003**, *42*, 3938–3941.

[104] A. Bax, R. Freeman, S. P. Kempsell, “Natural abundance carbon-13-carbon-13 coupling observed via double-quantum coherence”, *J. Am. Chem. Soc.* **1980**, *102*, 4849–4851.

[105] A. Bax, R. Freeman, “Relative signs of NMR spin coupling constants by two-dimensional Fourier transform spectroscopy”, *J. Magn. Reson.* **1981**, *45*, 177–181.

[106] M. Bourdonneau, B. Ancian, “Rapid-Pulsing Artifact-Free Double-Quantum-Filtered Homonuclear Spectroscopy”, *J. Magn. Reson.* **1998**, *132*, 316–327.

[107] K. Kazimierczuk, V. Orekhov, “Non-uniform sampling: Post-Fourier era of NMR data collection and processing”, *Magn. Reson. Chem.* **2015**, *53*, 921–926.

[108] E. J. Candès, J. K. Romberg, T. Tao, “Stable signal recovery from incomplete and inaccurate measurements”, *Comm. Pure Appl. Math.* **2006**, *59*, 1207–1223.

[109] K. Kazimierczuk, V. Y. Orekhov, “Accelerated NMR spectroscopy by using compressed sensing”, **2011**, *50*, 5556–5559.

[110] D. J. Holland, M. J. Bostock, L. F. Gladden, D. Nietlispach, “Fast Multidimensional NMR Spectroscopy Using Compressed Sensing”, *Angew. Chem.* **2011**, *123*, 6678–6681.

[111] M. D. Hanwell, D. E. Curtis, D. C. Lonie, T. Vandermeersch, E. Zurek, G. R. Hutchison, “Avogadro: an advanced semantic chemical editor, visualization, and analysis platform”, *J. Cheminform.* **2012**, *4*, 17.

[112] U. Sternberg, R. Witter, “Molecular dynamics simulations on PGLa using NMR orientational constraints”, *J. Biomol. NMR* **2015**, *63*, 265–274.

[113] S. W. Smith, “Chiral toxicology: It’s the same thing...only different”, **2009**, *110*, 4–30.

[114] R. J. Lewis, M. A. Bernstein, H.-F. Chang, D. Chapman, N. Pemberton, “Enantiomeric purity determination by NMR: Proving the purity of a single enantiomer”, *Tetrahedron: Asymm.* **2013**, *24*, 866–870.

[115] R. S. Cahn, C. Ingold, V. Prelog, “Specification of Molecular Chirality”, *Angew. Chem. Int. Ed.* **1966**, 385–415.

[116] C. Canlet, D. Merlet, P. Lesot, A. Meddour, A. Loewenstein, J. Courtieu, “Deuterium NMR stereochemical analysis of threo–erythro isomers bearing remote stereogenic centres in racemic and non-racemic liquid crystalline solvents”, *Tetrahedron: Asymm.* **2000**, *11*, 1911–1918.

[117] I. Canet, A. Meddour, J. Courtieu, J. L. Canet, J. Salaun, “New, and Accurate Method To Determine the Enantiomeric Purity of Amino Acids Based on Deuterium NMR in a Cholesteric Lyotropic Liquid Crystal”, *J. Am. Chem. Soc.* **1994**, *116*, 2155–2156.

[118] J. A. Peters, J. Huskens, D. J. Raber, “Lanthanide induced shifts and relaxation rate enhancements”, *Prog. Nucl. Magn. Reson. Spectrosc.* **1996**, *28*, 283–350.

[119] W. H. Pirkle, “The Nonequivalence of Physical Properties of Enantiomers in Optically Active Solvents. Differences in Nuclear Magnetic Resonance Spectra. I”, *J. Am. Chem. Soc.* **1966**, 1837.

[120] A. J. Wooten, P. J. Carroll, P. J. Walsh, “Impact of Na- and K-C pi-interactions on the structure and binding of M3(sol)n(BINOLate)3Ln catalysts”, *Org. Lett.* **2007**, *9*, 3359–3362.

[121] M. Pedziwiatr, N. M. Kosareff, G. Muller, A. Y. Koposov, V. N. Nemykin, J. P. Riehl, J. Legendziewicz, “Preparation, characterization, and circularly polarized luminescence of lanthanum and europium 1,1’-binaphthyl-2,2’-diyl phosphate complexes”, **2008**, *451*, 251–253.

[122] M. Reller, S. Wesp, Koos, Martin R. M., M. Reggelin, B. Luy, “Biphasic Liquid Crystal and the Simultaneous Measurement of Isotropic and Anisotropic Parameters by Spatially Resolved NMR Spectroscopy”, *Chem. Eur. J.* **2017**, *23*, 13351–13359.

[123] K. Stott, J. Stonehouse, J. Keeler, T.-L. Hwang, A. J. Shaka, “Excitation Sculpting in High-Resolution Nuclear Magnetic Resonance Spectroscopy: Application to Selective NOE Experiments”, *J. Am. Chem. Soc.* **1995**, *117*, 4199–4200.

[124] T. L. Hwang, A. J. Shaka, “Water Suppression That Works. Excitation Sculpting Using Arbitrary Wave-Forms and Pulsed-Field Gradients”, *J. Magn. Reson. A* **1995**, *112*, 275–279.

[125] Q. N. Van, A. J. Shaka, “Improved cross peak detection in two-dimensional proton NMR spectra using excitation sculpting”, *J. Magn. Reson.* **1998**, *132*, 154–158.

[126] B. Baishya, C. L. Khetrapal, “"Perfect echo" INEPT: more efficient heteronuclear polarization transfer by refocusing homonuclear J-coupling interaction”, *J. Magn. Reson.* **2014**, *242*, 143–154.

[127] L. Castañar, E. Sistaré, A. Virgili, R. T. Williamson, T. Parella, “Suppression of phase and amplitude J(HH) modulations in HSQC experiments”, *Magn. Reson. Chem.* **2015**, *53*, 115–119.

[128] T. Kajitani, K. Okoshi, S.-i. Sakurai, J. Kumaki, E. Yashima, “Helix-sense controlled polymerization of a single phenyl isocyanide enantiomer leading to diastereomeric helical polyisocyanides with opposite helix-sense and cholesteric liquid crystals with opposite twist-sense”, *J. Am. Chem. Soc.* **2006**, *128*, 708–709.

[129] K. C. Wolf, PhD thesis, Technische Universität, Darmstadt, **2018**.

[130] A. Kreiter, PhD thesis, Technische Universität, Darmstadt, **2017**.

[131] J. Furrer, M. John, H. Kessler, B. Luy, “J-Spectroscopy in the presence of residual dipolar couplings: determination of one-bond coupling constants and scalable resolution”, *J. Biomol. NMR* **2007**, *37*, 231–243.

[132] C. M. Thiele, W. Bermel, “Speeding up the measurement of one-bond scalar (1J) and residual dipolar couplings (1D) by using non-uniform sampling (NUS)”, *J. Magn. Reson.* **2012**, *216*, 134–143.

[133] W. Koźmiński, D. Nanz, "HECADE: HMQC- and HSQC-Based 2D NMR Experiments for Accurate and Sensitive Determination of Heteronuclear Coupling Constants from E.COSY-Type Cross Peaks", *J. Magn. Reson.* **1997**, *2*, 383–392.

[134] K. E. Kövér, G. Batta, K. Fehér, "Accurate measurement of long-range heteronuclear coupling constants from undistorted multiplets of an enhanced CPMG-HSQMBC experiment", *J. Magn. Reson.* **2006**, *181*, 89–97.

[135] S. Gil, J. F. Espinosa, T. Parella, "Accurate measurement of small heteronuclear coupling constants from pure-phase alpha/beta HSQMBC cross-peaks", *J. Magn. Reson.* **2011**, *213*, 145–150.

[136] J. Saurí, J. F. Espinosa, T. Parella, "A definitive NMR solution for a simple and accurate measurement of the magnitude and the sign of small heteronuclear coupling constants on protonated and non-protonated carbon atoms", **2012**, *51*, 3919–3922.

[137] J. Sauri, P. Nolis, L. Castanar, A. Virgili, T. Parella, "P.E.HSQMBC: simultaneous measurement of proton-proton and proton-carbon coupling constants", *J. Magn. Reson.* **2012**, *224*, 101–106.

[138] R. Thomas Williamson, Brian L. Márquez, William H. Gerwick, Katalin E. Kövér, "One- and two-dimensional gradient-selected HSQMBC NMR experiments for the efficient analysis of long-range heteronuclear coupling constants", *Magn. Reson. Chem.*, *2000*, 365–273.

[139] S. Gil, J. F. Espinosa, T. Parella, "IPAP-HSQMBC: Measurement of long-range heteronuclear coupling constants from spin-state selective multiplets", *J. Magn. Reson.* **2010**, *207*, 312–321.

[140] H. Koskela, I. Kilpeläinen, S. Heikkinen, "LR-CAHSQC: An application of a Carr–Purcell–Meiboom–Gill-type sequence to heteronuclear multiple bond correlation spectroscopy", *J. Magn. Reson.* **2003**, *164*, 228–232.

[141] I. Timári, L. Szilágyi, K. E. Kövér, "PSYCHE CPMG-HSQMBC: An NMR Spectroscopic Method for Precise and Simple Measurement of Long-Range Heteronuclear Coupling Constants", *Chem. Eur. J.* **2015**, *21*, 13939–13942.

[142] R. Freeman, W. A. Anderson, "Use of Weak Perturbing Radio–Frequency Fields in Nuclear Magnetic Double Resonance", **1962**, *37*, 2053–2073.

[143] H.-O. Kalinowski, St. Berger, S. Braun, *13 C-NMR-Spektroskopie: 200 Tabellen*, Georg Thieme Verlag, Stuttgart-New York, **1984**.

[144] S. Sparks, P. Ellis, "DEPT polarization transfer for the INADEQUATE experiment", *J. Magn. Reson.* **1985**, *62*, 1–11.

[145] P. J. Keller, K. E. Vogele, "Sensitivity enhancement of INADEQUATE by proton monitoring", *J. Magn. Reson.* **1986**, *68*, 389–392.

[146] J. Weigelt, G. Otting, "1H-Detected INEPT-INADEQUATE at Natural 13C Abundance", *J. Magn. Reson. A* **1995**, *113*, 128–130.

[147] B. Reif, M. Köck, R. Kerssebaum, J. Schleucher, C. Griesinger, "Determination of 1J, 2J, and 3J Carbon–Carbon Coupling Constants at Natural Abundance", *J. Magn. Reson. B* **1996**, *112*, 295–301.

[148] M. Köck, R. Kerssebaum, W. Bermel, “A broadband ADEQUATE pulse sequence using chirp pulses”, *Magn. Reson. Chem.* **2003**, *41*, 65–69.

[149] J. R. Garbow, D. P. Weitekamp, A. Pines, “Bilinear rotation decoupling of homonuclear scalar interactions”, *Chem. Phys. Lett.* **1982**, *93*, 504–509.

[150] D. Uhrin, T. Liptaj, K. E. Kover, “Modified BIRD Pulses and Design of Heteronuclear Pulse Sequences”, *J. Magn. Reson. A* **1993**, *101*, 41–46.

[151] A. V. Buevich, R. T. Williamson, G. E. Martin, “NMR Structure Elucidation of Small Organic Molecules and Natural Products: Choosing ADEQUATE vs HMBC”, *J. Nat. Prod.* **2014**, *77*, 1942–1947.

[152] R. A. Edden, J. Keeler, “Development of a method for the measurement of long-range 13C–1H coupling constants from HMBC spectra”, *J. Magn. Reson.* **2004**, *166*, 53–68.

[153] C. L. Dickson, C. D. Blundell, C. P. Butts, A. Felton, A. Jeffreys, Z. Takacs, “Accurate measurement of long range proton-carbon scalar coupling constants”, **2017**, DOI `10.1039/c6an02298g`.

[154] C. P. Butts, B. Heise, G. Tatolo, “SelEXSIDE: Fast and easy measurement of multiple-bond 1H,13C coupling constants for stereochemical analysis”, *Org. Lett.* **2012**, *14*, 3256–3259.

[155] R. R. Schendel, C. Karrer, D. Bunzel, M. Huch, A. A. Hildebrand, S. E. Kulling, M. Bunzel, “Structural Transformation of 8-5-Coupled Dehydrodiferulates by Human Intestinal Microbiota”, *J. Agric. Food Chem.* **2015**, *63*, 7975–7985.

[156] D. Schulze-Sunninghausen, J. Becker, B. Luy, “Rapid heteronuclear single quantum correlation NMR spectra at natural abundance”, *J. Am. Chem. Soc.* **2014**, *136*, 1242–1245.

List of Abbreviations

ADEQUATE	Adequate sensitivity DoublE-QUAntum spEctroscopy
AP	Anti-Phase
BEBE$^{\text{tr}}$	Broadband Excitation and time-reversed Broadband Excitation
BE$^{\text{tr}}$BE	time-reversed Broadband Excitation and Broadband Excitation
BEBOP	Broadband Excitation By Optimized Pulses
BIBOP	Broadband Inversion By Optimized Pulses
BIRD	BIlinear Rotation Decoupling
BUBI	Broadband Universal Broadband Inversion
BUBU	Broadband Universal Broadband Universal
BURBOP	Broadband Universal Rotation By Optimized Pulses
CD	Circular Dichroism
$CDCl_3$	Chloroform-D
CLIP	CLean In-Phase
COSY	COrrelation SpectroscopY
CPMG	Carr-Purcell-Meiboom-Gill
CSA	Chiral Solvating Agent
CS	Compressed Sensing
DC	Dipolar Coupling
8-5(c)-DFA	8-5(c)-DehydrodiFerulate
DMF-d_7	DiMethylFormamide-d_7
DMSO	DiMethyl SulfOxide
EFG	Electric Field Gradient
$Eu(BINOL)_3Li_3$	Tri lithium tris[(*R*)-1,1'-bi-2-naphtholate] europium(III)

Eu(pnb)$_3$	Europium(III) tris[(*R*)-1,1'-binaphthyl-2,2'-diyl phosphate]
Eu(hfc)$_3$	Europium(III) tris[3-(heptafluoropropylhydroxymethylene)-d-camphorate]
FID	Free Induction Decay
FWHM	Full Width at Half Maximum
HECADE	HEteronuclear Couplings from ASSCI-Domain experiments with E.COSY-type cross peaks
HMBC	Heteronuclear Multiple-Bond Correlation
HPLC	High Pressure Liquid Chromatography
HMBC	Heteronuclear Multiple Bond Correlation
HSQC	Heteronuclear Single-Quantum Correlation
HSQMBC	Heteronuclear Single-Quantum Multiple-Bond Correlation
INADEQUATE	Incredible Natural-Abundance DoublE-QUantum Transfer Experiment
INEPT	Insensitive Nuclei Enhanced by Polarization Transfer
IP	In-Phase
(−)-IPC	(−)-IsoPinoCampheol
(+)-IPC	(+)-IsoPinoCampheol
IST	Iterative Soft Thresholding
IRLS	Iterative Re-weighted Least Squares
LR	Low Rank
LSR	Lanthanoide Shift Reagent
ME	Maximum Entropy
MDD	Multidimensional Decomposition
MRI	Magnetic Resonance Imaging
NMR	Nuclear Magnetic Resonance
NOE	Nuclear Overhauser Enhancement
NOESY	Nuclear Overhauser Enhancement SpectroscopY
NUS	Non Uniform Sampling

PAA	Poly(AcrylAmide)
PAN	Poly(AcryloNitrile)
PCBDL	Poly-ϵ-CarboBenzyloxy-D-Lysine
PCBLL	Poly-ϵ-CarboBenzyloxy-L-Lysine
PDMS	Poly(DiMethylSiloxane)
PEDG	Poly-γ-Ethyl-D-Glutamate
PELG	Poly-γ-Ethyl-L-Glutamate
PEO-DA	Poly(Ethylene Oxide)-DiAcrylate
PBDG	Poly-γ-Benzyl-D-Glutamate
PBLG	Poly-γ-Benzyl-L-Glutamate
PCS	Pseudo Contact Shift
PFG	Pulsed Field Gradient
PMMA	Poly(MethylMethAcrylate)
PP	Point-to-Point
PRE	Paramagnetic Relaxation Enhancement
PS	PolyStyrene
PU	PolyUrethane
PVAC	Poly(VinylACetate)
RCSA	Residual Chemical Shift Anisotropy
RDC	Residual Dipolar Coupling
RMS	Root Mean Square
RMSD	Root Mean Square Deviation
RQC	Residual Quadrupolar Coupling
(*R*)-TFB	*R*-(−)-α-(TriFluoromethyl)Benzyl alcohol
SIFT	Spectroscopy by Integration of Frequency and Time Domain
SVD	Singular Value Decomposition
TFE	TriFluoroEthanol

THF	TetraHydroFurane
TOCSY	TOtal Correlation SpectroscopY
UR	Universal Rotation
VCD	Vibrational Circular Dichroism
VE	Virtual Echo

List of Figures

List of Tables

A. Appendix

A.1. Supplementary Information to 8-5(c)-DFA

A.1.1. Pdb-file for the (*R,R*)- or (*S,S*)-Configuration of 8-5(c)-DFA

```
REMARK   This PDB file was created by CS Chem3D.
COMPND    UNNAMED
AUTHOR    GENERATED BY OPEN BABEL 2.3.90
ATOM      1  C   UNK  1      2.440    0.752    1.479  1.00  0.00  C
ATOM      2  C   UNK  1      1.262    0.127    1.103  1.00  0.00  C
ATOM      3  C   UNK  1      1.280   -1.007    0.304  1.00  0.00  C
ATOM      4  C   UNK  1      2.462   -1.564   -0.161  1.00  0.00  C
ATOM      5  C   UNK  1      3.657   -0.942    0.219  1.00  0.00  C
ATOM      6  C   UNK  1      3.656    0.220    1.026  1.00  0.00  C
ATOM      7  C   UNK  1      4.947    0.811    1.405  1.00  0.00  C
ATOM      8  C   UNK  1      5.172    2.134    1.445  1.00  0.00  C
ATOM      9  C   UNK  1      6.465    2.727    1.812  1.00  0.00  C
ATOM     10  C   UNK  1     -0.148    0.513    1.396  1.00  0.00  C
ATOM     11  C   UNK  1     -0.850   -0.783    0.945  1.00  0.00  C
ATOM     12  O   UNK  1      0.025   -1.489    0.021  1.00  0.00  O
ATOM     13  C   UNK  1     -0.594    1.734    0.627  1.00  0.00  C
ATOM     14  C   UNK  1     -2.241   -0.630    0.359  1.00  0.00  C
ATOM     15  O   UNK  1     -1.572    2.409    1.271  1.00  0.00  O
ATOM     16  O   UNK  1     -0.180    2.139   -0.446  1.00  0.00  O
ATOM     17  C   UNK  1     -3.354   -0.571    1.215  1.00  0.00  C
ATOM     18  C   UNK  1     -4.635   -0.394    0.696  1.00  0.00  C
ATOM     19  C   UNK  1     -4.802   -0.271   -0.677  1.00  0.00  C
ATOM     20  C   UNK  1     -3.715   -0.320   -1.555  1.00  0.00  C
ATOM     21  C   UNK  1     -2.435   -0.500   -1.030  1.00  0.00  C
ATOM     22  O   UNK  1     -6.070   -0.093   -1.160  1.00  0.00  O
ATOM     23  O   UNK  1      6.679    3.925    1.868  1.00  0.00  O
ATOM     24  O   UNK  1      7.421    1.827    2.090  1.00  0.00  O
ATOM     25  O   UNK  1      2.347   -2.678   -0.940  1.00  0.00  O
ATOM     26  C   UNK  1      3.546   -3.227   -1.468  1.00  0.00  C
ATOM     27  O   UNK  1     -4.035   -0.176   -2.881  1.00  0.00  O
ATOM     28  C   UNK  1     -2.949   -0.219   -3.802  1.00  0.00  C
ATOM     29  H   UNK  1      2.412    1.636    2.110  1.00  0.00  H
ATOM     30  H   UNK  1      4.613   -1.338   -0.110  1.00  0.00  H
```

```
ATOM   31  H   UNK  1    5.742    0.105    1.634  1.00   0.00   H
ATOM   32  H   UNK  1    4.407    2.859    1.194  1.00   0.00   H
ATOM   33  H   UNK  1   −0.289    0.686    2.469  1.00   0.00   H
ATOM   34  H   UNK  1   −0.934   −1.457    1.812  1.00   0.00   H
ATOM   35  H   UNK  1   −1.811    3.132    0.652  1.00   0.00   H
ATOM   36  H   UNK  1   −3.231   −0.661    2.292  1.00   0.00   H
ATOM   37  H   UNK  1   −5.498   −0.350    1.354  1.00   0.00   H
ATOM   38  H   UNK  1   −1.565   −0.536   −1.680  1.00   0.00   H
ATOM   39  H   UNK  1   −5.961   −0.045   −2.130  1.00   0.00   H
ATOM   40  H   UNK  1    8.201    2.378    2.310  1.00   0.00   H
ATOM   41  H   UNK  1    3.276   −4.089   −2.087  1.00   0.00   H
ATOM   42  H   UNK  1    4.063   −2.506   −2.110  1.00   0.00   H
ATOM   43  H   UNK  1    4.201   −3.586   −0.667  1.00   0.00   H
ATOM   44  H   UNK  1   −3.361   −0.092   −4.808  1.00   0.00   H
ATOM   45  H   UNK  1   −2.248    0.604   −3.624  1.00   0.00   H
ATOM   46  H   UNK  1   −2.442   −1.188   −3.770  1.00   0.00   H
CONECT    1    6    2   29
CONECT    2    1   10    3
CONECT    3    2   12    4
CONECT    4    3   25    5
CONECT    5    4    6   30
CONECT    6    1    5    7
CONECT    7    6    8   31
CONECT    8    7    9   32
CONECT    9    8   23   24
CONECT   10    2   13   11   33
CONECT   11   10   14   12   34
CONECT   12    3   11
CONECT   13   10   15   16
CONECT   14   11   17   21
CONECT   15   13   35
CONECT   16   13
CONECT   17   14   18   36
CONECT   18   17   19   37
CONECT   19   18   22   20
CONECT   20   19   27   21
CONECT   21   14   20   38
CONECT   22   19   39
CONECT   23    9
CONECT   24    9   40
CONECT   25    4   26
CONECT   26   25   41   42   43
CONECT   27   20   28
CONECT   28   27   44   45   46
CONECT   29    1
```

```
CONECT   30    5
CONECT   31    7
CONECT   32    8
CONECT   33   10
CONECT   34   11
CONECT   35   15
CONECT   36   17
CONECT   37   18
CONECT   38   21
CONECT   39   22
CONECT   40   24
CONECT   41   26
CONECT   42   26
CONECT   43   26
CONECT   44   28
CONECT   45   28
CONECT   46   28
MASTER    0  0  0  0  0  0  0  0  46  0  46  0
END
```

A.1.2. Pdb-File for the (*R*,*S*)- or (*S*,*R*)-Configuration of 8-5(c)-DFA

```
REMARK   This PDB file was created by CS Chem3D.
COMPND    UNNAMED
AUTHOR    GENERATED BY OPEN BABEL 2.3.90
HETATM    1  C   UNK  1    -2.400   -3.687   -0.492  1.00   0.00  C
HETATM    2  C   UNK  1    -3.518   -3.323    0.154  1.00   0.00  C
HETATM    3  C   UNK  1    -4.775   -4.080    0.092  1.00   0.00  C
HETATM    4  C   UNK  1     1.243   -0.961    1.837  1.00   0.00  C
HETATM    5  C   UNK  1     2.325   -0.211    1.032  1.00   0.00  C
HETATM    6  O   UNK  1     2.402   -0.798   -0.299  1.00   0.00  O
HETATM    7  C   UNK  1     0.430   -0.079    2.744  1.00   0.00  C
HETATM    8  C   UNK  1     2.172    1.298    0.879  1.00   0.00  C
HETATM    9  O   UNK  1     1.161    0.409    3.769  1.00   0.00  O
HETATM   10  O   UNK  1    -0.761    0.175    2.669  1.00   0.00  O
HETATM   11  C   UNK  1     3.105    2.154    1.490  1.00   0.00  C
HETATM   12  C   UNK  1     2.973    3.538    1.385  1.00   0.00  C
HETATM   13  C   UNK  1     1.908    4.068    0.672  1.00   0.00  C
HETATM   14  C   UNK  1     0.961    3.247    0.052  1.00   0.00  C
HETATM   15  C   UNK  1     1.102    1.862    0.154  1.00   0.00  C
HETATM   16  O   UNK  1     1.797    5.430    0.589  1.00   0.00  O
HETATM   17  O   UNK  1    -5.797   -3.766    0.676  1.00   0.00  O
HETATM   18  O   UNK  1    -4.716   -5.176   -0.679  1.00   0.00  O
HETATM   19  H   UNK  1     3.297   -0.412    1.501  1.00   0.00  H
HETATM   20  H   UNK  1     1.697   -1.757    2.441  1.00   0.00  H
```

```
HETATM  21  O   UNK  1    1.663  -1.954  -2.709  1.00  0.00 O
HETATM  22  C   UNK  1    1.277  -2.578  -3.925  1.00  0.00 C
HETATM  23  O   UNK  1   -0.038   3.912  -0.612  1.00  0.00 O
HETATM  24  C   UNK  1   -1.055   3.107  -1.198  1.00  0.00 C
HETATM  25  H   UNK  1   -1.246  -2.428   1.671  1.00  0.00 H
HETATM  26  H   UNK  1   -0.741  -3.297  -2.522  1.00  0.00 H
HETATM  27  H   UNK  1   -2.385  -4.578  -1.116  1.00  0.00 H
HETATM  28  H   UNK  1   -3.570  -2.426   0.762  1.00  0.00 H
HETATM  29  H   UNK  1    0.532   0.980   4.263  1.00  0.00 H
HETATM  30  H   UNK  1    3.943   1.750   2.054  1.00  0.00 H
HETATM  31  H   UNK  1    3.696   4.199   1.855  1.00  0.00 H
HETATM  32  H   UNK  1    0.390   1.198  -0.325  1.00  0.00 H
HETATM  33  H   UNK  1    1.004   5.581   0.040  1.00  0.00 H
HETATM  34  H   UNK  1   -5.616  -5.556  -0.611  1.00  0.00 H
HETATM  35  H   UNK  1    2.047  -2.362  -4.672  1.00  0.00 H
HETATM  36  H   UNK  1    0.331  -2.170  -4.295  1.00  0.00 H
HETATM  37  H   UNK  1    1.220  -3.666  -3.810  1.00  0.00 H
HETATM  38  H   UNK  1   -1.788   3.778  -1.657  1.00  0.00 H
HETATM  39  H   UNK  1   -0.646   2.470  -1.989  1.00  0.00 H
HETATM  40  H   UNK  1   -1.576   2.513  -0.440  1.00  0.00 H
HETATM  41  C   UNK  1   -0.686  -2.333   0.745  1.00  0.00 C
HETATM  42  C   UNK  1    0.506  -1.625   0.723  1.00  0.00 C
HETATM  43  C   UNK  1    1.248  -1.529  -0.444  1.00  0.00 C
HETATM  44  C   UNK  1    0.841  -2.120  -1.632  1.00  0.00 C
HETATM  45  C   UNK  1   -0.370  -2.821  -1.620  1.00  0.00 C
HETATM  46  C   UNK  1   -1.147  -2.919  -0.444  1.00  0.00 C
CONECT    1   27   46    2
CONECT    2    1   28    3
CONECT    3    2   17   18
CONECT    4   20   42    7    5
CONECT    5    4   19    6    8
CONECT    6    5   43
CONECT    7    4    9   10
CONECT    8    5   15   11
CONECT    9    7   29
CONECT   10    7
CONECT   11    8   12   30
CONECT   12   11   31   13
CONECT   13   12   14   16
CONECT   14   13   23   15
CONECT   15    8   14   32
CONECT   16   13   33
CONECT   17    3
CONECT   18    3   34
CONECT   19    5
```

```
CONECT   20    4
CONECT   21   44   22
CONECT   22   21   35   36   37
CONECT   23   14   24
CONECT   24   23   38   39   40
CONECT   25   41
CONECT   26   45
CONECT   27    1
CONECT   28    2
CONECT   29    9
CONECT   30   11
CONECT   31   12
CONECT   32   15
CONECT   33   16
CONECT   34   18
CONECT   35   22
CONECT   36   22
CONECT   37   22
CONECT   38   24
CONECT   39   24
CONECT   40   24
CONECT   41   25   46   42
CONECT   42    4   41   43
CONECT   43    6   42   44
CONECT   44   21   43   45
CONECT   45   26   44   46
CONECT   46    1   41   45
MASTER  0  0  0  0  0  0  0  0 46  0 46  0
END
```

A.1.3. RDC Input File for the(*R*,*R*)- or (*S*,*S*)-Configuration of 8-5(c)-DFA Measured in PEO-DA

```
rdc_data {
        #C20H20  (Methyl)
        12       25      3.8     0.2
        12       27      3.8     0.2
        12       29      3.8     0.2
        #C19H19  (Methyl)
        14       30      0.8             0.1
        14       31      0.8             0.1
        14       32      0.8             0.1
        #C14H14
        5        22      −5.5    0.2
        #C17H17
```

```
        2        21        −6.0      0.2
        #C18H18
        1        20        −2.6      0.2
        #C10H10
        26       9         35.3      0.3
        #C11H11
        44       10        25.8      0.5
        #C9H9
        39       15        −0.7      0.4
        #C5H5
        43       16        −19.1     0.3
        #C3H3
        37       17        −3.0      0.3
        #C2H2
        38       18        −0.1      0.2
        #C12H10
        #46      9         −15.8     0.9
}
```

Table A.1.: Calculated versus Experimental RDCs for the (*R,R*)- or (*S,S*)- configuration of 8-5(c)-DFA in PEO-DA.

Assignment	$^1J_{\mathrm{CH\ exp}}$ [Hz]	$^1J_{\mathrm{CH\ calc}}$ [Hz]
A-C10	3.8 ± 0.2	2.86 ± 0.04
A-C10	3.8 ± 0.2	2.86 ± 0.04
A-C10	3.8 ± 0.2	2.86 ± 0.04
B-C10	0.8 ± 0.1	3.20 ± 0.04
B-C10	0.8 ± 0.1	3.20 ± 0.04
B-C10	0.8 ± 0.1	3.20 ± 0.04
B-C2	−5.5 ± 0.2	−10.59 ± 0.12
B-C5	−6.0 ± 0.2	−10.54 ± 0.12
B-C6	−2.6 ± 0.2	−3.54 ± 0.17
B-C8	35.3 ± 0.3	35.39 ± 0.25
B-C7	25.8 ± 0.5	25.04 ± 0.37
A-C6	−0.7 ± 0.4	−1.62 ± 0.30
A-C2	−19.1 ± 0.3	−9.94 ± 0.12
A-C7	−3.0 ± 0.3	−1.41 ± 0.14
A-C8	−0.1 ± 0.2	−1.03 ± 0.14

Table A.2.: Calculated versus Experimental RDCs for the (*R*,*S*)- or (*S*,*R*)-Configuration of 8-5(c)-DFA in PEO-DA.

Assignment	$^1J_{\mathrm{CH\ exp}}$ [Hz]	$^1J_{\mathrm{CH\ calc}}$ [Hz]
A-C10	3.8 ± 0.2	5.48 ± 0.09
A-C10	3.8 ± 0.2	5.48 ± 0.09
A-C10	3.8 ± 0.2	5.48 ± 0.09
B-C10	0.8 ± 0.1	2.46 ± 0.05
B-C10	0.8 ± 0.1	2.46 ± 0.05
B-C10	0.8 ± 0.1	2.46 ± 0.05
B-C2	−5.5 ± 0.2	−9.75 ± 0.14
B-C5	−6.0 ± 0.2	−9.60 ± 0.14
B-C6	−2.6 ± 0.2	13.19 ± 0.26
B-C8	35.3 ± 0.3	21.21 ± 0.32
B-C7	25.8 ± 0.5	6.88 ± 0.32
A-C6	−0.7 ± 0.4	−13.25 ± 0.27
A-C2	−19.1 ± 0.3	−15.36 ± 0.27
A-C7	−3.0 ± 0.3	−6.71 ± 0.18
A-C8	−0.1 ± 0.2	−5.86 ± 0.19

A.2. Pulse Programs for Phase-encoded and Slice Selective Excited Spectra

All pulse programs are in the Bruker Topspin format.

A.2.1. Pulse Program for Slice Selectively Excited Deuterium Spectrum

```
;zgesgp
;avance-version (12/01/11)
;1D sequence
;water suppression using excitation sculpting with gradients
;T.-L. Hwang & A.J. Shaka, J. Magn. Reson.,
;   Series A 112 275-279 (1995)
;
;$CLASS=HighRes
;$DIM=1D
;$TYPE=
;$SUBTYPE=
;$COMMENT=

prosol relations=<triple>

#include <Avance.incl>
#include <Grad.incl>
#include <Delay.incl>

"p2=p1*2"
"d12=20u"
"d11=30m"

"TAU=de+p1*2/3.1416+50u"

"acqt0=0"
baseopt_echo

1 ze
d11 LOCKDEC_ON
d11 H2_PULSE
2 30m
d12 pl1:f1 BLKGRAD
d1
p1 ph1

50u UNBLKGRAD
```

```
p16:gp1
d16 pl0:f1
50u
50u gron3
p12:sp1:f1 ph1
50u groff
4u
d12 pl1:f1

;  p2 ph3

4u
p16:gp1
d16
TAU
p16:gp2
d16 pl0:f1
50u
50u gron3
p12:sp1:f1 ph1
50u groff
4u
d12 pl1:f1

;  p2 ph5

4u
p16:gp2
d16

go=2 ph31
30m mc #0 to 2 F0(zd)
4u BLKGRAD

d11 H2_LOCK
d11 LOCKDEC_OFF
exit

ph1=0
ph2=0 1
ph3=2 3
ph4=0 0 1 1
ph5=2 2 3 3
ph31=0 ;2 2 0

```

```
;pl0 : 0W
;pl1 : f1 channel - power level for pulse (default)
;sp1 : f1 channel - shaped pulse 180 degree
;p1 : f1 channel -  90 degree high power pulse
;p2 : f1 channel - 180 degree high power pulse
;p12: f1 channel - 180 degree shaped pulse (Squa100.1000)   [2 msec]
;p16: homospoil/gradient pulse
;d1 : relaxation delay; 1-5 * T1
;d12: delay for power switching                             [20 usec]
;d16: delay for homospoil/gradient recovery
;ns: 8 * n, total number of scans: NS * TD0
;ds: 4

;use gradient ratio:    gp 1 : gp 2
;                         31 :   11

;for z-only gradients:
;gpz1: 31%
;gpz2: 11%

;use gradient files:
;gpnam1: SMSQ10.100
;gpnam2: SMSQ10.100

;$ Id: zgesgp,v 1.8.6.1 2012/01/31 17:56:41 ber Exp $
```

A.2.2. Pulse Program for Slice Selectively Excited Phase-Encoded Deuterium Spectrum

```
;2D sequence for z-imaging preserving chemical shift
;using a phase encoding gradient with slice selective excitation
; 2H-Version
;$CLASS=HighRes
;$DIM=2D
;$TYPE=
;$SUBTYPE=
;$COMMENT=
; after the experiment, 2h-lock might be deactivated
; run a regular proton experiment to reactivate

#include <Avance.incl>
#include <Grad.incl>
#include <Delay.incl>
#include<Sysconf.incl>

```

```
"cnst1=50.71736*0.95*0.8914027" ; gradient*integralfactor Gs/cm
"cnst2=41.07" ; gamma2H MTs
"p30=(td1/cnst0) * (1/cnst1) * (1/cnst2) *(2*3.14159265/100)* 0.5 s"

"l1=td1-1"
lgrad r1d = l1

"acqt0=-d21-p30-p1*2/3.1416"

1 ze
30m LOCKDEC_ON  ;this allows for 2h decoupling...?
30m H2_PULSE            ;switch off lock
30m H2_LOCK             ;switch on lock during d1
2 30m H2_LOCK           ;switch on lock during d1
3 d1
50u H2_PULSE UNBLKGRAD ;lock off for whole experiment
p16:gp4
d16
p1 ph1

50u UNBLKGRAD
p16:gp1
d16 pl0:f1
50u
50u gron3
p12:sp1:f1 ph1
50u groff
4u
d12 pl1:f1

;  p2 ph3

4u
p16:gp1
d16
TAU
p16:gp2
d16 pl0:f1
50u
50u gron3
p12:sp1:f1 ph1
50u groff
4u
d12 pl1:f1

```

```
;  p2 ph5

4u
p16:gp2
d16 BLKGRAMP

p30:gp6*r1d*0.95
5u
d21 BLKGRAD
go=2 ph31
30m H2_LOCK             ;switch on lock during d1
d1 wr #0 if #0 zd igrad r1d
lo to 3 times l1
goto 5
; dumme gradientenfunktion läuft nicht bis 1
; also noch einmal durchlaufen lassen mit r1d=1

4 30m H2_LOCK           ;switch on lock during d1
d1

5 50u H2_PULSE UNBLKGRAD ;lock off for whole experiment
p16:gp4
d16
p1 ph1

50u UNBLKGRAD
p16:gp1
d16 pl0:f1
50u
50u gron3
p12:sp1:f1 ph1
50u groff
4u
d12 pl1:f1

;  p2 ph3

4u
p16:gp1
d16
TAU
p16:gp2
d16 pl0:f1
50u
50u gron3
```

```
p12:sp1:f1 ph1
50u groff
4u
d12 pl1:f1

;  p2 ph5

4u
p16:gp2
d16 BLKGRAMP
p30:gp6*1*0.95
5u
d21 BLKGRAD
go=4 ph31

30m H2_LOCK
d1 wr #0 if #0 zd
30m LOCKDEC_OFF
exit

ph1=0 2 1 3
ph31=0 2 1 3

;sp1: f1 channel - shaped 180 degree pulse
;spnam1: Q3.1000
;p11: f1 channel -  180 degree shaped pulse
;cnst0 : z-Range in cm
;pl1 : f1 channel - power level for pulse (default)
;p1  : f1 channel -  90 degree high power pulse
;gpz6: 100% phase encoding gradient
;d1  : relaxation delay; 1-5 * T1
;d21: eddy current delay (Te)                   [100 us]
;NS: 1 * n
;DS: 1 * m
;td1: number of experiments
;FnMODE: QF

;choose p11 according to desired selectivity of the z-slice
;the flip-angle is determined by the amplitude
;use spoffs1 to set the spatial selectivity. If 0 (zero) the
;experiment is collected at the center of the coil
;use spoal1 = 1
; vary spoffs1 for different slice selection

;use gradient files:
```

```
;gpnam6: SMSQ10.32

;use phase PHC1:F1
;1 phc1 360*td1/2

;$Id: ledbpgp2s,v 1.7 2009/07/02 16:40:45 ber Exp $
```

A.2.3. Pulse Program for Slice Selectively Excited ^{13}C Spectrum

```
zg13c_zslice
;avance-version (06/03/21)
;1D sequence
;selective 13c excitation using a shaped pulse
;in presense of a z-gradient
;
;$CLASS=HighRes
;$DIM=1D
;$TYPE=
;$SUBTYPE=
;$COMMENT=
#include<Avance.incl>
#include<Sysconf.incl>
#include<Grad.incl>
"d11=30m"
"acqt0=-54u"
1 ze
d11 pl12:f2
2 30m do:f2
d1
4u pl0:f1
50u UNBLKGRAMP
50u gron1
p11:sp1:f1 ph1
50u groff
4u BLKGRAMP
go=2 ph31 cpd2:f2
30m do:f2 mc #0 to 2 F0(zd)
d11
d11
exit
ph1=0 2 2 0 1 3 3 1
ph31=0 2 2 0 1 3 3 1
;sp1: f1 channel - shaped ninety degree pulse
;spnam1: Q5.1000
;p11: f1 channel -  90 (or 270) degree shaped pulse
```

```
;d1 : relaxation delay; 1-5 * T1
;d11: delay for disk I/O                             [30 msec]
;NS: 1 * n, total number of scans: NS * TD0
;gpz1: gradient strength
;choose p11 according to desired selectivity of the z-slice
;the flip-angle is determined by the amplitude
;use spoffs1 to set the spatial selectivity. If 0 (zero) the
;experiment is collected at the center of the coil
;use spoal1 = 1
; vary spoffs1 for different slice selection
```

A.2.4. Pulse Program for Phase-Encoded ^{13}C Spectrum

```
;2D sequence for z-imaging preserving carbon chemical shift
;using a phase encoding gradien
;with gated decoupling
;
;$CLASS=HighRes
;$DIM=2D
;$TYPE=
;$SUBTYPE=
;$COMMENT=


#include <Avance.incl>
#include <Grad.incl>
#include <Delay.incl>

"p2=p1*2"
"cnst1=50.71736*0.95*0.8914027" ; gradient*integralfactor Gs/cm
"cnst2=67.262" ; gamma13C MTs
"p30=(td1/cnst0) * (1/cnst1) * (1/cnst2) *(2*3.14159265/100)* 0.5 s"
"DELTA2=p30+d21+4u"

"l1=td1-1"
lgrad r1d = l1

"acqt0=-d21-p30-p1*2/3.1416"

1 ze
30m pl12:f2
2 d1
do:f2
3 50u UNBLKGRAD
p1 ph1
```

```
DELTA2
p2 ph1
4u
p30:gp6*r1d*0.95
d21 BLKGRAD
go=2 ph31 cpd2:f2

;  d1 mc #0 to 2 F1QF(igrad r1d)
d1 do:f2 wr #0 if #0 zd igrad r1d
lo to 3 times l1

; dumme gradientenfunktion läuft nicht bis 1
; also noch einmal durchlaufen lassen mit r1d=1
goto 5
4 d1
do:f2

5 50u UNBLKGRAD
p1 ph1
DELTA2
p2 ph1
4u
p30:gp6*1*0.95
d21 BLKGRAD
go=4 ph31 cpd2:f2
d1 do:f2  wr #0 if #0 zd
exit


ph1= 0 2 1 3
ph31=0 2 1 3

;cnst0 : z-Range in cm
;pl1 : f1 channel - power level for pulse (default)
;p1  : f1 channel -  90 degree high power pulse
;gpz6: 100% phase encoding gradient
;d1  : relaxation delay; 1-5 * T1
;d21: eddy current delay (Te)                   [100 us]
;NS: 1 * n
;DS: 1 * m
;td1: number of experiments
;FnMODE: QF

;use gradient files:
;gpnam6: SMSQ10.32
```

```

;use phase PHC1:F1
;1 phcl 360*td1/2

;$Id: ledbpgp2s,v 1.7 2009/07/02 16:40:45 ber Exp $
```

A.2.5. Phase-Encoded Carbon Spectrum of the Mixed Polymer Sample *poly*-**1** and *poly*-**2**

The spectrum shown in Figure A.1 was recorded with 65 536 points in the direct dimension and 64 points in the indirect dimension with a sweep width for the direct dimension of 251.163 ppm and a corresponding acquisition time of 0.865 s. The recovery delay was set to 5 s. The spectrum was measured with 0 dummy scans and 32 scans per increment leading to an overall experimental time 5 h 41 min. The z-range was set to 5 cm. The gradient length for the phase-enconding was calculated to 139.2 s and the maximal gradient strength was 95 %. The spectrum was processed with 262 144 points and 64 points. To the direct dimension an exponential apodization function was multiplied. No apodization was multiplied to the indirect dimension. The spectrum was processed in magnitude mode.

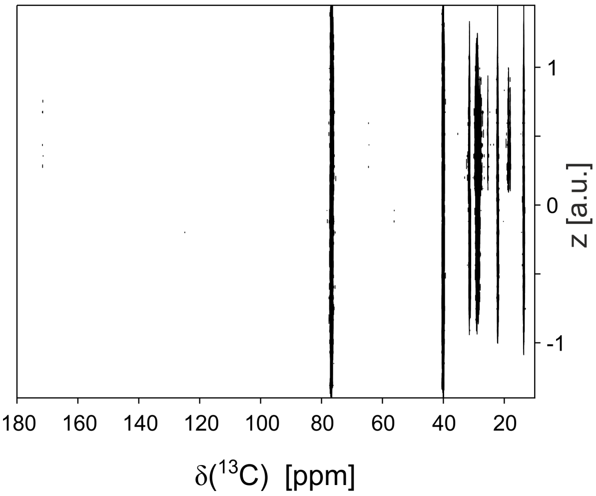

Figure A.1.: Phase-encoded carbon spectrum for the biphasic two polymer sample for **1** and **2**. The spectrum shows clearly the two phases and that the two polymers do not blend. The signal at 77 ppm is the chloroform signal. The signal at 40 ppm is resulting from the DMSO capillary in the sample.

A.2.6. 1D ^{13}C Spectra of 1 and 2

The 1D ^{13}C spectra for the monomer **1** and the monomer **2** are shown in Figure A.2 and Figure A.3, respectively.

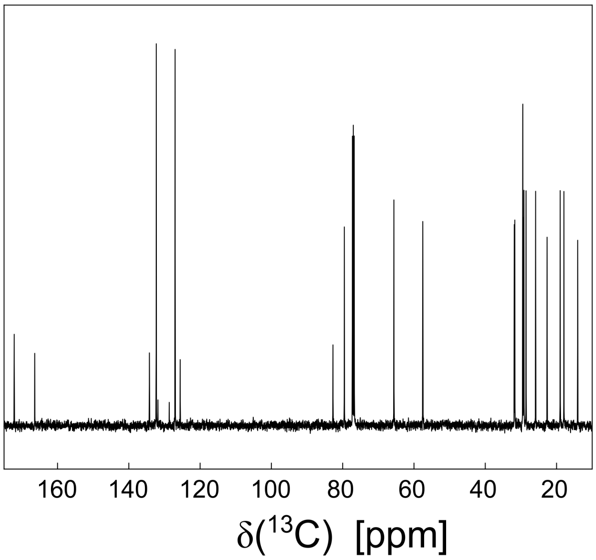

Figure A.2.: 1D ^{13}C spectrum for the monomer **1**.

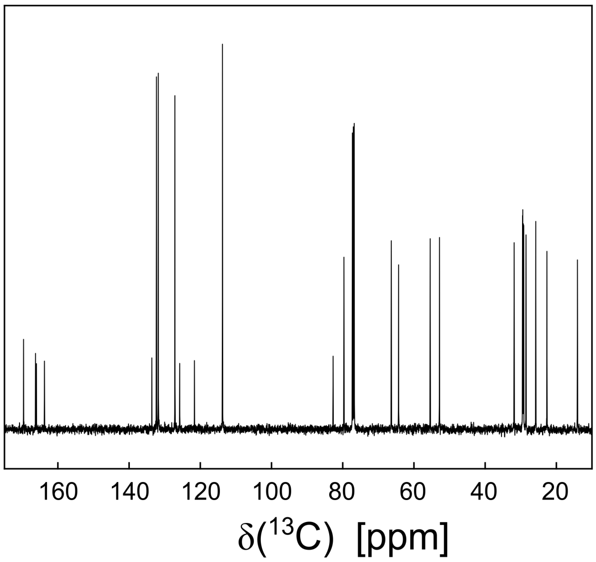

Figure A.3.: 1D ^{13}C spectrum for the monomer **2**.

A.2.7. Pulse Program for Slice Selectively Excited CLIP-HSQC Spectrum

```
;hsqcetgpsp.2
;avance-version (12/01/11)
;HSQC
;2D H-1/X correlation via double inept transfer
;phase sensitive using Echo/Antiecho-TPPI gradient selection
;with decoupling during acquisition
;using trim pulses in inept transfer
;using shaped pulses for inversion and refocussing on f2 - channel
;
;$CLASS=HighRes
;$DIM=2D
;$TYPE=
;$SUBTYPE=
;$COMMENT=

#include <Avance.incl>
#include <Grad.incl>
#include <Delay.incl>

"p2=p1*2"
"d4=1s/(cnst2*4)"
"d11=30m"

#   ifdef LABEL_CN
"p22=p21*2"
#   else
#   endif /*LABEL_CN*/

"d0=3u"

"in0=inf1/2"

"TAU=de+p1*2/3.1416+50u"

"DELTA1=d4-p16-larger(p2,p14)/2-de-8u-p3"
"DELTA2=d4-larger(p2,p14)/2"
"DELTA3=d4-p2/2-p1*2/PI"

#   ifdef LABEL_CN
"DELTA=p16+d16+larger(p2,p22)+d0*2"
#   else
"DELTA=p16+d16+p2+d0*2"
#   endif /*LABEL_CN*/
```

```

"acqt0=0"
baseopt_echo

1 ze
d11
2 d1
3 (p1 ph1)
;excitation sculpting
50u UNBLKGRAD
p16:gp3
d16 pl=0[Watt]:f1
4u
50u gron5
p12:sp1:f1 ph1
50u groff
4u
p16:gp3
d16
TAU
p16:gp4
d16
4u
50u gron5
p12:sp1:f1 ph1
50u groff

4u pl1:f1
p16:gp4
d16
;excitation sculpting end

DELTA2 pl0:f2
4u
(center (p2 ph1) (p14:sp3 ph6):f2 )
4u
DELTA2 pl2:f2 UNBLKGRAD
;p28 ph1
;4u
(p1 ph2) (p3 ph3):f2
d0

#   ifdef LABEL_CN
(center (p2 ph5) (p22 ph1):f3 )
#   else
```

```
(p2 ph5)
#   endif /*LABEL_CN*/

d0
p16:gp1*EA
d16 pl0:f2
4u
(p24:sp7 ph4):f2
4u
DELTA pl2:f2
(ralign (p1 ph1) (p3 ph4):f2 )
DELTA3 pl0:f2
(p2 ph2)
d4
(p1 ph2)
DELTA2
(center (p2 ph2) (p14:sp3 ph2):f2 )
4u
p16:gp2
DELTA1 pl2:f2
4u BLKGRAD
(p3 ph8):f2
go=2 ph31
d1  mc #0 to 2
F1EA(calgrad(EA), caldel(d0, +in0) & calph(ph3, +180) & calph(ph6, +180) & calph(ph31, +180))
exit

ph1=0
ph2=1
ph3=0 2
ph4=0 0 0 0 2 2 2 2
ph5=0 0 2 2
ph6=0
ph8=0 2
ph31=0 2 0 2 2 0 2 0

;pl0 : 0W
;pl1 : f1 channel - power level for pulse (default)
;pl2 : f2 channel - power level for pulse (default)
;pl3 : f3 channel - power level for pulse (default)
;pl12: f2 channel - power level for CPD/BB decoupling
;sp1: inversion pulse Q3.1000
;spnam1: Q3.1000
;sp3: f2 channel - shaped pulse 180 degree for inversion
```

```
;spnam3: jc03_BIBOP_600u_BW37.5_RF10_pm5_matched.pul
;sp7: f2 channel - shaped pulse 180 degree for refocussing
;spnam7: jc07_BURBOP_y_1100u_BW37.5_RF10_pm5_Hc0.999876221.pul
;p1 : f1 channel -  90 degree high power pulse
;p2 : f1 channel - 180 degree high power pulse
;p3 : f2 channel -  90 degree high power pulse
;p14: f2 channel - 180 degree shaped pulse for inversion
;p16: homospoil/gradient pulse
;p22: f3 channel - 180 degree high power pulse
;p24: f2 channel - 180 degree shaped pulse for refocussing
;p28: f1 channel - trim pulse
;d0 : incremented delay (2D)                         [3 usec]
;d1 : relaxation delay; 1-5 * T1
;d4 : 1/(4J)XH
;d11: delay for disk I/O                             [30 msec]
;d16: delay for homospoil/gradient recovery
;cnst2: = J(XH)
;inf1: 1/SW(X) = 2 * DW(X)
;in0: 1/(2 * SW(X)) = DW(X)
;nd0: 2
;ns: 1 * n
;ds: >= 16
;td1: number of experiments
;FnMODE: echo-antiecho

;use gradient ratio:    gp 1 : gp 2
;                         80 : 20.1    for C-13
;                         80 :  8.1    for N-15

;for z-only gradients:
;gpz1: 80%
;gpz2: 20.1% for C-13, 8.1% for N-15
;gpz3: 31%
;gpz4: 11%
;gpz5: 11.36%

;use gradient files:
;gpnam1: SMSQ10.100
;gpnam2: SMSQ10.100
;gpnam3: SMSQ10.100
;gpnam4: SMSQ10.100

;preprocessor-flags-start
;LABEL_CN: for C-13 and N-15 labeled samples start experiment with
;             option -DLABEL_CN (eda: ZGOPTNS)
```

```
;preprocessor-flags-end

;$Id: hsqcetgpsp.2,v 1.7.2.1.4.1 2012/01/31 17:56:32 ber Exp $
```

A.2.8. Pulse Program for Phase-Encoded CLIP-HSQC Spectrum

```
;hsqcgpph
;avance-version (13/09/11)
;HSQC
;2D H-1/X correlation via double inept transfer
;phase sensitive
;with decoupling during acquisition
;peak type selection using gradient pulses with coherence selection
;   step before t1
;use pulseprogram ’hsqcgpnd1d’ for setup
;
;$CLASS=HighRes
;$DIM=2D
;$TYPE=
;$SUBTYPE=
;$COMMENT=

#include <Avance.incl>
#include <Grad.incl>
#include <Delay.incl>

"p2=p1*2"
"p4=p3*2"
"d4=1s/(cnst2*4)"
"d11=30m"

"d0=3u"

"in0=inf1/2"

"DELTA=d0*2+p2"
"DELTA1=p16+d16+4u"
"DELTA2=d4-p16-d16-de+p1*2/PI-4u -d21 -p30 -p3" ; one ’-4u’ changed to ’-p3’ for clip-pulse

;imaging calculations
"cnst11=55.7*0.95*0.8914027" ; gradient*integralfactor Gs/cm
"cnst12=267.5" ; gammaH MTs
"p30=(100/cnst6)*(td2/cnst10) * (1/cnst11) * (1/cnst12) *(2*3.14159265/100)* 0.5 s"
```

```

"l1=td2-1"
lgrad r1d = l1
;end of imaging calc

"acqt0=0"
baseopt_echo

1  ze
d11 ;pl12:f2
2  d1 do:f2
3  (p1 ph1)
d4 pl2:f2
(center (p2 ph2) (p4 ph6):f2 )
d4
(p1 ph3) (p3 ph7):f2
DELTA1 UNBLKGRAD
(p4 ph8):f2
4u
p16:gp1
d16
(p3 ph9):f2
4u
p16:gp2
d16
(p3 ph10):f2
d0
(p2 ph4)
d0
(p4 ph11):f2
DELTA
(p3 ph11):f2
(p1 ph3)
d4
(center (p2 ph5) (p4 ph12):f2 )
4u
p16:gp3
d16
;IMAGING GRADIENT
p30:gp6*r1d*0.95
d21
;IMAGING GRADIENT
DELTA2 BLKGRAD ;pl12:f2
(p3 ph1):f2
go=2 ph31 ;cpd2:f2
```

```
d1 do:f2 mc #0 to 2
F2QF(calgrad(r1d))
F1PH(calph(ph10, +90), caldel(d0, +in0))
exit

ph1=0
ph2=0
ph3=1
ph4=0 0 2 2
ph5=0
ph6=0
ph7=1 1 1 1 3 3 3 3
ph8=0
ph9=3
ph10=0
ph11=0 2
ph12=0
ph31=0 2 0 2 2 0 2 0

;pl1 : f1 channel - power level for pulse (default)
;pl2 : f2 channel - power level for pulse (default)
;pl12: f2 channel - power level for CPD/BB decoupling
;p1 : f1 channel -  90 degree high power pulse
;p2 : f1 channel - 180 degree high power pulse
;p3 : f2 channel -  90 degree high power pulse
;p4 : f2 channel - 180 degree high power pulse
;p16: homospoil/gradient pulse
;d21: delay for imaging gradient recovery/ eddy currents
;d0 : incremented delay (2D)                  [3 usec]
;d1 : relaxation delay; 1-5 * T1
;d4 : 1/(4J)XH
;d11: delay for disk I/O                              [30 msec]
;d16: delay for homospoil/gradient recovery
;cnst10 : z-Range in cm [3]
;cnst2: = J(XH)
;cnst6 : 100; set equal to gpz6 gradient strength [100]
;inf1: 1/SW(X) = 2 * DW(X)
;in0: 1/(2 * SW(X)) = DW(X)
;nd0: 2
;ns: 1 * n
;ds: 16
;td1: number of experiments
;FnMODE: States-TPPI, TPPI, States or QSEQ
;cpd2: decoupling according to sequence defined by cpdprg2
;pcpd2: f2 channel - 90 degree pulse for decoupling sequence
```

```

;use gradient ratio:    gp 1 : gp 2 : gp 3
;                         80 :   30 : 20.1    for C-13
;                         80 :   30 :  8.1    for N-15

;for z-only gradients:
;gpz1: 80%
;gpz2: 30%
;gpz3: 20.1% for C-13, 8.1% for N-15
;gpz6: 100%; phase encoding gradient, reduce power and cnst6 if gradient pulse (p30) is too short

;use gradient files:
;gpnam1: SMSQ10.100
;gpnam2: SMSQ10.100
;gpnam3: SMSQ10.100
;gpnam6: SMSQ10.32

;$Id: hsqcgpph,v 1.5.4.1.4.3 2014/01/17 15:19:37 ber Exp $
```

A.2.9. pdb-File for (−)-IPC

```
REMARK   This PDB file was created by CS Chem3D.
HETATM    1  C  1  −4.404   0.574   0.660  C
HETATM    2  C  1  −5.858   1.009   0.413  C
HETATM    3  C  1  −6.938  −0.088   0.023  C
HETATM    4  C  1  −6.234  −0.004  −1.388  C
HETATM    5  C  1  −4.905  −0.754  −1.536  C
HETATM    6  C  1  −3.972  −0.542  −0.322  C
HETATM    7  O  1  −2.665  −0.214  −0.805  O
HETATM    8  C  1  −5.959   1.489  −1.067  C
HETATM    9  C  1  −4.207   0.162   2.119  C
HETATM   10  C  1  −8.393   0.424   0.055  C
HETATM   11  C  1  −6.919  −1.447   0.724  C
HETATM   12  H  1  −3.760   1.452   0.509  H
HETATM   13  H  1  −6.199   1.756   1.140  H
HETATM   14  H  1  −6.893  −0.171  −2.247  H
HETATM   15  H  1  −5.106  −1.827  −1.649  H
HETATM   16  H  1  −4.413  −0.442  −2.465  H
HETATM   17  H  1  −3.859  −1.493   0.211  H
HETATM   18  H  1  −2.369  −0.951  −1.366  H
HETATM   19  H  1  −6.783   2.177  −1.283  H
HETATM   20  H  1  −5.060   1.930  −1.511  H
HETATM   21  H  1  −3.161  −0.098   2.309  H
HETATM   22  H  1  −4.824  −0.698   2.392  H
HETATM   23  H  1  −4.478   0.984   2.791  H
HETATM   24  H  1  −8.739   0.525   1.090  H
HETATM   25  H  1  −8.526   1.397  −0.424  H
HETATM   26  H  1  −9.059  −0.281  −0.457  H
HETATM   27  H  1  −7.612  −2.142   0.236  H
HETATM   28  H  1  −5.943  −1.931   0.723  H
HETATM   29  H  1  −7.229  −1.345   1.770  H
CONECT    1    9    6    2   12
CONECT    2    1    8    3   13
CONECT    3   10   11    4    2
CONECT    4    8    3    5   14
CONECT    5    4    6   15   16
CONECT    6    7    1    5   17
CONECT    7    6   18
CONECT    8    2    4   19   20
CONECT    9    1   21   22   23
CONECT   10    3   24   25   26
CONECT   11    3   27   28   29
CONECT   12    1
CONECT   13    2
```

```
CONECT   14    4
CONECT   15    5
CONECT   16    5
CONECT   17    6
CONECT   18    7
CONECT   19    8
CONECT   20    8
CONECT   21    9
CONECT   22    9
CONECT   23    9
CONECT   24   10
CONECT   25   10
CONECT   26   10
CONECT   27   11
CONECT   28   11
CONECT   29   11
END
```

A.2.10. RDC-Input File for (−)-IPC Measured in *poly*-**4**

```
rdc_data {
#C10H10 (Methyl)
9       21      11.9    0.3
9       22      11.9    0.3
9       23      11.9    0.3
#C9H9 (Methyl)
10      24      -8.7    0.6
10      25      -8.7    0.6
10      26      -8.7    0.6
#C8H8 (Methyl)
11      27      5.6             0.4
11      28      5.6             0.4
11      29      5.6             0.4
#C4H4x
5       16      -19.7   0.4
#C4H4n
5       15      56.0    0.4
#C7H7a
8       19      -4.7    0.5
#C7H7s
8       20      -0.5    3.0
#C1H1
2       13      9.8             0.6
#C2H2
1       12      34.2    0.7
```

```
#C3H3
6        17        21.6     0.3
#C5H5
4        14        -25.2    0.4
}
permutations {
#4ab
15 16
#7ab
19 20
}
```

Table A.3.: RDCs determined for (+)-IPC in *poly*-**4** with the slice selective CLIP-HSQC.

Assignment	δ ^{13}C [ppm]	δ ^{1}H [ppm]	$^{1}J_{\mathrm{CH}}$ [Hz]	$^{1}T_{\mathrm{CH}}$ [Hz]	$^{1}D_{\mathrm{CH}}$ [Hz]
C3	71.88	4.05	142.0 ± 0.9	181.2 ± 0.8	39.2 ± 0.9
C1	48.05	1.79	141.6 ± 1.2	133.3 ± 1.7	−8.3 ± 1.7
C2	47.91	1.92	126.4 ± 0.7	148.3 ± 4.7	21.9 ± 4.7
C5	41.98	1.91	142.0 ± 1.1	123.3 ± 0.9	−18.7 ± 1.1
C4-H4s	39.2	2.5	126.6 ± 1.0	150.8 ± 0.5	24.2 ± 1.0
C4-H4a	0	1.69	126.7 ± 0.5	141.2 ± 1.0	14.5 ± 1.0
C6	38.36	-	-	-	-
C7-H7s	34.58	2.35	135.0 ± 0.8	123.7 ± 1.1	−11.3 ± 1.1
C7-H7a	0	1.02	137.0 ± 0.6	129.3 ± 1.1	−7.7 ± 1.1
C8	27.87	1.2	124.5 ± 0.7	134.6 ± 0.6	10.1 ± 0.7
C9	23.88	0.9	123.5 ± 0.5	110.4 ± 2.7	−13.1 ± 2.7
C10	20.93	1.11	124.6 ± 0.4	120 ± 1	−4.6 ± 1.0

A.3. Assignment of (+)-Isopinocampheol

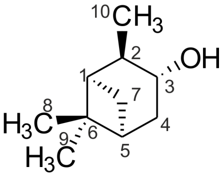

Figure A.4.: Numbered structure (+)-Isopinocampheol.

Table A.4.: Assignment of (+)-Isopinocampheol with corresponding $^{1}J_{\mathrm{CH}}$.

Zuordnung	δ ^{13}C [ppm]	δ ^{1}H [ppm]	$^{1}J_{\mathrm{CH}}$ [Hz]	Δ [Hz]
C3	71.87	4.07	142.1	0.1
C1	48.06	1.81	140.9	0.3
C2	47.91	1.94	126.6	0.2
C5	41.99	1.94	141.2	0.3
C4, H4s	39.22	2.52	126.6	0.3
H4a		1.72	126.9	0.2
C6		-		
C7, H7s	34.59	2.38	135.2	0.4
H7a		1.05	137.0	0.1
C8	27.84	1.22	124.6	0.1
C9	23.84	0.93	123.6	0.1
C10	20.95	1.14	124.8	0.2

Table A.5.: All couplings from the spectrum recorded with the ω_1-coupled ADEQUATE sequence in Figure 6.6 (+)-IPC (part one).

Assignment	^{13}C $_{\text{DQ,calc}}$ [ppm]	^{13}C $_{\text{DQ,meas}}$ [ppm]	δ 1H [ppm]	$^{1+2}J_{\text{CH}}$ [Hz]	Error [Hz]	$^{1}J_{\text{CH}}$ [Hz]	$^{2}J_{\text{CH}}$ [Hz]
C3-C2	75.29	74.62	4.04	259.3	0.2	142.1	-12.5
C3-C4	66.58	66.07		121.7	1.7	126.6	-4.9
		66.07		140	1.7	142.1	-2.1
C4-C3	66.58	65.88	2.45	384.1	0.7	142.0	-14.0
C4-C5	36.68	36.16		384.6	0.9	141.0	-12.8
C7-C1	38.13	37.63	2.34	138	0.7	135.2	2.8
				404.3	1.0	137.0	267.3
C7-C5	32.06	31.65		138.5	0.7	135.2	3.3
				404.5	1.0	137.0	267.5
C2-C3	75.29	74.62	1.93	259	1.0	142.1	-12.6
C2-C10	24.36	24.2		120.5	0.7	126.6	-6.1
C2-C10				364.6	0.4	124.8	-3.3
C5-C4	36.68	36.26	1.92	122.7	0.4	126.6	-3.9
C5-C6	35.84	35.40		123.2	0.9	141.2	-18.0
C5-C7	32.06	31.59		132	1.4	135.2	-3.2
C5-C7				138.4	1.6	141.2	-2.8
C1-C2	51.46		1.78	139	0.8		139.0
C1-C6	41.91	41.46		139	0.8	140.9	-1.9
C1-C7	38.13	37.64		132.3	1.4	135.2	-2.9
				139.3	1.3	137.0	2.3

Table A.6.: All couplings from the spectrum recorded with the ω_1-coupled ADEQUATE sequence in Figure 6.6 for (+)IPC (part two).

Assignment	^{13}C $_{\mathrm{DQ,calc}}$ [ppm]	^{13}C $_{\mathrm{DQ,meas}}$ [ppm]	δ 1H [ppm]	$^{1+2}J_{\mathrm{CH}}$ [Hz]	Error [Hz]	$^{1}J_{\mathrm{CH}}$ [Hz]	$^{2}J_{\mathrm{CH}}$ [Hz]
C4-C3	61.96	65.97	1.70	140.2	0.3	142.1	-1.9
C4-C3				119.4	0.6	126.6	-7.2
C4-C5	-5.3	36.20		139.6	0.6	141.2	-1.6
C4-C5				385.2	0.6	126.6	1.8
C8-C6	21.7	21.32	1.20	120.6	0.3	124.6	-4.0
				361.7	0.2	124.6	-4.0
C10-C2	24.36	23.79	1.11	121.4	0.5	126.6	-5.2
				363	0.6	124.8	-3.8
C7-C1	38.13	37.62	1.04	138.3	0.2	140.9	-2.6
				265	1.3	272.2	-7.2
C7-C5	32.06	31.55		138.8	1.1	141.2	-2.4
				265.5	0.8	272.2	-6.7
C9-C6	17.74	17.28	0.91	119.3	0.3	123.6	-4.3
				357.8	0.3	123.6	-4.3

A.4. Assignment of (*S*)-Ibuprofene

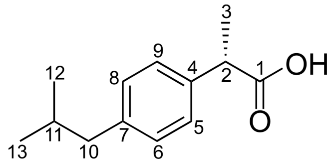

Figure A.5.: Numbered Structure of (*S*)-Ibuprofene

Table A.7.: Assignment of (*S*)-Ibuprofene.

Assignment	δ ^{13}C [ppm]	δ ^{1}H [ppm]	$^{1}J_{CH}$ [Hz]	Δ [Hz]
Cq, C1	180.55			
C7	140.87			
C4	136.98			
C5-C6	129.4	7.1	157.2	0.8
C8-C9	127.28	7.22	156.7	0.9
C10	45.05	2.45	125.4	0.3
C2	44.92	3.71	130.2	0.4
C11	30.16	1.85	127.1	0.4
C12,C13	22.39	0.9	124.6	0.2
C3	18.12	1.5	129.1	0.1

Table A.8.: Extracted splittings for all cross peaks of the ω_1-coupled ADEQUATE for the (*S*)-Ibuprofene.

Assignment	^{13}C $_{\text{DQ}}$ [ppm]	^{1}H [ppm]	$^{1+2}J_{\text{CH}}$ [Hz]	Δ [Hz]	$^{1}J_{\text{CH}}$ [Hz]	$^{2}J_{\text{CH}}$ [Hz]
C5,C9-C4	184.68	7.22	169.3	1.3	156.7	12.6
C5,C9-C5,6	177.15		315.1	4.2	156.7	0.85
C8,C6- C7	190.64	7.11	165.9	1.1	157.2	8.7
C8, C6 - C5, C9	177		319.4	1	157.2	2.5
C2-C1	145.8	3.71	122.3	2.2	130.2	-7.9
C2-C4	102.3		126	0.9	130.2	-4.2
C2-C3	-16.52		121.8	2.3	130.2	-8.4
C10-C7	106.29	2.45	242.4	1.2	125.4	-4.2
C10-C11	-4.46		123.6	1.5	125.4	-1.3
C10-C11			364.8	1.1	125.4	-1.3
C11-C10	-4.4	1.85	364.4	2.4	127.1	-5.6
C11-C12u.C13	-27.06		122.3	1.8	127.1	-4.8
			118.6	3.7	127.1	-8.5
C3-C2	-16.72	1.5	125.8	2.3	129.1	-3.3
			123.2	0.9	129.1	-5.9
C12,C13-C11	-27.06	0.9	123.1	1.6	124.6	-1.5

Table A.9.: Extracted splittings for all cross peaks of the ω_1-coupled-BIRD$^{\text{r}}$ ADEQUATE for the (*S*)-Ibuprofene.

Assignment	^{13}C $_{\text{DQ}}$ [ppm]	^{1}H [ppm]	$^{1+2}J_{\text{CH}}$ [Hz]	Δ [Hz]	$^{1}J_{\text{CH}}$ [Hz]	$^{2}J_{\text{CH}}$ [Hz]
C5,C9-C4	184.68	7.22	157.7	2	156.7	1
C5,C9-C5,6	177.15		317.4	2.7	156.7	2
C8,C6- C7	190.64	7.11	156.4	2.9	157.2	-0.8
C8, C6 - C8, C9	177		316.6	1.5	157.2	1.1
C2-C1	145.8	3.71	120.7	1.6	130.2	-9.5
C2-C4	102.3		122.7	4	130.2	-7.5
C2-C3	-16.52		123.7	2.6	130.2	-6.5
C10-C7	106.29	2.45	240.3	1.8	125.4	-5.25
C10-C11	-4.46		123.9	3.4	125.4	-1.5
C10-C11			364.8	1.7	125.4	-1.3
C11-C10	-4.4	1.85	366.3	2.6	127.1	-5
C11-C12u.C13	-27.06		121.8	2.8	127.1	-5.3
			119.9	2.9	127.1	-7.2
C3-C2	-16.72	1.5	127.7	1.7	129.1	-1.4
C3-C2			124.3	1.2	129.1	-4.8
C12,C13-C11	-27.06	0.9	121.5	2.4	124.6	-3.1

A.5. Assignment of Strychnine

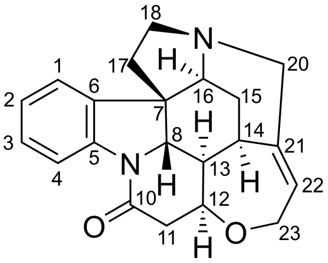

Figure A.6.: Numbered structure of strychnine.

Table A.10.: Assignment of strychnine and corresponding $^1J_{CH}$ coupling constants.

Assignment	δ ^{13}C [ppm]	δ ^{1}H [ppm]	$^1J_{CH}$ [Hz]	Δ [Hz]
C10	169.48	-	-	-
C5	142.41	-	-	-
C21	140.71	-	-	-
C6	132.34	-	-	-
C3	128.75	7.18	158.9	1.6
C22	127.47	5.83	159.0	0.2
C2	124.40	7.02	160.4	0.5
C1	122.46	7.09	158.2	0.3
C4	116.42	8.02	168.4	0.1551
C12	77.80	4.21	149.0	0.2
C23	64.80	4.07	145.3	0.1
C23		3.99	137.1	0.2
C16	60.41	3.87	146.5	0.2
C8	60.30	3.78	144.9	0.1
C20	52.87	3.63	138.5	0.2
C20		2.66	138.2	0.2
C7	51.92	-	-	-
C18	50.54	3.13	145.9	0.4
C18		2.80	131.0	1.1
C13	48.42	1.20	124.8	0.2
C17	43.05	1.82	132.5	0.5
C11	42.69	3.04	135.2	0.1
C11		2.6	125.5	0.2
C14	31.79	3.07	131.1	0.2
C15	27.04	2.29	130.8	0.3
C15		1.38	129.7	0.3

Table A.11.: Extracted double quantum frequencies of the carbon with the corresponding proton frequency for strychnine, the extracted sums ($^{1+2}J_{CH}$) of the signals, the corresponding $^1J_{CH}$ from the CLIP-HSQC spectrum and the calculated $^2J_{CH}$ value (Equation: 6.9). The spectrum was recorded with the ω_1-coupled ADEQUATE (Figure 6.6) and the full spectrum is shown in Figure 6.12A.

	$^{13}C_{DQ}$ [ppm]	^1H [ppm]	$^{1+2}J_{CH}$ [Hz]	Δ [Hz]	$^1J_{CH}$ [Hz]	$^2J_{CH}$ [Hz]	Assignment
C4,C5	177.87	8.11	165.3	4.6	168.4	-3.1	C5-H4
C1,C6	174.39	7.11	160.6	4	158	2.6	C6-H1
C22,C21	187.29	5.92	158.8	3	158.8	0	C21-H22
C16, C7	31.64	3.96	147.8	4.7	146.5	1.3	C7-H16
C7, C8	31.46	3.87	143.5	3.5	144.9	-1.4	C7-H8
C20, C21	112.66	3.72	269.6	4.3	276.8	-7.2	C21-H20
C14, C21	91.53	3.16	126.1	3.2	131.2	-5.1	C21-H14
C10, C11	131.26	3.13	246.4	0.8	260.7	-14.3	C10-H11
C20, C21	112.67	2.74	271.4	2.5	276.8	-5.4	C21-H20
C10, C11	131.25	2.68	246.1	0.5	260.7	-14.6	C10-H11
C17, C7	14.28	1.92	258.6	1.1	265.6	-7	C7-H17

Table A.12.: Extracted double quantum frequencies of the carbon with the corresponding proton frequency for strychnine, the extracted sums (${}^{1+2}J_{\mathrm{CH}}$) of the signals, the corresponding ${}^{1}J_{\mathrm{CH}}$ from the CLIP-HSQC spectrum and the calculated ${}^{2}J_{\mathrm{CH}}$ value (Equation 6.9). The spectrum where the values were extracted, was recorded with the sequence shown in Figure 6.9 and the full spectra are shown in Figure 6.12B.

	${}^{13}\mathrm{C}_{\mathrm{DQ}}$ [ppm]	${}^{1}\mathrm{H}$ [ppm]	${}^{1+2}J_{\mathrm{CH}}$ [Hz]	Δ [Hz]	${}^{1}J_{\mathrm{CH}}$ [Hz]	${}^{2}J_{\mathrm{CH}}$ [Hz]	Assignment
C4,C5	177.94	8.02	166.1	1	168.4	-2.3	C5-H4
C1,C6	174.4	7.09	159.6	1.4	158	1.6	C6-H1
C22,C21	187.24	5.83	160.8	0.8	158.8	2	C21-H22
C16, C7	31.68	3.88	145	1	146.5	-1.5	C7-H16
C7, C8	31.53	3.79	141.9	1.8	144.9	-3	C7-H8
C20, C21	112.56	3.64	269.5	1.7	276.8	-7.3	C21-H20
C14, C21	91.5	3.07	124.7	1.8	131.2	-6.5	C21-H14
C10, C11	131.21	3.04	246.4	2.6	260.7	-14.3	C10-H11
C20, C21	112.56	2.66	269.7	2	276.8	-7.1	C21-H20
C10, C11	131.26	2.6	246.5	1.5	260.7	-14.2	C10-H11
C17, C7	14.8	1.82	259.1	1	265.6	-6.5	C7-H17

A.6. Pulse Programs for $^2J_{\mathrm{CH}}$ Coupling Measurement

All pulse programs are in the Bruker Topspin format.

A.6.1. Pulse Program for ω_1-coupled ADEQUATE

```
4u
DELTA5 pl0:f2
(p24:sp7 ph8):f2
4u
DELTA5 pl2:f2
(p3 ph9):f2
d0
;(p2 ph1)
d0
DELTA1 pl0:f2 ;UNBLKGRAD
(p24:sp7 ph11):f2
3u
p16:gp1
d16 pl2:f2
(p0 ph10):f2
4u
p16:gp2
d16
DELTA3 pl0:f2
(p24:sp7 ph11):f2
4u
DELTA5 pl2:f2
(center (p1 ph1) (p3 ph5):f2 )
;4u
;DELTA6 pl0:f2
d24 pl0:f2 pl0:f1
(p24:sp2 ph1) (p24:sp7 ph12):f2
d24 pl2:f2 pl1:f1
;4u
;DELTA6 pl2:f2
(center (p1 ph2) (p3 ph6):f2 )
;4u
;DELTA4 pl0:f2
d4 pl0:f2 pl0:f1
(p14:sp1 ph1:r) (p14:sp3 ph1):f2
d4 pl1:f1
;4u
;DELTA4
```

```
(p1 ph1)
DELTA2
(p2 ph1)
3u
p16:gp3*EA
d16 pl12:f2
3u BLKGRAD
go=2 ph31 cpd2:f2
d1 do:f2 mc #0 to 2 F1EA(calgrad(EA) & calph(ph6, +180), caldel(d0, +in0))
exit

ph1=0
ph2=1
ph4=0 2
ph5=0 0 2 2
ph6=1 1 3 3
ph7=0
ph8=0
ph9=0 0 0 0 2 2 2 2
ph10=0 0 0 0 0 0 0 0 2 2 2 2 2 2 2 2
ph11=0
ph12=0
ph31=0 2 2 0 2 0 0 2 2 0 0 2 0 2 2 0

;pl0 : 0W
;pl1 : f1 channel - power level for pulse (default)
;pl2 : f2 channel - power level for pulse (default)
;pl12: f2 channel - power level for CPD/BB decoupling

;sp1: f1 channel - shaped pulse (180degree refocussing)
;sp3: f2 channel - shaped pulse (180degree inversion)
;sp2: f1 channel - shaped pulse (180degree refocussing)
;sp7: f2 channel - shaped pulse (180degree refocussing)

;spnam1: jc02_BURBOP_x_600u_BW10_RF20_pm20_matched
;spnam3: jc03_BIBOP_600u_BW37.5_RF10_pm5_matched
;spnam2: BUBU180x_1H_1000u_BW10_RF18.5_pm20_matched
;spnam7: BUBU180x_13C_1000u_BW37.5_RF20_pm5_matched

;p0 : f2 channel -  60 degree high power pulse
;p1 : f1 channel -  90 degree high power pulse
;p2 : f1 channel - 180 degree high power pulse
;p3 : f2 channel -  90 degree high power pulse
;p13: gradient to destroy Boltzmann 13C
                    [1 ms]
```

```
;p14: f1 and f2 channel - 180 degree shaped pulse - inversion for 13C - refocusing for 1H
;     = 600usec for matchted jc02_BURBOP an jc03_BIBOP
;p16: homospoil/gradient pulse
;p24: f1 and f2 channel - 180 degree shaped pulse for refocussing
;     = 1msec for BUBU180x_13C and BUBU180x_1H

;d0 : incremented delay (2D)                         [3 usec]
;d1 : relaxation delay; 1-5 * T1
;d4 : 1/4J(CH)
;d11: delay for disk I/O                             [30 msec]
;d16: delay for homospoil/gradient recovery
;d23: 1/(4J(CC))
;d24: 1/(4J)CH for CH
;     1/(6J)CH for all multiplicities
;cnst2 : J(CH) = 127 .. 160 Hz
;cnst3 : J(CC) = 35 .. 55 Hz
;cnst11: for multiplicity selection = 4 for CH, 6 for CHn
;cnst17: = -0.5 for Crp60comp.4
;inf1: 1/SW(DQ-C) = 4 * DW(C)
;in0: 1/(2 * SW(DQ-C)) = 2 * DW(C)
;nd0: 2
;ns: 16 * n
;ds: >= 16
;td1: number of experiments
;FnMODE: echo-antiecho
;cpd2: decoupling according to sequence defined by cpdprg2
;pcpd2: f2 channel - 90 degree pulse for decoupling sequence

;use gradient ratio:    gp 1 :  gp 2 : gp 3
;                      -78.4 : -77.4 :  -59    for C-13

;for z-only gradients:
;gpz1: -78.4%
;gpz2: -77.4%
;gpz3: -59%

;gp13: 40%

;use gradient files:
;gpnam1: SMSQ10.100
;gpnam2: SMSQ10.100
;gpnam3: SMSQ10.100

;cnst17: Factor to compensate for coupling evolution during a pulse
```

```
;       (usually +1). A positive factor indicates that coupling
;       evolution continues during the pulse, whereas a negative
;       factor is necessary if the coupling is (partially) refocussed.

;F1 reverse: true
```

A.6.2. Pulse Program for ω_1-coupled-BIRD^{r} ADEQUATE

```
;adeq11etgpsp
;avance-version (12/01/11)
;1,1-ADEQUATE: 2D-HSQC-1J(CC)-ADEQUATE
;                 using sensitivity improvement
;phase sensitive using Echo/Antiecho gradient selection
;with decoupling during acquisition
;not decoupled during t1
;using shaped pulses for 180degree pulses on f2 - channel
;modified with Sebastian's and Tony's 180degree pulses on both channels (October 2016)
;
;B. Reif, M. Koeck, R. Kerssebaum, H. Kang, W. Fenical & C. Griesinger
;   J. Magn. Reson. A118, 282-285 (1996).
;
;$CLASS=HighRes
;$DIM=2D
;$TYPE=
;$SUBTYPE=
;$COMMENT= ADEQUATE mit BIRDr Filter in der indirekten Dimension;

#include <Avance.incl>
#include <Delay.incl>
#include <Grad.incl>

"p2=p1*2"
"d0=3u"
"d11=30m"

"p0=p3*0.667"
"d4=1s/(cnst2*4)"
"d2=1s/(cnst2*2)"
"d23=1s/(cnst3*4)"
"d24=1s/(cnst2*cnst11)"

"in0=inf1/2"

"DELTA1=p16+d16-d0*2+3u"
```

```
"DELTA2=p16+d16+6u+de-p1*0.78"
"DELTA3=d23-p16-d16-p24/2-4u"
"DELTA5=d23-p24/2-4u"
"DELTA7=d2-p16-d16-larger(p2,p39)/2"

"acqt0=0"
baseopt_echo

1 ze
d11 pl12:f2
2 d1 do:f2

; destroy Boltzmann 13C
4u pl2:f2
50u UNBLKGRAD
(p3 ph1):f2
4u
p13:gp13
d16
; start experiment

3 (p1 ph1)
d4 pl0:f2 pl0:f1
(p14:sp1 ph1) (p14:sp3 ph1):f2
d4 pl1:f1 pl2:f2
(p1 ph2) (p3 ph4):f2
4u
DELTA5 pl0:f2
(p24:sp7 ph8):f2
4u
DELTA5 pl2:f2
(p3 ph9):f2

;bird filter
d0
(p1 ph1)
p16:gp4
d16
DELTA7 pl0:f2
(center (p2 ph1) (p39:sp4 ph1):f2 )
DELTA7
p16:gp4
d16
(p1 ph7)
(p39:sp4 ph1):f2
```

```
d0
; end bird filter

DELTA1 pl0:f2 UNBLKGRAD
(p24:sp7 ph11):f2
3u
p16:gp1
d16 pl2:f2
(p0 ph10):f2
4u
p16:gp2
d16
DELTA3 pl0:f2
(p24:sp7 ph11):f2
4u
DELTA5 pl2:f2
(center (p1 ph1) (p3 ph5):f2 )
d24 pl0:f2 pl0:f1
(p24:sp2 ph1) (p24:sp7 ph12):f2
d24 pl2:f2 pl1:f1
(center (p1 ph2) (p3 ph6):f2 )
d4 pl0:f2 pl0:f1
(p14:sp1 ph1:r) (p14:sp3 ph1):f2
d4 pl1:f1
(p1 ph1)
DELTA2
(p2 ph1)
3u
p16:gp3*EA
d16 pl12:f2
3u BLKGRAD
go=2 ph31 cpd2:f2
d1 do:f2 mc #0 to 2 F1EA(calgrad(EA) & calph(ph6, +180), caldel(d0, +in0))
exit

ph1=0
ph2=1
ph4=0 2
ph5=0 0 2 2
ph6=1 1 3 3
ph7=2
ph8=0
ph9=0 0 0 0 2 2 2 2
ph10=0 0 0 0 0 0 0 0 2 2 2 2 2 2 2 2
ph11=0
```

```
ph12=0
ph31=0 2 2 0 2 0 0 2 2 0 0 2 0 2 2 0

;pl0 : 0W
;pl1 : f1 channel - power level for pulse (default)
;pl2 : f2 channel - power level for pulse (default)
;p39: f2 channel - 180 degree shaped pulse for refocussing
;                      Bip720,100,10.1 (100us at 600.13 MHz)
;pl12: f2 channel - power level for CPD/BB decoupling

;sp1: f1 channel - shaped pulse (180degree refocussing)
;sp3: f2 channel - shaped pulse (180degree inversion)
;sp4: f2 channel - shaped pulse (180degree refocussing)[20khz rf-amplitude]
;sp2: f1 channel - shaped pulse (180degree refocussing)
;sp7: f2 channel - shaped pulse (180degree refocussing)

;spnam1: jc02_BURBOP_x_600u_BW10_RF20_pm20_matched
;spnam3: jc03_BIBOP_600u_BW37.5_RF10_pm5_matched
;spnam2: BUBU180x_1H_1000u_BW10_RF18.5_pm20_matched
;spnam7: BUBU180x_13C_1000u_BW37.5_RF20_pm5_matched

;p0 : f2 channel -  60 degree high power pulse
;p1 : f1 channel -  90 degree high power pulse
;p2 : f1 channel - 180 degree high power pulse
;p3 : f2 channel -  90 degree high power pulse
;p13: gradient to destroy Boltzmann 13C
                    [1 ms]

;p14: f1 and f2 channel - 180 degree shaped pulse - inversion for 13C -
    refocusing for 1H
;     = 600usec for matchted jc02_BURBOP an jc03_BIBOP
;p16: homospoil/gradient pulse
;p24: f1 and f2 channel - 180 degree shaped pulse for refocussing
;     = 1msec for BUBU180x_13C and BUBU180x_1H

;d0 : incremented delay (2D)                         [3 usec]
;d1 : relaxation delay; 1-5 * T1
;d4 : 1/4J(CH)
;d11: delay for disk I/O                             [30 msec]
;d16: delay for homospoil/gradient recovery
;d23: 1/(4J(CC))
;d24: 1/(4J)CH for CH
;     1/(6J)CH for all multiplicities
;cnst2 : J(CH) = 127 .. 160 Hz
;cnst3 : J(CC) = 35 .. 55 Hz
```

```
;cnst11: for multiplicity selection = 4 for CH, 6 for CHn
;cnst17: = -0.5 for Crp60comp.4
;inf1: 1/SW(DQ-C) = 4 * DW(C)
;in0: 1/(2 * SW(DQ-C)) = 2 * DW(C)
;nd0: 2
;ns: 16 * n
;ds: >= 16
;td1: number of experiments
;FnMODE: echo-antiecho
;cpd2: decoupling according to sequence defined by cpdprg2
;pcpd2: f2 channel - 90 degree pulse for decoupling sequence

;use gradient ratio:    gp 1 :  gp 2 : gp 3
;                      -78.4 : -77.4 :  -59    for C-13

;for z-only gradients:
;gpz1: -78.4%
;gpz2: -77.4%
;gpz3: -59%
;gpz4: 11%
;gpz13: 40% destroy Sz

;use gradient files:
;gpnam1: SMSQ10.100
;gpnam2: SMSQ10.100
;gpnam3: SMSQ10.100
;gpnam4: SMSQ10.100
;gpnam13: SMSQ10.100

;cnst17: Factor to compensate for coupling evolution during a pulse
;       (usually +1). A positive factor indicates that coupling
;       evolution continues during the pulse, whereas a negative
;       factor is necessary if the coupling is (partially) refocussed.

;F1 reverse: true
```

B. Danksagung

Hier möchte ich allen danken, die mich während der Zeit und bei der Anfertigung dieser Arbeit betreut, unterstützt, beeinflusst oder ermutigt und aufgemuntert haben.

Prof. Dr. Burkhard Luy für die Aufnahme in seinen Arbeitskreis, die herausfordernden Projekte, bei denen er mich sowohl unterstützt und auch meinen eigenen Weg hat gehen lassen, und die Geduld bei der Lehre der NMR-Spektroskopie.
Prof. Dr. Peter Roesky für die Übernahme des Zweitgutachtens und ihm und seinem Mitarbeiter Christoph Schoo für die Zusammenarbeit und gemeinsame Synthese der Europiumkomplexe.
PD Dr. Claudia Muhle-Goll die Gespräche, für ihren unermüdlichen Einsatz bei der Organisation des Arbeitskreises, des Bioanalytikpraktikums und der Unterstützung.
Dr. Pavleta Tzvetkova für ihre Tipps, Antworten auf alle Fragen, ihre selbstloses Engagement für die Sprektrometer und den Mittagspausen.
Dr. Tony Reinsperger und Thomas Gloge für die aufbauenden und ausschweifenden Gespräche, fachlichen Diskussionen, lustigen Mittagspausen und die Schnöselkaffees.
Dr. Maria Enrica di Pietro, die mir bei der Herstellung der Proben geholfen hat, ihre positive Art und dafür mich an das Gute im Menschen und mir zu erinnern.
Allen anderen Mitgliedern des Arbeitskreises für die schöne und kameradschaftliche Zeit, die Kaffeepausen und Diskussionen.
Prof. Dr. Michael Reggelin und seinen Mitarbeitern Svenja Wesp und Kai Wolf für die Idee eines gemeinsamen Projekts, der Durchführung dessen und der erfolgreiche Abschluss davon.
Prof. Dr. Peter Roesky und seinem Mitarbeiter Christoph Schoo für die Zusammenarbeit und gemeinsame Synthese der Europiumkomplexe. Prof. Dr. Manfred Wilhelm und Dr. Johannes Höpfner für die Messzeit und Hilfestellungen am Magritek-Spektrometer und die Geduld mir bei der Aufarbeitung der Daten zur Seite zu stehen.
Allen, die meine Arbeit unterstützt haben, durch Korrekturlesen, Unterstützung und gemeinsamen Mittagspausen.
Meinen Freunden, den Theatermenschen, meiner Band und dem UTO für die Ablenkung, die lustigen Partys und die Anteilnahme an den vielschichtigen Prozessen innerhalb der Promotionszeit.
Meiner Familie. Ich danke euch, dass ihr immer für mich da seid, an mich glaubt und mir das auch immer wieder vermittelt!
Dem wichtigsten Menschen in meinem Leben, Jan! Ich danke dir so sehr, dass du mich bei allen meinen Ideen unterstützt und mir dabei hilfst, sie umzusetzen. Außerdem bringst du mich regelmäßig zur Vernunft und zum Lachen, danke dafür!